UNIVERSITY OF LIÈGE

FACULTY OF APPLIED SCIENCES

Feasibility of a UV imager onboard a Cubesat platform

Master thesis

Thesis submitted in partial fulfilment of the requirements for the degree of Master in Engineering Physics by Kintziger Christian.

STUDENT:	Christian KINTZIGER
JURY:	Pr. Serge HABRAKEN, ULg, CSL
	Pr. Gaëtan KERSCHEN, ULg
	Pr. Jean SURDEJ, ULg
SUPERVISOR:	Pr. Pierre ROCHUS, ULg, CSL

Academic year: 2012-2013

Table of contents

List of acronyms

ACS	-	Attitude Control System
ADCS	-	Attitude Determination and Control System
ADS	-	Attitude Determination System
ALL-STAR	-	Agile Low-cost Laboratory for Space Technology Acceleration and Research
APS	-	Active Pixel Sensor
AWSS	-	Autonomous Wireless Sun Sensors
BFL	-	Back Focal Length
C&DH	-	Command and Data Handling
CAD	-	Computer-Aided design
CADRE	-	Cubesat Investigating Atmospheric Density Response to Extreme Driving
CCD	-	Charge-Coupled device
CMG	-	Control Moment Gyros
CMOS	-	Complementary Metal Oxide Semiconductor
COTS	-	Commercial Off-The-Shelf
CSL	-	Centre Spatial de Liège
DC	-	Direct Current
DOD	-	Depth Of Discharge
DQE	-	Detective Quantum Efficiency
EBCCD	-	Electron-Bombarded CCD
EFL	-	Effective Focal Length
EPD	-	Entrance Pupil Diameter
EPS	-	Electrical Power Subsystem
EUI	-	Extreme Ultraviolet Imager
EUV	-	Extreme Ultraviolet
FEA	-	Finite Element Analysis
FIDI	-	Flare Initiation Doppler Imager
FoV	-	Field of View
GENSO	-	Global Educational Network for Satellite Operations
GPS	-	Global Positioning System
GSD	-	Ground Sample Distance
HEO	-	High Earth Orbit
HETE	-	High Energy Transient Explorer
HST	-	Hubble Space Telescope
HUT	-	Hopkins Ultraviolet Telescope
ICCD	-	MCP-Intensified CCD
IMAGE	-	Imager for Magnetopause-to-Aurora Exploration
IMU	-	Inertial Measurement Unit
IR	-	Infrared
IRTF	-	Infrared Telescope Facility
ISS	-	International Space Station

I-V	-	Current-Voltage
JPL	-	Jet Propulsion Laboratory
KISS	-	Keep It Simple, Stupid
LEO	-	Low Earth Orbit
LOS	-	Line-Of-Sight
LPAP	-	Laboratory of Planetary and Atmospheric Physics
LV	-	Launch Vehicle
LYRA	-	Large Yield RAdiometer
MBE	-	Molecular Beam Epitaxial
MCP	-	Microchannel Plate
MEMS	-	MicroElectroMechanical Systems
Micro-PPT	-	Micro Pulsed Plasma Thrusters
MISC	-	Miniature Imaging Spacecraft
MIT	-	Massachusetts Institute of Technology
MLI	-	Multi-Layer Insulation
MPPT	-	Maximum Power Point Tracking
MTF	-	Modulation Transfer Function
NASA	-	National Aeronautics and Space Administration
NoP	-	Number of Pixels
NSF	-	National Science Foundation
OBC	-	OnBoard Computer
OPD	-	Optical Path Difference
P-POD	-	Poly-PicoSatellite Orbital Deployer
PROBA	-	Project for On-Board Autonomy
PSF	-	Point-Spread Function
P-V	-	Peak-to-Valley
RAAN	-	Right Ascension of the Ascending Node
RAP	-	Radio Amateur Platform
RMS	-	Root Mean Square
RSS	-	Root Sum Square
RTICC	-	Rapid Terrestrial Imaging Cubesat Constellation
SBC	-	Single-Board Computer
SD	-	Secure Digital
SDK	-	Software Development Toolkit
SDS-1	-	Sun Devil Satellite 1
SDSL	-	Sun Devil Satellite Laboratory
SFoV	-	Semi-Field of View
SiC	-	Silicon Carbide
SNR	-	Signal-to-Noise Ratio
SSO	-	Sun-Synchronous Orbit
STK	-	Satellite Tool Kit
STSat-1	-	Science and Technology Satellite-1
SWAP	-	Sun Watcher using APS detectors and image Processing
TFSC	-	Thin Film Solar Cells
TGF	-	Terrestrial Gamma-ray Flashes

THEIA	-	Telescopic High-definition Earth Imaging Apparatus
U	-	Unit
UHF	-	Ultra High Frequency
UIT	-	Ultraviolet Imaging Telescope
UNISEC	-	UNIversity Space Engineering Consortium
USB	-	Universal Serial Bus
UV	-	Ultraviolet
UVIS	-	Ultraviolet Imaging Spectrograph Subsystem
VHF	-	Very High Frequency
VUV	-	Vacuum Ultraviolet
WFE	-	Wavefront Error
WINCS	-	Wind Ion Neutral Composition Suite
WSO-UV	-	World Space Observatory - Ultraviolet
WUPPE	-	Wisconsin Ultraviolet Photo-Polarimetry Experiment
XACT	-	fleXible ADCS Cubesat Technology

List of figures

List of tables

Abstract

This Master thesis presents the feasibility study of an ultraviolet imager onboard a Cubesat platform. The goal is to observe the Io's torus with the help of a triple unit Cubesat. Similar projects are studied to identify possible components for the mission. A mission analysis is carried out to highlight suitable intervals of time to observe the Io's torus when considering different orbits. Then optical design processes are performed to obtain a telescope that fits in the Cubesat platform. Eventually a final design that fulfils all the scientific requirements is introduced and a few perspectives are proposed for the future studies.

Key words: Cubesat, UV imager, Io's torus, Jupiter, optical design, optimization process, ray-tracing, Code V.

Kintziger Christian
Faculty of Applied Sciences
University of Liège

Acknowledgement

The first person I would like to thank is Professor Pierre Rochus who gave me the opportunity to perform my Master Thesis at the Centre Spatial de Liège and to rub shoulders with all the scientists who actively participate in the development of space missions. To discuss with them and benefit from their advice was actually an attractive feature in the acquisition of professional experience.

I really thank Pr. Serge Habraken for his valuable help in the optical design of the telescope and his availability during my work. His advice really helped me to carry out the project.

Thanks to Pr. Gaëtan Kerschen and Lamberto Dell'Elce for their help in mission analysis and attitude control systems.

I thank Pr. Jean Surdej who gave me the opportunity to take part in an astronomy project which enabled me to have a practical approach of space observation.

Many thanks to Lucas Salvador for his encouragement, support, advice, help and huge patience during my thesis. I really thank him for all the time he dedicated to me in his office.

Thanks to Bertrand Bonfond and Denis Grodent for their time to explain me the scientific aspects of the mission.

Many thanks to Alexandra Mazzoli, Lionel Clermont and Nathalie Ninane for all the explanations they provided me about *Code V*.

Thanks to my all my family for their patience and amiability.

Chapter 1

Introduction

1.1. Mission study

1.1.1. Scientific goals

The primary aim of the mission is to capture the physics of the Io's torus, one of Jupiter's satellites, in order to identify its relations with the Jupiter's auroras. The period of observation would typically last several weeks or months, possibly one year. The initial idea was to complement the results of the JUNO observatory once in orbit.

A great mass loss from Io is induced by the interaction between its atmosphere and Jupiter's magnetosphere. Actually, volcanoes on Io induce the sublimation of SO_2 frost and approximately $1\ ton$ of SO_2 is released every second by Io's atmosphere in the form of a neutral cloud (Bonfond, et al., 2011). A part of this material directly comes from Io's exosphere in the form of ions while a significant portion is made up of molecules and neutral atoms. These particles are principally sulphur and oxygen atoms and their compounds. All of this matter follows Io on its orbit around Jupiter and a half become ionized through charge exchange and electron impact. These charged particles are accelerated in the corotational plasma flow and constitute a torus of ions called the *Io plasma torus* as represented in Figure 1. The other half of this matter escapes the magnetosphere and becomes energetic neutral atoms through charge exchange (Thomas, Bagenal, Hill, & Wilson, 2004).

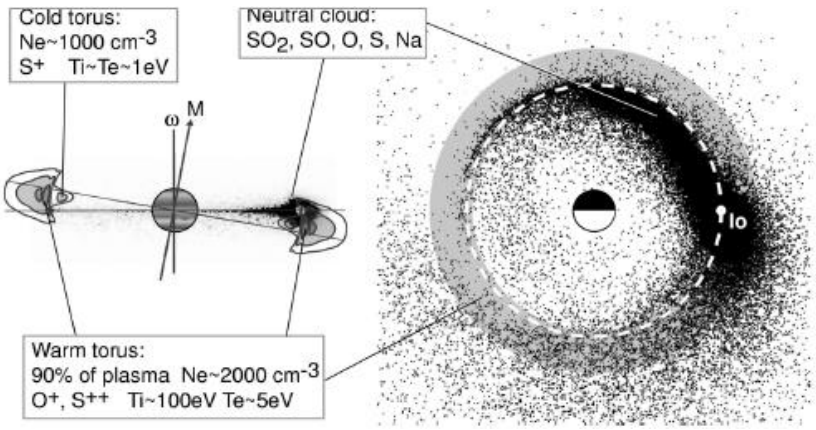

Figure 1 - The Io's plasma torus (Thomas, Bagenal, Hill, & Wilson, 2004)

Sodium D-line was the first evidence of this phenomenon in a "cloud" near Io. *Voyager 1* highlighted a SO_2 atmosphere and a surface mainly composed of sulphur. Since its emission is 30 times more intense in the visible range than any other, sodium is the most

often observed specie. *Pioneer 10* was the first to investigate the Io's torus composition by means of a UV photometer but most of its results have been proven incorrect (Thomas, Bagenal, Hill, & Wilson, 2004).

Great measurements during *Voyager 1* mission have provided scientists a benchmark of low energy heavy ions population for almost 20 years and is still used nowadays. This distribution is shown in Figure 2 and is highly variable with time (Thomas, Bagenal, Hill, & Wilson, 2004).

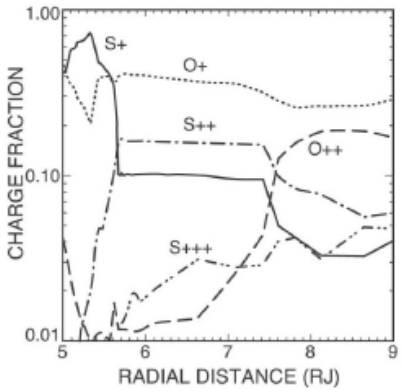

Figure 2 - Ion composition derived from emissions measured by *Voyager 1* (Thomas, Bagenal, Hill, & Wilson, 2004)

The relationship between the Jupiter's auroras and the Io's torus may be volcanoes on Io that would be the source of large variations of multiple components of the auroras. Therefore, the idea is to monitor the Io's torus while the JUNO observatory is in orbit around Jupiter to be able to correlate their physical behaviour and identify the mechanisms connecting them and the involved chemical species (Bonfond, et al., 2011).

Figure 3 shows pictures of the Jupiter's auroras acquired less than two hours apart in June 2007 taken by the Hubble Space Telescope (HST) and the NASA Infrared Telescope Facility (IRTF). The upper HST picture represents the Jupiter's northern hemisphere in the UV domain while the bottom side IRTF image shows the southern hemisphere in the IR spectrum (Bonfond, et al., 2011).

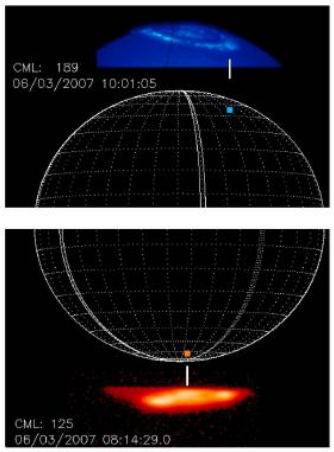

Figure 3 - Jupiter auroras (Bonfond, et al., 2011)

Figure 4 shows another view of the northern hemisphere where we can distinguish Io's footprint (Bonfond, et al., 2011):

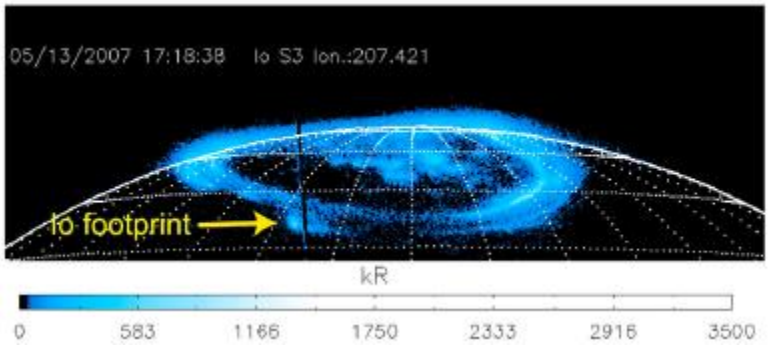

Figure 4 - Jupiter's northern hemisphere and Io's footprint (Bonfond, et al., 2011)

The Io's torus spectral characteristics are shown in Figure 5 (Salvador, 2012). Four spectral ranges have been selected as potential candidates for the mission within the main ion species that are $O(II)$, $S(III)$, $S(II)$, $S(IV)$ and $O(III)$:

- $710\ \text{Å} \pm 40\ \text{Å}$ (to avoid the emission from $S(III)$)
- $1020\ \text{Å} \pm 40\ \text{Å}$ (to isolate $S(III)$, $S(II)$ species and the Jupiter's aurora emissions)
- $1410\ \text{Å} \pm 40\ \text{Å}$ (to avoid emission from Earth at $1356\ \text{Å}$)
- $1725\ \text{Å} \pm 40\ \text{Å}$ (to reduce the solar emissions beyond $1700\ \text{Å}$)

These wavelength belong the to the far ultraviolet (FUV) spectrum domain and the baseline wavelength that is chosen is $141\ nm$.

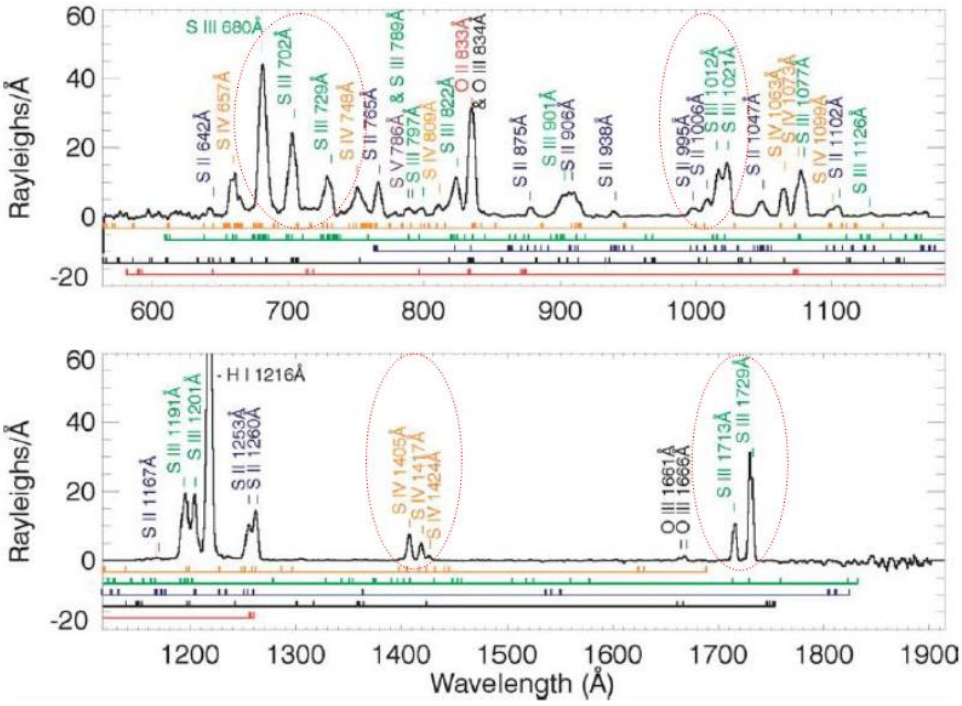

Figure 5 - The Io's torus spectral characteristics and selected ranges (Salvador, 2012)

Figure 6 illustrates UVIS-EUV channel spectral images representing the Io's torus in open and edge-on configurations taken during *Cassini*'s flyby of Jupiter (October,2000 - March, 2001) where the Jovian north is on the left (Steffl, Stewart, & Bagenal, 2004). One interesting thing is that the spectral characteristics presented in Figure 5 are well distinguishable in this figure.

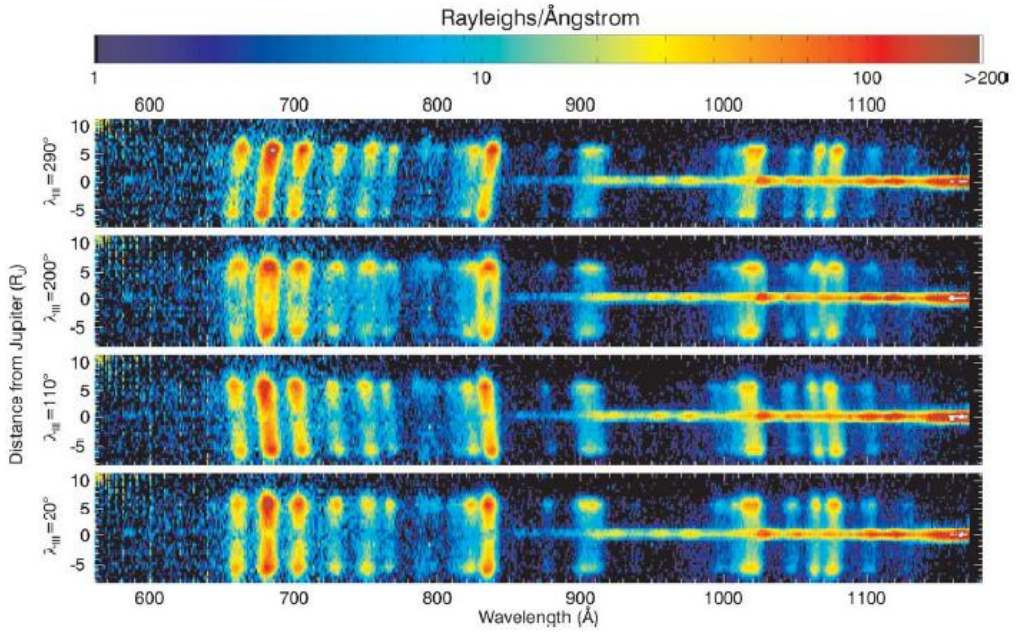

Figure 6 - UVIS-EUV channel spectral images showing the Io torus (Steffl, Stewart, & Bagenal, 2004)

1.1.2. Cubesat platform

The *Cubesat* Pumpkin platform is the result of an international collaboration between more than 40 universities, high schools and private firms all around the world (Pumpkin, 2013). Professors Jordi Puig-Suari and Bob Twiggs, respectively from California Polytechnic State University (Cal Poly) and Stanford University, began in 1999 to elaborate Cubesat specifications in order to allow universities to access to space science at a low cost (Cubesat, 2013). Its aim is thus mainly educational and allows designing low cost space projects with an existing modular structure.

The Cubesat standards typically consist in a volume of one litre ($10\ cm^3$) and a mass of less than $1.33\ kg$ (Lee). The extreme simplification of the satellite structure allows the production of low cost satellites. In the same line, Commercial Off-the-shelf (COTS) electronics components are usually used with the intent to lower as much as possible the Cubesat's price. That is the main reason why a Cubesat platform was chosen to serve our scientific purposes.

The Cubesat basic structure has the standard size of $10cm * 10cm * 10cm$. Other possibilities involve a larger size in one direction so that a three-unit ($3U$) structure can be used for example. A few typical configurations are shown in Figure 7 (Pumpkin, 2013). In

particular because of the limited space available, a $3U$ structure was chosen for the purposes of our UV imager. Indeed the instrument must have a sufficient aperture to collect more photons and provide a better signal-to-noise ratio. Moreover there must be some space also for the detector and proximity electronics. Finally we wanted our imager to be built in a modular structure, i.e. easily pluggable to another Cubesat part. For these reasons we selected a $1.5\ U$ CubeSat structure to host the instrument. The other $1.5\ U$ is then used for the spacecraft bus (ADCS, Power, OBC).

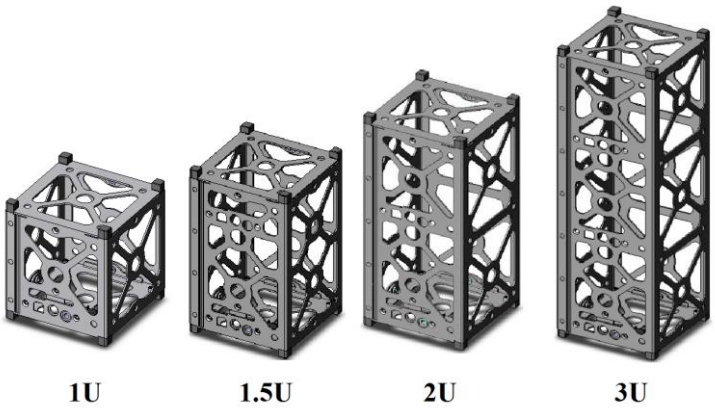

Figure 7 - *Cubesat* family (Pumpkin, 2013)

The first proposed optical design consists in a *Cassegrain*-type telescope which should be placed in a single unit of $10\ cm^3$. However, by placing the detector in the middle unit near the electronics, we can separate the mirrors a bit more from each other and benefit from a longer focal length (Habraken, Salvador, & Kintziger, 2013, February 27). In Figure 8 a schematic view of the two optical system configurations is represented.

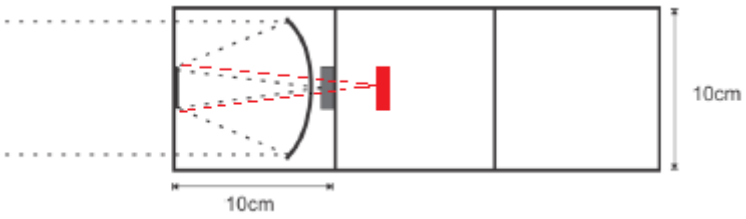

Figure 8 - Optical system configurations (Adapted from (Salvador, 2012))

Many Cubesats serve as amateur radio delays while others can be designed in order to image the Earth surface or detect earthquakes. Some others conduct onboard biological experiments or achieve atmospheric sensing (Thomsen, 2005). Many platforms are finally used in order to demonstrate the use of new technologies in space at lower price or to prove the viability of some COTS components into space (Thomsen, 2005).

Because Cubesats generally consist in a secondary payload which is launched at the same time of a primary one, the separation mechanism between the Cubesat and the launch vehicle (LV) must be highly reliable and safe. This is achieved by elaborating a versatile system called a Poly-PicoSatellite Orbital Deployer (P-POD) that is able to eject three $1U$

Cubsesats at a time or one $3U$ spacecraft. This system is illustrated in Figure 9 (Cubesat, 2013).

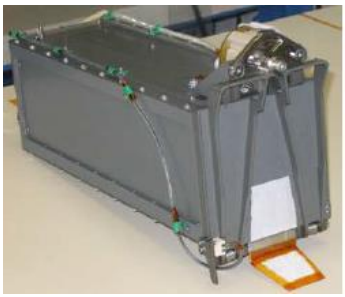

Figure 9 - Poly-PicoSatellite Orbital Deployer (P-POD) (Cubesat, 2013)

This mechanism is a rectangular box equipped with a door and a spring. Once the LV sends a deployment signal to the P-POD, the door opens and the Cubesats are released into space with the help of a spring that pushes them on rails (Lee).

Figure 10 - P-POD rails (Lee)

To be approved, a Cubesat has to meet special conditions to ensure the success of the planned mission. Cal Poly has edited these rules in order to ensure the safety of both the LV and all the Cubesats onboard. Moreover, these specifications dictate how engineers have to design, test and check their systems in order not to damage the primary payload and the other satellites inside the LV and jeopardize the whole mission. For example, dimension requirements ensure that all Cubesats fit the P-POD interface and do not interfere with other payloads (Lee).

1.1.3. Detector

A detector that is sensitive in the considered spectral range has to be chosen. Indeed, even if the detector accounts for a small part of the entire satellite, it is frequently the item that limits the overall quality of a telescope of a given aperture and determines the feasibility of the science projects (Joseph, 1995). This component therefore deserves particular attention. Different UV detectors exist and studies are performed to improve their efficiency. For example, typical CCD sensors are not sensitive enough in the UV domain and have to be cooled down in order to keep the dark noise as low as possible. Other detectors are thus preferred (Lapington, 2007). We could think that using a CCD sensor with a

detective quantum efficiency (DQE) of 20% in the UV and an aluminium filter that exhibits a visible transmission of 10^{-4} is enough to observe astronomical objects in these wavelengths. However, they usually emit 10^4 to 10^8 visible photons for each UV photon and thus if the detector has its maximum sensitivity in the visible, the data will be full of background contribution and noise (Joseph, 1995).

Different classes of image sensors exist (See Figure 11)(Joseph, 1995). The photoconductive and photoemissive sensors are differentiated by considering the selected wavelength range. Indeed, each is sensitive to different wavelengths and is suitable for different energetic radiations. In general, photoconductive devices have sensitivities over a broad spectrum while photoemissive detectors use photocathodes that are designed for a limited-wavelength interval (Joseph, 1995).

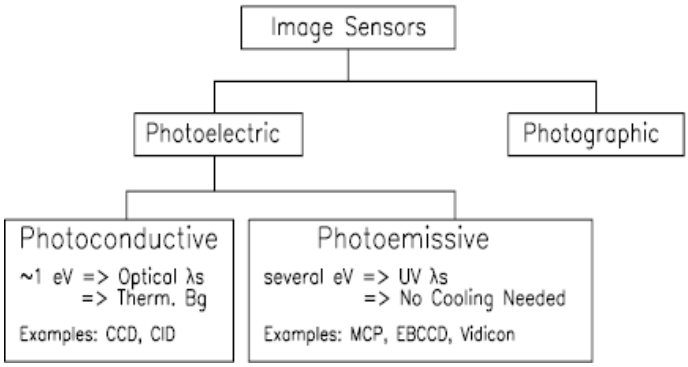

Figure 11 - Image sensors categories (Joseph, 1995)

The mechanisms that take place in the different sensors are not the same and this is why they are not suited for any wavelength. In photoconductive devices, an electron is transferred to the conduction band by the incident photon in a semiconductor substrate. This is for example what happens in silicon-based CCDs. This process is induced by photons of approximately $1\,eV$ and photoconductive devices are thus sensitive to IR and visible wavelengths. In photoemissive sensors, the electron is ejected from a photocathode material and therefore more energetic radiations are needed. These detectors are suitable for UV observations but a single photoelectron cannot generally be detected without amplification. High voltages are often used and difficulties appear. If the intensification is high enough, photon counting detectors can be manufactured with zero read-noise. This task is rarely achieved with CCDs due to the inherent read-noise of such sensors (Joseph, 1995). However, some classes of detectors overlap. For example, new photoconductive sensors are being tested with $GaAlN$, diamond and various other substrates and can be potentially superior UV sensors to current CCDs (Joseph, 1995).

Diamond detectors are however expensive and their cutoff frequency is not adjustable, this is why actual researches are often focused on $AlGaN$ materials (Feautrier, 2011). Recent Schottky diodes have been designed with a visible light rejection ratio of 10^4 and 10^2 for wavelengths upper than $350\ nm$ and $200\ nm$ respectively.

The SWAP's detector onboard PROBA-2 is a CMOS sensor that is covered with scintillation coating $P43$ from Applied Scintillation Technologies that allows the conversion of incident radiation at $17.5\ nm$ into visible light (Lecat, Thome, & Defise, 2005).

The Astro Observatory NASA mission was a system of telescopes designed to fly multiple times on the Space Shuttle. Three instruments were onboard: the Ultraviolet Imaging Telescope (UIT), the Hopkins Ultraviolet Telescope (HUT) and the Wisconsin Ultraviolet Photo-Polarimetry Experiment (WUPPE) (Dixon, Blair, Kruk, & Romelfanger, 2013). The Ritchey-Chrétien UIT gathered imagery in the spectral range of $120\ nm$ to $310\ nm$. The HUT performed spectrophotometry tasks between $42.5\ nm$ and $185\ nm$ and the WUPPE was a spectrapolarimeter ranging from $125\ nm$ to $320\ nm$.

The UIT's detector was a CsI photocathode which is insensitive to long wavelengths ($> 200\ nm$). The filter avoided shorter wavelengths to reach the detector. The HUT's detector was made of a microchannel plate (MCP) and a CsI photodiode. A MCP is a two-dimensional periodic array of tiny glass capillaries fused together and slice in a thin plate (See Figure 12)(DelMarPhotonics, 2013).

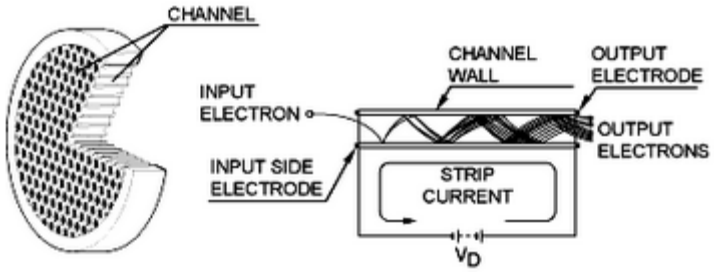

Figure 12 - MCP device (DelMarPhotonics, 2013)

When a particle enters a channel, an electron is emitted from the wall and is accelerated by an electric field between both ends of the MCP. This electron then hits the wall and produces in turn secondary electrons. This mechanism is repeated and results in a cascade process which yields to a cloud of several thousands of electrons. The output signal is read with the help of different kinds of anodes or phosphor screen. This device exhibits properties like high gain, high spatial resolution and high temporal resolution (DelMarPhotonics, 2013).

Detectors based on MCPs are generally made of three components: a converter, an assembly of MCP and a readout device. The converter is used to transform the initial particle into photons or electrons. The assembly of MCPs then amplifies the signal into an electron pulse. Finally, the readout device detects the electron avalanche. In this case, MCP are directly sensitive to VUV and a converter is not necessary. In imaging applications the readout device choice depends on the needed temporal resolution. For low temporal resolution applications, a phosphor screen coupled with a CCD camera can be used. If faster devices are required, different anodes (resistive, wedge, strip, etc) are available. The MCP spatial resolution depends on the channel's diameter and varies from $5\ \mu m$ to $15\ \mu m$. Cleanliness is very important in MCP devices to avoid destructive discharges (Joseph, 1995).

MCPs can be used as photon-counting detectors since a huge number of electrons is induced by a single incident photon. Another advantage of such a device is its inherent solar blindness. Indeed, as explained before, wavelengths above $200\,nm$ do not have enough energy to eject an electron from the MCP walls (Joseph, 1995). The major disadvantage of MCPs is the need of an amplification system and the use of high voltages. Therefore, scientists try to enhance the CCD's sensitivity to UV radiation. Lighter, smaller and less complex photoconductive devices are thus under development to avoid the use of high voltage MCPs. Moreover, the MCP's gain highly depends on the incidence angle: if photons enter the capillaries along their axis and do not hit the walls, no electron cascade is induced. However, MCPs and CCDs are not totally independent. Indeed, both can be combined to obtain a MCP-Intensified CCD (ICCD). Photons reach a photocathode and produce electrons avalanches inside a MCP (See Figure 13). These electrons then strike a phosphor plate to produce photons and illuminate a CCD with the help of a fiber optic bundle.

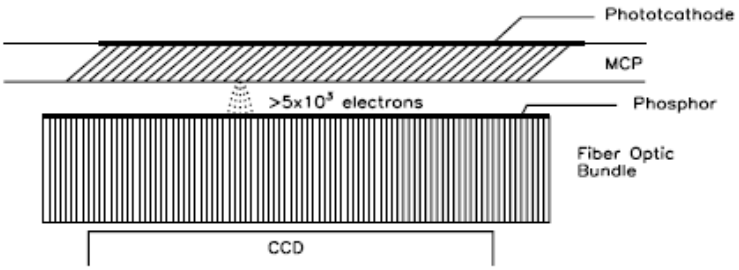

Figure 13 - ICCD (Joseph, 1995)

For example, such a device is proposed for the World Space Observatory - Ultraviolet's (WSO-UV) FUV detector as illustrated in Figure 14 (Uslenghi, 2007). The signal from a photocathode is amplified with 3 MCPs. The electrons then hit a phosphor screen to illuminate a CCD sensor. The main drawback of such a device is its slowness due to the phosphor screen (Joseph, 1995).

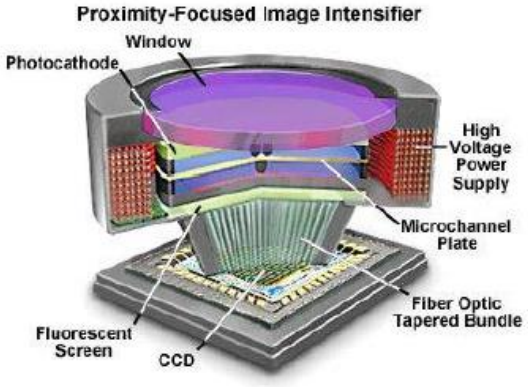

Figure 14 - WSO-UV FUV detector (Uslenghi, 2007)

MCP detectors are used for example onboard the Imager for Magnetopause-to-Aurora Exploration (IMAGE) spacecraft. Its FUV spectrographic imager, that was tested and

calibrated at CSL, incorporates MCP detectors with KBr photocathodes (eoPortal, 2013). These have a sensitivity of 20% at $121.6\ nm$ and 10% at $135.6\ nm$.

The size of MCP detectors, which is often large, has to be taken into account. Some Cubesats incorporate such MCP detectors. The Cubesat Investigating Atmospheric Density Response to Extreme Driving (CADRE) is the next space weather mission sponsored by the National Science Foundation (NSF) (Cutler, Ridley, & Nicholas, 2011). It is a $3U$ Cubesat that aims to perform temperature, density and composition measures of the thermosphere.

This intends for example to elaborate more accurate drag models and predict forces that undergo space platforms. The Wind Ion Neutral Composition Suite (WINCS) payload from NASA is designed to measure thermospheric and ionospheric composition, temperature and winds. Four instruments are used for a total power consumption of $2W$. Small MCP detectors are used for ions detection (See Figure 15)(Cutler, Ridley, & Nicholas, 2011).

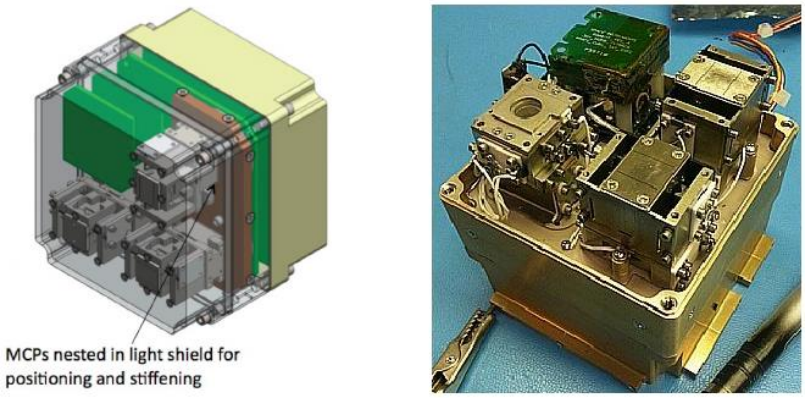

Figure 15 - WINCS payload and MCPs (Adapted from (Cutler, Ridley, & Nicholas, 2011))

The NASA Firefly mission is a $3U$ Cubesat that aims to study the relation between lightning and Terrestrial Gamma-ray Flashes (TGF) that are sudden energetic bursts in the upper atmosphere (Rowland, 2009). It incorporates a gamma ray detector that uses a microchannel plate. Another small MCP ($2.5\ cm * 2.5\ cm$) is used onboard the Science and Technology Satellite-1 (STSat-1). It is used to convert incident FUV light into an electrical signal in a FUV spectrograph (eoPortal, 2013).

The University of Leicester develops a Capacitive Division Image Readout (C-DIR) for MCPs. The output of the MCP (the cloud of electrons) is capacitively coupled to a readout anode through a ceramic back plate as shown in Figure 16 (Conneely & Lapington, 2011). This pure capacitive coupling between the array of electrodes and the MCP avoids several complications. Indeed, the readout anode and electronics are kept isolated from the detector and the high voltages. Discharges and complex wiring mechanisms are thus avoided (Conneely & Lapington, 2011).

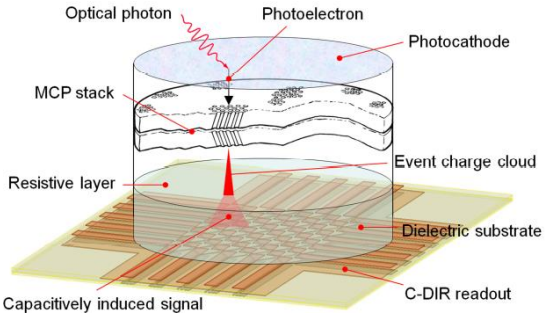

Figure 16 - C-DIR MCP sensor (Conneely & Lapington, 2011)

Typical performances of detectors are illustrated in Figure 17 (Joseph, 1995). Solar blind means that if the detector is sensitive to wavelengths different than UV, a filter is used. Electron-Bombarded CCD (EBCCD) is another kind of CCD that is designed for UV observation. It is not discussed here since the volume and mass considered are too large for a Cubesat platform. Efficiencies in the FUV domain were not really high and studies were needed to improve them (Joseph, 1995).

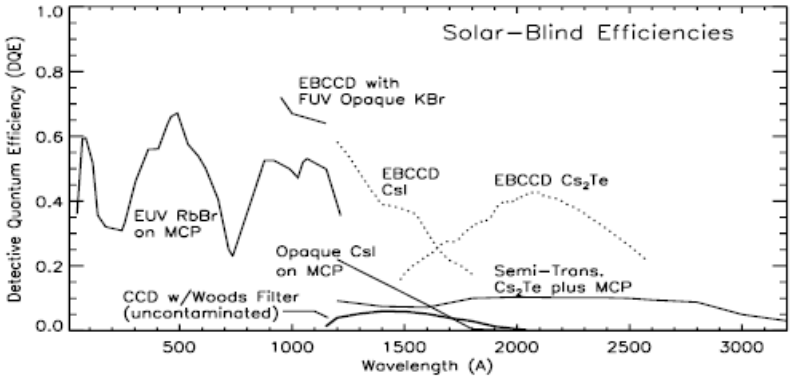

Figure 17 - Solar-blind efficiencies of actual detectors (Joseph, 1995)

Another important point is the lifetime of the detectors. For CCDs, the charge transfer efficiency is degraded and the dark levels increased by cosmic rays, particularly in high earth orbits (HEO) (Joseph, 1995). MCP gains also diminishes with time and an increase in the voltage can be necessary.

The reliability and compactness of CCDs are so desirable qualities that scientists try to make them sensitive to UV. Indeed, the solar blind DQE of common CCDs approaches $1\text{-}5\%$ compared to that of MCPs of $15\text{-}20\%$. The actual problem of CCDs when used in the UV spectrum is that they required to be cooled in order to limit the dark current. Contamination then forms on the cold surfaces and attenuates the UV transmission even in space. Warm windows can be used to avoid such problems only for wavelengths longer than $120\ nm$ but they typically exhibit a transmission of $60\text{-}70\%$ (Joseph, 1995). Thinning CCDs and illuminating them from the back improves their efficiency at all wavelengths (Joseph, 1995). For example, phosphor coated thin CCDs with a DQE of 6% have been achieved down to $120\ nm$. However, the problem of such sensor is that phosphor outgases and this can lead to coating alterations. Similar developments have been performed on a thinned back-

illuminated CMOS sensor for Solar Orbiter (Waltham, Prydderch, Mapson-Menard, Pool, & Harris, 2006). A problem that remains with this CCDs is that UV photogenerated charges are formed on the CCD near surface, typically at a maximal depth of $10\,nm$ (Joseph, 1995). These charges are then lost through recombination without being detected. Different complex mechanisms are under development to overcome this problem.

The Jet Propulsion Laboratory (JPL) performed studies on phosphor coated CCDs. The key is to attenuate the background induced by visible wavelengths in order to increase the SNR. Another effort was to eliminate the unwanted recombination near the surface. Actually surface damage when doping the material can lead to an increase of charges' mobility and thus easier recombination. JPL tried to implement a new molecular beam epitaxial (MBE) method to implant the ions inside the substrate to reach highly-stable surface structure (Joseph, 1995).

New solar-blind sensors have been developed for the PROBA-2 Large Yield RAdiometer (LYRA) instrument. These are a pin-photodiode and a metal-semiconductor-metal (MSM) photoconductor based on diamond material. They show a high responsivity around $200\,nm$ and a visible rejection of six and four orders of magnitude respectively (BenMoussa, et al., 2005). Moreover, these sensors exhibit stability, linearity and homogeneity in the wavelength range of $1\,nm$ to $220\,nm$. Due to their inherent solar blindness, the needed number of filters is reduced and their UV attenuation is avoided. Then, small dark currents were measured at room temperature. The problem of background signal of common CCDs does not exist here. The sensor is not sensitive to radiations more energetic than UV since they produce charges that are rapidly lost through recombination. The near-surface recombination problem that JPL had to face acts as a lower wavelength filter (BenMoussa, et al., 2005).

Activated diamond photocathodes with $> 50\%$ DQE have also been achieved by the Space Sciences Laboratory of the University of California (Siegmund, Vallerga, McPlate, & Tremsin, 2004). The wide band gap of diamond matches the UV photons' energy and makes it insensitive to visible light. Therefore, such a material is suitable for UV sensing detectors. Other diamond's advantages are its chemical and mechanical stabilities under hard external conditions. Moreover, it easily dissipates heat and exhibits radiation hardness (Siegmund, Vallerga, McPlate, & Tremsin, 2004). Actual CsI and $CsTe$ photocathodes are not efficient between $100\,nm$ and $300\,nm$. Another disadvantage of such devices is that they are sensitive to contamination and are not tolerant to gas exposure. New nitride photocathodes are under development to overcome these problems. Semiconductors like GaN, AIN and their alloys $Al_xGa_{l-x}N$ are attractive UV photo-converters. Indeed, their band gaps match the UV radiation energy and they are robust and stable over period of several years (Siegmund, Vallerga, McPlate, & Tremsin, 2004). Moreover, they can be re-activated several times and their efficiency drops rapidly around $380\,nm$. They also develop new Si MCPs with lower background and higher gain than common devices.

1.1.4. Requirements

Some optical requirements have been imposed by scientists on the properties of the optical system (Bonfond & Kintziger, (Personal communications), 2013, March 26) (Salvador, 2012):

- the space resolution must be enough to discriminate the north and south poles of Jupiter, where the auroras occur,
- the whole Io's torus must be visible,
- the system shall take an image at least every one or two hours since the total mission duration is at least several weeks,
- the sample must last less than 5 hours since the Io's torus tilts in phase with Jupiter's rotation ($\sim 10h$),
- a signal-to-noise ratio of 10 has to be achieved,
- the MTF value at Nyquist frequency must be greater than 10%[1],

The dimensions of the optical system must fit the $1.5U$ Cubesat platform. Therefore, the diameter of the primary mirror is limited to $8\ cm$. Then, the distance between the two mirrors must be less than $8\ cm$[2] and the maximum backfocus[3] that is tolerated is equal to $13\ cm$ (Habraken, Salvador, & Kintziger, (Personal communications), 2013, February 27). The pixel size that is considered here is equal to $15\ \mu m$ since no detector is chosen yet. This is a quite common size that CCD sensors exhibit as well as the diameter of MCP channels.

The table below summarizes the requirements that the optical design must verify.

Parameter	Value
Primary mirror's diameter	$8\ cm$
Distance between the two mirrors	$8\ cm$
Backfocus	$13\ cm$
Pixel's size	$15\ \mu m$
Field of view	$5.059\ arcmin$[4]
Frequency	$1\ image\ /(1\ or\ 2\ hours)$
Signal-to-noise ratio	10
MTF at Nyquist frequency	10%

Table 1 - Requirements for the UV imager

None tolerances were defined for this project. Indeed, it depends on the global budget allowed to the mission and thus the level of quality that could be asked to the

[1] The signification of "MTF" and "Nyquist frequency" are explained further in this report.
[2] The mirrors have to be located in a single unit. If we consider that their thickness is approximately equal to $1\ cm$, the mirror interdistance has to be shorter than $8\ cm$.
[3] The backfocus is the distance between the last surface of the optical system and the focal plane. In this case, this is the distance between the secondary mirror and the focal plane.
[4] I introduce further in this report the calculation of the field of view

company that is in charge of the mirrors' fabrication. I therefore looked for typical tolerancing values presented in Table 2 (Yoder, 2008). This one presents typical tolerances that optical designers should respect when elaborating optical systems. These are said "*tight*" when a severe, which means tiny, tolerance is needed on a given parameter. Thus a small variation of this latter induces large perturbations on the system optical quality. On the other hand, "*loose*" tolerances characterize less sensitive parameters: a small variation of it does not affect dramatically the optical performance of the telescope. Of course as the tolerances become tight, the cost fabrication grows. With this table, I elaborated a versatile $Macro$ file that can be used for all my designs.

Parameter	Units	Tolerance		Approximate limiting value
		Loose	Tight	
Index of refraction	--	0.003	0.0003	0.00003[a]
Radius departure from test plate	fringes[b]	10	3	1
Departure from spherical or flat	fringes[c]	4	1	0.1
Element diameter	mm	0.5	0.075	0.005
Element thickness	mm	0.25	0.025	0.005
Element wedge angle	arcmin	3	0.5	0.25
Air space thickness	mm	0.25	0.025	0.005
Decenter, mechanical	mm	0.1	0.010	0.005
Tilt, mechanical	arcsec	3	0.3	0.1
Dimensional errors of prisms	mm	0.25	0.01	0.005
Angle errors: prisms and windows	arcmin	5	0.5	0.1

Table 2 - Typical tolerances for optical systems (Yoder, 2008)

Chapter 2

State of the art

This section exposes a few promising projects with regards to scientific Cubesat missions, some of them using optical payloads. Nowadays, such spacecraft are used more and more by universities due to the low-cost development considered.

2.1. ExoplanetSat

2.1.1. Overview

ExoplanetSat is a project under development presented by the Massachusetts Institute of Technology (MIT) the goal of which is to detect exoplanets transiting around the nearest and brightest stars that look like our Sun. This Cubesat is $3U$ long and incorporates a telescope in order to target a star from a low Earth orbit (LEO). Designing such a satellite raises many technical problems that have to be carefully tackled. Inventive solutions are presented below in order to overcome the challenges that faced MIT scientists (Smith, et al., 2012).

The final issue of such a mission is to detect Earth-like planets orbiting in the habitable zone of a Sun-like star. This habitable zone is defined as the place where water can exist in the liquid form thanks to suitable temperature conditions. Moreover, ExoplanetSat will look for planets similar to the Earth, which means a small rocky one. If these objectives are reachable, bigger planets than the Earth could also be detected.

2.1.2. Method

To characterize the atmosphere of the exoplanet, specific imaging methods must be used. The direct imaging and the transit method are some of the ways to accomplish such a task. Although using a coronagraph or an interferometric method could also lead to potential results, these two concepts cannot be used nowadays on such a platform due to a lack of technology (Smith, et al., 2012).

Therefore, the transit has been chosen by the MIT to detect exoplanets with their Cubesat. This approach consists in measuring the variation in the flux of a star. This can be thought as a tiny eclipse made by the planet so that the intensity of the star decreases a little bit (actually by a factor equal to the planet-to-star ratio) when measured from the Earth. This procedure allows scientists to know plenty of useful information about the observed planet. A simple measure of the flux drop first reveals the planet's size if that of

the star is known. Then, spectral characteristics of its atmosphere can be deduced by analyzing its transmission spectrum. Indeed, when the planet is crossing the star flux, some of the starlight passes through its thin atmosphere and spectral features can be revealed. By dividing the spectrum of both the planet and the star by the spectrum of the star, the desired spectral characteristics can be obtained (Smith, et al., 2012).

The strategy is to target the brightest and nearest stars in the sky ($0 < V < 5$[5]) and follow it if an exoplanet is detected. Since the field of view (FoV) of a single spacecraft is too limited to monitor several stars, the final goal would be to deploy a fleet of many ExoplanetSats.

2.1.3. Strategy

The scheme would be to observe different stars with the aim of multiple satellites on low-inclination LEO at about $650\,km$ altitude. Due to many constraints like lighting problems, the satellites will operate in eclipse. Since a transit typically lasts $13\,hours$, a typical LEO cadence of $30\,min$ in eclipse and $60\,min$ in sunlight is sufficient to catch such an event. When illuminated the spacecraft orients its solar panels towards the sun in order to charge its batteries. Once again in eclipse ExoplanetSat starts acquiring its target back.

2.1.4. Systems

A brief presentation of ExoplanetSat's systems is presented below. As every Cubesat designers do, the MIT scientists tried to use as many COTS components as possible to diminish the mission cost. Figure 18 shows the baseline configuration of this Cubesat (Smith, et al., 2012).

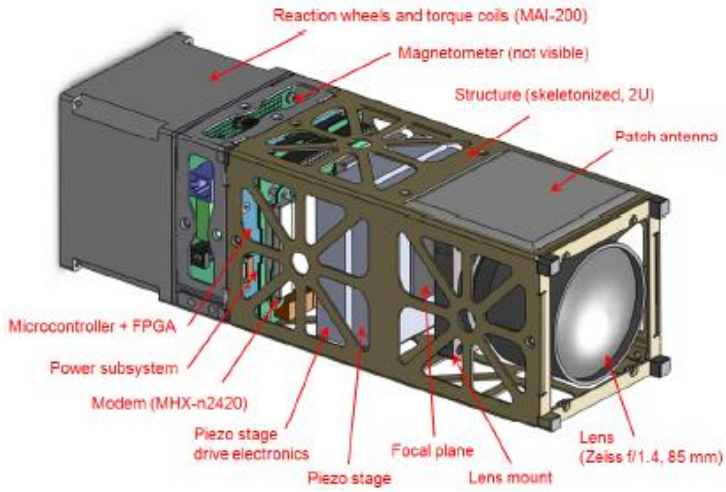

Figure 18 - ExoplanetSat configuration (Smith, et al., 2012)

[5] The magnitude of an object is a logarithmic measure of its brightness at a specific wavelength.

ExoplanetSat uses a $2U$ Cubesat structure as presented before on which is fixed the MAI-200 Attitude Determination and Control System (ADCS). The electronic cards inside are attached to rails that run along the interior cage. Other fixation systems, except the piezo mount that is described hereafter, are COTS components.

2.1.4.1. EPS

The principle power source will be deployable solar panels in a "cross" configuration as illustrated in Figure 19 (a) (Smith, et al., 2012). The expected power production in this arrangement rises up to $31\ W$. The second option, called "table" configuration, should offer an electrical power of $36.5\ W$ and a good shelter from the Sun during orbital daylight. This helps the detector not to overheat. Another advantage of the table alternative is easier slew maneuvers at orbital dawn and dusk. The reason why the latter is not the baseline option is that its deployment mechanism is not available up to date while that of the cross hinges is.

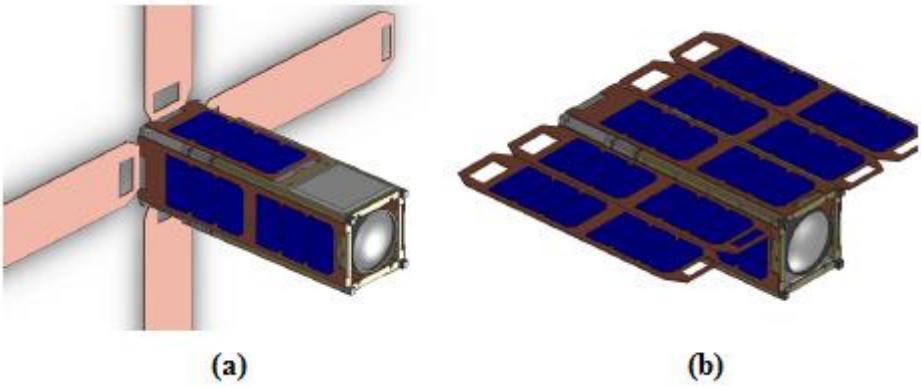

Figure 19 - Solar panels configurations: cross *(Left)* and table *(Right)*(Smith, et al., 2012)

The power consumption in eclipse is evaluated to be $17.6\ W$ to operate the ADCS, detector, avionics and communications while during orbital day the satellite is supposed to consume approximately $28.5\ W$. This power is used to supply the ADCS, avionics, communications and batteries. The solar arrays are COTS parts from *Clyde Space* (panels and cells) and *Pumpkin, Inc* (spring loaded hinges). While in the P-POD, the arrays are stack along the Cubesat and once ejected from it, they deploy passively. In addition to these, others are placed on the Cubesat's body in order to furnish the needed energy while de-tumbling or in case of an attitude control malfunctioning.

Finally, the power regulator is an Electrical Power Subsystem (EPS) board fabricated by *Clyde Space* and eight lithium-cobalt batteries store the electrical power.

2.1.4.2. ADCS

The pointing accuracy of ExoplanetSat has to be extremely precise. Indeed, if the target star moves through the focal plane, different pixels of the CCD are involved during this movement. Therefore, the measured signal suffers from the dissimilar pixel gains and this induced noise makes any sensible flux variation measurement impossible. The goal of the ADCS is thus to keep as stationary as possible the target on the focal plane.

To achieve this high level precision requirement, two different pointing mechanisms are used. A first coarse attitude control is achieved with the help of reaction wheels with an accuracy of approximately $60\ arcsec$ in all three axes. Then, a piezoelectric stage removes the remaining pointing error by translating the CCD in the two directions defined by the focal plane. These two techniques thus keep the star on the same group of pixels and avoid flux variation measure due to pixel gain non-uniformity over the whole CCD.

In most cases, this jitter noise is typically solved by flat-fielding the detector. This means that a flat-field image is taken in order to take into account the difference between pixel response. The final treated image is then the original one divided by the flat-field. In this case, ExoplanetSat lacks space for an internal flat-field source and moreover intrapixel sensitivity variations (it means variations of pixel response inside itself) would even be neglected with this technique (Smith, et al., 2012).

The pointing accuracy that is expected to be reached with these two mechanisms is about 0.1 to $1\ arcsec$.

2.1.4.3. Avionics

This subsystem is responsible for the attitude control loop that must read extremely rapidly the pictures from the focal plane. Indeed, this method is based on a star tracking algorithm using a Kalman filter that governs the different actuators. This image treatment really drives the avionics architecture since it detects the stationary position of the star on the CCD detector.

2.1.4.4. Communications

The telecommunications system is composed of a transmitter/receiver and two antennas. The modem that was chosen is the Microhard $n2420$ because of its compactness ($32mm * 51mm * 6.35mm,\ 19g$). One of the antennas is characterized by a high gain in order to send scientific data at high speed to the ground station. During commissioning phase where accurate pointing has not yet been established and in case of an attitude control loss, a lower gain antenna is required to maintain a connection with the ground.

ExoplanetSat benefits from already existing ground stations that have been created by the MIT and worldwide partners of the High Energy Transient Explorer (HETE-II) mission which are located on a nearly equatorial ground track in Kwajalein, Singapore and Cayenne.

2.1.4.5. Thermal control

Only passive methods are used since ExoplanetSat designers had to deal with critical volume and power constraints. The component that has to be cooled down as much as possible is the detector in order to minimize dark current noise. Strategies to achieve this goal are still under development. Maybe the best solution for the moment would be to place a thermally conductive strap between the CCD and the lens surrounding. Indeed, this contact with space would act as a radiator (Smith, et al., 2012).

2.1.4.6. Payload

The optical payload of ExoplanetSat is composed of a COTS camera lens and a focal plane covered by a CCD detector placed in the middle of multiple CMOS chips as can be seen in Figure 20 (Smith, et al., 2012).

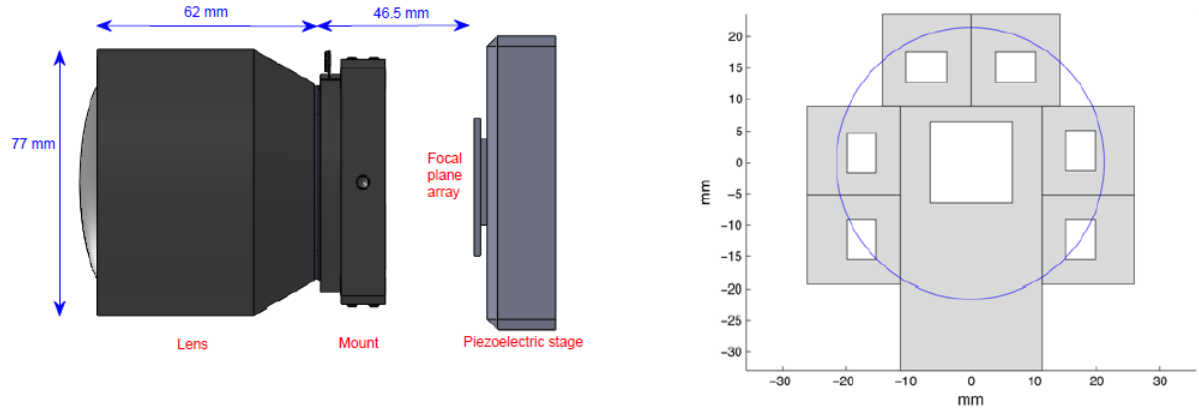

Figure 20 - ExoplanetSat's optical payload (Smith, et al., 2012)

Large diameter lenses were MIT prior choice in order to collect as many photons as possible and to measure tiny variations in the incident flux. The CCD detector shown in Figure 20 accomplishes the photometry measurements during an integration time of approximately $10\ sec$ while the surrounding CMOS follow the centroids of other guide stars at a very high speed. Actually, these CMOS sensors perform the task of an extremely fast star tracker (Smith, et al., 2012).

2.2. MISC

2.2.1. Overview

The Miniature Imaging Spacecraft (MISC) Cubesat is a 2008 Pumpkin project that was developed to prove the possibility of implementing a useful scientific payload onboard a 3U

Cubesat platform. The payload consists in a $7.5\ m\ GSD$ multispectral imagery from a circular orbit of $540\ km$. Each spacecraft is supposed to be operational during 18 months. Indeed, a whole constellation of such Cubesats is considered. The MISC design combines a robust miniature imager with an existing Cubesat Kit-based bus and a distributed ground station architecture (Kalman, Reif, Berkenstock, Mann, & Cutler, 2008).

The goal of this spacecraft is the same as every Cubesat: offering an alternative option to expensive larger payloads. MISC combines COTS components with other nanosatellite missions' components and a custom imager payload. The severe space constraints make the integration of such a payload inside the platform the major design challenge.

One MISC spacecraft is designed for a mission lifetime that allows imaging approximately $75\ million\ km^2$ of the Earth surface. This miniature imaging spacecraft represents therefore an interesting low-cost alternative to other expensive missions (Kalman, Reif, Berkenstock, Mann, & Cutler, 2008).

2.2.2. Systems

2.2.2.1. Payload

The optical payload of the MISC Cubesat is a $35\ mm$ lens similar to those used by astronauts in the International Space Station (ISS) when they photograph the Earth (Kalman, Reif, Berkenstock, Mann, & Cutler, 2008). The components were chosen in order to minimize the effects of vibrations at launch: delicate mechanical parts were banned. The diameter of the lens is also limited to $113\ mm$ by the length of the Cubesat's side[6]. The resolution limit of such a system is thus given by the Rayleigh criterion:

$$Res = 1.22\ \lambda\ \frac{f}{D}$$

If we consider a wavelength equal to $550\ nm$ and the dimensions above, this leads to a resolution limit in the visible spectrum of $5.5\ \mu m$. This therefore limits the detector choice (Kalman, Reif, Berkenstock, Mann, & Cutler, 2008). Finally, the designer decided that the payload should fit in an entire unit of the Cubesat.

The sensor is a $16\ MP$ CCD sensor with arrays of $7.4\ \mu m$ square pixels. This allows a large FoV and satisfies the limit of resolution calculated above. In order to prevent the detector from stray light that could enter the FoV of the lens (for example the sun), the MISC team developed a 4-panel deployable lens shade because commercially available ones were too expensive for a Cubesat mission.

[6] The component can exceed the Cubesat structure by 6.5 mm on each side.

Metal construction were preferred when the team looked for potential COTS lenses because they are more robust to mechanical perturbations and that plastic outgassing in space could be a problem.

At the considered altitude of $540\ km$, the GSD is equal to $7.5\ m$ and the ground patch measures $32.5\ km * 21.6\ km$. This means that the $16\ MP$ detector is able to image a total surface of $702\ km^2$. In order to reduce the image blur, exposure times should be kept under $0.5\ ms$.

The complete imager payload of the MISC Cubesat is illustrated in Figure 21.

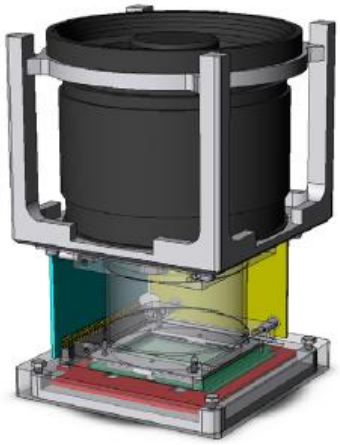

Figure 21 - *MISC* 's optical payload (Kalman, Reif, Berkenstock, Mann, & Cutler, 2008)

Multiple custom aluminium parts are designed in order to assemble the different components, namely, the lens, the sensor and the needed circuitry. The panel hinges are also included in this top unit of the Cubesat.

2.2.2.2. ADCS

The 3-axis pointing accuracy of the MISC spacecraft is approximately equal to $1°$ which is delivered by the IMI-100 ADCS from IntelliTech Microsystems (MaylandAerospace, 2009). This value is acceptable while considering the earth imaging goal of the mission (Kalman, Reif, Berkenstock, Mann, & Cutler, 2008). This $1U$ system is located in the central unit of the Cubesat. This pointing accuracy level allows MISC to only use transmition antennas that are more directional to those of common Cubesat. Indeed, Cubesats generally use passive pointing techniques to stabilize the spacecraft whereas in this case an active pointing mechanism is used. These antennas are positioned towards the Earth to reduce as much as possible the needed slew maneuvers to transmit data to the ground station. Finally, this ADCS permits to orient the lens shades in the needed optimal position (Kalman, Reif, Berkenstock, Mann, & Cutler, 2008).

2.2.2.3. Single-board computer (SBC)

A COTS SBC was chosen for the camera computer to which it is connected by a USB. All kinds of image treatments and settings are performed by a software development toolkit (SDK). These are image compression, exposure settings or database management.

2.2.2.4. VHF-UHF transceiver and C&DH

All these systems are COTS components. The C&DH system is a space-proven unit with $2\ GB$ storage.

2.2.2.5. EPS

The EPS is a factory-optioned space component from Clyde Space while the transceivers come from CubeSat Kit. Deployable solar panels are used in the same "cross" configuration as for ExoplanetSat. These are attached to the payload unit with the help of hinges. The panels deploy automatically after MISC's ejection from the P-POD.

Figure 22 - Rear view of *MISC* Cubesat

The lens shade is also fixed to the satellite with these hinges and deploys with the solar panels.

2.2.2.6. Assembly

The overall Cubesat is qui heavy since it weighs approximately $4.49\ kg$. However, the centre of gravity shift due to the mass location towards the optical payload unit is limited and other Cubesats have already been launched with such overweights (Kalman, Reif, Berkenstock, Mann, & Cutler, 2008). This only induces additional launch costs.

2.3. RTICC

2.3.1. Overview

The Rapid Terrestrial Imaging Cubesat Constellation (RTICC) project consists in a constellation of Cubesats designed for an Earth imaging application with a Maksutov telescope. The image resolution is $3\,m$ from an altitude of $520\,km$. The constellation is made of 33 different planes with 10 Cubesats per plane. A custom carrier system is proposed to release 10 satellites at a time. The RTICC satellite and the custom carrier are illustrated in Figure 23 (Bernhardt, et al., 2009).

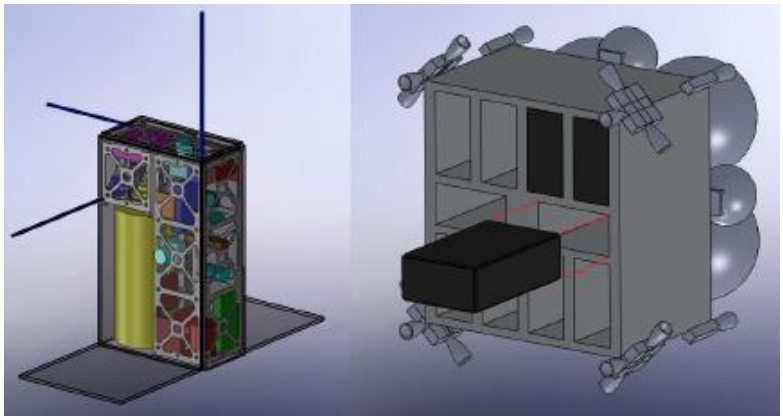

Figure 23 - RTICC Cubesat *(Left)* and custom carrier *(Right)* (Bernhardt, et al., 2009)

2.3.2. Constellation

A LEO constellation is chosen to minimize the focal length and the diameter of the telescope and achieve the required resolution. The initial design was a constellation of polar orbits to provide a full Earth coverage. However, the best coverage in such a situation is at the poles and this is not the prior target of the mission. Moreover, a direct launch into polar orbit rarely happens and thus the Cubesats have to be launched at a lower inclination orbit. Then, they have to perform a maneuver to change their orbit's inclination which is expensive in terms of Δv[7] (Bernhardt, et al., 2009). This option is therefore ruled out. A better option is a *Walker* constellation. All the orbital planes have the same inclination but differ from their right ascension of the ascending node (RAAN) and are equally spaced over $360°$. This option leads to a situation where the Cubesats are distributed over the globe. Therefore, a smaller number of satellites is required. The two constellations are shown in Figure 24 (Bernhardt, et al., 2009).

[7] Indeed, a change in the orbit's inclination is extremely expensive for a satellite. Actually, a maneuver to change the inclination of $24°$ requires a Δv that is approximately equal to 42% of the satellite's velocity.

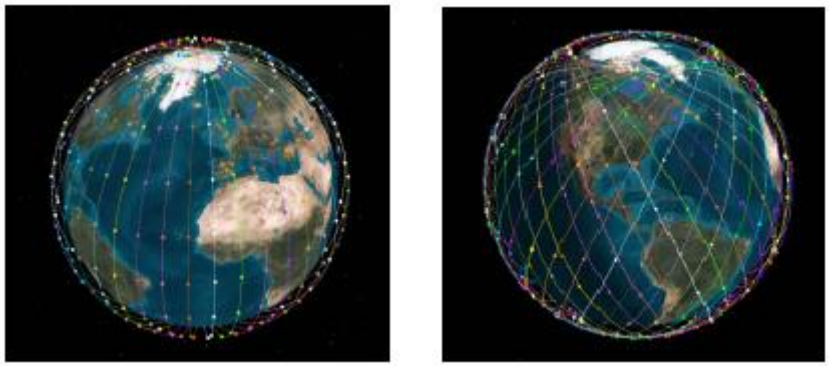

Figure 24 - Polar *(Left)* and Walker *(Right)* constellations (Adapted from (Bernhardt, et al., 2009))

The altitude of the satellites have to be between 400 and $550\ km$. Indeed, a lower altitude orbit degrades too fast and induces too many boosts while a higher one requires larger diameters and focal lengths for the telescope.

Different strategies are imagined to deploy such a high number of Cubesats in a short time. The best proposed is to use carriers that host all the Cubesats of a single plane. All the carriers are launched to an orbit with a given inclination and the first carrier performs a small inclination change maneuver to reach the required one while the others stay on the initial launch orbit. The remaining carriers then use the initial orbit's precession to reach their final RAAN and perform the required change of inclination once they have reached it. If a single launch is done, this mechanism is supposed to last two years but it can be significantly reduced if several launches are performed to allow different groups of satellites to precess the Earth (Bernhardt, et al., 2009).

Once all the Cubesats are on their respective orbital planes, the carriers have to enter an elliptical phasing orbit to evenly space e ach spacecraft along the orbit. The period of this phasing orbit has to be slightly shorter or longer than the target period to release each satellite with the appropriate time spacing. In order to reduce the needed energy consumption, the carrier must perform a single release per orbit instead of placing all the Cubesats in a single orbit[8]. A longer period orbit is chosen as the baseline option as illustrated in Figure 25 where the red outer orbit is that of the carrier.

[8] The carrier can either adopt an elliptical orbit the period of which is longer than the nominal orbit one by the time spacing or follow an orbit whose period is equal to the time spacing.

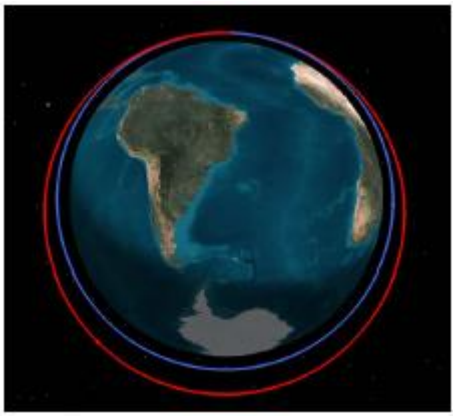

Figure 25 - Carrier *(red)* and nominal *(blue)* orbits (Bernhardt, et al., 2009)

2.3.3. Systems

2.3.3.1. Propulsion

Three stages of the mission deployment need a propulsion system. All the steps between launch and the carrier elliptical orbit need maneuvers. The second stage is the separation of the carrier and the Cubesats and finally station-keeping of the spacecrafts needs a propulsion system.

The carrier propulsion system is made of a monopropellant engine because of its simplicity as opposed to bipropellant systems. Indeed, a single tank is needed and the failure potential is lower while performance characteristics are similar in this case (Bernhardt, et al., 2009).

The Cubesat's propulsion system selection is based on the lifetime requirement of one year. The propulsion system shall compensate for the atmospheric drag in the considered range of altitude. However, the loss of altitude do not perturb the mission imaging goal and only attitude control is performed (Bernhardt, et al., 2009). Four Micro Pulsed Plasma Thrusters (Micro-PPT) are chosen for their small size and mass.

2.3.3.2. Payload

A two-mirror design is selected for mass and cost saving. The optical system consists in a COTS Maksutov-Cassegrain telescope associated to a $10\ MP$ detector. This system is free of spherical aberration thanks to its corrector plate and is not an expensive solution (Bernhardt, et al., 2009). The diameter and EFL of the telescope are respectively $9\ cm$ and $1.25\ m$.

2.3.3.3. Navigation System

The position of each Cubesat has to be known to select the nearest one from the desired imaging target. Station-keeping also requires orbit propagation from previous satellites' positions so this is why they have to be precisely calculated.

The method to locate the satellites is the Global Positioning System (GPS). The GPS is chosen because it is the most accurate navigation device that functions within LEO (Bernhardt, et al., 2009). Only COTS components are considered and the position knowledge has an accuracy of $5\ m$ at the satellites' altitude.

2.3.3.4. ADCS

A precise ADCS is required here because the ground target must be pointed with an accuracy of $200\ m$. This corresponds to an angular pointing accuracy of $0.022°$. Therefore, an active three-axis control system is needed.

A star tracker is selected to precisely know the satellite's attitude. Since this sensor requires some time to acquire data, an Inertial Measurement Unit (IMU) provides rapid attitude knowledge between the star tracker updates (Bernhardt, et al., 2009). Magnetometers and sun sensors are also used for coarse pointing in case the star tracker is blinded by the sun. All the sensors are COTS components except the star tracker that may be custom since the available ones are too expensive.

Custom Control Moment Gyros (CMG) are selected for main attitude control while magnetorquers serve for the fine control. The thrusters are also used for orbit maintenance. Reactions wheels are not considered as the final option due to their fast saturation and complex process (Bernhardt, et al., 2009).

2.3.3.5. Communications

The communication network is composed of the Cubesats and a ground station. The ground station has an updated knowledge of the constellation and therefore only a small group of satellites is used for communications. By computing the right Cubesat node order, a relay chain from the ground station to the target and back to the ground station is used for data acquisition. This mechanism intends to reduce the energy consumption and is illustrated in Figure 26 (Bernhardt, et al., 2009).

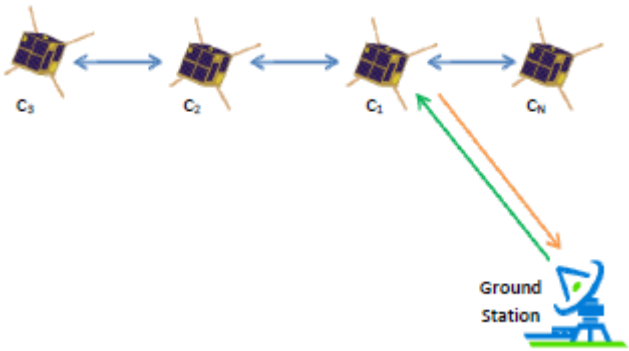

Figure 26 - Communication relay chain (Bernhardt, et al., 2009)

Since 40% of the orbit is in eclipse and that images cannot be taken during this period of time, communication tasks are performed in priority by the dark-side satellites. Indeed, the imaging operation is the most computationnally intensive and these Cubesats have more power available to communicate.

Monopole antennas perpendicular to each other are used for the inter-satellites and satellites to ground station communications. Another issue studied: using the carriers as downlink nodes to allow greater access time and a higher data transfer for downlink communications (Bernhardt, et al., 2009).

2.3.3.6. EPS

Solar panels provide the needed power during light-side operations while battery cells are used in eclipse. Triple junction cells are chosen in order to benefit from the best efficiency (Bernhardt, et al., 2009). All the spacecraft's body is covered with solar cells except the top and the bottom. The desired bus tension is $9\,V$ and DC-DC converters are used to supply lower tensions to components. A study reveals that the solar panels have to be perpendicular to the Cubesat's body in order to benefit from the highest efficiency (See Figure 27) (Bernhardt, et al., 2009)).

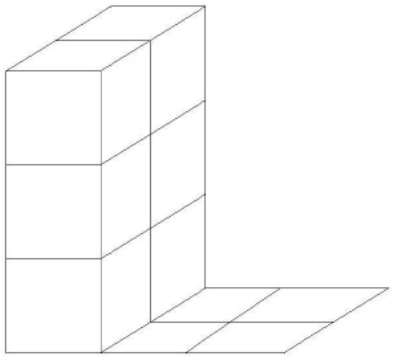

Figure 27 - Solar panel configuration (Bernhardt, et al., 2009)

Finally, even if only two batteries are necessary to supply power all the eclipse long, three are used to decrease the required depth of discharge (DOD). Indeed, the cycle life characteristics of the batteries remain unknown.

2.3.3.7. Thermal Control

Even if further analyses are required, the equilibrium temperatures that undergo the satellite's components are in first approximation inside the required temperature ranges (Bernhardt, et al., 2009). Therefore, only passive techniques are used except for the batteries where heaters are needed because charge and discharge voltages vary with temperature. The battery insulation is of importance to avoid high power consumption from the heaters.

2.4. ALL-STAR

2.4.1. Overview

The Agile Low-cost Laboratory for Space Technology Acceleration and Research (ALL-STAR) satellite is a $3U$ Cubesat that can support a one-year on-orbit operation of multiple space-based research payloads. These can be configured and ready for flight in 6 months thanks to a simplified payload hardware and software interface (Brown, 2010). This program intends to accelerate the rate at which technology payloads are able to be launched by providing the satellite bus (eoPortal, 2013). This one includes the satellite structure, ADCS, CD&H and position knowledge.

The feature of this satellite is an external shell and solar panel wings deployment after the P-POD ejection to expand the available surface area of the satellite. This mechanism is entirely developed by the University of Colorado. Figure 28 illustrates the satellite in fully deployed configuration (Brown, 2010). Both the body and the solar panels are deployed after ejection from de P-POD. The bottom part of the satellite hosts the electronics and the payload. The shell and the wings constitute the upper part of the satellite.

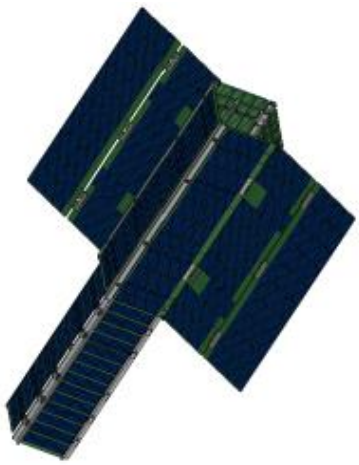

Figure 28 - ALL-STAR in fully deployed configuration (Brown, 2010)

2.4.2. Systems

2.4.2.1. Payload

The available space that is dedicated to the payload corresponds approximately to that of a single unit. Figure 29 illustrates the space repartition inside the ALL-STAR Cubesat (eoPortal, 2013).

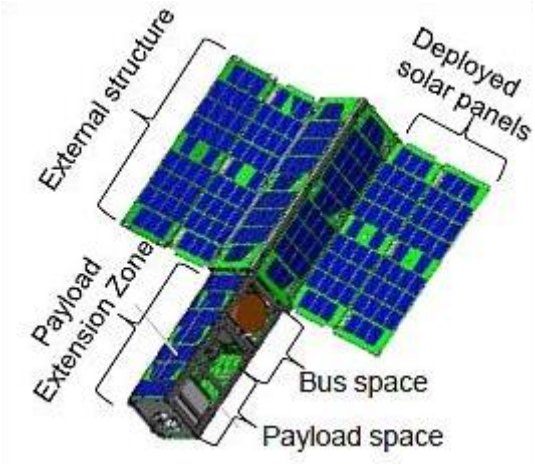

Figure 29 - ALL-STAR's system configuration (eoPortal, 2013)

A compatible optical payload is also proposed: the Telescopic High-definition Earth Imaging Apparatus (THEIA). This optical system intends to prove the capabilities of the Cubesat bus on orbit and provide a marketable proof of concept (eoPortal, 2013).

The proposed payload is comprised of a refractor system and a CMOS detector. The first is an achromatic doublet, i.e. two cemented lenses with different dispersive behaviours, that aims to reduce the chromatic aberration[9] of the system.

THEIA intends to observe the Earth in full colour with a semi-field of view (SFoV) of $1°$. The target angular resolution is $0.0017°$ and a $5\,\mathrm{MP}$ sensor is used. The full optical payload is presented in Figure 30 (eoPortal, 2013). A baffle system is implemented in order to reduce the off-axis stray-light that enters the optical system and reaches the detector.

The lens mounting is made of Invar[10] in order to produce minimal rotational and translational misalignment at differing temperatures (eoPortal, 2013).

[9] When different wavelengths pass through a refractive optical system, *dispersion* appears since the refractive index of the glass depends on the wavelength. The rays are not deviated in the same direction and do not focus at the same point. This is called *chromatic aberration*.

[10] Invar is also generically called $FeNi36$ since it is a nickel iron alloy with 36% of nickel. It is known for its low coefficient of thermal expansion. This is why it is called *Invar* which comes from the word *invariable*.

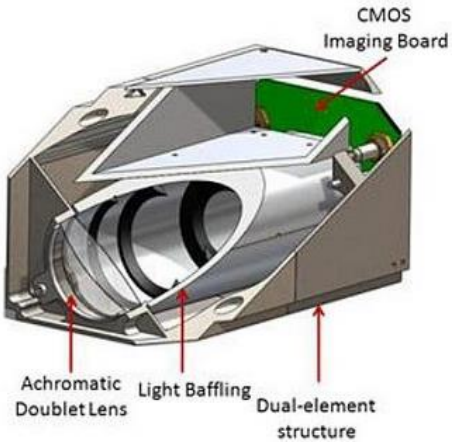

Figure 30 - Full THEIA optical payload of ALL-STAR Cubesat (eoPortal, 2013)

2.4.2.2. ADCS

The ADCS provides 3-axis stabilization. It is composed of different attitude sensors and actuators. A 3-axis magnetometer, a star tracker and gyroscopes perform the attitude sensing while three reaction wheels control it. Magnetorquer are also used for the momentum dumping of the wheels. These are shown in Figure 31 (eoPortal, 2013).

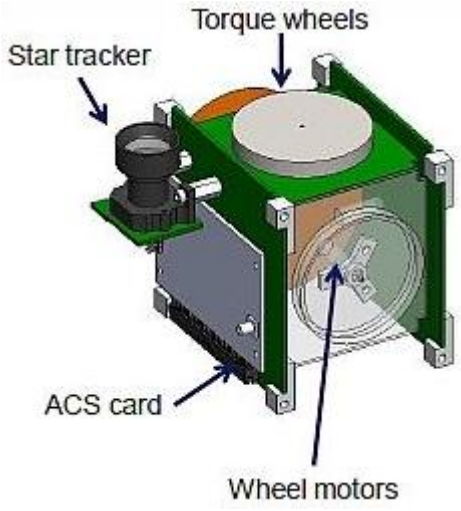

Figure 31 - ALL-STAR's ADCS (eoPortal, 2013)

Knowing the SFoV of the optical payload, the pointing accuracy has to respect a few restrictions. Indeed, the satellite must be able to locate the target even if the ADCS does not exactly point it. This means that the FoV has to be large enough to take into account the pointing error. Actually, the target that the satellite is supposed to observe is for sure situated in a circle the radius of which is equal to the pointing accuracy. Therefore, the SFoV of the optical system has to be equal to the pointing accuracy value. This situation is illustrated in Figure 32 (eoPortal, 2013).

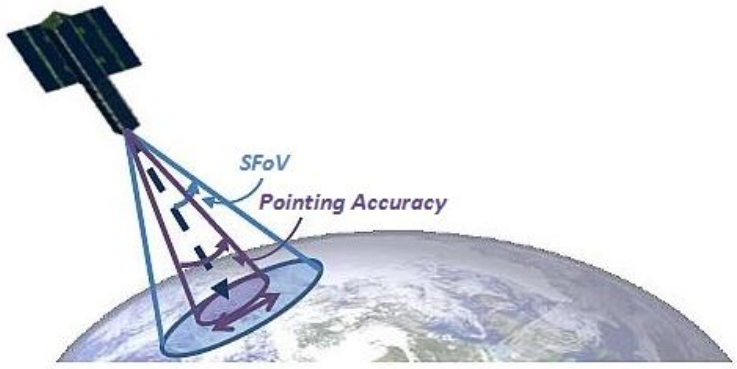

Figure 32 - FoV and pointing accuracy of ALL-STAR (Adapted from (eoPortal, 2013))

2.4.2.3. C&DH

All the C&DH components are COTS parts. The memory parts are magnetoresistive memories designed for space applications. Micro SD cards can also be used in order to expand the spacecraft's memory. All the subsystems' interfaces are electrically identical to facilitate their interconnection.

2.4.2.4. EPS

The nominal power consumption of the Cubesat is approximately $10\ W$ while $30\ W$ power peaks appear during $15\ min$ every two orbits when communicating with the ground. A total of 918 solar cells are used thanks to the deployable structure of the satellite to charge 4 batteries. A Maximum Power Point Tracking (MPPT) system is used to benefit from the maximum available power given by the solar cells.

2.4.2.5. Propulsion

The propulsion system is optional and can be attached to the payload section of ALL-STAR (eoPortal, 2013). A cold gas propulsion system is proposed with a single nozzle.

2.5. Delfi-C³

2.5.1. Overview

The Delfi-C³ satellite is a $3U$ Cubesat that carries two scientific experiments for industrial companies and also aims to demonstrate new electronics design methods. In particular, the satellite is equipped with a transponder to communicate with the radio amateur community and two measurement boards for a thin film solar cell experiment (See Figure 33). The satellite does not incorporate any battery because it is the source of many problems that have already led missions to fail (Verhoeven & Ubbels). The satellite is thus shut down during orbital eclipse and reboots afterwards. In order to save the satellite parameters, a little non-volatile memory is used to store its status before each eclipse.

Figure 33 - Delfi-C³ Cubesat: the thin film solar cells are mounted on the far end of the solar panels (eoPortal, 2013)

The satellite follows the common philosophy of the Cubesat community: Keep it simple, stupid (KISS): systems work better when they are kept simple rather than made complex (Bouwmeester, Aalbers, & Ubbels).

2.5.2. Systems

2.5.2.1. Payloads

Delfi-C³ carries out two scientific experiments. The first one has the purpose to demonstrate the use of thin film solar cells (TFSC) in space. The second experiment is a wireless sun-sensor proof-of-concept (Verhoeven & Ubbels).

The first experiment intends to test the prototype TFSC's of Dutch Space in real space conditions. The main goal is to record their I-V curve related to temperature[11]. Two sets of these solar cells are placed at the end of the solar panels. The goal of such a kind of device is to reach lighter and cheaper solar cells than can be used in space missions.

Finally, two Autonomous Wireless Sun Sensors (AWSS) from TNO are tested. They produce their own needed power by onboard solar cells. A COTS transceiver is used to establish the contact between these parts and the on-board computer. These wireless communications allow weight and volume reduction. Indeed, cables and connectors are not needed anymore (Verhoeven & Ubbels). Tests are thus performed in order to check the feasibility of such a wireless system and the operation of the sun sensor in a variable sunlight exposition.

[11] Indeed, this photovoltaic characteristic depends on many factors like the temperature, the illumination or the cell's age. This curve is non-linear and is also influences by the load that is connected to the cells. This is why MPPT systems are often used to track the optimal functioning point on this curve with respect to all factors.

Figure 34 illustrates these two components under test.

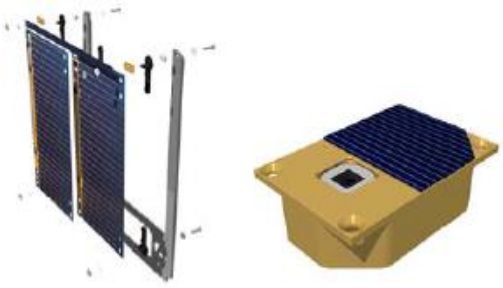

Figure 34 - TFSC *(Left)* and AWSS *(Right)* (Bouwmeester, Aalbers, & Ubbels)

2.5.2.2. ADCS

The ADCS is separated into two unconnected systems which are the Attitude Determination System (ADS) and the Attitude Control System (ACS).

The attitude of the satellite is not known with a high accuracy (DelfiSpace). The sun vector is evaluated with the help of the AWSS's when the sun is in their FoV. Then, the attitude towards the sun is deduced thanks to photodiodes placed on the solar panels. They evaluate the solar flux and correlate the results to the TFSC's and the AWSS's results.

A complete passive system is used to limit the rotation rates of the satellite. Indeed, the Cubesat is free to rotate about all its axes and therefore magnetic hysteresis rods material and a permanent magnet are employed to slow the satellite's rotation using the Earth's magnetic field.

2.5.2.3. Communications

Two tasks are performed by this subsystem: the first is the telemetry downlink and telecommand uplink while the second is an amateur radio transponder service that allows operators to communicate with each other. The communication system is made of two COTS Radio Amateur Platforms (RAP). The eight antennas of the satellite are stowed in launch configuration inside a small box and then deployed by melting a restraining wire (See Figure 35) (DelfiSpace).

Figure 35 - RAP's *(Left)* and antenna box of Delfi-C³ *(Right)* (Adapted from (DelfiSpace))

2.5.2.4. EPS

The energy production of the satellite is accomplished by four solar arrays which are composed of high performance triple junction cells. However, the performance of solar cells is highly dependent on the temperature and the incident radiation. Therefore, an offset angle of $35°$ exists between each solar array and the Cubesat's body to be sure that sufficient power production is available in any attitude (DelfiSpace).

Then, no energy storage is implemented in Delfi-C³: The required energy is only available when the solar arrays are illuminated. The spacecraft thus shuts down at each eclipse and reboots when it is sunlit.

A regulated bus is implemented since its voltage directly depends on the solar array energy production. Each solar panel is thus associated to a DC/DC converter that imposes a $12\ V$ output voltage to the bus whatever the input value[12]. Only the needed power, which is far less than the maximum one, is removed from the solar panels and thus a large part of the I-V curve is used (DelfiSpace). All the individual components finally divide the bus tension locally to use it in a proper way.

2.5.2.5. Structure

The body of Delfi-C³ is based on the $3U$ solid chassis from Pumpkin except the top and bottom panels that are replaced by custom ones in order to host the AWSS and the four antenna boxes. The outer panels of the structure are used to absorb the mechanical loads at launch and to provide an electrical ground as they form a Faraday cage. Finally, four rods run the entire structure length to support all the electronic cards. These components are shown in Figure 36 (DelfiSpace).

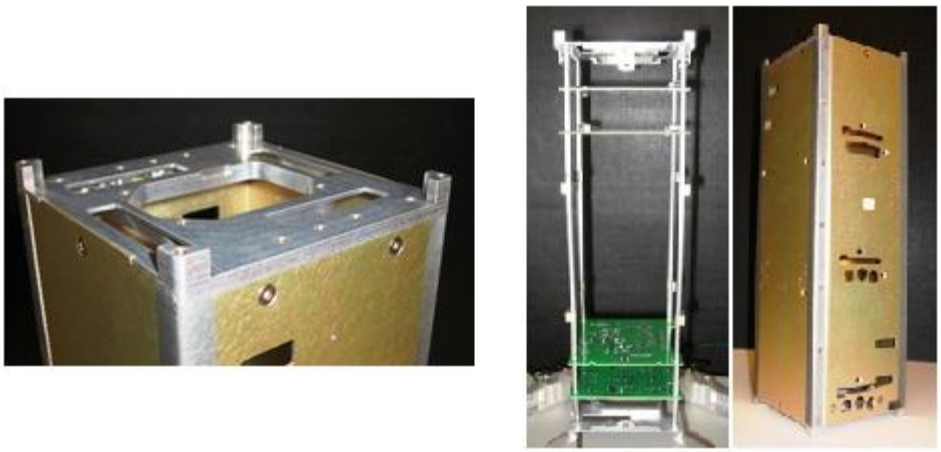

Figure 36 - Upper plate *(Left)*, inside structure and solid chassis *(Right)* (Adapted from (DelfiSpace))

[12] Except if this value a too small to permit the conversion (e.g. in eclipse).

2.5.2.6. Mechanical subsystem

Two different deployment mechanisms are used but the same release system is employed. The solar panels' mechanism consists in a custom hinge that connects them to the structure. The panels are stowed in the P-POD until ejection thanks to Dyneema[13] wires that are under pretension to prevent the solar panels from vibrating at launch (DelfiSpace). These are then melted with resistors to let springs perform the deployment. Plunger springs then limit the angle between the body and the panels to $35°$. Finally, the release method is used for the antennas that are stored in boxes.

2.5.2.7. Thermal control

The thermal control subsystem (TCS) is in charge of regulating the temperature inside the Cubesat and keep it within the allowable range. The TCS monitors the different components' temperatures and a complete passive system is used to evacuate the excess heat towards space. No heater or cooler are incorporated in the baseline design due to stringent mass and power limitations. There is no dedicated radiator because the satellite is spinning and thus all surfaces receive heat fluxes at arbitrary times (DelfiSpace). Therefore, the radiating surfaces are also sunlit and thermal tapes are used to reflect part of the sunlight (Weggelaar, 2008).

2.6. SDS-1

2.6.1. Overview

The Sun Devil Satellite 1 (SDS-1) is a $3U$ Cubesat project of the Sun Devil Satellite Laboratory (SDSL) that aims to take photos of the Sun to capture solar flares as they emerge (PhysOrg, 2012). The principle payload onboard is the Flare Initiation Doppler Imager (FIDI) developed by NASA. This project will advance EUV imaging capability and demonstrate the use of new technologies on a Cubesat platform (Daw, 2012).

In particular, the first use of a back-illuminated CMOS active pixel sensor is attempted to reduce power, mass and volume of EUV imaging systems. Then, a new Doppler imaging technique of EUV emission lines aims to prove the value of using a low-cost platform for solar science missions. Figure 37 illustrates the $SDS\text{-}1$ Cubesat's model (Goldstein & Kady, 2012). The payload location is at the front half of the satellite. Two deployable solar panels are used to supply the electrical energy while a patch antenna downlinks twice a day the scientific data to the ground. A 3-axis ADCS is used to achieve the pointing accuracy requirement.

[13] This material is stronger and has a lower melting temperature than Nylon.

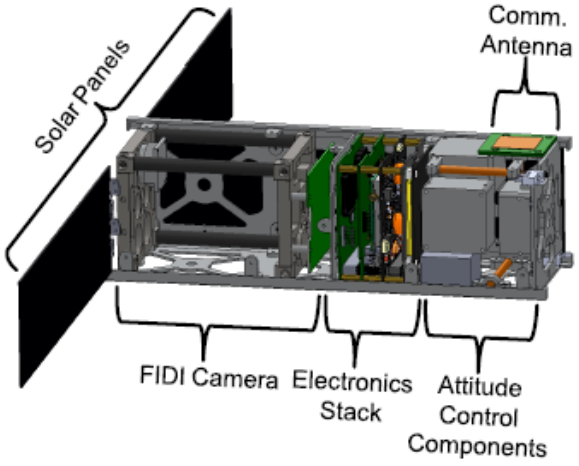

Figure 37 - SDS-1 Cubesat model (Goldstein & Kady, 2012)

Observing Doppler shifts during solar flares with a slit spectrometer is really difficult: it has been achieved only twice up to now (Daw, 2012). FIDI aims to observe multiple M[14] class flares and larger flares as well with a significant probability. The mission life is estimated to several months. The spatial resolution of the instrument is approximately $10\ arcsec$ to fit the typical scale of active region features such as loop foot points. Indeed, coronal heating and electrons beams can produce fast upflows of evaporated chromospheric material in these regions (Daw, 2012).

The goal of the Doppler shift measures in the $Fe\ XVI$ emission line is to provide energy constraints during the flare impulsive phase. Indeed, solar flares can be the sign of gigantic solar storms. These can propel charged particles from the Sun to the Earth and cause for example power blackouts. A better understanding of such phenomenon and forecasting them may avoid such catastrophes (PhysOrg, 2012).

The chosen orbit is a LEO. Atmospheric drag is thus the most significant disturbance that the satellite undergoes. The orientation of the satellite is of importance to decrease the aerodynamic torque: the lower moment arm between the centre of pressure and that of mass, the lower disturbance. Solar pressure is neglected in this study because of small importance in comparison with the aerodynamic drag. Indeed, the satellite is always sun pointed thus the moment arm is extremely small (Goldstein & Kady, 2012). Finally, the gravity gradient torque is also neglected because of the symmetry in the inertia tensor (Goldstein & Kady, 2012).

[14] Different classes of solar flares exist and are named A, B, C, M or X according to their peak flux (W/m^2) of 100 to $800\ pm$ X-rays near Earth.

2.6.2. Systems

2.6.2.1. Payload

The FIDI payload (See Figure 38) is designed to perform a monitoring of the entire solar disk to provide spatially resolved Doppler shifts during the impulsive phase of solar flares (Daw, 2012). High-reflectivity SiC/Mg multilayer coatings are applied on two co-aligned telescopes to image the solar disk in two bandpasses. The difference of the two images then provides a measure of the Doppler shift in the observed emission line. A single thinned back-illuminated CMOS sensor is used to capture the two side-by-side images at the same time. Aluminium filters are located on the optical path to avoid the focal plane to be illuminated by visible light. In addition, they protect the optics from contamination (Daw, 2012).

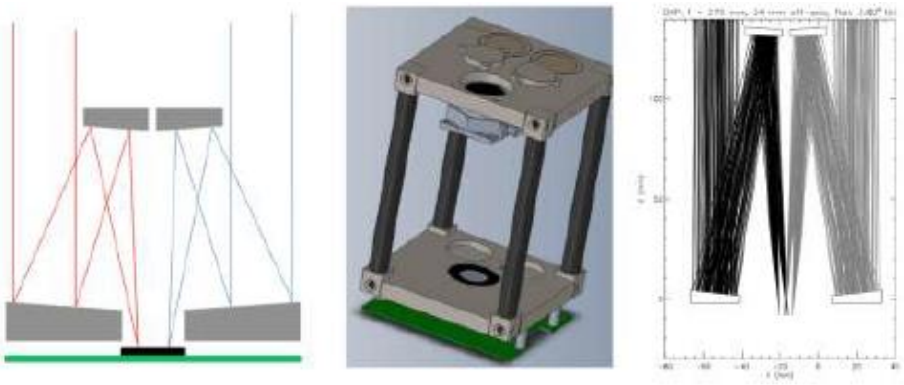

Figure 38 - FIDI optical payload: the two bandpasses *(left)*, the structure *(middle)* and the ray-tracing *(right)* (Daw, 2012)

A short exposure time permits to limit the effects of jitter noise while respecting the needed signal-to-noise ratio (SNR). The distances between the primaries, secondaries and focal plane are kept constant with the help of COTS carbon fiber tubes.

2.6.2.2. ADCS

The ADCS is composed of two actuators and three sensors. Reaction wheels and torque rods are used to provide a pointing accuracy of $\pm 0.2°$. A fine sun sensor, an IMU and a magnetometer are used for attitude knowledge.

Two control modes can be selected. When the wheels saturate the first mode is activated in order to get the wheels back to their functioning momentum range. The second one consists in using the reaction wheels to provide attitude control. This attitude control strategy is shown in Figure 39 (Goldstein & Kady, 2012).

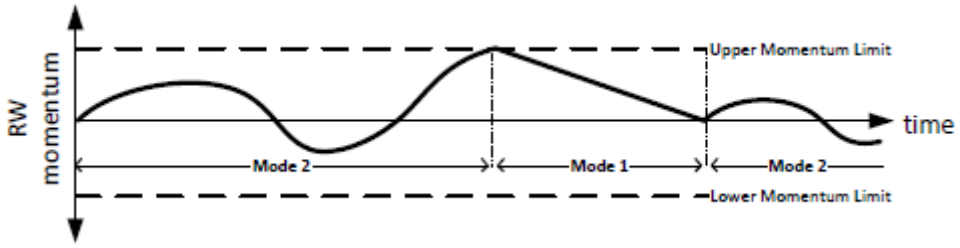

Figure 39 - Control mode (Goldstein & Kady, 2012)

The torque determination algorithm works as follows: the needed reaction wheel torque is determined by subtracting the rod torque to the total desired torque. This way, the reaction wheels supply the additional torque that is required to that of the rods to perform a maneuver. This mechanism is illustrated in Figure 40 (Goldstein & Kady, 2012).

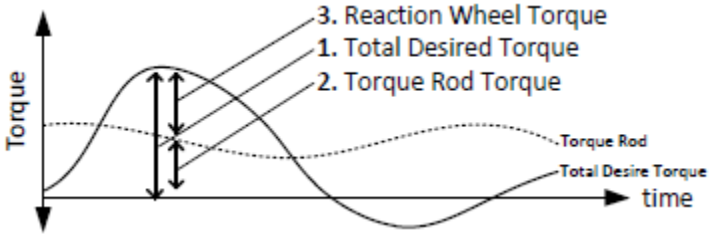

Figure 40 - Torque determination (Goldstein & Kady, 2012)

The ACS is designed in such a way that it can be scaled up or down depending on the need. For example, the torque rods, which depend on the Earth magnetic field, can be replaced with cold gas thrusters (Goldstein & Kady, 2012).

2.7. Cubesat subsystems

2.7.1. ADCS

The ADCS system can be an heritage from ExoplanetSat, ALL-STAR and SDS-1. ExoplanetSat for example achieves a pointing accuracy of $60\ arcsec$ with the $MAI\text{-}200$ (CubeSatKit) and custom sensors. This ADCS is a $1U$ system that performs tree-axis stabilization.

The $iADCS\text{-}100$ can also be used. This system has a volume of approximately $1/3\ U$ and incorporates three orthogonal reaction wheels, three magnetorquers, a star tracker and MEMS sensors (gyroscope, accelerometer, magnetometer). Additional sensors can also be plugged to this device such as GPS and sun sensors. It weighs only $250\ g$ and has nominal and peak consumptions of $0.5\ W$ and $1.8\ W$ respectively (BerlinSpacetechnologies).

The $XACT$ from Blue Canyon Technologies is a $0.5\ U$ ADCS that can perform three-axis attitude control with a pointing accuracy of $\pm 0.02°$. It incorporates a micro star tracker and a micro reaction wheel assembly. This device can be used in LEO orbits between $160\ km$

and $2000\ km$. The nominal and peak power consumptions are lower than $0.5\ W$ and $2\ W$ respectively (BlueCanyonTechnologies).

Finally, an algorithm that evaluates the Cubesat drift by following the pixels illuminated by the Jupiter's auroras may be elaborated (Salvador, 2012).

2.7.2. EPS

Most Cubesats presented above use COTS electronic components and this mission does not show any particularity that needs the use of complex components. Similar solar panels configurations to ExoplanetSat, MISC, DELFI-C³ or SDS-1 can be used. Typical power generations of $20\text{-}60\ W$ may be generated by solar arrays of actual Cubesats in full sunlight (Salvador, 2012). For example, the peak power consumption of ExoplanetSat rises to $35\ W$ so power generation should not be a problem in this case (Smith, et al., 2012). A power budget has to be performed to know if using a deployable structure is required.

Batteries are needed in this case because the actual strategy is to observe in eclipse. The lithium-ion technology's density is well suited for the Cubesat platform (Woellert, Ehrenfreund, Ricco, & Hertzfeld, 2010). Moreover, their "memory effect" is quite low, i.e. they do not have to be totally discharged before being recharged. However, a proper management of these cycles is appropriate to extend their life. Indeed, their characteristics depend on temperature for example and heaters may be needed to keep the batteries in their operating temperature range (Woellert, Ehrenfreund, Ricco, & Hertzfeld, 2010). Depending on the satellite's orbit, heaters may be needed to achieve this goal. Further analyses have to be performed to take into account the satellite's orbit and check if the available sunlit period is long enough to charge the batteries.

2.7.3. Communications

This system is critical since it receives and operates the commands that are sent from the ground station and allows the images to be downloaded from space. For imaging system, the data can range from tens to thousands of kilobytes (Woellert, Ehrenfreund, Ricco, & Hertzfeld, 2010). The communications system can consume a lot of power during the few minutes of functioning per orbit. Actually, up to 50% of the total available energy can be consumed by communications (Woellert, Ehrenfreund, Ricco, & Hertzfeld, 2010). A difficult task with Cubesats is to communicate during their short passage above the ground stations. Indeed, since they are on LEO, they pass relatively fast and the downlink time is limited.

An advantage of $3U$ Cubesat with respect to single unit platforms is that they often can incorporate more complex communication systems. For example, CanX-2 has three communication subsystems: a VHF beacon, a high data-rate S-band transmitter and a full duplex amateur radio transmitter (Woellert, Ehrenfreund, Ricco, & Hertzfeld, 2010). The S-band data rate varies from $32\ kbps$ to $1\ Mbps$ depending on the link condition.

ExoplanetSat has both low and high gain antennas to take into account possible control lost of the satellite and the detumbling phase (Smith, et al., 2012). Indeed, a global coverage is needed when the satellite's attitude is not under control. Such a solution could be implemented here: the high gain antenna may be used when the three-axis attitude control is operational and the low gain antenna in other cases.

Finally, a proliferation of ground station networks for small satellites is happening and will eventually allow near-continuous periods of satellite communications with the ground segment (Woellert, Ehrenfreund, Ricco, & Hertzfeld, 2010). The ESA Education Office sponsors for example the Global Educational Network for Satellite Operations (GENSO), a peer-to-peer client server network of ground stations that are interconnected via the internet. Any educational satellite can elect to be part of GENSO and use any participating ground station. The University Space Engineering Consortium (UNISEC) is another non-profit ground station network that incorporates several universities all around the world. Developing ground stations dedicated to a single Cubesat induces a cost of several tens of thousands dollars so this is a great advantage to be allowed to take advantage of such networks.

2.7.4. Thermal Control

The Cubesat's philosophy consists in using as many passive techniques as possible. Therefore coatings and straps should be used as much as possible as it is done for ExoplanetSat (Smith, et al., 2012). Heaters may be required to keep the batteries in their operating temperature range and to avoid the detector to suffer from contamination. This can lead to a defocus of the optical system and stresses due to differences between thermal expansion coefficients. The objective is thus to isolate the optical payload from the sunlight and the Earth albedo radiations with the help of coatings. The attitude control may also be optimized to achieve this task and deployable solar panels[15] may be used to shade the telescope.

[15] If the power consumption needs deployable solar panels.

Chapter 3

Mission analysis

3.1. Overview

Since the Io's torus tilts in phase with the Jupiter's rotation ($\sim 10\ h$), the intervals between each acquisitions have to be less than $5\ h$. If the total mission life is several weeks, an image every one or two hours should be acceptable and corresponds to approximately one image every orbit in LEO (Salvador, 2012). Jupiter's visibility during the mission period has to be checked to be sure that the telescope is able to observe the Io's torus. Memory capacities, telemetry, power and pointing accuracy have also to be investigated to be sure that these parameters do not bring further constraints (Salvador, 2012). The actual strategy is to observe the Io's torus in eclipse to benefit from the shadow of the Earth and avoid stray light problems. This strategy also simplifies the attitude control: one recharge phase when the spacecraft is sunlit and one phase of scientific observation in eclipse (Salvador, 2012). The same plan is chosen for ExoplanetSat (Smith, et al., 2012). The goal is thus to maximize the time that the spacecraft spends in eclipse. The *beta angle* is a useful parameter to characterize the orbital thermal environment, specially for low orbits. The orbit's beta angle is the minimum angle between the orbit plane and the solar vector (Salvador, Spacecraft payload design, 2012). It can be calculated as follows:

$$\beta = \text{asin}(\cos\delta_s \sin i \sin(\Omega - \Omega_s) + \sin\delta_s \cos i)$$

where δ_s is the declination of the Sun, i the orbit's inclination, Ω the RAAN and Ω_s the right ascension of the Sun. This parameter varies with time because of the nodal regression and the change in the Sun's right ascension and declination over time. Different beta angle configurations are illustrated in Figure 41 with in particular the extreme situations where the beta angle is $0°$ and $90°$ (Salvador, Spacecraft payload design, 2012). These latter correspond to the orbits that exhibit the maximum and minimum eclipse durations respectively.

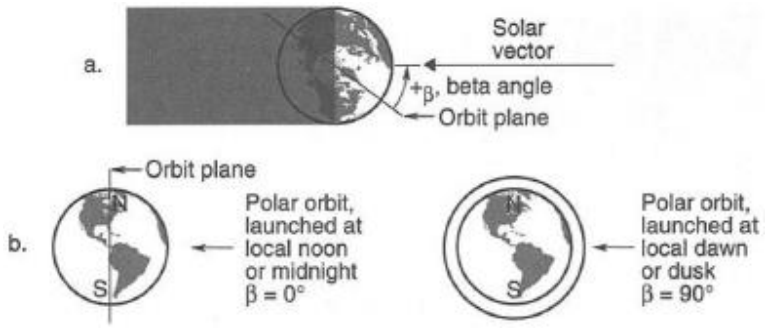

Figure 41 - Beta angle (Salvador, Spacecraft payload design, 2012)

Indeed, as β increases, the satellite passes over parts of the planet further from the subsolar point. The albedo loads are reduced and the spacecraft spends a larger percentage of the orbit in sunlight and less in eclipse. The evolution of the fraction of orbit in eclipse when the beta angle varies is illustrated in Figure 42 (Salvador, Spacecraft payload design, 2012).

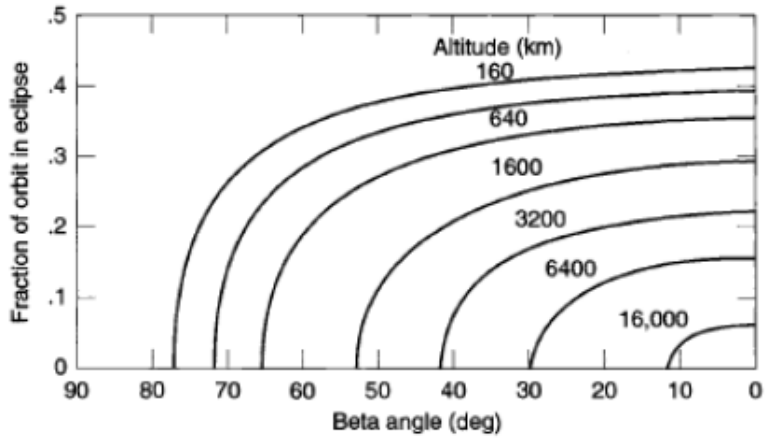

Figure 42 - Eclipse duration with respect to the beta angle (Salvador, Spacecraft payload design, 2012)

Therefore, to maximize the eclipse duration, small beta angles orbit should be considered. A $12{:}00\ AM$ sun-synchronous LEO orbit may be a good preliminary candidate.

3.2. Earth-Jupiter Distance

To investigate which orbit is the best for this mission, I used the Satellite Tool Kit (STK) software from AGI. This program is a powerful tool that can propagate orbits, perform maneuvers and simulate communications with ground stations for example. I represented the different objects of interest such as the Earth, Jupiter, Io and the spacecraft. This latter is first supposed to be on a $12{:}00\ AM$ sun-synchronous orbit (SSO) at $800\ km$. Since Cubesats are launched as secondary payloads, the orbit is fixed by the primary one and cannot really be chosen. I therefore chose this first orbit because it is the one in which Cubesats are often launched (Kerschen & Kintziger, 2013, March 13).

I first analyse the evolution of the distance between the Earth and Jupiter during the mission life of Juno. Indeed, this parameter is used further in this report to calculate the focal length of the telescope. Since they evolve on elliptic orbits, the distance between the two planets does not follow an exact sinusoid but the maxima and minima distance values continuously vary. This is illustrated in Figure 43 when considering the Mission life of Juno. Actually, I should not consider the entire period 2014-2017 since the Juno spacecraft only reaches Jupiter in 2016. It is then designed to observe Jupiter for a year so this 2016-2017 interval of time should only be considered for the Cubesat lifetime. However, we could think of launching the Cubesat earlier and start the observations before the Juno spacecraft reaches Jupiter.

The maxima and minima situations correspond to the positions when Jupiter and the Earth are in opposition phase and in phase respectively. Indeed, as represented in Figure 44, these are the configurations when the two planets are the farthest and the nearest. These values vary in function of the position of each planet on their respective orbit. The maximum and minimum distances, $d_{1,min}$ and $d_{1,max}$, are approximately equal to $965\,486\,177\ km$ and $629\,872\,394\ km$ respectively and occur on 25^{th} September 2016 and 4^{th} January 2014.

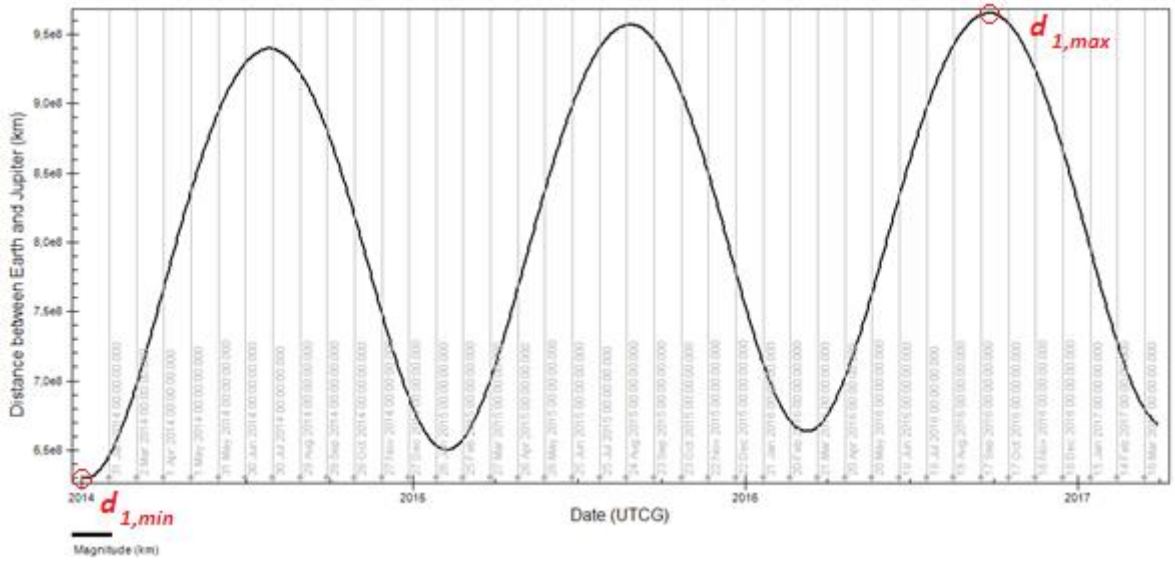

Figure 43 - Distance between the Earth and Jupiter during the Mission life of Juno

The period between two extreme values corresponds to the *synodic period* of Jupiter and the Earth. This corresponds to the interval of time that is needed for an object to reappear at the same position with respect to other ones. This period can be calculated as follows:

$$T_{syn} = \left|\frac{T_{Jup} * T_{Earth}}{T_{Jup} - T_{Earth}}\right| = \frac{4335.355 * 365.25}{4335.355 - 365.25} = 398.85\ days$$

This result corroborates the period that can approximately be measured from Figure 43.

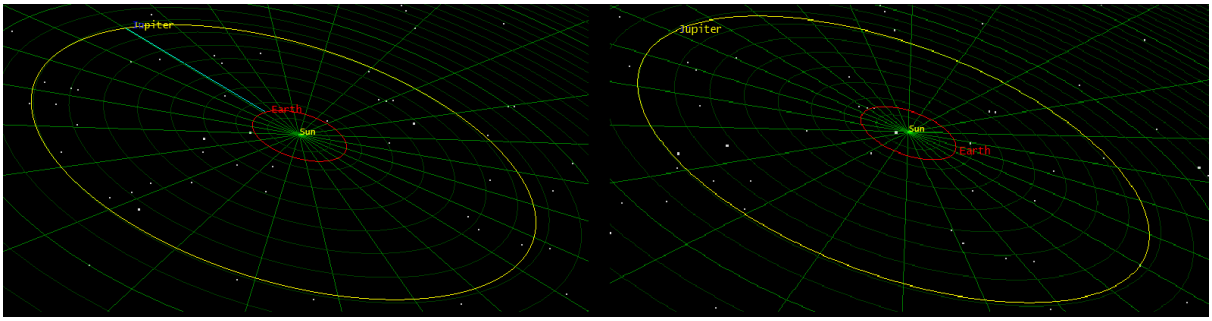

Figure 44 - Jupiter and Earth in phase and opposition phase configurations example

The maximum angular diameter of the Io's torus has to be calculated since it corresponds to the minimum FoV that the system must image. It must be determined at the minimum distance $d_{1,min}$ and is equal in first approximation to the diameter of the torus divided by $d_{1,min}$. The resulting minimum field of view is $5.059\ arcmin$.

3.3. Imaging timeline

STK is also able to calculate accesses from an object to another one. This allows the calculation of observation windows of the Io's torus during the mission life. Constraints can also be defined such as being in eclipse or durations longer than $10.5\ min$ in this case[16]. The results for the first $12{:}00\ AM$ sun-synchronous orbit are illustrated in Figure 45. The abscissa axis is the *Jovian* date.

The upper value of the accesses corresponds to the total eclipse duration. The Io's torus is not accessible with such an orbit during three periods of the mission life: from $16th$ May 2014 to $28th$ September 2014, from $13th$ June 2015 to $1st$ November 2015 and from $10th$ July 2016 to $9th$ December 2016[17]. The spacecraft is thus able to observe the Io's torus during a maximum duration of approximately eight months.

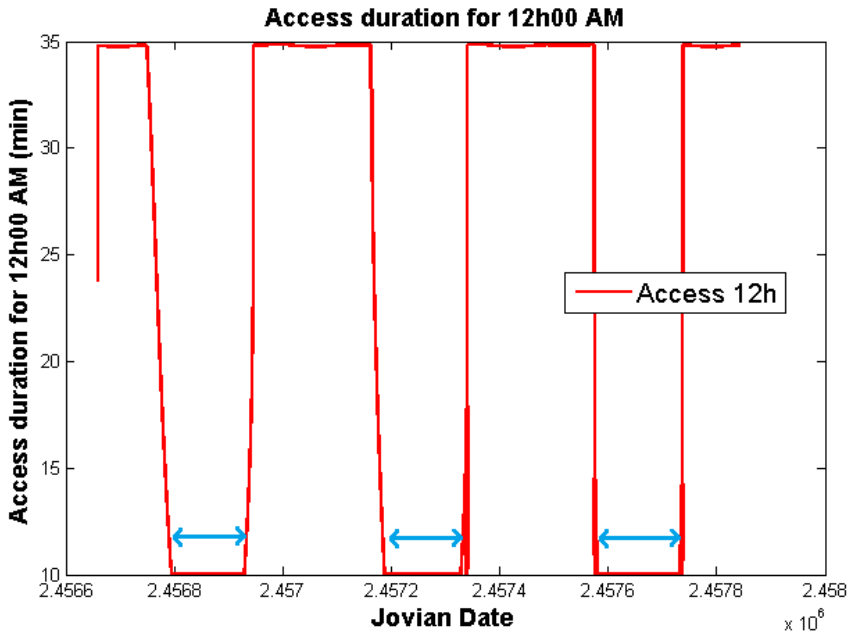

Figure 45 - Access duration in *minutes* of the 12h:00 AM SSO spacecraft. The blue arrows identify the periods during which the eclipse duration is not sufficient to reach the desired SNR

The observation duration depends on the launch date and it should not happen during any of the period where the eclipse time is not sufficient. Finally, such SSO orbits have

[16] With the help of a photometric budget we determine in this work that the observation time must be longer than $10.5\ min$ to reach a SNR greater than 10.

[17] Since a duration constraint was put in STK, only the accesses that are longer than $10.5\ min$ are represented. However, Matlab links by a line two observable periods and it looks like an access of exactly $10.5\ min$ exists but it does not actually. The blue arrows identify intervals of time where no access exists.

a period of approximately $1h\ 40\ min$ and the spacecraft is able to take at least an image at each eclipse during the observable periods. Indeed, the eclipse is $35\ min$ long and a single acquisition lasts at least $10\ min$. Therefore, this kind of orbit verifies the sampling requirement since an image must be taken every one or two hours.

Since the spacecraft's orbit cannot be predicted until a launch vehicle is selected, I now analyse the evolution of the observation windows with respect to a change in the orbit's RAAN[18]. I implemented in STK a Walker constellation (See Figure 46) with a different orbit at each RAAN hour to investigate if other orbits are better suited for the observation.

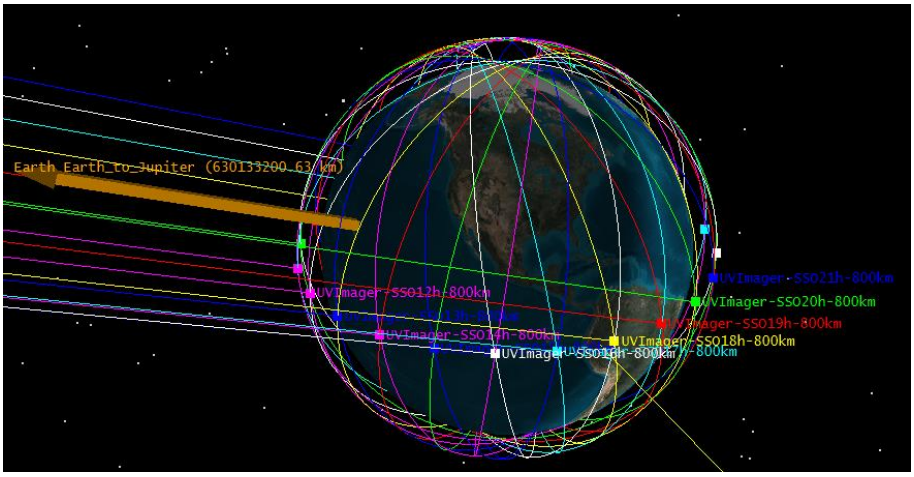

Figure 46 - Walker constellation of SSO orbits

I then calculated all the accesses for each orbit and plotted them by groups. This is illustrated in Figure 47. The maximum observation durations are reached by the $12{:}00\ AM$ and $00{:}00\ AM$ orbits that are actually symmetrical. Only the $16{:}00$ orbit has an eclipse duration of at least $10\ min$ during all the mission life. Even if the maximum eclipse duration is not as long as that of $12{:}00\ AM$ configuration, this orbit allows the spacecraft to observe the Io's torus during the whole mission duration of Juno.

Sometimes, the time that the spacecraft spends in eclipse is just enough to acquire enough signal but this does not take into account the maneuvers or the period to target Jupiter[19]. At these moments, the Cubesat may not be able to observe the Io's torus but these are quite rare when compared to the 4-5 months of inactivity of the $12{:}00\ AM$ orbit.

This $16{:}00$ orbit seems to be more appropriate to observe the Io's torus during the lifetime of Juno but we should keep in mind that choosing an orbit is quite inappropriate

[18] Further analyses shall study the variations of all the orbit's parameters but this work only focused on the common SSO orbit to which Cubesats are often launched.

[19] For example, the $iADCS100$ and $XACT$ ADCS flyers state that their slew rates are better than $1.5°/s$ (BerlinSpacetechnologies) (BlueCanyonTechnologies). If we consider a maneuver that needs a single-axis rotation of $180°$ and a slew rate of $1.5°/s$, this leads to an operation duration of $1m\ 30sec$. However, we may start the maneuver while still in sunlight and point Jupiter before being in eclipse.

with Cubesats. This analysis aims to predict the observation windows when considering a few orbits more than advising which orbit should be selected.

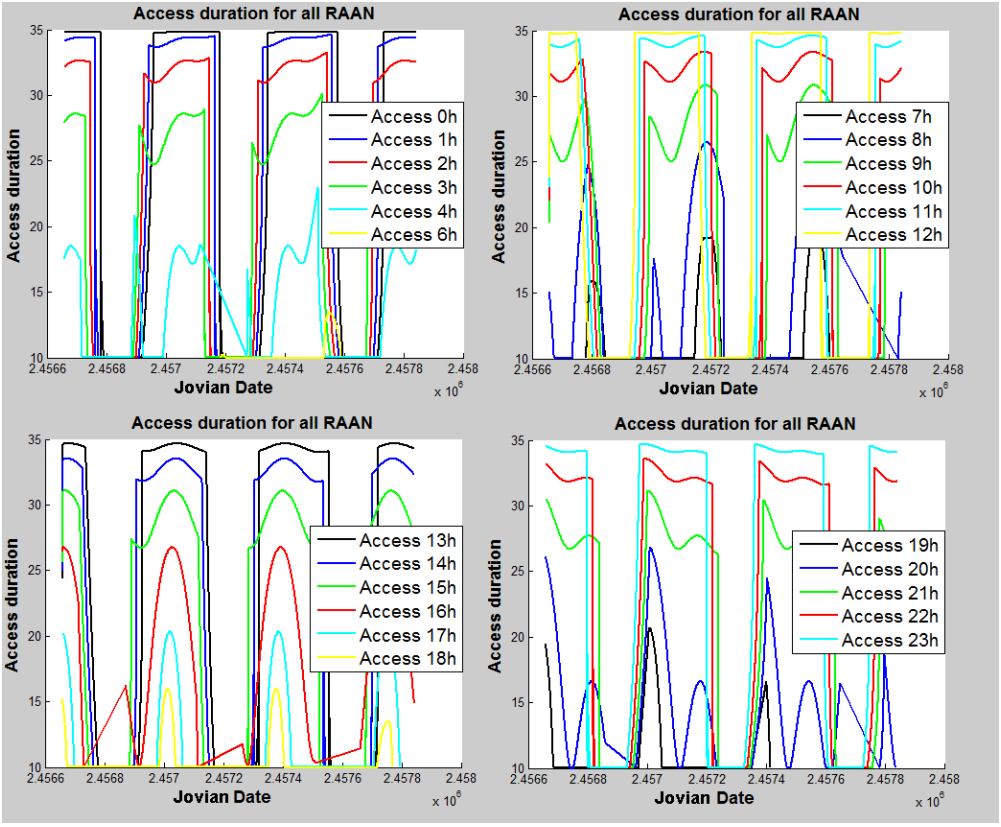

Figure 47 - Access duration in minutes for the Walker constellation

What could also be envisaged is a constellation of Cubesats as many other projects plan to do. The $8{:}00\ AM$, $12{:}00\ AM$ and $16{:}00$ orbits can be associated to reach a better coverage of the mission life. The accesses durations of this configuration are illustrated in Figure 48 where the green zone represents the maximum access duration that is available.

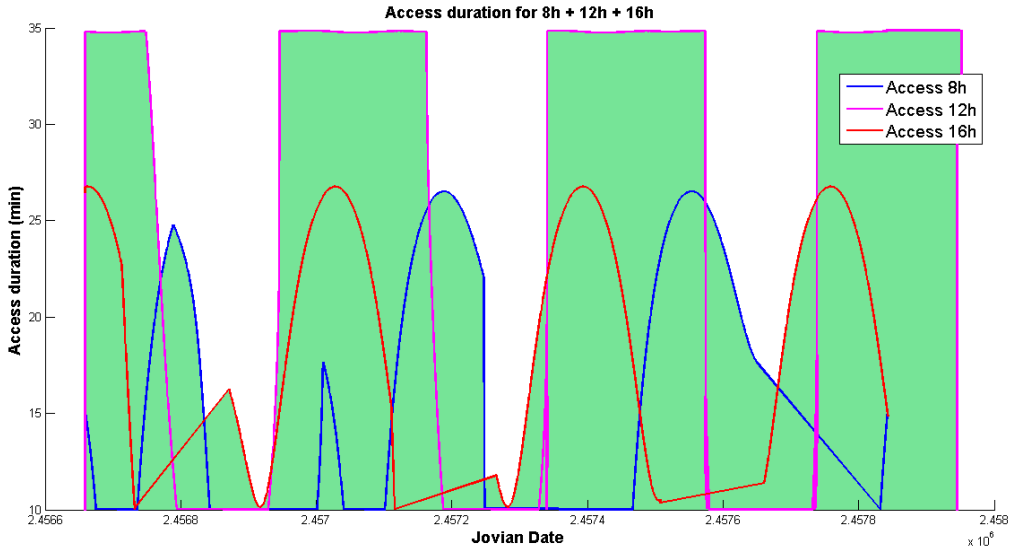

Figure 48 - Access duration of the constellation of three SSO orbits: 8:00 AM, 12:00 AM and 16:00

This way, the access to the Io's torus are always greater than $10\ min$ and the observation is possible during the whole mission life.

Finally such a constellation allows taking a greater number of images of the Io's torus and verifying the sampling requirement during nearly the whole mission life. Indeed, the eclipse duration is exactly $10\ min$ at some times and thus the observation may not be possible. The three spacecrafts may thus be phased in such a way that they are not at the same time in eclipse to observe the target in a continuous way. Since the orbit's period is $1\ h\ 40\ min$ it may be possible to phase the satellites in such a way that the eclipses follow each other. However, the accesses to the Io's torus do not happen as soon as the spacecraft enters in eclipse since it depends on the Jupiter's location. Further analyses shall be performed to investigate an optimal configuration of the Cubesats inside such a constellation.

3.4. Attitude control

Provided an access exists between the satellite and Jupiter, I impose that the spacecraft has to track Jupiter and I recorded its attitude during these intervals of time (See Figure 49). I therefore obtained the pitch, roll and yaw values that were needed to follow the target in real time. These parameters can be useful to assess the saturation problem of the reaction wheels. Indeed, when the reaction wheels are used to control the attitude of the Cubesat, these can perform it as long as they do not saturate. Once they are saturated, they have to be reset with for instance magnetorquers that are usually incorporated inside the overall ADCS (it is the case of the $iADCS$-100 and the $XACT$).

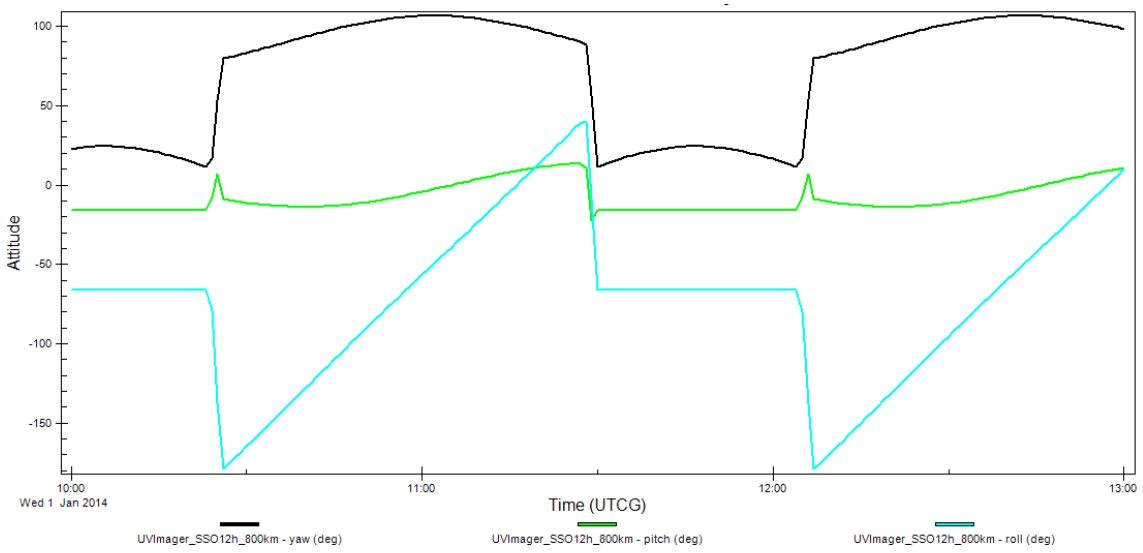

Figure 49 - Pitch, roll and yaw of the Cubesat during two accesses

When this happens, the satellite cannot track the target anymore and the observation is jeopardized. To avoid such problems, the saturation of the wheels has to be controlled and allowed only out of observation periods. By knowing the required attitude

parameters with the help of Figure 49 and the inertia momentum of the satellite, assessing the saturation of the wheels is feasible (Salvador & Kintziger, (Personal Communications), 2013).

Yet the saturation of the wheels depends on many factors like the satellite orbit, the control strategy, the Cubesat's interior configuration and the satellite's shape for example (Dell'Elce & Kintziger, 2013). Moreover, in general the reaction wheels are not the only mechanisms that are used to control the satellite but magnetorquers are also used at the same time. This depends on the control strategy that is employed. For example, the $iADCS$-100 uses the magnetorquers simultaneously to decrease the reaction wheels' velocity and avoid their saturation. Similar control modes were introduced when talking about the SDS-1 Cubesat for which the reaction wheels only provided the needed momentum that was required in addition to that of the magnetorquers. If the reaction wheels saturated, then the magnetorquers were used to desaturate them. Further analyses have to be performed to establish an attitude control strategy that minimizes the risk of saturating the wheels while targeting the Io's torus.

Eventually, elaborating a constellation strategy is complex since no launcher is chosen yet. The deployment of the Cubesats may be inspired from that of RTICC for example, i.e. with carriers of three spacecrafts.

Chapter 4

Optics theory

4.1. Optical design theory and Code V presentation

4.1.1. Basic optics

4.1.1.1. Basic parameters

The goal of all optical systems is to resolve a specified minimum-sized detail over an entire object which is the *field of view (FoV)*. The FoV can be designated as a spatial or angular extent in the object space. In this case, the angular extent of the Io's torus constitutes the minimum FoV that the optical system has to image. The minimum-sized detail that the system has to be able to distinguish is called the *resolution*. This is the smallest element in the image that has to be identified in order to be able to understand the image (Fischer, Tadic-Galeb, & Yoder, 2008). In this case, the Laboratory of Planetary and Atmospheric Physics (LPAP) of the University of Liège required that Jupiter shall be imaged on at least 4 pixels. Thus, the minimum angular resolution of the system is half the angular radius of Jupiter.

The lens example below intends to introduce some typical optical parameters that are usually used. Light rays from infinity strike the lens through its *clear aperture diameter*. The rays go through the different elements till being focused on the focal plane. If we follow these rays (solid lines) back from the detector to the entrance of the optical system as if they were not bent by the lenses (dashed lines), the intersection between these imaginary rays and the incoming ones determine the *focal length*. This is the distance between this intersection point and the image plane.

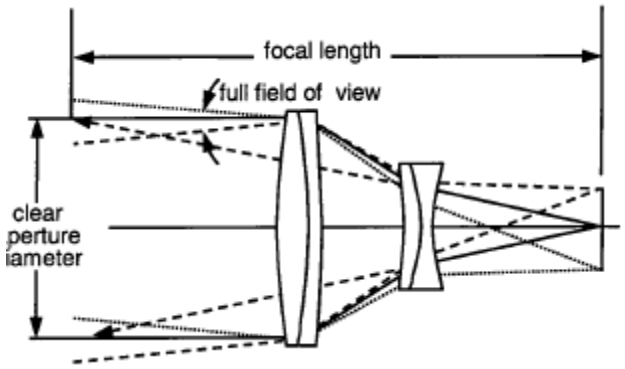

Figure 50 - Basic lens example (Fischer, Tadic-Galeb, & Yoder, 2008)

We can also define the imaging cone that reaches the centre of the image by a parameter that is called the $f/number$ or $f/\#$. This angle is defined by the relation below:

$$\frac{f}{number} = \frac{focal\ length}{clear\ aperture\ diameter}$$

The *effective focal length* (*EFL*) is the focal length of a system composed by multiple optical subsystems (Fischer, Tadic-Galeb, & Yoder, 2008). Then, the *back focal length* (BFL) or *backfocus* is the distance between the last surface of the optical system and the focal point (Smith W. J., 2008).

When pixelated detectors like CCD or CMOS sensors are used, a rule of thumb is to match the smallest desired resolution element to the detector's pixel size (Fischer, Tadic-Galeb, & Yoder, 2008). We explain later that this was used to determine the needed focal length of the system to fulfil the resolution requirement. In fact, a simple equation links the image height to the angle of incidence of off-axis rays (1). This is shown in Figure 51 where θ is the incidence angle of the rays and f the focal length (Fischer, Tadic-Galeb, & Yoder, 2008).

$$y = f \tan\theta \qquad (1)$$

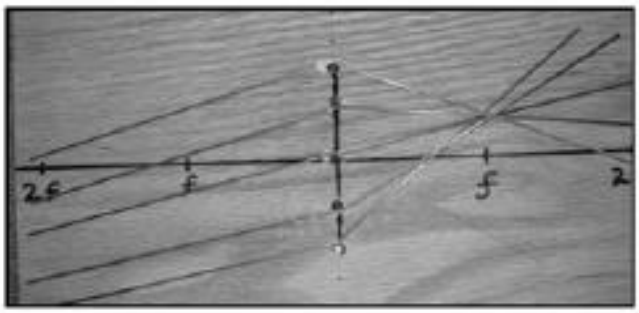

Figure 51 - Link between off-axis rays' incidence angle and image height (Fischer, Tadic-Galeb, & Yoder, 2008)

When we talk about FoV, we should take care about the exact signification of it. Indeed, we have to mention if it is the *total field of view* , that is, a given value that the system images from up and down (which is usually expressed as $\pm X°$) or a particular subset of it. For example, one could specify its own optical system with a *diagonal field of view* but has to mention it not to confuse other users.

Another system specification is the *spectral range* or *wavelength band* over which the system is supposed to be used. One important thing is to specify at least three or five particular wavelengths and their respective *weights* (Fischer, Tadic-Galeb, & Yoder, 2008). These latter are the importance factors that will guide the system optimization with respect to the considered wavelengths. If the detector used is less sensitive in the red spectral range,

the optimized optical system can be less efficient in these wavelengths since no perceptible image degradation will be noticed. Figure 52 illustrates the way these weights are calculated for five different wavelengths. The first step is to select the five wavelengths distributed over the spectral curve and divide the curve into bands. The boundaries of these bands can be chosen for example between the wavelengths. The weights that have to be associated to each wavelength are then the integral within each band considered.

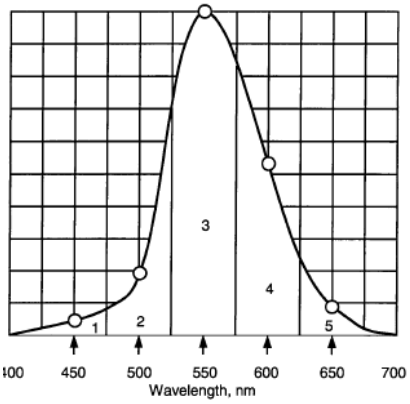

Figure 52 - Weights calculation

Even if the spectral range is narrow, its bandwidth must be taken into account. Designing a system for which the spectrum consists in a single ray is an error. Its broadened spectrum must be considered. Only laser systems can usually be designed with the specific laser wavelength (Fischer, Tadic-Galeb, & Yoder, 2008).

The *aperture stop* of an optical system is usually a mechanical diaphragm that is intended to limit the bundles of rays which pass through the optical system. Thus, its main goal is to adjust the brightness of the image. It is located where all the chief rays from the different object points cross the optical axis and seem to pivot about (Fischer, Tadic-Galeb, & Yoder, 2008). The *chief rays* are those that seem to have not been deflected while passing through the optical system. The image of the aperture stop when observed from the front of the optical system is called the *entrance pupil*. Its location can be found by extending the entering chief ray as if it was not deviated until it reaches the optical axis. The intersection is then located at the entrance pupil.

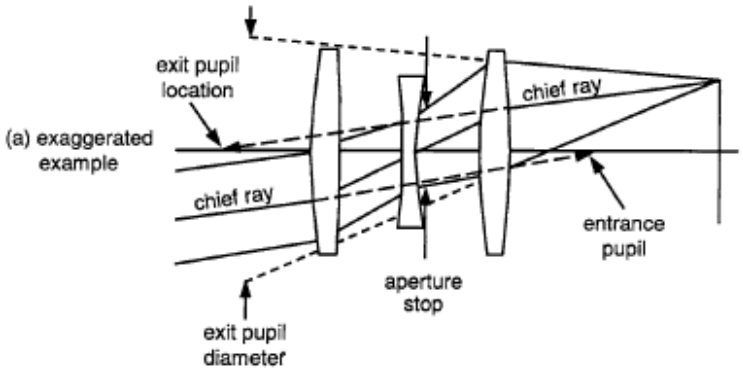

Figure 53 - Aperture stop, entrance and exit pupils (Fischer, Tadic-Galeb, & Yoder, 2008)

On the other hand, the *exit pupil* is the image of the aperture stop when viewed from the image plane. The same construction by starting from the leaving chief ray locates the exit pupil.

4.1.1.2. Vignetting

The pupils of a system and the size of its elements determine the amount of light through the optical system. If the apertures do not truncate or clip the bundles of rays from all points in the FoV which fill the aperture stop, the system does not suffer from any *vignetting* (Fischer, Tadic-Galeb, & Yoder, 2008).

In some cases, optical system deliberately introduce vignetting in order to reduce the system aberrations. Indeed, in the example below where lenses are used, the rays at the edge of the lens (situations A and B) undergo severe bending since the lens is more curved and the aberrations are thus greater. A solution is thus to limit the lens aperture ($D \rightarrow 0.7\ D$) to limit these effects. However, vignetting is induced and light energy is reduced inside the system but this can lead to thinner and smaller devices (Fischer, Tadic-Galeb, & Yoder, 2008).

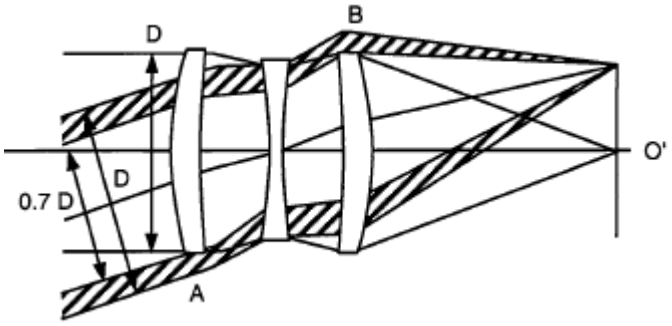

Figure 54 - Lens vignetting (Fischer, Tadic-Galeb, & Yoder, 2008)

4.1.1.3. Diffraction

When considering light as a wave, this one can interact with the sharp limiting edge of an optical system. As a consequence, when the system images a single point, the result is actually not a point but a more complicated pattern.

Diffraction phenomena can easily be understood by the help of waves on the surface of a swimming-pool as Fischer explains it (See Figure 55). By throwing a rock into this swimming pool at one of its side, concentric waves emanate and propagate to the other side. If the swimming-pool is long enough, these waves are straight and parallel to each other when reaching it. Let us now imagine that these waves strike an obstacle, then instead of inducing a sharp step in the water, new concentric waves are generated. This phenomenon is called *diffraction* (Fischer, Tadic-Galeb, & Yoder, 2008).

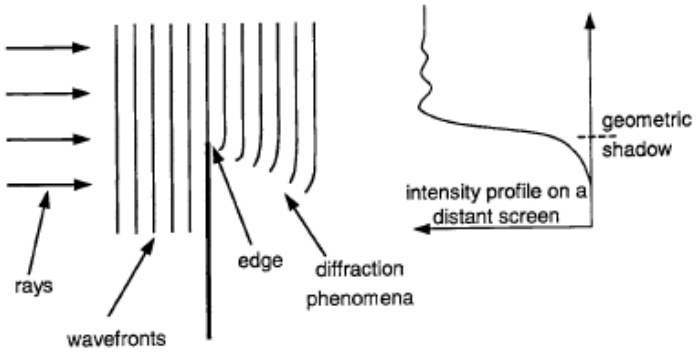

Figure 55 - Diffraction phenomenon (Fischer, Tadic-Galeb, & Yoder, 2008)

Similar phenomena happen when considering light since the two mechanisms consist in wave propagation problems. A more accurate mathematical way to describe diffraction phenomena uses the *Fourier Transform*. When the *Fraunhofer conditions*[20] are fulfilled, the diffraction pattern that is observed in the image plane is the Fourier transform of the aperture field distribution (Goodman, 1996).

By considering different aperture shapes, the Fraunhofer diffraction pattern can be predicted by calculating the Fourier transform of the aperture distribution. Indeed, if we consider a rectangular aperture, the diffraction pattern field follows a $sinc$ law in each direction whereas a circular aperture exhibits a *Bessel* function pattern in the image plane. These two examples are illustrated in Figure 56.

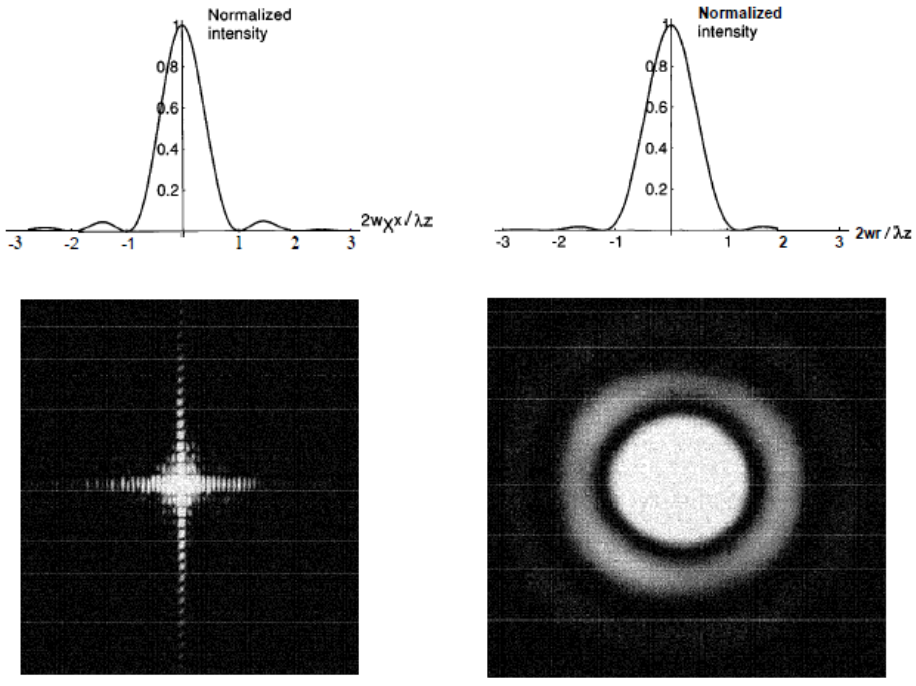

Figure 56 - *Fraunhofer* diffraction patterns of a rectangular aperture (*left*) and a circular aperture (*right*) (Adapted from (Goodman, 1996))

[20] This approximation considers the image object far from the optical system and that this distance is much larger than the diffracting aperture size.

Actually, the *complex field strength* is the Fourier transform of the aperture field distribution while the intensity, the interesting parameter that we actually see and measure, is the square of this latter. So, the previous patterns are respectively $sinc^2$ and $Bessel\ function^2$ in each direction. When considering a circular aperture we recover the famous *Airy disk* diffraction pattern of light. These diffraction patterns are commonly called *point-spread function* (PSF).

When the system is aberration-free, the diffraction blur is dominated by the diffraction pattern. In this case, the system is said *diffraction-limited*. By considering the Bessel functions, the physical diameter of the Airy disk (the separation between the two first minima $+1$ and -1) can be expressed with the following equation:

$$Airy\ disk\ diameter = 2.44\ \lambda\ \frac{f}{D} = 2.44\ \lambda\ \frac{f}{number} \qquad (2)$$

4.1.1.4. Optical path difference (OPD) and Rayleigh criteria

One way to measure the optical performance of a system is to compare the image wavefronts to those which are perfectly spherical, concentric and centred at the point image. If both are identical for a given FoV, the system is geometrically perfect or diffraction limited (Fischer, Tadic-Galeb, & Yoder, 2008).

Figure 57 illustrates the optical path difference concept. If we consider for example a perfect lens, i.e. aberration-free, its induced wavefront is perfectly spherical and concentric. The rays, which are perpendicular to the wavefronts, are thus concentrated to a single point. The *optical path difference* is the difference between the real wavefront, generated by a real aberrated lens, and a reference spherical wavefront that is usually selected to be a near best fit of the aberrated wavefront. The Rayleigh criterion then says that the optical performance of the system is not altered if the OPD is less than or equal to a quarter of a wavelength (Fischer, Tadic-Galeb, & Yoder, 2008).

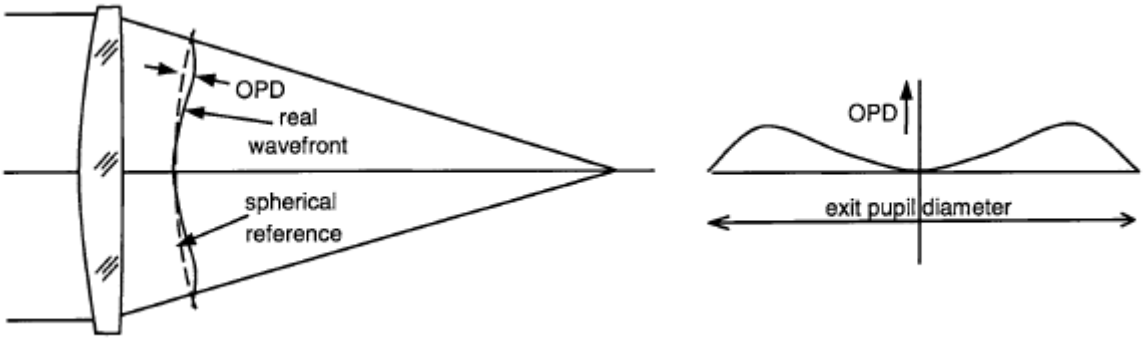

Figure 57 - Optical path difference (Adapted from (Fischer, Tadic-Galeb, & Yoder, 2008))

Provided this criterion is respected the image of a point object is nearly the diffraction pattern of the optical system. Two methods exist to measure the OPD *peak-to-valley* (P-V) and *RMS wavefront error (WFE)*. The first describes the difference between the nearest and the farthest from the image's real wavefront values while the second consists in an average measure. Indeed, this latter is the square root of the sum of the squares of the OPD's with respect to the best-fit reference wavefront over the entire wavefront. These definitions are illustrated in Figure 58 (Fischer, Tadic-Galeb, & Yoder, 2008).

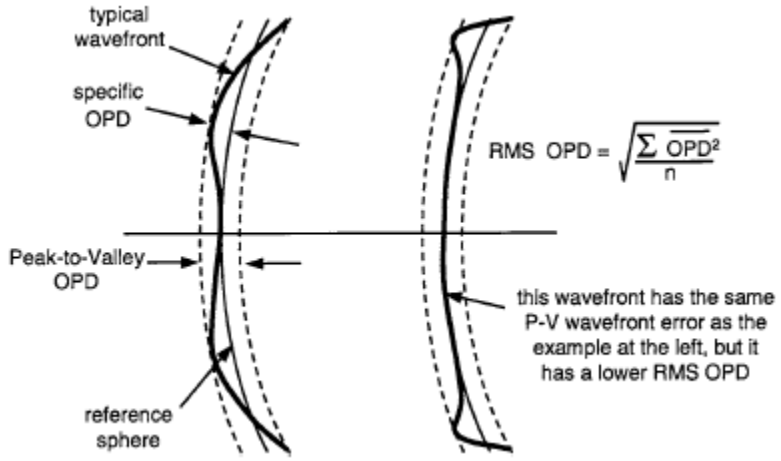

Figure 58 - Peak-to-valley and RMS wavefront errors (Fischer, Tadic-Galeb, & Yoder, 2008)

Even if this tool is very useful for examining the optical performance of a system, it is more quantitative and not completely infallible and should be used as a relative measure (Fischer, Tadic-Galeb, & Yoder, 2008).

4.1.1.5. Wave aberration polynomial

Geometrical aberrations are the main reason for which an optical system is not able to form a perfect geometrical image. In the case of rotationally symmetric systems, the optical path difference, or *wave aberration function*, can be expressed with a polynomial.

When a ray enters a system, its characteristics can be described in terms of object plane and entrance pupil coordinates (see Figure 59). Then, the wave aberration function can be expressed as a Taylor expansion polynomial involving these parameters. When considering rotationally symmetric optical systems, this function can actually be simplified and only some of the terms of the series are involved in the polynomial (See (3)). The first two terms do not represent any system aberrations but focal shifts while those at the power of four correspond to what is called *the primary aberrations* of the optical system. The higher powers describe the *higher-order* aberrations that characterize the system.

$$W = k_{020}\ \rho^2 + k_{111}\,\sigma\,\rho\cos\phi + k_{040}\,\rho^4 + k_{131}\,\sigma\,\rho^3\cos\phi + k_{222}\,\sigma^2\,\rho^2\,(\cos\phi)^2 + k_{220}\,\sigma^2\,\rho^2 + k_{311}\,\sigma^3\,\rho\cos\phi + \cdots (higher\ order\ terms)$$

$$\Leftrightarrow W(\sigma,\rho,\phi) = \sum k_{l+n,m+n,n}\, \sigma^{l+n}\, \rho^{m+n} \cos^{n}\phi \tag{3}$$

where

- σ is the object height,
- ρ and ϕ are the polar coordinates of the ray in the entrance pupil plane,
- l, m are even positive integers or zero and n any positive integer or zero.

These coordinates are shown in Figure 59.

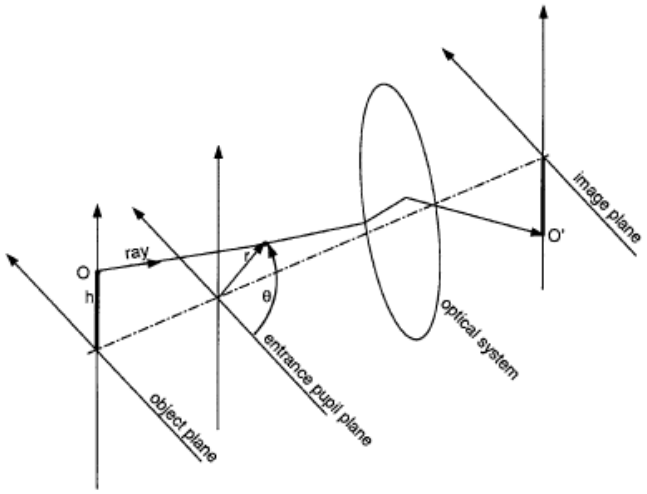

Figure 59 - Ray coordinates (Fischer, Tadic-Galeb, & Yoder, 2008)

On the other hand, the easiest way to obtain the coefficients of the wave aberration polynomial is to trace as much as possible rays through the system and then fit the data to the polynomial. Only a few rays are needed to obtain the third order aberrations while the fifth order ones require more calculations. This can now be achieved easily with the help of computer softwares.

Actually, the person who demonstrated that these parameters could only appear in this polynomial in the form of r^2, h^2 and $r\, h \cos\theta$ is *Hamilton*. He demonstrated in 1833 that, based on the symmetry of centred optical system, one could express the wave aberration polynomial by the help of three fundamental parameters: r, h and θ (Wilson, 2007). He actually called it the *Characteristic Function*. From this wave aberration polynomial the aberrations of the system can be analyzed. In fact, the type of aberrations depends on the parameters r and $\cos\theta$ while h informs about their variation through the field. Table 3 shows first, third and fifth order aberrations of this polynomial (Wilson, 2007). In each column an aberration type is presented (each one is denominated by a n value) which is an infinite series of powers of ρ. We can now define what is called the *order* of the aberration by the parameter:

$$N_H = (Sum\ of\ powers\ of\ \sigma\ and\ \rho) - 1$$

m	$n=0$	$n=1$	$n=2$	$n=3$	Order
0 2	 $_0k_{20}\rho^2$	$_1k_{11}\sigma\rho\cos\phi$			First: $N_H=1$ $(l+m$ $+2n=2)$
0 2 4	 $_2k_{20}\sigma^2\rho^2$ $_0k_{40}\rho^4$	$_3k_{11}\sigma^3\rho\cos\phi$ $_1k_{31}\sigma\rho^3\cos\phi$	$_2k_{22}\sigma^2\rho^2\cos^2\phi$		Third: $N_H=3$ $(l+m$ $+2n=4)$
0 2 4 6	 $_4k_{20}\sigma^4\rho^2$ $_2k_{40}\sigma^2\rho^4$ $_0k_{60}\rho^6$	$_5k_{11}\sigma^5\rho\cos\phi$ $_3k_{31}\sigma^3\rho^3\cos\phi$ $_1k_{51}\sigma\rho^5\cos\phi$	$_4k_{22}\sigma^4\rho^2\cos^2\phi$ $_2k_{42}\sigma^2\rho^4\cos^2\phi$	$_3k_{33}\sigma^3\rho^3\cos^3\phi$	Fifth: $N_H=5$ $(l+m$ $+2n=6)$

Table 3 - Aberration types (Wilson, 2007)

Each line is therefore devoted to an aberration order so the first line contains the *first order aberrations*. The two terms that belong two this line, as said before, do not really represent aberrations. The term for which $n=0$ indicates a defocus of the image while the $n=1$ term induces a lateral shift of it since it is proportional to the field size. Then, the five fourth power terms are gathered in the second line of the table. They are the *monochromatic third order aberrations* or *Seidel aberrations*. These are the main sources of errors in telescope and general optical system images (Wilson, 2007).

We now explain each type of aberration, thus scanning all the different values of n of this class. The first column ($n=0$) contains terms that are all ϕ-independent. This aberration effect is thus symmetrical to the optical axis. In particular, the term $k_{040}\,\rho^4$ is called *spherical aberration* while the second one, $k_{220}\,\sigma^2\,\rho^2$ is the *field curvature aberration*. The next column also contains two terms. The term $k_{131}\,\sigma\,\rho^3\cos\phi$ is called *third order coma*, it is one of the most important aberration in telescope optics (Wilson, 2007). The second term, $k_{311}\,\sigma^3\rho\,\cos\phi$, is also a lateral shift as presented before with the first order aberrations but now, this aberration is proportional to the third power of the field size. This is not anymore only a scale error but consists in *distortion*. The image quality is not reduced by this mechanism but the image is displaced in a non-linear manner. Finally the examination of the last column of the second line reveals a last third order aberration. The term $k_{222}\,\sigma^2\,\rho^2\cos^2\phi$ consists in what is called *astigmatism*. This last aberration is once again extremely important in telescope optics (Wilson, 2007). The fifth order aberrations can also be interpreted but I do not explain all of them since they are not preponderant in the optical designs this work deals with.

Besides when considering third order aberrations, spherical aberration is independent of the field whereas coma is linearly dependent. Then, astigmatism is

proportional to the square of the field while distortion is to the cube. This is reminded later when analyzing ray trace curves of further designs.

It can be shown that the ray coordinates in the image plane are directly linked to the partial derivatives of this polynomial (Fischer, Tadic-Galeb, & Yoder, 2008). Indeed, if we denote these latter by $\partial x'$ and $\partial y'$, we have:

$$\partial y' \propto -\frac{\partial W}{\partial y} \qquad \partial x' \propto -\frac{\partial W}{\partial x} \tag{4}$$

Therefore, once the OPD is known, the ray intersections in the image plane can be easily obtained. The exponent of the pupil radius term (ρ) is higher by one in the wave aberration ((3)) polynomial than that in the ray-intercept equations ((4)) since they are related by a derivative operator (Fischer, Tadic-Galeb, & Yoder, 2008).

4.1.1.6. Aberrations

The effects on the image degradation due to the multiple aberrations introduced hereabove are exposed in this section. In *paraxial optics*, that is when considering small incidence angles ($\sin\alpha \approx \alpha$), there is no geometrical aberration. Therefore, the optical system image of a point is perfectly a point[21]. In a real system, incidence angles a large enough for the paraxial approximation to become invalid. This leads to geometrical aberration effects and the previous example of a point image now becomes a deformed pattern (Fischer, Tadic-Galeb, & Yoder, 2008).

A first distinction has to be done between *achromatic aberrations*, presented in the previous section, and the *chromatic aberrations*. The latter are due to refraction index variations with respect to the wavelength, which is called *dispersion*. When such a phenomenon appears in the system, the resulting image is a superposition of patterns at each wavelength which are degraded by the monochromatic aberrations. The spot thus consists in a multicolour and deformed pattern. This is not discussed here because reflective surfaces are considered and these aberrations only affect refractive materials.

Spherical aberration

If we consider an optical system that is made of a converging lens through which on-axis rays pass, those near the optical axis focus at the *paraxial focus*. As explained before, *paraxial focus* is the point where low incidence rays focus. When considering rays further from the axis, they converge closer to the optical system. This increasing departure from the paraxial focus as we consider rays far from the axis is called *spherical aberration* and is shown in Figure 60 (Fischer, Tadic-Galeb, & Yoder, 2008).

[21] Actually, it is the perfect diffraction pattern of the optical system.

When measuring the spherical aberration along the optical axis, it is called *longitudinal spherical aberration* while if it is measured at a certain point with respect to the on-axis chief ray, it is named *transverse spherical aberration*.

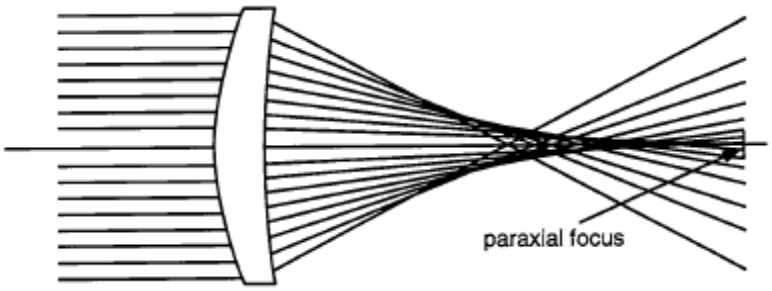

Figure 60 - Spherical aberration (Fischer, Tadic-Galeb, & Yoder, 2008)

Coma aberration

Figure 61 represents a situation where off-axis rays pass through an optical system. These rays strike the optical system at some angle and are then focused at a certain height in the image plane. *Coma aberration* is the phenomenon that appears when these rays do not focus at the same height from the optical axis. The image created by the optical system is then non-rotationally symmetric and looks like a comet (Fischer, Tadic-Galeb, & Yoder, 2008).

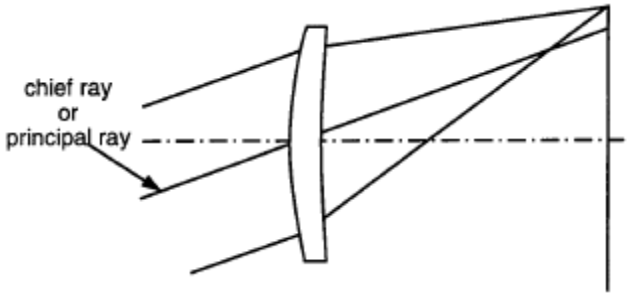

Figure 61 - Coma aberration (Fischer, Tadic-Galeb, & Yoder, 2008)

In the same way as before, the transverse aberration is measured with respect to the chief ray. As the image height differs for each incoming ray after it passes through the optical system, coma is often referred as the variation of magnification over the aperture (Fischer, Tadic-Galeb, & Yoder, 2008).

Astigmatism

To understand what *astigmatism* is, we have first to define new ray definitions. If we consider the axis system defined in Figure 62, *meridional rays* are those that belong to the YZ plane, where the Z axis is along the optical axis and points towards the focal plane (Fischer, Tadic-Galeb, & Yoder, 2008). On the other hand, rays that belong to the XZ plane, which is perpendicular to the YZ plane, are called *sagittal rays*. Both planes have in common a chief ray. Finally, other rays are called *skew rays*.

Astigmatism occurs when meridional and sagittal rays do not focus at the same distance from the optical system. Thus meridional and sagittal rays converge respectively along a line which is perpendicular to the meridional and the sagittal plane.

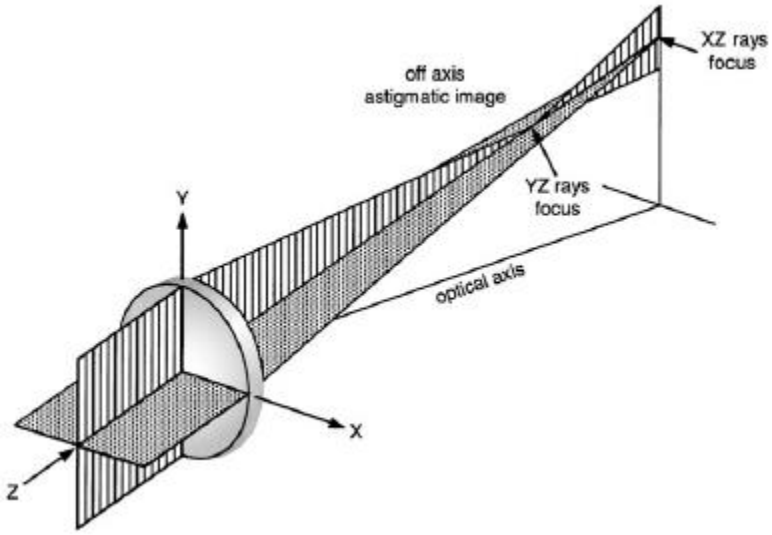

Figure 62 - Astigmatism aberration (Adapted from (Fischer, Tadic-Galeb, & Yoder, 2008))

The shape of the imaged spot can therefore be predicted. If we consider a given astigmatic focus, where all meridional or sagittal rays are focused, the image is a straight line. If we consider now a position where none of the sagittal and meridional rays have focused, the imaged spot looks like an ellipse. The best focus point is actually situated between the two astigmatic foci where the image is a circle (Fischer, Tadic-Galeb, & Yoder, 2008).

Field Curvature

Field curvature appears when an optical system produces an image which lies on a curved plane, called the *Petzval surface*. As we can see in Figure 63, the focal points describe a curved shape instead of a vertical straight line when considering different field angles (Fischer, Tadic-Galeb, & Yoder, 2008). This is what happens when the optical system suffers from field curvature.

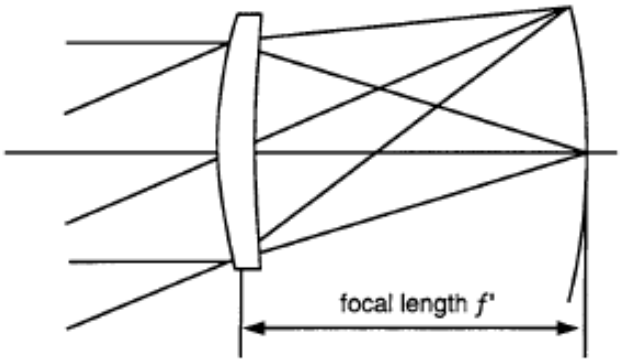

Figure 63 - Field curvature aberration (Fischer, Tadic-Galeb, & Yoder, 2008)

Distortion

The *distortion* aberration is the only one which does not create a blurred image but actually deforms it. Two types of distortion can be mentioned: *positive* or *pincushion distortion* and *ne*gative or *barrel* distortion. These two different distortions are shown in Figure 64 (Fischer, Tadic-Galeb, & Yoder, 2008).

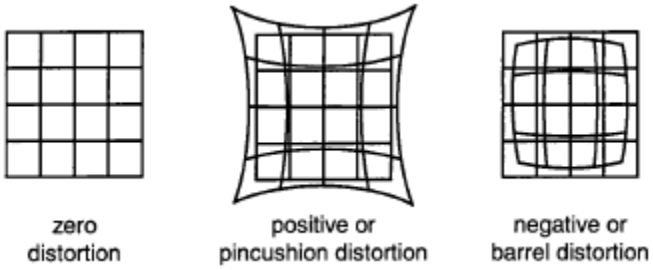

Figure 64 - Distortion aberration (Fischer, Tadic-Galeb, & Yoder, 2008)

Generally, a distortion aberration of 2% to 3% can be tolerated visually (Fischer, Tadic-Galeb, & Yoder, 2008).

4.1.2. The optical design process

The optimization of an optical system does not only mean running a software and start the optimization process. Actually, the designer has to perform much more tasks and ensure that everything is under control and well understood.

In particular, first order parameters of the system have to be respected in order to fulfil the mission objectives. Then, the right FoV and spectral band, associated to the right weights, have to be implemented into the software. If the optical quality of the system is not met, then the optimization process must be reiterated in order to reach the appropriate design.

Secondly, taking into account all the environmental effects that the real system will undergo is really important since the optical quality could be jeopardized. Therefore variations of temperature or pressure have to be included in the optimization process.

A tolerance analysis is also needed in order to check the assembly and manufacturability of the system at reasonable cost. Indeed, if the system is too sensitive with respect to small dimension variations, its fabrication should therefore respect very tight constraints and could be too expensive for a given budget.

Finally, stray light problems should be taken into account to be sure that the image quality is not perturbed by any light noise from other sources (Sun, Moon, Earth for example). However, this analysis is out of the scope of this work and is not performed.

4.1.2.1. Optimization algorithm

The optimization process of an optical system is at first glance a quite complex task since a simple association of some optical surfaces exhibits a large number of degrees of freedom. Indeed, in order to improve the optical quality of such a system, we may change the radii of curvature, thicknesses, conic constants, etc, and an considerable number of permutations is thus possible.

Nowadays, computers have made feasible what was before a tedious and time-consuming, maybe impossible, task (Fischer, Tadic-Galeb, & Yoder, 2008). In fact, computing power has constantly increased and hand calculations left the room for highly efficient algorithms. The following section intends to explain the main steps of such an algorithm in order to understand a bit more the functioning of Code V.

The first step is to introduce into the software a first guess optical design. Then, each parameter of the optical elements that have been entered as *variable* are changed in turn by a small increment. Once a parameter has been changed by a small variation, the overall optical quality is computed and stored. Then, this operation is repeated for all parameters.

The way that the software measures this performance at each increment is called an *error* or *merit function*. This is a quantitative way to characterize both the optical performance of the design and the fact that user-defined constraints are well met or not. This results in a single scalar number which indicates the system's performance: as this number decreases, the optical quality increases[22]. Typical error function criteria are RMS spot diameter, encircled energy and Modulation Transfer Function (MTF) (Fischer, Tadic-Galeb, & Yoder, 2008).

Once all the performance variations with respect to the variable parameters are compiled, the software obtains the corresponding partial derivatives of the performance with respect to these parameters. If we call P the optical performance of the system and V_1, V_2,... V_N the variable parameters, the partial derivatives are:

$$\frac{\partial P}{\partial V_1}, \frac{\partial P}{\partial V_2}, \dots \frac{\partial P}{\partial V_N}$$

These partial derivatives indicate to the software in which direction it has to change the parameters in order to optimize the system.

The previous operation is then repeated until it reaches a stationary point which is an optimum solution of the system. What is actually difficult in this process is to reach the *global* minimum of the error function. In fact, when the algorithm finds a minimum solution of the problem, nothing actually tells to the designer if this is the best solution that can be reached and if another better solution does not exist. Therefore, the designer has the task to

[22] When considering the selected optical quality criterion.

investigate if the best solution has been reached, according to the design he would like to have. A great analogy is proposed by Fischer and illustrated in Figure 65 (Fischer, Tadic-Galeb, & Yoder, 2008). Let us imagine that we are blind and placed in a 3-D space covered by hills and valleys and that we have to find the minimum altitude point with the help of a stick. What we can do is thus scanning in all directions the altitude change in order to find the best path to the lowest point. Once this task is achieved, we thus follow that direction by an increment equal to the stick's length and repeat the same operation till reaching a point where the altitude grows up in every direction. We have thus reached a minimum altitude point.

But what if another even lower point existed? This is a really difficult mathematical problem. We could think to change the length of the stick, so the algorithm's increment, and try to reach another better solution. Many algorithms were developed in order to solve such a problem but the issue is so nontrivial and nonlinear that these software are still quite elusive (Fischer, Tadic-Galeb, & Yoder, 2008). Indeed, I expose later a problematic situation that I encountered due to this phenomenon. In fact, nothing says that the optimal solution of the problem is not far away from that reached in the n-dimensional space of the problem.

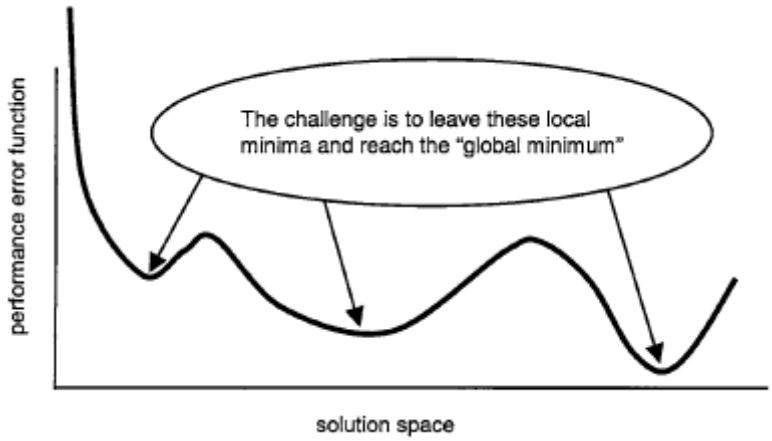

Figure 65 - Optimization algorithm (Fischer, Tadic-Galeb, & Yoder, 2008)

Yet sometimes, there is no need to find this global minimum solution. Indeed, many other factors influence the global quality of the system and the optical quality is not the only one that has to be considered. Actually, the designers must take into account other parameters such as tolerancing, environmental change, viability of materials, etc, in order to find the best suited design. The global optimum solution could in fact lead to several problems as being sensitive to small dimensions changes during fabrication or exhibit exotic dimensions. A *tolerancing* analysis has to be done to check the first problem while state-of-the-art values can be consulted to tackle the second one. All these parameters have to be taken into account to obtain an optimized design (Fischer, Tadic-Galeb, & Yoder, 2008).

4.1.2.2. Optical design procedure

Specific steps shall be followed in order not to miss any detail. The typical procedure that follows an experienced optical designer and I applied during my optical design process is presented in Figure 66 (Fischer, Tadic-Galeb, & Yoder, 2008).

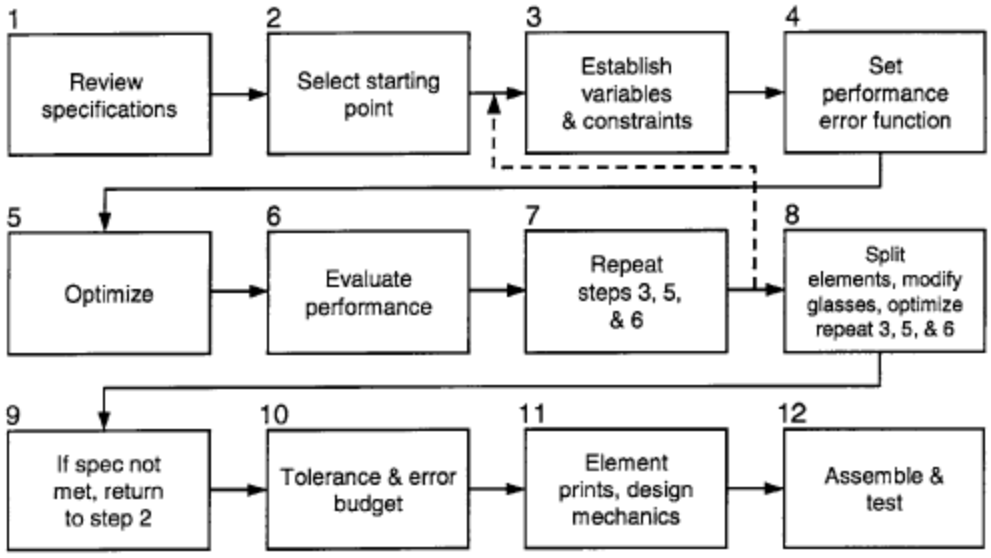

Figure 66 - Optimization procedure (Fischer, Tadic-Galeb, & Yoder, 2008)

The first step is to set the specifications that the optical system must verify. In this work, they are derived from the mission requirements. These are for example the focal length, the FoV or the desired optical performance.

Then, a starting point must be selected. Of course the optimization has to be run from a first design. This first optical system should represent a viable solution for further developments.

Once these two steps are carried out, the *constraints* and *variables* of the problem can be set. The variables of the problem are the parameters that the software can modify to reach an optimal solution while the constraints are the boundaries that they cannot violate. Indeed, the user has to define ranges inside which the parameters are allowed to vary in order to respect certain dimension or fabrication specifications. Wavelength and field positions can also be specified at this step.

The next step in the design process is to choose the error function. Usually, predefined error functions are available in optical design softwares like the RMS spot diameter. The user can also create its own error function in specific cases.

Then, the optimization process can take place. The time needed to achieve this task and reach a local minimum can vary from a few seconds to several hours depending on the complexity of the system (number of wavelengths, field positions, elements, etc) and the

computer's performances. Once the software has reached a stationary point, the routine stops.

A few tools allow evaluating the optical performances of the design. These can be the MTF, the spot diagram or the encircled energy for example.

If the optical quality requirements are not met, the variables and constrains of the problem should be modified and the optimization routine run again as many times as needed to reach a satisfying optical system. Step 8 is not applied here as it introduces refractive systems.

Even by changing the constraints and variables, the designer might not reach an appropriate optical system. If this happens, a new starting point must be chosen to follow another optimizing path.

Once an acceptable optimized design is obtained, a tolerancing analysis has to be performed. Indeed, as explained before, the optimum solution optical quality could be too sensitive to fabrication and assembly errors. If this is the case, another starting point must be implemented.

At the end the optical parts can be manufactured as well as their housing. A permanent contact with the mechanical designer is needed to be sure that the optical system is mechanically acceptable.

Finally, the assembly and tests can take place. Cleanliness and precision are required for this task and tests are needed to check if the optical quality is that predicted.

4.1.3. Computer performance evaluation

Many ways exist to characterize the optical quality of an optical system but some of them are often used as the *spot diagram*, the *modulation transfer function* or the *encircled energy*. We could also talk about the *resolution* of the system and the *Rayleigh* criterion is then helpful to understand this notion.

As explained before, geometrical aberrations, diffractions, tolerances and other disturbing factors induce image degradation. The different tools that are presented below intend to characterize the effects of these perturbations on the system's optical quality.

In a real case, all the components of the entire imaging system have to be taken into account to assess the optics quality. For example sensor and electronics have also degrading effects that have to included (Fischer, Tadic-Galeb, & Yoder, 2008). The sections below only consider the effects of optical components.

4.1.3.1. Resolution and Rayleigh criterion

The classical definition of resolution is the ability of an optical system to distinguish two point sources at a considered distance (Fischer, Tadic-Galeb, & Yoder, 2008). If we now consider an aberration-free optical system whose circular aperture is D, two point sources both produce a perfect diffraction pattern which is the Airy disk. The *Rayleigh criterion* says that if the two central peaks of these diffraction patterns are separated by at least the radius of the Airy disk then the two points are resolvable. The limit of resolution is thus reached when these two diffraction figures are separated by an Airy disk radius and the intensity between the two peaks is then equal to 0.74 of the maximum. This situation is presented in Figure 67 (Fischer, Tadic-Galeb, & Yoder, 2008).

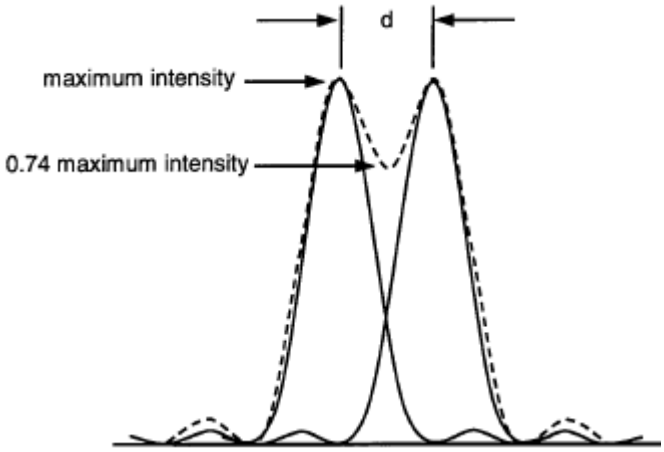

Figure 67 - Resolution limit (Fischer, Tadic-Galeb, & Yoder, 2008)

.

4.1.3.2. Ray Trace Curves

Analyzing the *Ray trace curves* of a system is the best way to identify the aberrations from which it suffers. Actually, even if the following tools are really powerful, they do not provide information as clear as this one does. Some aberrations can be identified by looking at the spot diagram to the naked eye but this is clearly more difficult. Indeed, an experienced designer can identify the existing aberrations, estimate their relative importance and order by simply looking at this graphical tool.

To explain how this analysis tool works, we take the example of third order coma aberration. In Figure 68 we see an optical system through which different off-axis rays pass and produce a typical spot that looks like a comet. The chief ray and the upper and lower marginal rays are also shown. These latter pass respectively at the upper and lower limit of the optical system's exit pupil.

As explained before, the chief ray can be used to measure the transverse aberration which is the height at which the other rays hit the image plane with respect to the chief ray

reference height. Now the ray trace curves consist in reporting these different heights, the transverse aberration, while scanning all the position between the upper and lower marginal rays. The sets of coordinates that are usually used are the normalized exit pupil's radius in the Y direction for the abscissa and the ordinate is the distance above or below the chief ray at which the rays hit the image plane (Fischer, Tadic-Galeb, & Yoder, 2008).

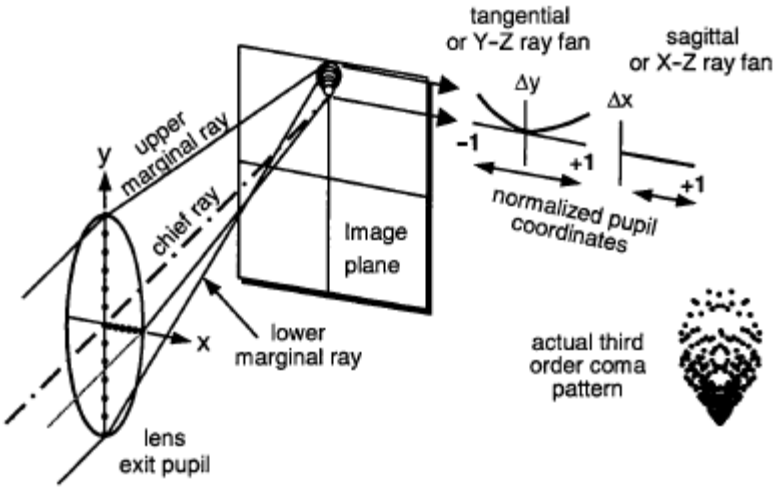

Figure 68 - Third order coma ray trace curves (Fischer, Tadic-Galeb, & Yoder, 2008)

The resulting curve is a parabola because third-order coma is proportional to the square of the aperture. By doing the same in the X direction we find the X-Z ray fan which is a horizontal line since there is no departure in this direction. Thus, if this parabolic curve in the Y fan and zero departure in the X fan are observed, one can conclude directly that third order coma is present in the system (Fischer, Tadic-Galeb, & Yoder, 2008).

This analysis can be done for all kind of aberrations and a typical pattern of ray traces curves is thus associated to each aberration type. The typical patterns that are associated to each aberration are visible in Figure 69.

Each aberration has a quite different pattern and it is thus sometimes quite simple to identify the aberrations of a system from its ray-trace curves[23] (Fischer, Tadic-Galeb, & Yoder, 2008). In addition aberrations add algebraically. Hence, superposition of several aberrations still permits to distinguish its components. These ray trace curves are used later to analyze and check the aberrations that are present in my optimized designs.

[23] When third-order aberrations dominate but this is usually the case.

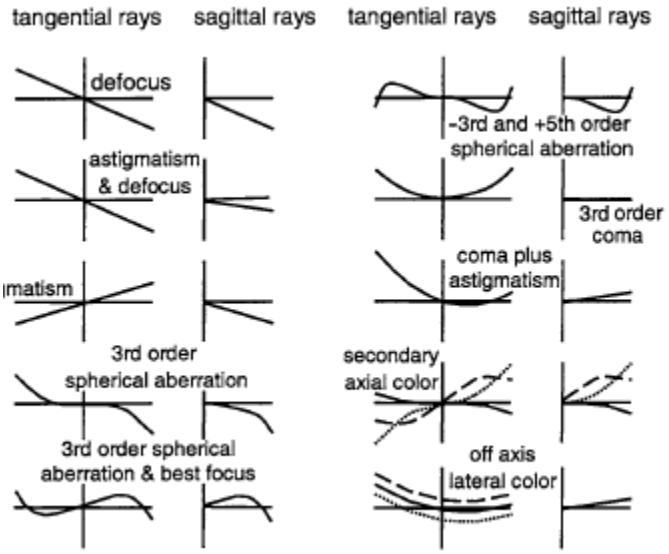

Figure 69 - Typical aberration ray trace curves (Fischer, Tadic-Galeb, & Yoder, 2008)

4.1.3.3. Spot diagram

The *spot diagram* of a system is the image of a point object realized by the system. This is a highly useful analysis tool to check if the spot is for example well included in a given pixel's size when using a pixelated detector.

Generally, the RMS spot diameter is used to measure the size of the image spot. This parameter corresponds to the diameter of a circle containing approximately 68% of the total spot energy (Fischer, Tadic-Galeb, & Yoder, 2008). Indeed, this is a more adequate way to measure the average diameter of the spot compared to the 100% diameter that can be formed by only a few rays (Mazzoli & Kintziger, 2013, March 28).

When talking about spot size, the user should be careful because this signification differs from sources. Indeed, it can either represent the spot diameter or its radius. Moreover, if nothing as RMS or 100% is precised, confusion can be induced as well as errors. All following spot sizes are expressed as the diameter of the spot and the RMS or 100% character of the parameter is specified.

4.1.3.4. Encircled energy

The *encircled energy* is a plot relating the percentage of energy that is encircled with respect to a considered circle's diameter. Once again, this tool is really useful when considering the use of a pixelated sensor.

A good specification is that 80% of the energy is concentrated inside a circle the diameter of which is the pixel's size (Fischer, Tadic-Galeb, & Yoder, 2008). If we use a squared pixel with a $15\ \mu m$ side size, the previous requirement states that 80% of the energy should be encircled by a $15\ \mu m$ diameter circle.

4.1.3.5. Modulation Transfer Function (MTF)

The *Modulation Transfer Function (MTF)* measures the ability of an optical system to transfer the intensity modulation of an object (the target) to the image that it creates of it. Due to aberrations, diffraction and other disturbing effects, the image *contrast* is not the same as that of the object. This means that the dark parts are not as dark and the bright ones are not as bright as in the original pattern (Fischer, Tadic-Galeb, & Yoder, 2008).

In order to define the MTF, we first have to define what an image modulation is:

$$Modulation = \frac{I_{max} - I_{min}}{I_{max} + I_{min}}$$

This definition is illustrated in Figure 70 where a simple periodic object is considered and of which intensity is varying sinusoidally (Fischer, Tadic-Galeb, & Yoder, 2008). When imaged by the optical system, aberrations and other disturbing effects induce a drop of contrast since the highest and lowest intensities have respectively decreased and increased.

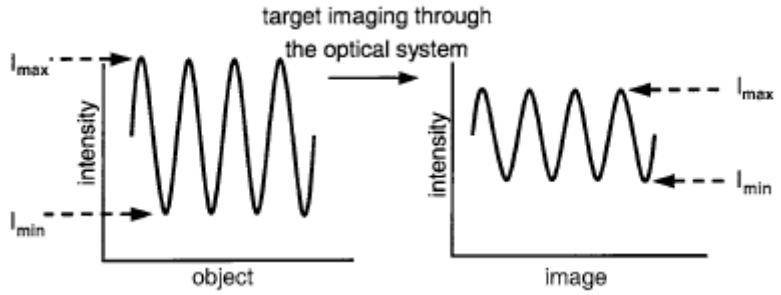

Figure 70 - Modulation of intensity (Fischer, Tadic-Galeb, & Yoder, 2008)

Now, as presented above, the MTF is the ratio of the modulation in the image by the one in the object:

$$MTF = \frac{Modulation\ in\ image}{Modulation\ in\ object}$$

The MTF is expressed as a function of spatial frequency which is generally in the form of *line pairs per millimeter*. It thus expresses the transfer by the optical system of modulation from the object to the image as a function of spatial frequency (Fischer, Tadic-Galeb, & Yoder, 2008).

In Figure 71 typical MTF curves are shown (Fischer, Tadic-Galeb, & Yoder, 2008). The MTF of a perfect system without any obstruction is presented and we can see that when an obstruction is inserted into the optical system, such as in Cassegrain telescopes, the diffraction that is induced degrades the MTF. A real system has of course an even lower MTF when, for example, aberrations are taken into account.

When obstruction is inserted into the system, the MTF curve is lower at low frequencies while it may go upper the diffraction-limited system's curve at higher frequencies. This means that the amount of light inside the Airy disk is transferred from the central disk to outer secondary ones. Therefore, finer details can be captured by the optical system and, for example, this can be used in order to separate two close point objects in an astrometric work (Fischer, Tadic-Galeb, & Yoder, 2008).

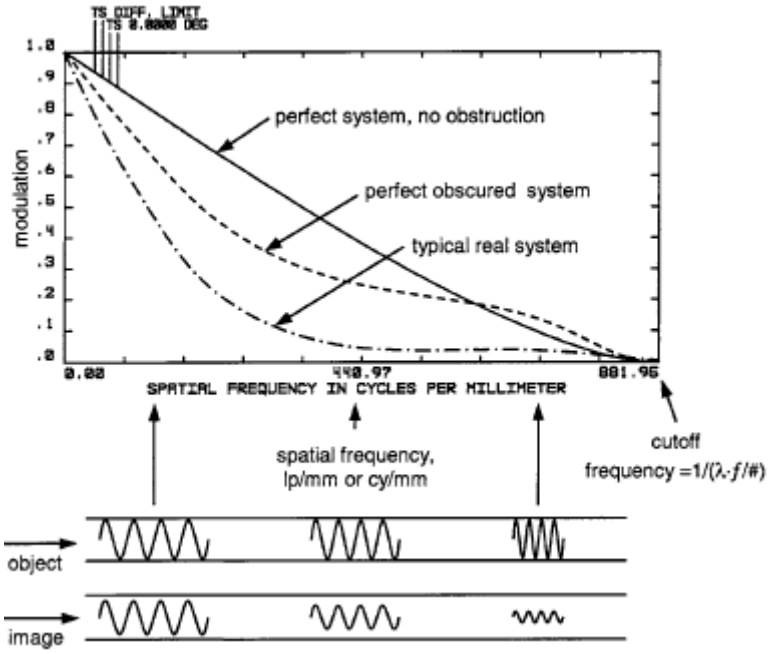

Figure 71 - Modulation Transfer Function (Fischer, Tadic-Galeb, & Yoder, 2008)

This situation is presented in Figure 72 where we can see that the light inside the first Airy disk ring is transferred to other outer ones as the obscuration ratio increases (Fischer, Tadic-Galeb, & Yoder, 2008).

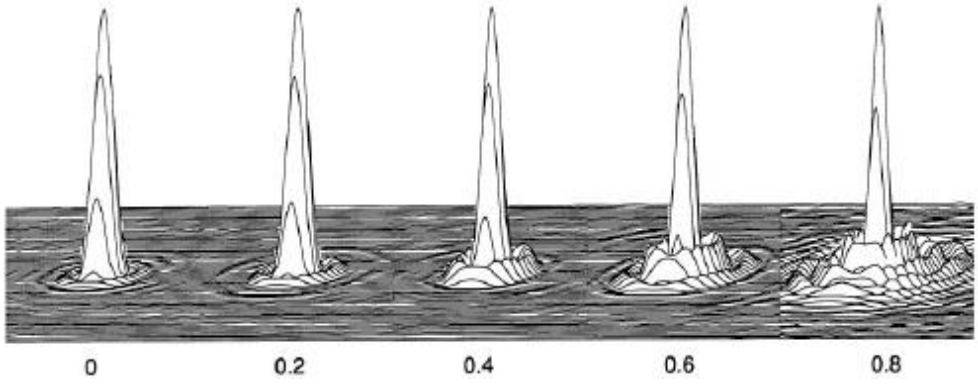

Figure 72 - Obscuration effect on the *PSF* (Fischer, Tadic-Galeb, & Yoder, 2008)

The *cutoff frequency* is also presented in Figure 71. This is the frequency at which the MTF goes to zero. It can be calculated with the help of this formula:

$$\nu_{cutoff} = \frac{1}{\lambda(f/\#)} = \frac{1}{\lambda(f/D)}$$

We can express in this formula the wavelength in millimeters in order to directly get the cutoff frequency in *line pairs/mm*.

The MTF of a system that is extremely degraded can eventually drops below zero. This negative value actually means that a phase reversal appears, that is, bright parts of the image become dark and the dark ones become bright.

The effect of a pixelated sensor on the MTF of an optical system has to be taken into account. The first effect of such a sensor is that the cutoff frequency of the entire system is limited by that of the detector (Fischer, Tadic-Galeb, & Yoder, 2008). This phenomenon is called *aliasing*. Actually, a pixel is able to distinguish different spatial frequencies if they are below what is called its *Nyquist frequency*. It can be expressed as:

$$Pixel's\ Nyquist\ Frequency = \nu_{Nyquist} = \frac{1}{2p}$$

where p is the pixel's size. This mechanism can be understood by taking again the example of the object of which intensity is sinusoidal as shown in Figure 73 (Fischer, Tadic-Galeb, & Yoder, 2008). The maximal observable frequency that the pixel can undergo is when maxima and minima each correspond to a single pixel. In this case, the Nyquist frequency of the pixel is reached because if the object's spatial frequency increases, maxima and minima are situated on a single pixel and the result is neither a white dot nor a black one but a grey one. When this happens, the frequency detected is not as high as it is in reality, but becomes lower (Fischer, Tadic-Galeb, & Yoder, 2008).

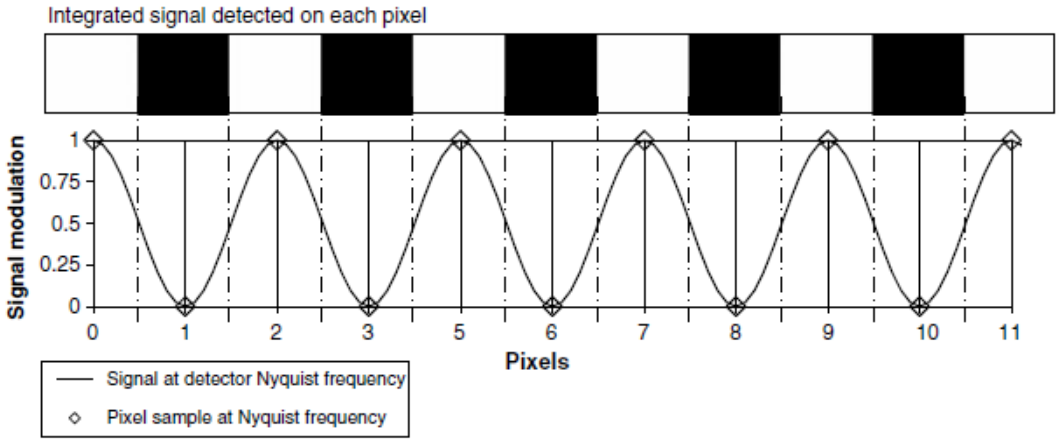

Figure 73 - Pixel's Nyquist frequency (Fischer, Tadic-Galeb, & Yoder, 2008)

In this case, the pixel size is $15\ \mu m$ so the maximum spatial frequency is:

$$\nu_{Nyquist,15\mu m} = \frac{1}{2 * 15\mu m} \approx 33.3\ line\ pairs/mm$$

Besides a pixelated detector acts as a finite-sized sampling window on the MTF of an entire optical system. Therefore, a pixel MTF must be considered when evaluating the

optical performance of a system with MTF curves. What can be done in first approximation is to consider the pixel's MTF equal to the Fourier transform of a rectangle function which is a $sinc$ function (Fischer, Tadic-Galeb, & Yoder, 2008). Therefore we have:

$$MTF_{detector} = sinc(p\ f) = \frac{\sin(\pi\ p\ f)}{\pi\ p\ f}$$

where p is the pixel's size. In a real case, we should also take into account the interval separating two pixels on the detector, referred as the pitch. In this case, the additional MTF would be the same as the pixel's MTF but the size would be that of the pixel's pitch. However no detector has been defined for this mission yet.

4.1.4. Code V presentation

The software that is used for all the following optical designs is *Code V* which is a product from *Optical Research Associates* (Synopsys, Code V Reference Manual, 2012). This program allows the user to perform different optimization processes and analyze the results with the help of several tools as spot diagrams or MTF. Tolerancing studies can be performed as well to check the viability of the optical system. The user can also specify different system data like the considered temperature and pressure in order to perform environmental change analyses.

The following sections of this chapter introduce the basic functionalities of Code V to learn a bit more about this program.

4.1.4.1. Lens Data Manager (LDM)

The first thing that the user has to do when using Code V is to specify surfaces. The *Lens Data Base* is actually a database in which all the system optical elements' characteristics are gathered. These properties are for example radii of curvature, thicknesses, apertures, etc, and represent the information on which Code V work.

A global view of the Lens Data Manager is presented in Figure 74. This interactive program proposes different operations as creating, deleting or modifying the optical elements' properties. Drawing the lens or performing simple aberration analyses is also possible.

Some surface properties can be seen in Figure 74. $Surface\ type$ defines the shape that the user wants to attribute to a given surface. It can be for example a spheric or a conic surface. The radius of curvature and the thickness can also be defined. To simulate a planar surface, an infinite radius of curvature can be utilized. Then, the glass type can be mentioned in Code V. If this case is left empty, Code V considers that air is located after the given surface. The refractive or reflective character of the surface must also be set in order to

inform Code V if mirrors or lenses are employed. Finally, the semi-aperture and a name can be specified.

Lens Data Manager

System Data... | Surface Properties...

Surface #	Surface Name	Surface Type	Y Radius	Thickness	Glass	Refract Mode	Y Semi-Apert
Object		Sphere	Infinity	Infinity		Refract	
1	Obscuration	Sphere	Infinity	90.0000		Refract	40.0000
Stop	Primary_mirror	Conic	-233.5238 V	-80.0000 V		Reflect	40.0000
3	Secondary_mirror	Conic	-102.5031 V	130.0000 V		Reflect	13.0921
Image		Sphere	Infinity	0.0000		Refract	2.5533
End Of Data							

Figure 74 - Lens Data Manager

The coordinate system of Code V is presented in Figure 75. It consists in defining a right-handed local coordinate system at each surface and separating them by each surface thickness. Therefore, the glass type specification always applies from one system coordinate to the next one. The optical axis is the Z axis.

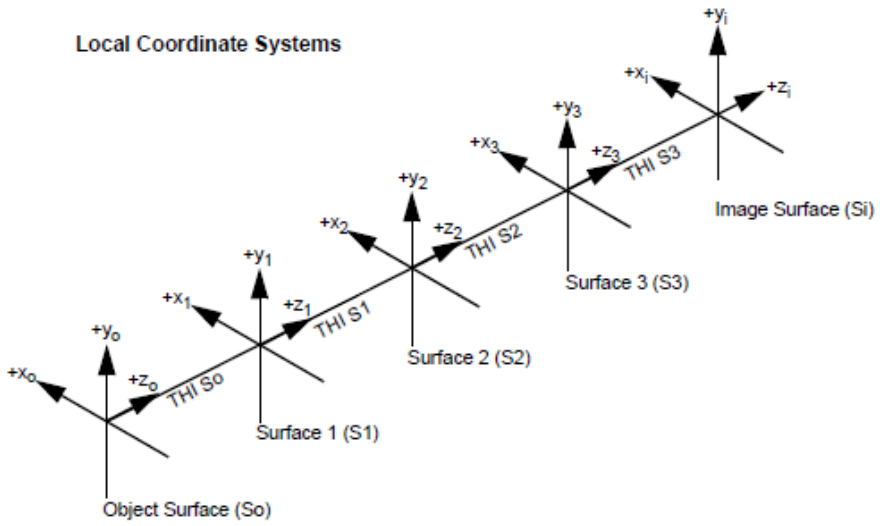

Figure 75 - Code V coordinate systems (Synopsys, Code V Reference Manual, 2012)

The object is considered to be far enough to be represented by a plane whose radius of curvature is infinite while the detector is situated in the image plane. Each parameter in the LDM can be defined as *variable* or *frozen*. When it is defined as variable, the optimization process that Code V runs can modify its value in order to improve the optical quality of the system. A little red "v" is displayed next to this type of variables. On the other hand, a frozen parameter cannot be modified.

Some other Code V programs can also modify the LDM parameters such as the environmental and tolerancing analyses. These are explained later.

Once all the system's parameters are set, they appear in the $Surface\ Properties$ window (See Figure 76). The primary goal of this section is to gather all the information related to a given surface. Advanced characteristics can also be set such as conic constants, decenters, tolerances and coatings.

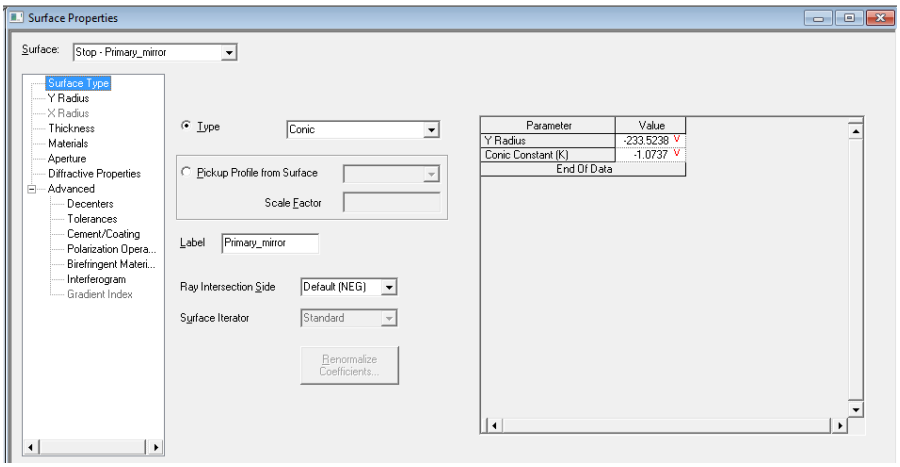

Figure 76 - Surface properties

4.1.4.2. System Data

While specific surface parameters are defined in the LDM, the $System\ Data$ window is used to specify the overall characteristics of the whole optical system (See Figure 77).

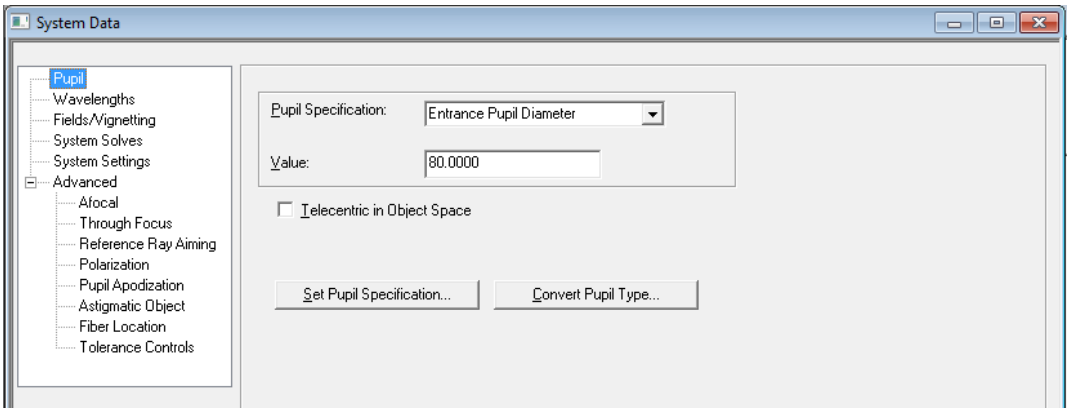

Figure 77 - System Data: Pupil

The first parameter that has to be set is the $Pupil\ Specification$. There are four ways in Code V to define it, two referenced to object space and two referenced to image space (Synopsys, Code V Reference Manual, 2012). They define the first-order cones of light that enter the optical system. Relationships exist between the four pupil specifications and the user can choose the most appropriate one or let Code V calculating it on its own. The $Entrance\ Pupil\ Diameter\ (EPD)$ was used here.

The wavelength specification is the second System Data part. Code V, when running the optimization algorithm and analyses tools, takes into account these wavelengths and respective weights, which are calculated as presented before.

Actually, the user can calculate them on his own or ask Code V to do it with the help of the $Spectral\ Analysis\ (SPE)$ option. This option can generate pre-stored typical response curves or analyze user-entered ones. Code V proposes different types of filters as well (Synopsys, Code V Reference Manual, 2012). When personalized response curves are entered into the software, Code V calculates the respective weights and can replace the current values by new ones.

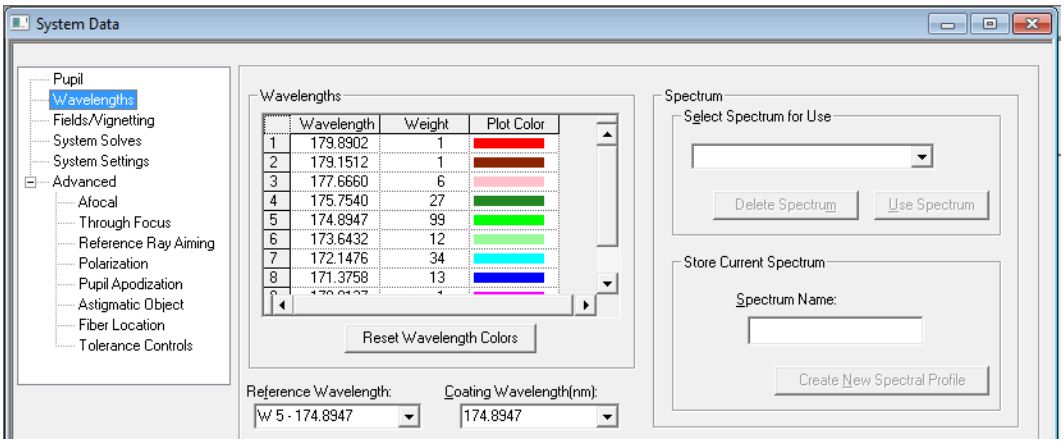

Figure 78 - System Data: Wavelengths

The $Fields/Vignetting$ information is the next System Data part, represented in Figure 79. In Code V, the field coverage is specified by several field points (Synopsys, Code V Reference Manual, 2012). Up to 25 different field points can be entered into the software. As for the pupil section, different manners exist to define these parameters: by field angle, object height, paraxial image height or real image height. For this purpose, object angle was selected.

Each field position is expressed in terms of two components: $X\text{-}Angle$ and $Y\text{-}Angle$. The calculations of such positions for the present mission are presented in the next chapter. They are all numbered and analyses that are performed with Code V show results for each field position. Indeed, aberrations for example, depend on these parameters and therefore spot diagrams and ray trace curves are different when considering each field position.

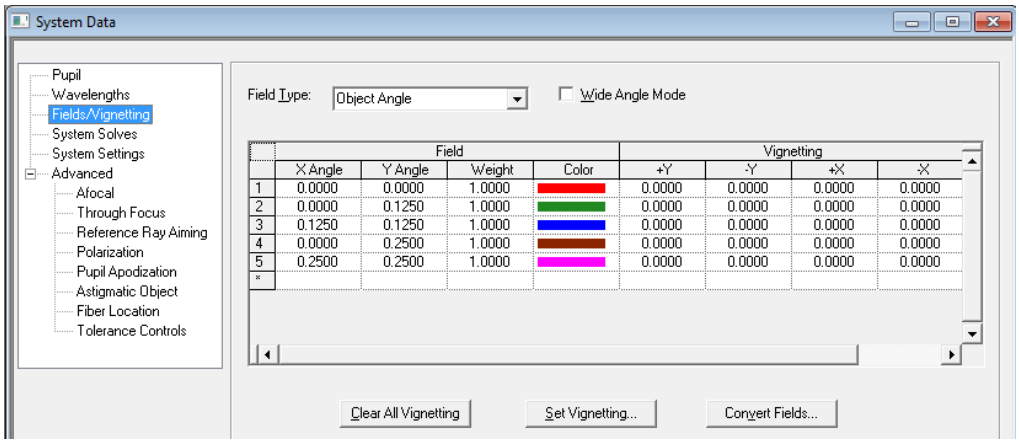

Figure 79 - System Data: Fields/Vignetting

Finally, the last part of the System Data section is the $System\ Settings$ (See Figure 80). This part of the software is aimed to define parameters such as the considered temperature and pressure, the system unit or some display modes. The default temperature and pressure conditions considered by Code V are respectively $20°C$ and $760\ mm\ Hg$. These parameters remain usually unchanged during the design process of the optical system except the considered temperature and pressure that will automatically be changed for an environmental analysis.

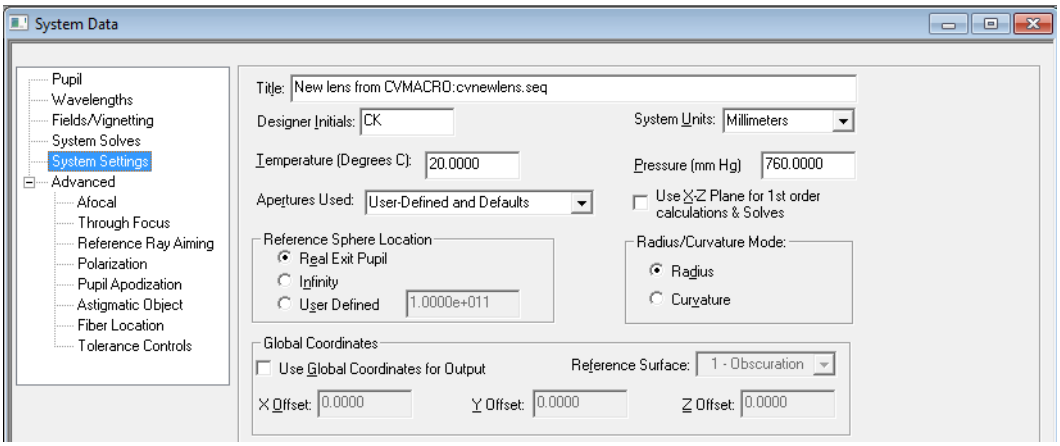

Figure 80 - System Data: System Settings

4.1.4.3. Optimization tool

The Code V optimization process implements an algorithm that operates in a similar manner to that presented before. Indeed, it consists in minimizing an error function that can be defined in different ways. These are typically the RMS spot size, the MTF or other similar criteria.

The $Automatic\ Design$ window of Code V is presented in Figure 81. The first control panel that appears is the error function type selection. For all following optimization processes, I use the $Transverse\ Ray\ Aberration$ error function. Indeed, aberrations and spot size are directly linked so this kind of optimization was appropriate to obtain a spot size that could fulfil the respective mission requirement. For example, when using the default transverse ray error function, its value is the square of the weighted spot radius in microns (Synopsys, Code V Reference Manual, 2012).

Instead of this automatic design Code V option, the $Global\ Optimization$ could also be used. The Automatic Design procedure only finds the nearest optimal solution but does not check if better ones still exist. On the other side, Global Optimization performs this verification by changing the increment value once the algorithm has reached a stationary point to explore other possible solutions.

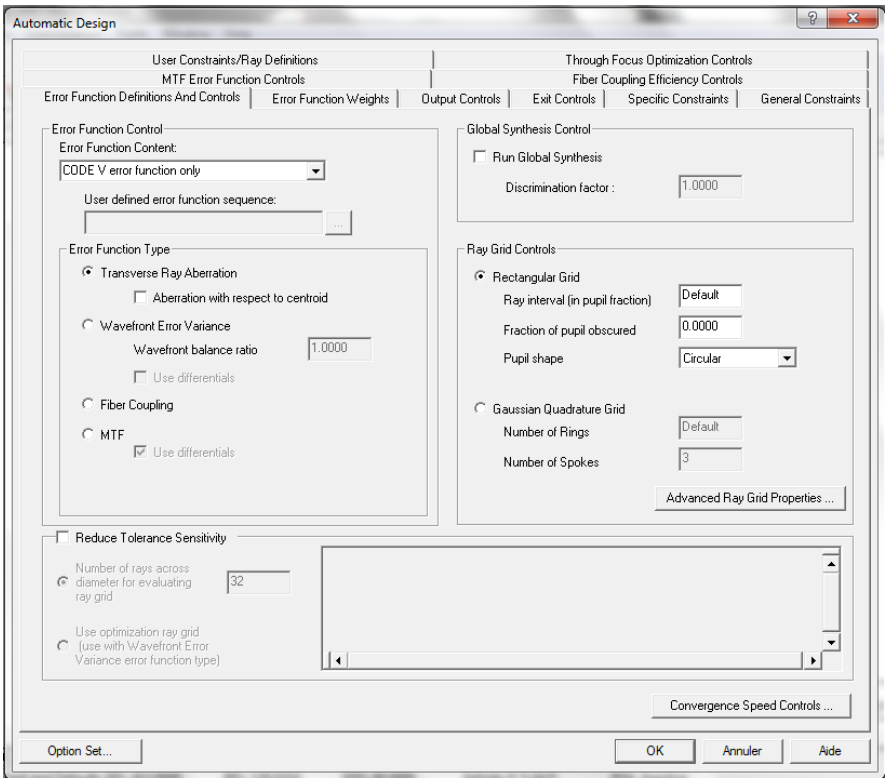

Figure 81 - Automatic Design

The problem of doing so is that such optimal solutions can be very sensitive with respect to small variations in component's dimensions. This is why this method is rarely recommended (Fischer, Tadic-Galeb, & Yoder, 2008). Indeed, reaching the best problem solution is sometimes useless since tolerancing and environmental analyses have also to be taken into account later in the design process. These investigations can become important factors when choosing the most appropriate design for the considered situation. Therefore, the Automatic Design is always used in this work.

The constraints imposed to the software during the optimization process are defined in the $Specific\ Constraints$ tab. In Figure 82 a few examples of constraints are presented. These can be equality as well as inequality relations. For example, the first one fixes the EFL that the optical system must exhibit after optimization while the others limit the system dimensions.

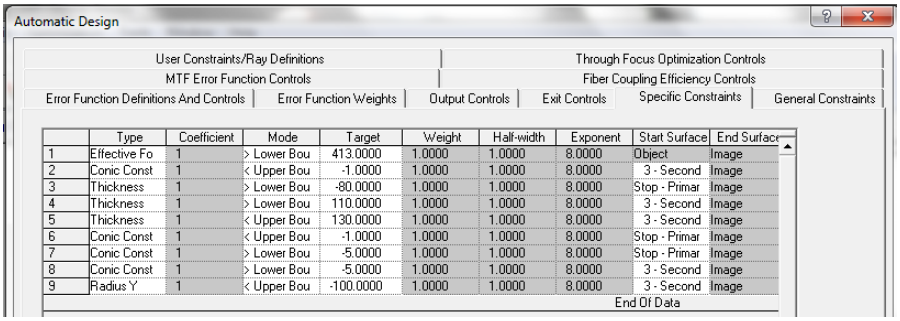

Figure 82 - Automatic Design: Specific Constraints

4.1.4.4. Tolerancing

When optimizing optical systems, algorithms reach optimum designs of which performance are theoretical. Achieving the best performance with the help of aberration theory and search algorithms lead to what is sometimes called "$the\ paper\ design$" (Fischer, Tadic-Galeb, & Yoder, 2008). The optical performance of this theoretical optical system absolutely does not take into account manufacturing errors. This process is called $tolerancing$. Even if the paper design's performances are of importance, the real-world related manufacturing degradations can surpass the image degradations of the design itself and jeopardize the requirement fulfilment.

Tolerancing is the science of distributing and error budgeting the manufacturing errors of all the assembly's components throughout the system to certify that the required level of performance is met at a reasonable cost (Fischer, Tadic-Galeb, & Yoder, 2008). Sometimes, highly efficient optical systems are theoretically designed in order to balance, for example, higher order aberrations with the help of steep bendings and high angles. Unfortunately, this kind of optical systems may be very sensitive to tolerances due to high angles of incidence and higher-order aberrations. On the other hand, a different configuration with reduced incidence angles, even if it may be less efficient, could be less sensitive to tolerances (Fischer, Tadic-Galeb, & Yoder, 2008).

Even if the paper design is excellent, taking into account all the manufacturing, assembly and alignments errors is really important since they often are a major contributor to the whole optical performance of the system. Tolerances have to be attributed to all optical and mechanical components in order to establish a performance error budget with which the designer can predict with confidence the level of performance that he can expect from his optical system.

A typical tolerancing procedure is shown in Figure 83 (Fischer, Tadic-Galeb, & Yoder, 2008). The first step is to assign to all parameters of the system viable tolerances. Actually, the required level of performance establishes the tightness of these first candidates.

$Adjusting\ parameters$ or $compensators$ must then be chosen. These are variable parameters that are allowed to be adjusted during the final assembly and testing. $Back\ Focus$[24] is often selected as a final adjusting parameter.

The tolerancing routine can then be run. This generates the performance degradation sensitivities for all the system parameters. This means that every manufacturing, assembly and alignment tolerance is evaluated and sensitivities are determined.

The next step is to reevaluate the effect of each tolerance on the selected optical performance criterion. This can be the RMS spot size or a given value of the MTF at a

[24] The distance between the last surface and the detector.

chosen spatial frequency. This intends to identify the sensitive parameters in the system and chose the tolerances that can be relaxed and the other ones that must be tightened.

Other parameters may be added to the analysis. These can be more complex and specific variables such as atmospheric turbulence or surface irregularities.

The overall error budget and performance prediction is then generated. It is quite common to obtain only a small subset of parameters that appear to be sensitive while others are not (Fischer, Tadic-Galeb, & Yoder, 2008). Each time, performance prediction is re-calculated and this process is iterated until reaching the required performance at a reasonable cost. The fact that the designer has to tighten only a few parameters instead of the entire set is a great payoff with respect to fabrication cost.

Finally, if the performance goal is not achieved, a total redesign might be needed to be able to loosen some parameters of the system.

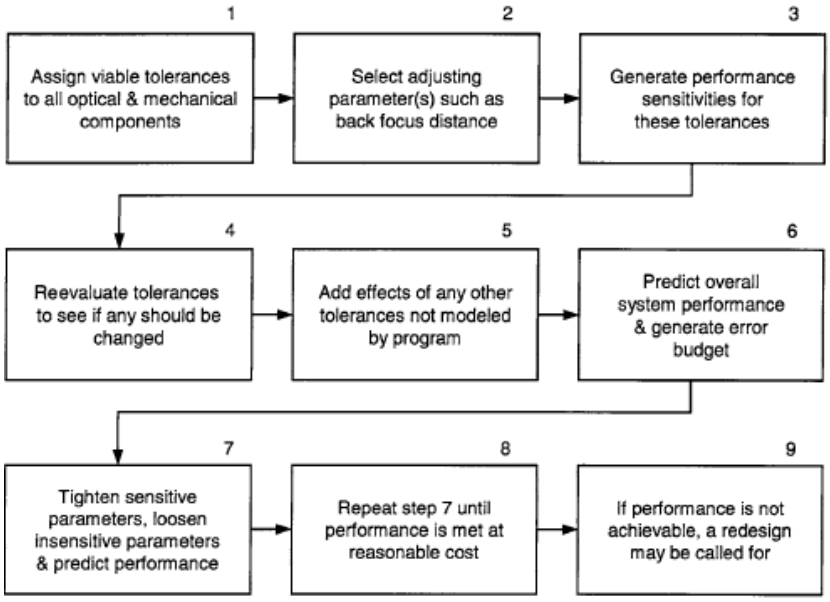

Figure 83 - Tolerancing procedure (Fischer, Tadic-Galeb, & Yoder, 2008)

Different ways exist to enter Code V tolerances. The *Tolerances and Compensators* window can be used in order to attribute to a single lens or a group of surfaces tolerances and select the compensator(s). This can also be done by using the $Surface\ Properties$ window to apply a tolerance value on a specific surface.

The performance evaluation in Code V can be carried out with the help of several tolerancing tools. In the following tolerancing analyses, the $TOLDIF$ option is used. This sequence performs a finite difference analysis by perturbing the lens for each individual tolerance. The $TOLDIF$ method perturbs the optical system several times and presents statistical curves describing the optical performance criterion values. In this case, the RMS spot diameter criterion was used. In fact, each tolerance is represented by a distribution curve (a Gaussian for example) and at each tolerance analysis, values are taken randomly

from all those tolerance curves to obtain a statistical sensitivity analysis after having repeated this process several times.

An easier way to proceed would be to add each tolerances as a $Root\ Sum\ Square\ (RSS)$, i.e. the total degradation of the system is the square root of the sum of the squares of the individual degradations. If the tolerances are of the same form, this method leads to a level of confidence of 95%. However, an inconvenient of such a method is that when different kinds of aberrations are added to each others, for example tilts and airspace thicknesses degradations, this kind of analysis becomes less accurate. Indeed, these parameters lead to different aberrations. For example, a thickness variation can induce defocus and spherical aberration while a tilt may cause coma and the *RSS* method does not handle properly this mix of aberrations. This is why I used the *TOLDIF* option which is more adequate for such problems (Fischer, Tadic-Galeb, & Yoder, 2008).

4.1.4.5. Environmental analysis

All the optical designs that are optimized by Code V are assumed to be used at sea level at $20°C$. Indeed, these are the default temperature and pressure conditions that are pre-entered into Code V System Data section. However, real usage conditions can differ from this standard ones. The temperature changes that will undergo the spacecraft can induce thermal expansion of the materials and cause optical degradation.

The $Environmental\ Change$ Code V option (See Figure 84) evaluates and applies the primary changes in the constructional parameters due to these perturbations (Synopsys, Code V Reference Manual, 2012). This option is able to simulate thermal gradients inside specific surfaces and the presence of filling gases at different pressures as well. The environmental analysis only works with rotationally symmetric systems (this is the case for Cassegrain telescopes).

This Code V option does not perform any analysis but only applies the calculated dimension changes to the actual design. Then, the user can run any kind of typical analysis as a spot diagram or MTF to evaluate the induced image degradation. As shown in Figure 84, the user has to specify in Code V the different surface materials, if they appear in the available database, or their thermal expansion coefficients as well as the new temperature and pressure conditions.

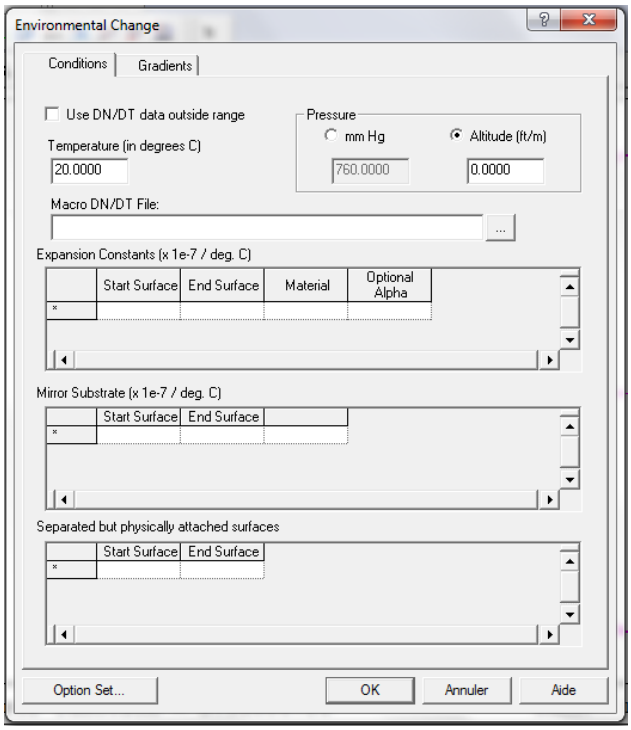

Figure 84 - Code V Environmental Change option

Chapter 5

Optical design

5.1. Preliminary calculations

5.1.1. Focal length determination

In order to determine the focal length of the optical system, we have to use some characteristics of the Jupiter's orbit and dimensions as well as the requirement on the telescope's optical resolution, which stands that we must discriminate a quarter of Jupiter's diameter.

The first step consists in computing the angular resolution that the optical system must check to verify the requirement on the resolution. This is done with the help of a few trigonometry calculations as shown in Figure 85.

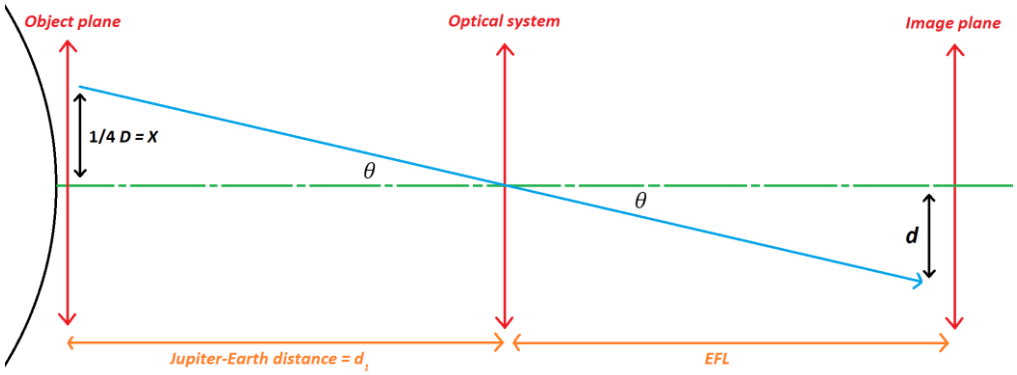

Figure 85 - *EFL* calculation

The annotations in Figure 85 are as follows:

- D: the Jupiter's diameter
- d_1: the distance between Jupiter and the Earth
- d: the detector pixel's size ($15\ \mu m$)
- EFL: the effective focal length of the optical system
- θ: the angular resolution of the optical system

From the schema and using (1), we can deduce the needed effective focal length. Indeed, we have:

$$\tan\theta = \frac{x}{d_1} = \frac{d}{EFL} \qquad (5)$$

$$\Leftrightarrow EFL = \frac{d * d_1}{x}$$

We can see that the EFL of the telescope depends on the distance between Jupiter and the Earth[25]. Therefore, this focal length varies during the entire mission as this distance does, so that the requirement on the resolution is satisfied. We can still calculate the upper and lower boundaries of the interval that the EFL should cover:

$$EFL_{min} = \frac{d * d_{1,min}}{x} = \frac{15\ 10^{-6} * 629872394}{\frac{1}{4} * 139822} \approx 275\ mm$$

$$EFL_{max} = \frac{d * d_{1,max}}{x} = \frac{15\ 10^{-6} * 965486177}{\frac{1}{4} * 139822} \approx 413\ mm$$

where $d_{1,min}$ and $d_{1,max}$ are the minimum and maximal distances between Jupiter and the Earth during the Mission life of Juno. They were determined in the chapter dedicated to the mission analysis (See Figure 43). These focal lengths directly impact the optical resolution of the telescope. Indeed, from (5), if the EFL increases while the pixel size is kept the same, the optical resolution increases[26]. The optimal solution could be to design a telescope that fits the required angular resolution, and thus the needed focal length, during the whole mission. Therefore, the minimum required EFL to reach this goal had to be determined.

First, I try to implement a basic telescope the EFL of which is approximately $275\ mm$ to check if the Cubesat platform is suitable. Then, I extend the EFL to observe the Io's torus with the required resolution as long as possible through the considered mission lifetime.

5.1.2. Field of view and required number of pixels

For each focal length design, we can calculate the value of θ and the number of pixels needed in order to cover the entire FoV. The latter is determined for the maximum FoV, i.e. at the minimum distance between Jupiter and the Earth to obtain the minimum required number of pixels forming the detector.

The first step is to calculate the value of θ for both cases of different focal lengths. The short and long EFL values are represented by $\theta_{min\ EFl}$ and $\theta_{max\ EFl}$ respectively. We deduce them using (5):

$$\theta \approx \tan\theta = \frac{x}{d_1} = \frac{d}{EFL}$$

[25] Actually, the distance between Io and the Cubesat has to be used in case of an exact calculation but this method represents a good approximation.

[26] θ decreases thus the smallest element that the optical system can distinguish becomes smaller and the resolution increases.

$$\Leftrightarrow \theta_{min\ EFl} = \frac{d}{EFL_{min}} = \frac{15\ 10^{-6}}{275\ 10^{-3}} \approx 0.003° \approx 0.19\ arcmin$$

$$\Leftrightarrow \theta_{max\ EFl} = \frac{d}{EFL_{max}} = \frac{15\ 10^{-6}}{413\ 10^{-3}} \approx 0.002° \approx 0.12\ arcmin$$

We determined earlier the maximum FoV that the system shall have, which is actually the angular diameter of the Io's torus, $5.058\ arcmin$. Now, we can calculate the minimum number of pixels in order to capture the entire Io's torus for both cases (with NoP the number of pixels):

$$NoP_{EFL\ min} = \frac{FoV}{\theta_{min\ EFl}} = \frac{5.058}{0.19} = 26.57 \approx 27\ pixels$$

$$NoP_{EFL\ max} = \frac{FoV}{\theta_{max\ EFl}} = \frac{5.058}{0.12} = 40.63 \approx 41\ pixels$$

These are the dimensions of a square detector necessary to get the Io's entire torus, in both cases respectively. Of course, such dimensions are not commercially available and we have to take into account some margins. We expose later that the imaged FoV has to be enlarged to locate the target and fix the telescope on it. Therefore, we need to first benefit from a larger FoV to coarsely detect Jupiter and then centre it on the detector. Indeed, the pointing accuracy of the ADCS in not high enough to limit the FoV to the Io's angular diameter as I explain later.

Finally, the use of a long focal telescope surpasses the requirement, which stands that Jupiter has to be discretized by at least four pixels, when the Earth and Jupiter are at the minimum distance configuration. We can also deduce how many pixels Jupiter covers at the minimum distance, that is, for the maximum FoV. In this configuration the angular diameter of Jupiter is (with the approximation $\tan\alpha \approx \alpha$):

$$\frac{139822}{629872394}\ rad \approx 0.7631\ arcmin$$

Thus,

$$NoP_{Jupiter} = \frac{Angular\ diameter\ of\ Jupiter}{Angular\ resolution} = \frac{0.7631}{0.1245} = 6.1293\ pixels$$

This telescope then needs seven pixels to image Jupiter for this configuration and the requirement on the resolution is fulfilled during the whole mission. However, we must check that such a design fits in a Cubesat platform.

5.1.3. Filter and coating

5.1.3.1. Filter

A filter is needed to select the desired spectral range. The baseline wavelength is $141\ nm$ but this selected wavelength cannot be used because the imaging time is too long as I show in the following section. The second wavelength that is chosen is the emission triplet of $SIII$ at approximately $172\ nm$. Other shorter wavelengths can be problematic when choosing adequate coatings for the mirrors and are thus avoided (Habraken, Salvador, & Kintziger, (Personal communications), 2013, March 19). On the other hand, this second choice still fulfils the objectives of monitoring the Io's torus since $SIII$ is also involved in the chemical reactions that occur within the torus (Bonfond & Kintziger, (Personal communications), 2013, March 26).

Typical filters that are used in UV applications are made of aluminium. They are selected to reject visible and IR radiation from the incident light. For example, two $150\ nm$ aluminium filters are used on the Extreme Ultraviolet Imager (EUI) on Solar Orbiter to protect the detector from IR and visible light while their transmission in the EUV spectrum is higher than 80% (Halain & Auchère, 2010).

Two $150\ nm$ aluminium filters are also used on PROBA-2 to prevent the SWAP detector from being illuminated by visible light (Lecat, Thome, & Defise, 2005). Two elements are used for the sake of redundancy.

The UIT is equipped with a six-position filter wheel in front of the detector. The implemented filters are interference filters, crystalline plates or fused quartz. The crystals are MgF_2, CaF_2 and SrF_2 and crystalline quartz. These are illustrated in Figure 86. For this mission, the $B5$ filter is the best (Stecher, et al., 1992).

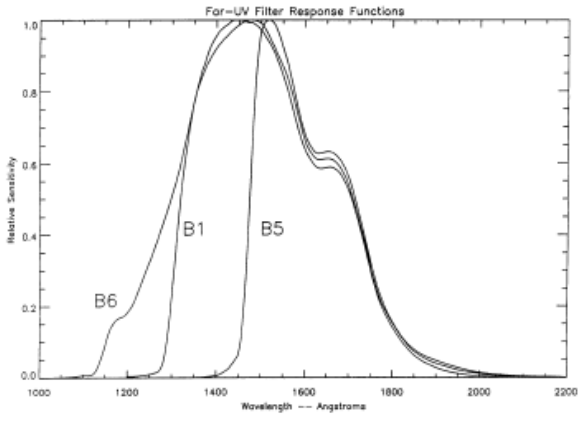

Figure 86 - FUV filters of UIT (Stecher, et al., 1992)

A filter wheel is also used on the HUT to select the different spectral ranges. Al and CaF_2 filters are used to select the FUV spectral range (Durrance, Kriss, Blair, Kruk, & Espey, 1994).

For our purposes, a suitable filter is available from Princeton Instruments. It is a bandpass filter centred around $170\ nm$ with a peak transmission of approximately 17%. Its transmission curve is illustrated in Figure 87 (Princeton Instruments).

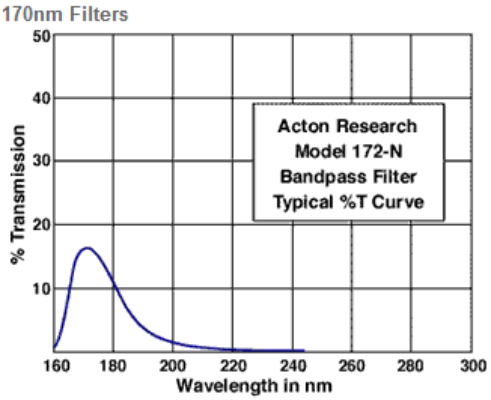

Figure 87 - 170 *nm* bandpass filter (Princeton Instruments)

5.1.3.2. Coating

Coatings have to be applied on the mirrors of the telescope in order to improve their reflectivity in the considered wavelength range. They are also used in some cases to provide a finer spectral selection than the filters used (Halain & Auchère, 2010). A multilayered coating was thus used for EUI in addition to the two aluminium filters.

The SWAP mirrors were covered by a Mo/Si coating to improve their reflectivity in the EUV range (Lecat, Thome, & Defise, 2005). Then, the FUV reflectivity of the HUT's iridium mirrors was multiplied by a factor of two with the help of a silicon carbide (SiC) coating (Durrance, Kriss, Blair, Kruk, & Espey, 1994).

An example of a suitable coating for the present mission and selected wavelength ($172.5\ nm$) is presented below (CVIMellesGriot). Its reflectance curve is presented in the vacuum ultraviolet (VUV)[27] spectrum domain. The reflectivity at the wavelength of $172.5\ nm$ is approximately 80%.

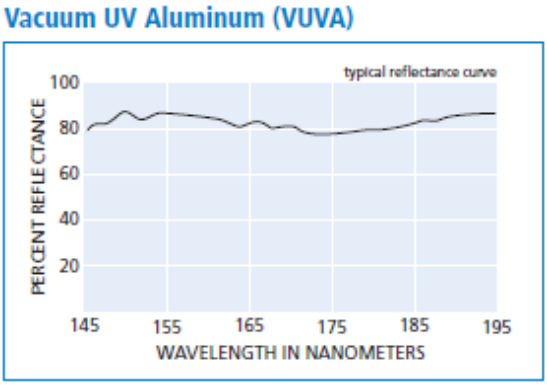

Figure 88 - Vacuum UV Aluminium coating (CVIMellesGriot)

[27] Wavelengths between $10\ nm$ and $200\ nm$ belong to the VUV domain.

A second possible $AlMgF_2$ coating for the mirrors is presented in Figure 89 (Princeton Instruments). The average reflectivity at the wavelength of $172.5\ nm$ approaches 90%.

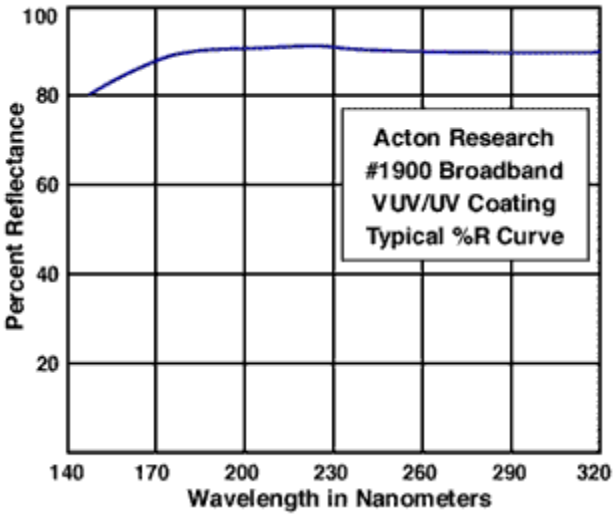

Figure 89 - Broadband metallic mirror coating (Princeton Instruments)

These coatings are not simulated in Code V due to the lack of information for now, none coating was simulated in Code V. They are however taken into account when I perform the photometric budget.

5.1.4. Photometric budget

A first preliminary photometric budget is performed to evaluate the observation time that is needed to achieve the required SNR of 10 (Salvador, 2012). The reflectivity of the mirrors and the transmission of the filter are supposed to be equal to 80% and 15% respectively[28]. The primary mirror's diameter is equal to $80\ mm$ while that of the secondary mirror is $13\ mm$[29]. Both circular and squared primary mirrors are considered here. In order to calculate the observation time required to reach a SNR of 10, the only noise that is implemented is the Poisson distribution of light since the detector still remains unknown. In further analyses, the dark current noise, read noise and the thermal noise shall also be taken into account once the detector is selected. Since the arrival of signal photons on the detector is governed by Poisson statistics, the shot noise is the following:

$$N_{shot} = \sqrt{S\ t_{int}}$$

where S is the target's signal in $photons/s$ and t_{int} the integration time. The SNR can thus be calculated as follows:

[28] These values corroborate the coatings' reflectivity from CVI Melles Griot ($\sim 80\%$) and Princeton Instruments ($\sim 90\%$) at $172.5\ nm$ and the filter's transmission of $\sim 17\%$ from Princeton Instruments.
[29] These are the dimensions of the last optical design that I introduce further in this report.

$$SNR = \frac{S\ t_{int}}{N_{shot}} = \frac{S\ t_{int}}{\sqrt{S\ t_{int}}} = \sqrt{S\ t_{int}}$$

Knowing the intensities of each emission lines of the Io's torus with the help of Figure 5[30] and those of the Jupiter's auroras, the observation time can be evaluated. The results for the Io's torus are illustrated in Figure 91.

A first remark is that the required acquisition time when considering the baseline wavelength and a circular aperture is approximately $1680\,\mathrm{sec} = 28\,min$. This is far too long since the average access time to the Io's torus is $30\,min$. Another wavelength must be chosen. As the wavelength becomes shorter, problems appear to benefit from high reflectance coatings and acceptable transmittance filters (Habraken, Salvador, & Kintziger, (Personal communications), 2013, March 19).

A longer wavelength is thus preferred and the only one that remains is the $172.5\ nm$ $SIII$ doublet. The Io's torus emissions exhibit much higher intensities in this bandpass and the observation at this wavelength is still useful for the scientific requirements (Bonfond & Kintziger, (Personal communications), 2013, March 26). The $172.5\ nm$ wavelength is thus a good candidate to decrease the required acquisition time. Indeed, the observation time is now $630\ sec = 10.5\ min$. This is much better and actually the best that can practically be achieved with the actual dimension constraints and a circular aperture.

The size constrains of the Cubesat platform induce specific mirror design and sizing. In particular, the small aperture of the satellite may lead to a customized primary mirror with square edges that fits the satellite's cross section in order to increase the number of incident photons. Such a squared-edge mirror is presented in Figure 90 (Salvador, 2012) (Habraken, Salvador, & Kintziger, 2013, February 27).

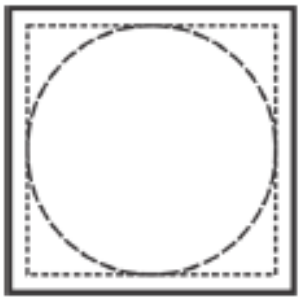

Figure 90 - Primary mirror inside the Cubesat satellite (Salvador, 2012)

The photometric budget for a squared primary mirror is also investigated. The results are illustrated in Figure 91.

[30] The intensity of each bandpass is the integral under the respective emission multiplet. The area under these peaks can be in first approximation calculated with triangles (Bonfond & Kintziger, (Personal communications), 2013, March 26).

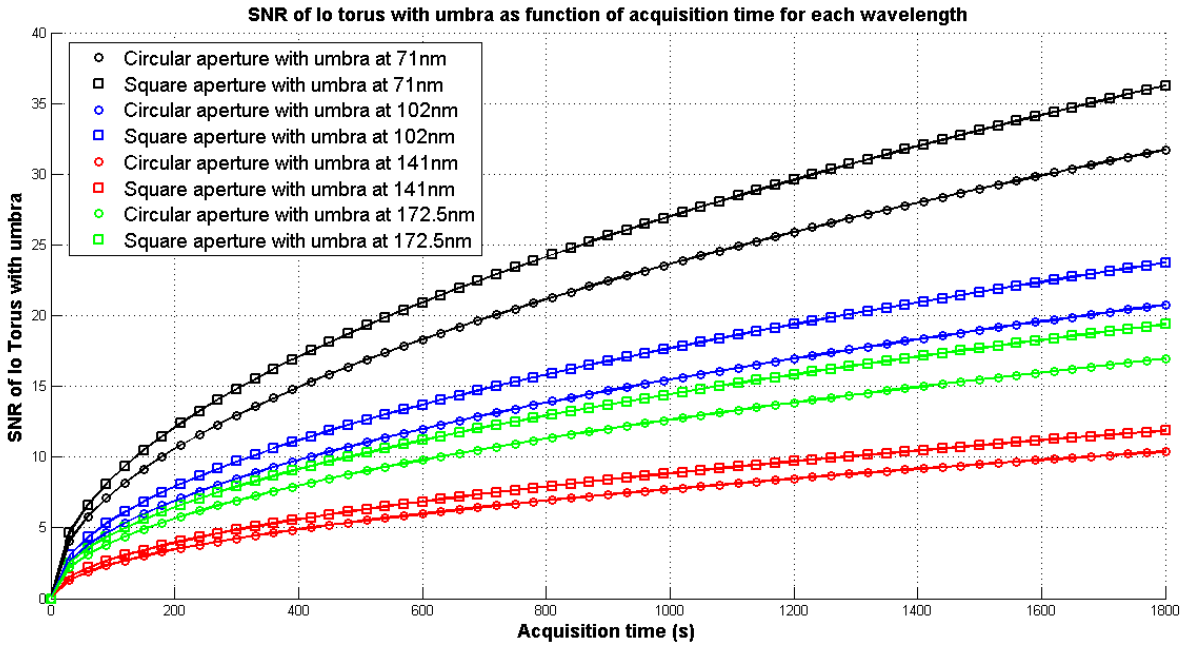

Figure 91 - SNR of the Io's torus with respect to the acquisition time

The use of a squared aperture significantly reduces the acquisition time. Indeed, when considering the $172.5\ nm$ wavelength, it decreases from $630\ sec$ to $480\ sec = 8\ min$. Two and a half minutes are therefore saved. But such a mirror may not be manufactured at a reasonable cost because it is not common. In this chapter the optical performances are always checked for each design, when the primary mirror is replaced by a squared-edged mirror.

The results for the Jupiter's signal are represented in Figure 92.

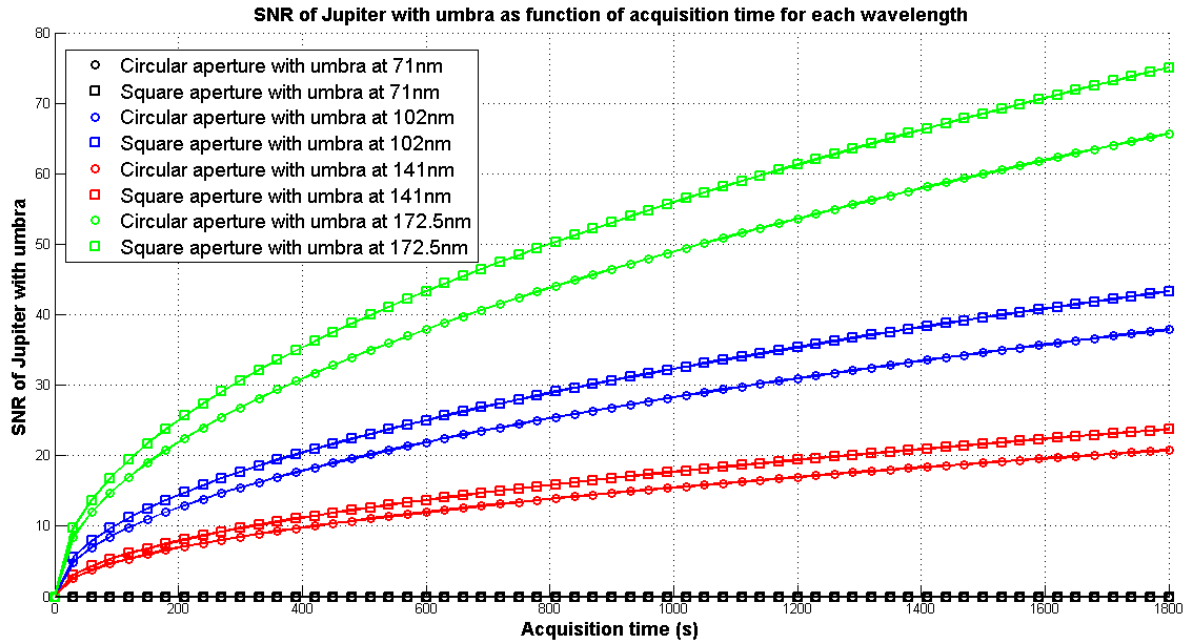

Figure 92 - SNR of the Jupiter's auroras with respect to the acquisition time

The acquisition time required to reach a SNR of 10 when observing the Jupiter's auroras at the wavelength of $172.5\ nm$ is $60\ sec$. Thus only one minute is needed to the telescope to detect Jupiter and therefore locate the torus. Looking at the Jupiter's auroras, which are brighter than the Io's torus, may be also used for attitude control of the spacecraft in real time. Indeed, once the auroras are acquired, an algorithm could be used to track them and centre the telescope on it (Salvador, 2012).

5.2. Optimization process

This chapter exposes the optical optimization in Code V and the guidelines followed to verify all the requirements presented in the previous chapters.

5.2.1. First design - Preliminary Study

The first optical design intends to check if a Cubesat platform is suitable to host a Cassegrain telescope with a focal length of $275\ mm$. This system is quite useless since it would respect the requirement on the resolution only at a single instant[31]. We verify here if the Cassegrain solution is viable or if a completely different implementation is required.

I started with an existing example the dimensions of which did not fit with the Cubesat platform. I resized it by means of an homothety. This gave me a basic design that I could afterwards optimize and make appropriate to a Cubesat satellite (Habraken, Salvador, & Kintziger, 2013, February 27).

The system performance is evaluated by using different tools as the MTF or the $Spot\ diagram$ in order to check if the image quality satisfies the requirements.

5.2.1.1. Field of view

As we determined earlier the FoV of the optical system that is required to visualize the whole torus, we can calculate the $entire$ or $diagonal\ field\ of\ view$ as follows (if we consider a squared detector):

$$FoV_{diag} = \frac{FoV}{\cos 45°} = \frac{5.05888}{\frac{\sqrt{2}}{2}} arcmin = 7.154\ arcmin \quad (6)$$

This diagonal FoV is visible in Figure 93 as well as the effective SFoV. When performing an optical design with Code V, the FoV has to be mentioned in the program. Indeed, rays with different angles of incidence come into the aperture of the telescope and these are subject to different aberrations. The field positions that I put in Code V take into account these different ray angles.

[31] This moment corresponds to when the Earth and Jupiter are the nearest.

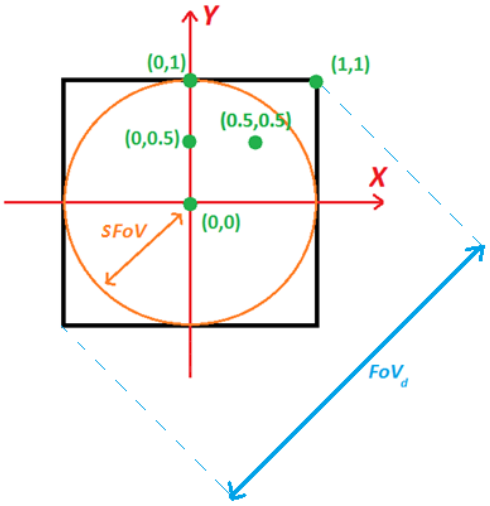

Figure 93 - Field positions of the first design

As mentioned in Figure 93 in green, the field positions that I chose are situated in a single quadrant. This implementation is sufficient as the Cassegrain system that is implemented is rotationally symmetric. These positions are also expressed as "normalized positions" which means that they are scaled by the effective FoV. Their respective real values are represented in Table 4.

Field position	X coordinate (°)	Y coordinate (°)
Field 1 (0,0)	0	0
Field 2 (0,0.5)	0	0.021078
Field 3 (0.5,0.5)	0.021078	0.021078
Field 4 (0,1)	0	0.042157
Field 5 (1,1)	0.042157	0.042157

Table 4 - Field positions of the first design (*Object Angle Field* option in Code V)

We then have an idea of the aberrations thanks to these arbitrary off-axis field positions.

5.2.1.2. Spectrum

This first model only takes into account the baseline wavelength, that is, $172.5\ nm$. Normally, we should take into account a larger spectrum, the filter's response and the detector's response however this first design goal is to check the potential feasibility of the Cassegrain telescope and these parameters are added in further designs.

The only wavelength that I entered into the LDM is thus $172.5\ nm$ and no weight is needed since only one wavelength is considered (it is automatically fixed to 1).

5.2.1.3. Optimization process

At the beginning, the first model parameters are entered in the LDM window to start the optimization process.

Constraints

The global requirement used to establish the constraints that Code V had to respect during the optimization process are shown in Table 5.

Variable	Value
Focal length	$275\ mm$
Primary-secondary distance	$< 7.5\ cm$
Backfocus	$< 12.5\ cm$
Secondary conic constant	< -1

Table 5 - Optimization constraints of the first design

These constraints are imposed to force a Cassegrain-type design that can be positioned into the Cubesat.

Results

When the error function comes to a minimum (several "click's" were actually needed to reach the global minimum around the first local one that Code V reached after optimization), an optimized system respecting all the defined constraints is obtained.

In Table 6 the dimensions of this optimized and constrained system are provided. Code V does not take advantage of the whole available space since the distance between the two mirrors is lower than the maximum $7.5\ cm$ allowed.

Surface #	Surface Name	Surface Type	Y Radius	Thickness	Glass	Refract Mode	Y Semi-Aperture
Object		Sphere	Infinity	Infinity		Refract	
1	Obscuration	Sphere	Infinity	70.0000		Refract	40.0000
Stop	Primary_mirror	Conic	-202.8877 V	-58.9765 V		Reflect	40.0000
3	Secondary_mirror	Conic	-134.5792 V	115.1225 V		Reflect	17.0335
Image		Sphere	Infinity	0.0000		Refract	0.2896
End Of Data							

Table 6 - Dimensions of the first design in *mm*

Important remark: We can see in the LDM window that the first defined surface after the object plane is not the primary mirror. In fact, because Code V is a sequential ray-tracing program, the surface order is of importance. Actually, rays go from the first surface to the second, from the second to the third and so on... In a Cassegrain system, the secondary mirror (the second surface) is before the primary and thus constitutes an obstruction but in a sequential program the rays pass through since they do not have yet reached the primary mirror (the first surface). The consequence of this phenomenon causes some rays to pass through the secondary and the primary hole to reach the image plane which is in reality impossible. The technique to avoid such a problem is to insert a virtual surface before the primary mirror that is perfectly transparent to the incident rays except in its centre. This latter is a circle (since the secondary mirror is a circle) that exhibits the same dimensions as

the secondary mirror. In the surface order, this obscuration has the number "0", the primary mirror is the "1" and the secondary mirror the "2". This way, rays are blocked before reaching the secondary even though the real secondary mirror has not yet been encountered. Of course, this surface has as a thickness equal to the separation between the primary and the secondary in order to be stuck to this mirror. I show the impact of such an obstruction on the MTF shape and prove the previous chapter statements in Appendix A.

The secondary mirror's diameter is quite large. Indeed, it is nearly (40%) as big as half that of the primary so the resulting obscuration is high ($40\%^2 = 16\%$ of shadow). This is of course a disadvantage when considering the signal-to-noise ratio since it decreases while the observation time increases.

Figure 94 illustrates the optical system with the help of $2D$ and $3D$ models. In the $2D$ drawing only a few field positions are distinguishable because this is the YZ cross section and fields 2 and 4 are superimposed with fields 3 and 5 respectively.

The obscuration surface is represented (on the right) by a blue translucent disk. We cannot actually see the obscuration in its centre but it can be imagined since rays that are in the centre of the aperture and on the way of the secondary mirror are blocked and do not reach the detector. If this surface was not there, they would continue down their path through the secondary mirror without any perturbation[32].

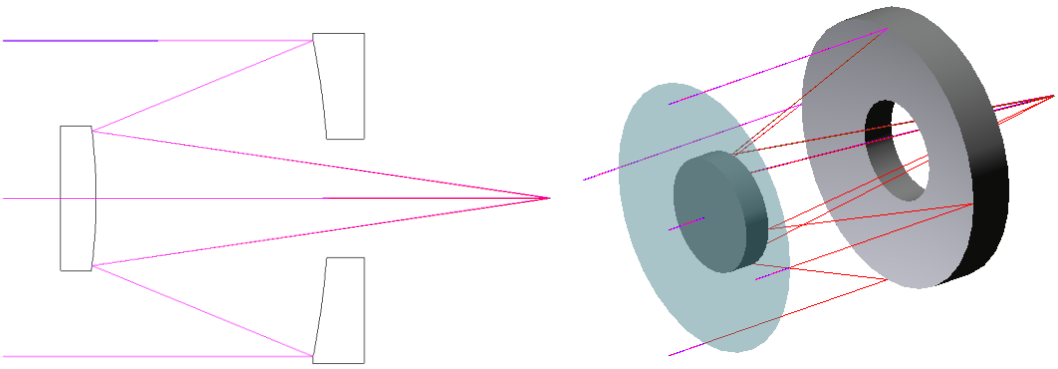

Figure 94 - *2D* and *3D* views of the first design

5.2.1.4. Image quality analysis

This section exposes the optical performance of the telescope that Code V generated after optimization. Indeed, the optimization does not always imply good performances because Code V tries to minimize the error function whilst complying with the user-entered constraints. These may be too severe to obtain a high quality optical system respecting all of them. As I show with other designs hereafter, sometimes the user needs to relax a little bit

[32] A second remark is that we could think by looking at the $2D$ sketch (YZ cross section) of the telescope that some rays pass through the secondary mirror but it is actually not the case. This can be understood by looking at the $3D$ drawing of the system: these rays belong in reality to the XZ cross section of the telescope and get around the secondary mirror.

the working limitations of the ray-tracing software in order to reach a system which exhibits the wanted characteristics. Indeed, some constraints on the system's dimensions are sometimes too restrictive to reach an optimum solution.

The tools that I use to evaluate the optical properties of the Cassegrain telescope are the $Spot\ Diagram$, the $Ray\ Aberration\ Plot$, the $Modulation\ Transfer\ Function$ and the $Encircled\ Energy$. As mentioned in the previous chapter, I should also examine if the optimized design can be manufactured, that is, if it can be fabricated while respecting reasonable tolerances. On the other hand, the design must withstand the environmental changes so that the performances are not too degraded. However, these last steps are only done on the last optimized optical system since it is the most adequate among all designs, considering the resulted optical performances.

Spot diagram

The first analysis tool I use is the Spot diagram. This represents the optical spot on the detector plane made by the intersection between the incident rays, while considering all wavelengths and field positions. As I mentioned earlier, this first design only takes into account the baseline wavelength and the field covered by the Io's torus so this first test is a really simplified situation but corresponds to a mandatory step.

Figure 95 illustrates the spot diagram of the optimized telescope. In order to easily visualize the requirement on the spot size, which stands that its size has to be lower than the pixel dimension of $15\ \mu m$, a black square is drawn on each spot diagram to depict the detector's pixel. This way, it is easy to see if the spot diagram is included or not inside a single pixel.

Moreover, the spot diagram also includes the diffraction limit pattern of the telescope. This means that, if the optical system was free of any geometrical aberration, the optical spot would have this size. This constitutes the lower limit in spot size that can be reached if the telescope can be designed in a way that completely annihilates the optical aberrations. In reality, this goal is never reached and the spot diagram is always greater than the diffraction limit. The diameter of this Airy disk can be evaluated with the help of (2):

$$Airy\ disc\ diameter = 2.44\ \lambda\ \frac{f}{D} = 2.44\ 172.5\ 10^{-9}\ \frac{275\ 10^{-3}}{4\ 10^{-2}} \approx 2.893\ \mu m$$

The RMS and 100% sizes of the spot diagram are indicated on the right of the image in millimeters. The maximum spot size rises approximately to $4.32\ \mu m\ RMS$ for the (1,1) field position. The spot diagram is well smaller than the $15\ \mu m$ requirement. As expected, it is bigger than the diffraction limit, which is obviously the proof of the presence of geometrical aberrations in the optical system.

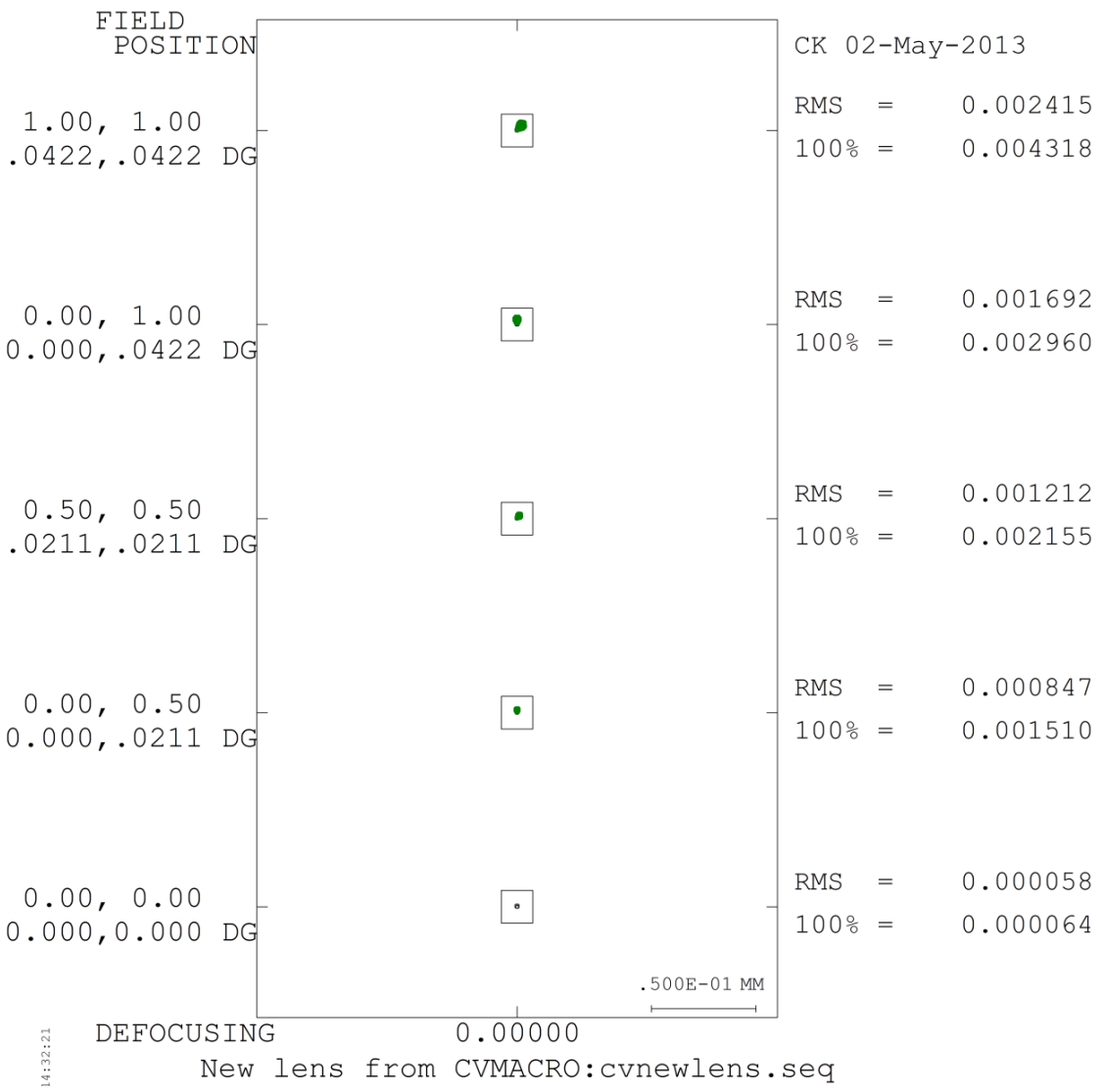

Figure 95 - Spot diagram of the first design

In all following design analyses, I use the RMS spot size in order to measure the spot diameter. The reason is that if some particular rays go far from the other ones, the 100% spot size automatically increases. A more appropriate way to characterize the spot size is thus to take the RMS measure since it informs about the behaviour of the majority of the traced rays (Mazzoli & Kintziger, 2013, March 28).

Ray aberration curves

The ray aberration curves for this design are quite interesting to observe since they highlight the main aberration of Cassegrain telescopes: the coma aberration (Fischer, Tadic-Galeb, & Yoder, 2008). Indeed, Cassegrain telescopes are usually replaced by a Ritchey-Chrétien solution where the conic constant of the primary is different from -1. Its surface then leaves the parabola shape to become a hyperbola.

In Figure 96 the typical pattern of third order coma aberration can effectively be recognized. Indeed, the U-shape of the ray-trace curves testifies to the presence of coma aberration in the optical system.

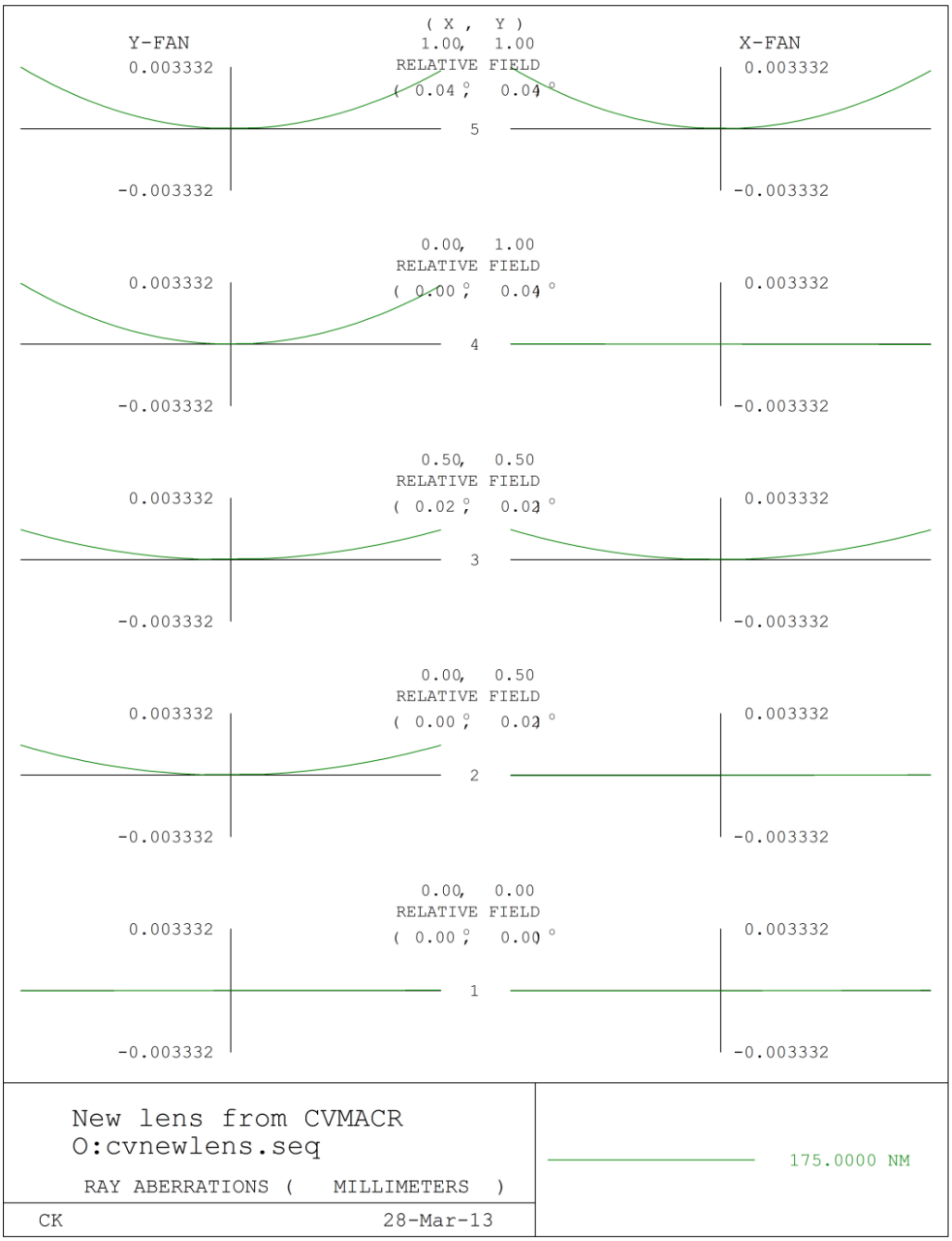

Figure 96 - Ray trace curve of the first design

Coma only appears for off-axis rays, indeed, as mentioned in theory, coma is linearly proportional to the field size and this is logical that these rays, or their off-axis components, do not suffer from this aberration. Code V also provides more details about the aberration analysis that are shown in Table 7. Actually, both 3^{rd} and 5^{th} order aberrations can be analyzed but since the system aperture and FoV are really small, third order aberrations dominate and I only analyze these ones since fifth order aberrations are insignificant (Fischer, Tadic-Galeb, & Yoder, 2008).

```
THO SO..I

    New lens from CVMACRO:cvnewlens.seq
                Position  1, Wavelength =   175.0 NM
          SA          TCO         TAS         SAS
  1    0.000000    0.000000    0.000000    0.000000
STO   -2.107394    0.033402   -0.000118    0.000000
      2.107394    0.000000    0.000000    0.000000
  3    1.043320   -0.017374    0.000008   -0.000057
      -1.043377   -0.011483   -0.000042   -0.000014

SUM   -0.000056    0.004545   -0.000152   -0.000071
```

Table 7 - Aberration analysis of the first design

The different acronyms SA, TCO, TAS and SAS respectively stand for spherical aberration, tangential coma, tangential astigmatism and sagittal astigmatism (Synopsys, Code V Prompting Guide, 2002). As we can see, coma is effectively the predominant aberration in the system.

Modulation Transfer Function

Figure 97 below illustrates the MTF of the designed telescope that Code V produced. This figure, as explained in the previous chapter, illustrates the amplitude response of the telescope as a function of the spatial frequency. This MTF only takes into account the optical system however the detector's contribution has still to be included. Different curves are represented together with that of the diffraction limit as a dotted curve. The five MTF curves associated to the different fields are illustrated with the help of different colours. Code V traces the MTF curves in both X and Y directions and these correspond to dash-dot and solid lines respectively.

For symmetric field positions, with identical X and Y coordinates (Fields 1, 3 and 5), the X and Y curves are indistinguishable. Of course, as field curves approach that of the diffraction limit, the optical performance of the system is closer to an idealized perfect system.

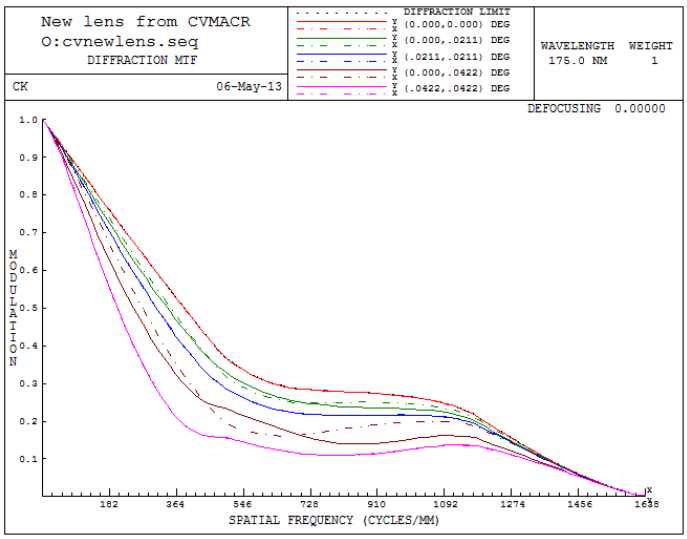

Figure 97 - Optical *MTF* of the first design

As I mentioned before, the discretized sensor composed of geometrical apertures (the pixels) influences the MTF shape. The final MTF is the product of the $optical\ MTF$, which is calculated by Code V, and the pixilated sensor's MTF (Smith W. J., 2008). At first approximation, we can assimilate this latter to the $Fourier\ Transform$ of a $15\ \mu m$ square aperture. Two effects can be mentioned: the MTF is degraded and the spatial frequency is limited to the Nyquist frequency. Indeed, above this spatial frequency of $33.3\ lines/mm$, the object is not resolved.

In order to check if the requirement on the MTF value at the Nyquist frequency is fulfilled, we have to consider this total $instrument\ MTF$. Moreover, I decided to treat the worst case in terms of field positions, in the corner of the sensor ($(1,1)$ field position) since the aberrations are greater for this position. In order to calculate this total MTF, I used the output Code V MTF as input for Matlab software. In this environment, I implemented the detector MTF and obtained the resultant one by multiplying them with each other. The figure below illustrates the total instrument MTF of the first design:

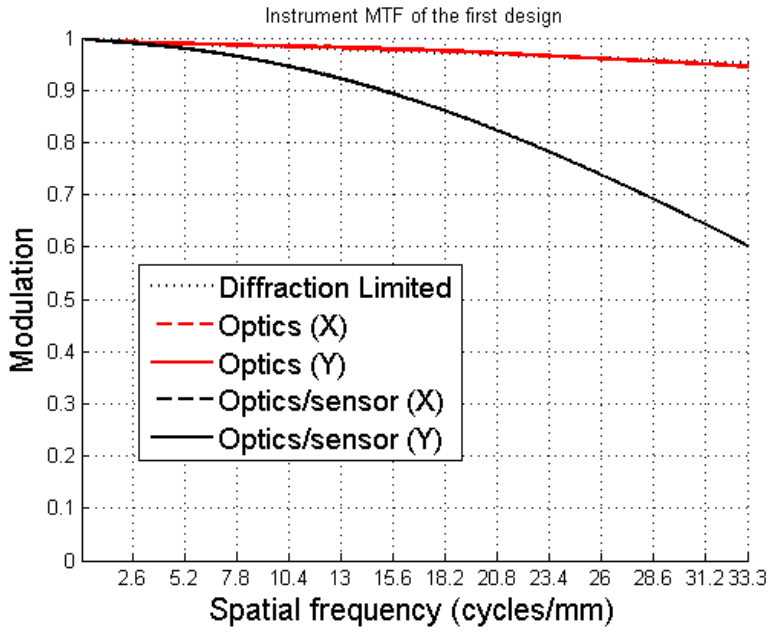

Figure 98 - Instrument *MTF* of the first design

The MTF value is well over the 10% required from the specifications. Yet we have to keep in mind that this design is far from being realistic and that more parameters have still to be taken into account. We can however see that the degradation induced by the detector MTF is really important since the MTF value drops from 0.95 to 0.6.

Encircled energy

This analysis tool expresses the percentage of encircled of energy as a function of the considered circle's diameter. This informs us about the power of ray concentration of the telescope and constitutes a second way to check if the rays are well focused on a single

pixel. Figure 99 shows the results of this analysis for the first Cassegrain telescope that I obtained.

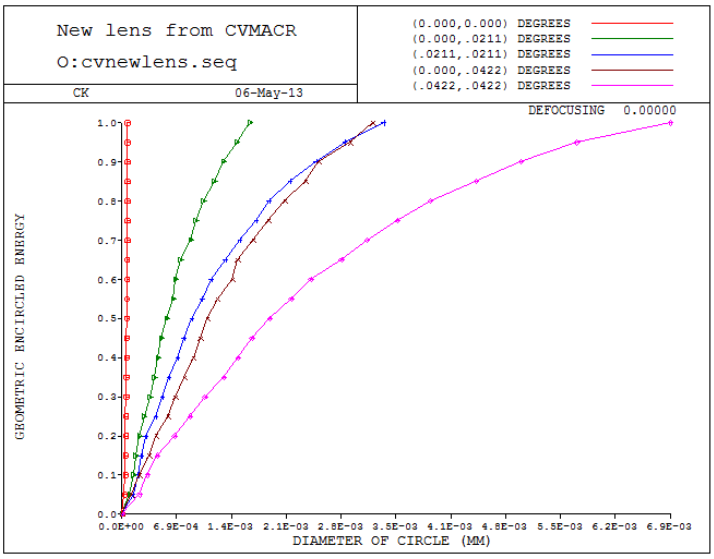

Figure 99 - Radial energy analysis of the first design

The energy is well concentrated on a single pixel since the spot diagram is extremely small. Indeed, 80% of the spot energy is included in a circle the diameter of which is approximately $4\ \mu m$. This spot grows in size by adding real parameters like a broadened spectrum, as other designs show further in this chapter.

5.2.1.5. Squared primary mirror

As presented in the signal-to-noise ratio section, the use of a squared primary mirror is really useful in order to diminish the observation time and thereof relax the requirements on the ADCS. This section thus investigates if such a primary mirror alters the optical quality of the telescope.

I then re-optimized the system in order to reach the best solution with these new parameters. The new dimensions for the telescope are shown in Table 8. A little square in the semi-aperture column mentions that the primary mirror has now a square shape.

Surface #	Surface Name	Surface Type	Y Radius	Thickness	Glass	Refract Mode	Y Semi-Aperture
Object		Sphere	Infinity	Infinity		Refract	
1	Obscuration	Sphere	Infinity	69.0000		Refract	40.0000
Stop	Primary_mirror	Conic	-200.7171 V	-59.9327 V		Reflect	40.0000
3	Secondary_mirror	Conic	-127.3135 V	110.7733 V		Reflect	16.3951
Image		Sphere	Infinity	0.0000		Refract	0.2896
End Of Data							

Table 8 - Dimensions of the first design with a squared primary mirror in *mm*

The $2D$ and $3D$ representations of the first design where the circular primary mirror is replaced by a squared one is illustrated in Figure 100.

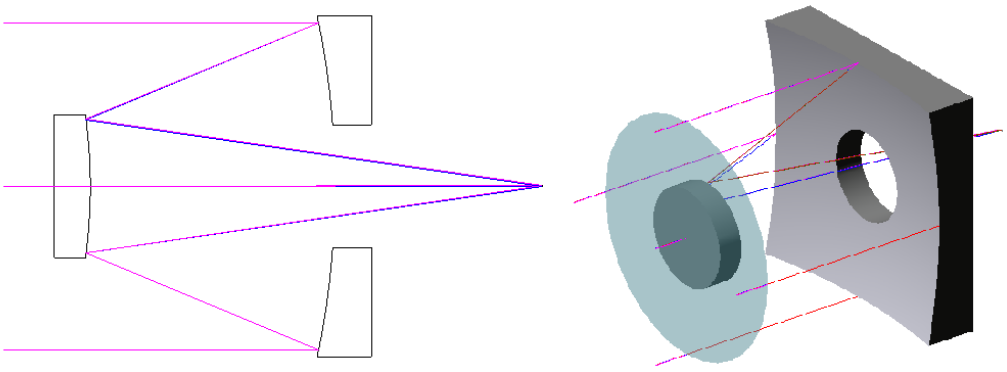

Figure 100 - *2D* and *3D* views of the first design with a squared primary mirror

Spot diagram

The spot diagram is shown in Figure 101. As we can see, the spot sizes of this new option are nearly identical to those presented before. Indeed, the maximum spot size is equal to $2.417\ \mu m$ for the (1,1) field position as opposed to the previous design for which it is $2.415\ \mu m$.

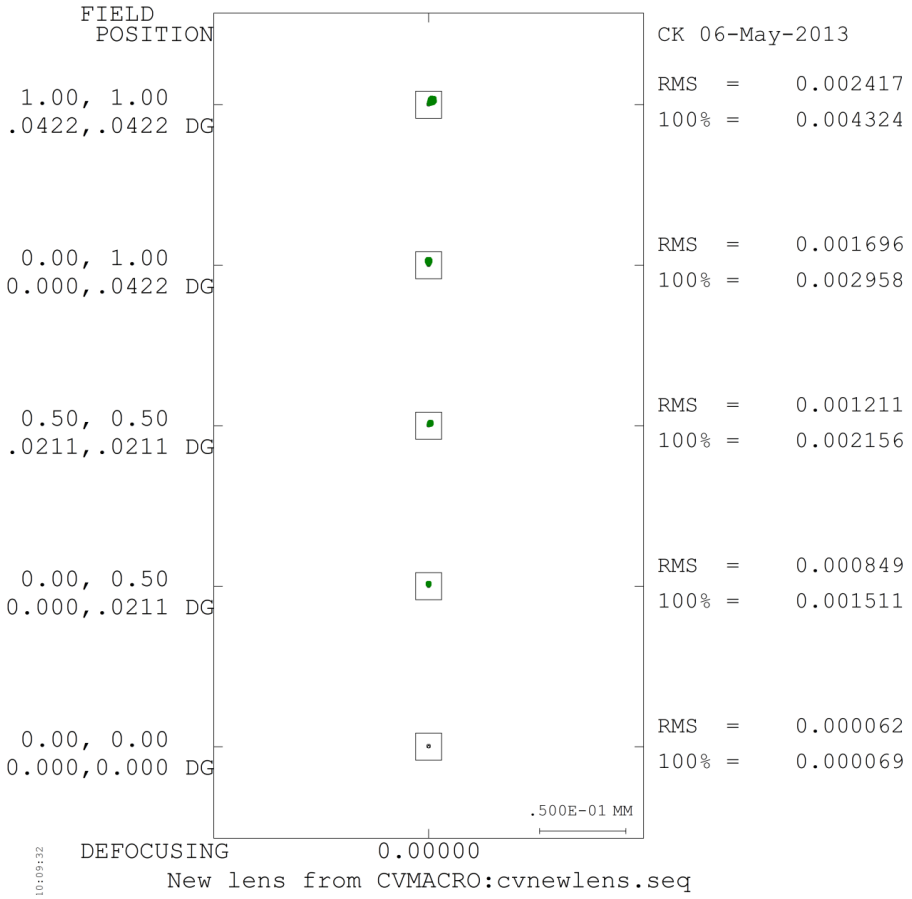

Figure 101 - Spot diagram of the first design with a squared primary mirror

All the spots are included in the $15\ \mu m$ pixel hence, the requirement is fulfilled. I only consider the RMS spot sizes but in this case the rays are so concentrated and the spot so tiny that RMS and 100% spot sizes are quite the same.

Indeed, the FoV, i.e. the Io's torus angular diameter, is extremely narrow and the coma aberration only applies to off-axis rays. In fact, as spherical aberration is not significant in Cassegrain telescopes, on-axis rays are well focused on the same point. With the next designs, I expose further in this chapter that as the FoV increases, the coma aberration clearly appears and the spot diameter grows.

Once this optical tool was checked, I then investigated the ray trace curve to try to identify the aberrations from which the system suffered.

Ray aberration curves

The ray aberration curves of this new telescope are presented in Figure 102. A simple look at this picture directly reveals that coma is still the predominant aberration in the optical system. I therefore checked this assumption by running the aberration analysis tool of Code V. The results that appeared are presented in Table 9.

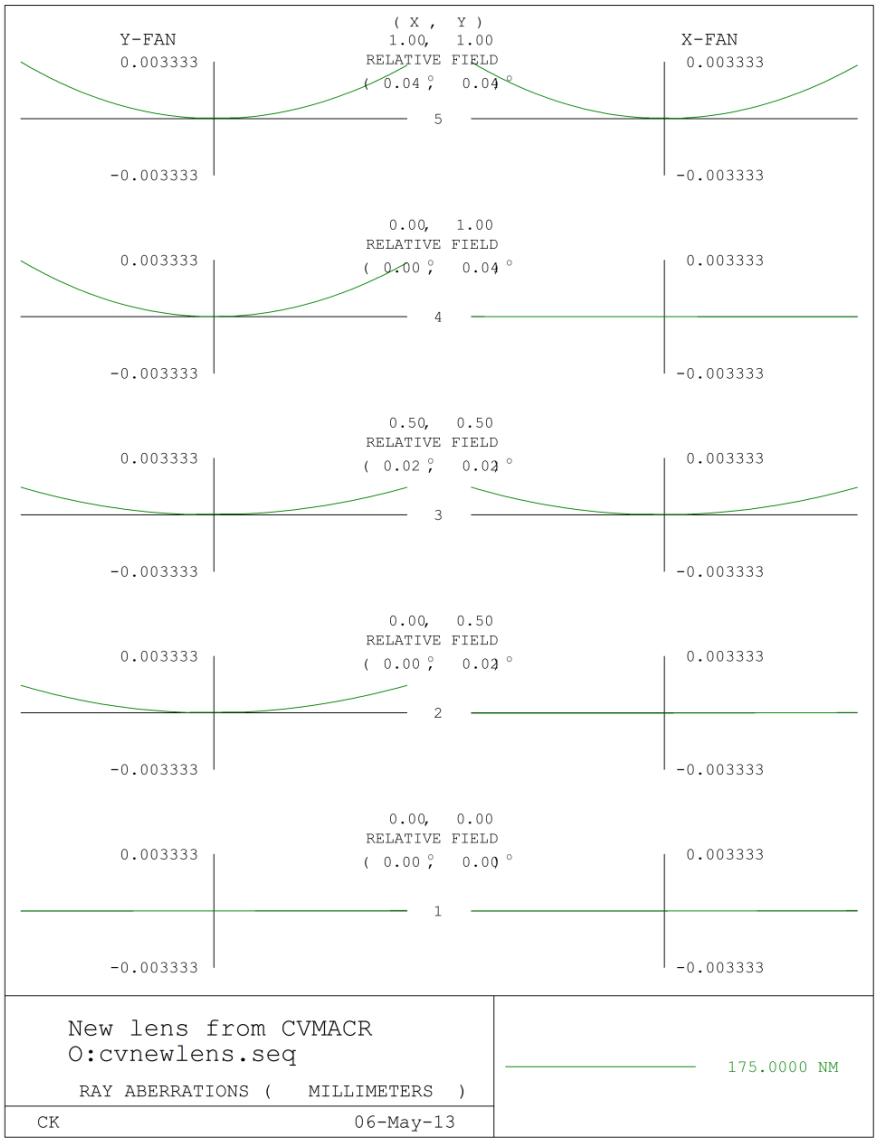

Figure 102 - Ray trace curve of the first design with a squared primary mirror

THO SO..I

New lens from CVMACRO:cvnewlens.seq
Position 1, Wavelength = 175.0 NM

	SA	TCO	TAS	SAS
1	0.000000	0.000000	0.000000	0.000000
STO	-2.176504	0.034128	-0.000119	0.000000
	2.176504	0.000000	0.000000	0.000000
3	1.037304	-0.017526	0.000005	-0.000061
	-1.037363	-0.012057	-0.000047	-0.000016
SUM	-0.000059	0.004545	-0.000161	-0.000076

Table 9 - Aberration analysis of the first design with a squared primary mirror

We can see that once again coma is the predominant source of aberrations since others are 40 to 400 times smaller. The conclusions on the spot diagrams provided above are then verified by these ray aberration curves.

Modulation transfer function

The MTF analysis tool can now be applied to this new Cassegrain telescope. All the MTF curves (the instrument ones) represented in Figure 103 are identical to these of the circular primary telescope developed before.

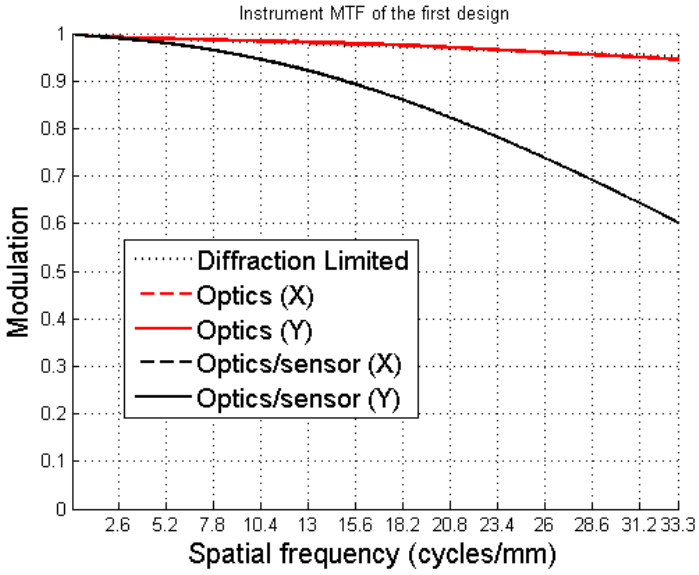

Figure 103 - Instrument *MTF* of the first design with a squared primary mirror

Encircled energy

As we saw earlier, the energy concentration is still very high in this squared primary Cassegrain telescope. Indeed, the curves are highly inclined, that is, the energy amount increases rapidly with the considered circle's diameter.

We can see in Figure 104 that 90% of the total energy of the $(1,1)$ field is concentrated in a circle whose diameter approaches $4.7\ \mu m$.

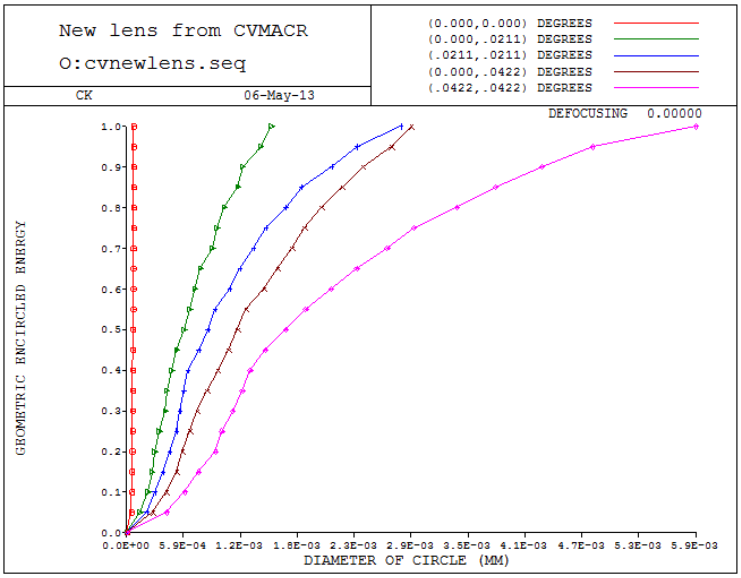

Figure 104 - Radial energy analysis of the first design with a squared primary mirror

5.2.1.6. Conclusion

A brief conclusion can already be drawn from this first attempt to obtain a desired Cassegrain telescope. A first telescope was designed to determine if this is a feasible option for a Cubesat platform. Indeed, the constraints induced by such a satellite could have led to too severe mechanical constraints. In particular, the small dimensions of a Cubesat could have jeopardized the fixed requirements of the mission.

A basic design respecting the requirements of the mission was eventually found. The spot size is totally included inside a single pixel of the detector and the MTF criterion is also verified. However, the available space in the Cubesat is not completely used and Code V did not take full advantage of the constraints.

Besides, the use of a squared primary mirror does not affect so much the optical properties of this first design. This remarkable fact is quite interesting since the signal-to-noise ratio showed that the observation time was effectively reduced by using such a mirror shape. Indeed, the aperture of the telescope is increased in comparison with a circular primary mirror. However, the manufacturability of such a mirror has to be checked in order to be sure that this option is not too expensive.

Another ascertainment is that the diameter of the secondary mirror is quite large, increasing the obscuration on the primary mirror. On the one hand, this degrades the image quality (we checked it with the help of the MTF) and on the other hand it causes an increase of the observation time.

Finally, very simplified parameters were used in order to produce this telescope and a short focal length was considered. These first results are now used to conceive a better and more realistic Cassegrain telescope.

5.2.2. Second design - Longer *EFL*

Once I checked the optical feasibility of elaborating a Cassegrain telescope onboard the Cubesat platform, I then decided to improve its optical properties. The first thing was the increase of its focal length to respect the resolution requirement as long as possible. As mentioned before, a focal length of $413\ mm$ is enough to achieve this goal during the period of time 2014-2017, that is, the period of the Juno's observation. Therefore, the second design is a Cassegrain telescope with an EFL of $413\ mm$ or as long as possible if this length is not reachable.

I start the optimization from the first design, of which the EFL is $275\ mm$. All parameters are kept from the first design, except the EFL.

5.2.2.1. Field of view

The FoV for this design is thus the Io's torus angular diameter which is approximately equal to $5.058\ arcmin$. The $Object\ angle\ field$ option is selected and it is the case for all the following telescopes. This optical optimization only takes into account the baseline wavelength of $172.5\ nm$.

5.2.2.2. Optimization process

The only thing to do here was to change the constraint on the focal length to let Code V increase it by changing the telescope parameters.

Constraints

The global requirements that I used in order to establish the constraints that Code V had to respect during the optimization process are shown in Table 10.

Variable	Value
Focal length	$413\ mm$
Primary-secondary distance	$< 7.5\ cm$
Backfocus	$< 12.5\ cm$
Secondary conic constant	< -1

Table 10 - Optimization constraints of the second design

These constraints were imposed in order to obtain a Cassegrain-type design that can be positioned into the Cubesat.

Results

The dimensions of the system that Code V generated after optimization are presented in the table below.

Surface #	Surface Name	Surface Type	Y Radius	Thickness	Glass	Refract Mode	Y Semi-Aperture
Object		Sphere	Infinity	Infinity		Refract	
1	Obscuration	Sphere	Infinity	85.0000		Refract	40.0000
Stop	Primary_mirror	Conic	-215.1051 V	-75.0000 V		Reflect	40.0000
3	Secondary_mirror	Conic	-88.0296 V	125.0000 V		Reflect	12.2739
Image		Sphere	Infinity	0.0000		Refract	0.4324
End Of Data							

Table 11 - Dimensions of the second design in *mm*

We can notice that Code V separates as much as possible the two mirrors. If the constraint on the distance between the two mirrors was forgotten, wrong designs would be induced.

Secondly, the radius of curvature of the secondary mirror is now largely reduced, hence this mirror is more curved than before. Another thing that is worth being mentioned is that it is also fairly smaller now. However, the smaller the secondary mirror, the smaller the obscuration so this is an advantage compared to the previous situation. Since the diameter of the secondary is $12.2739\ mm$, the fraction of the primary that is now obscured is decreased to 9.42%. This induces an improvement in the SNR and reduce the needed observation time.

Then, in opposition to the previous design, Code V now takes advantage from the available space in the Cubesat.

In Figure 105, the $2D$ and $3D$ representations of the telescope are represented. The rays that appear in this figure are obviously not the only ones that Code V traces during the optimization and analysis processes but only a part of a huge number distributed over the entire entrance pupil.

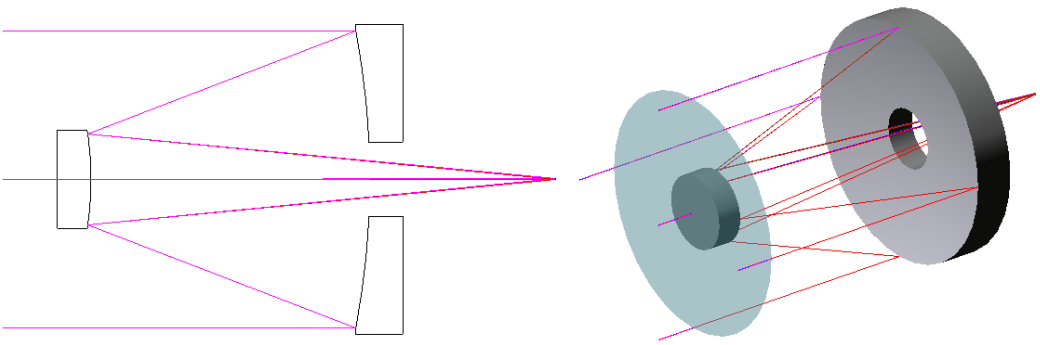

Figure 105 - *2D* and *3D* views of the second design

5.2.2.3. Image quality analysis

Once Code V reached the optimized system with respect to the constraints, I analyzed its optical performance in order to check if this design was acceptable. I used the same tools as presented before: the spot diagram, the ray aberration plot, the MTF and the radial energy analysis.

Again I still did neither implement the tolerances (manufacture and assembly) in the design nor check if the environmental changes were of importance. As mentioned before these steps are carried out on the last design presented, after a few iterations are performed with the current designs..

Spot diagram

The first thing I do is to check if the spot diagram exhibits a spot size larger than the requirement. It appears, as shown in Figure 106, that the RMS spot size is smaller than $15\ \mu m$ for all field positions.

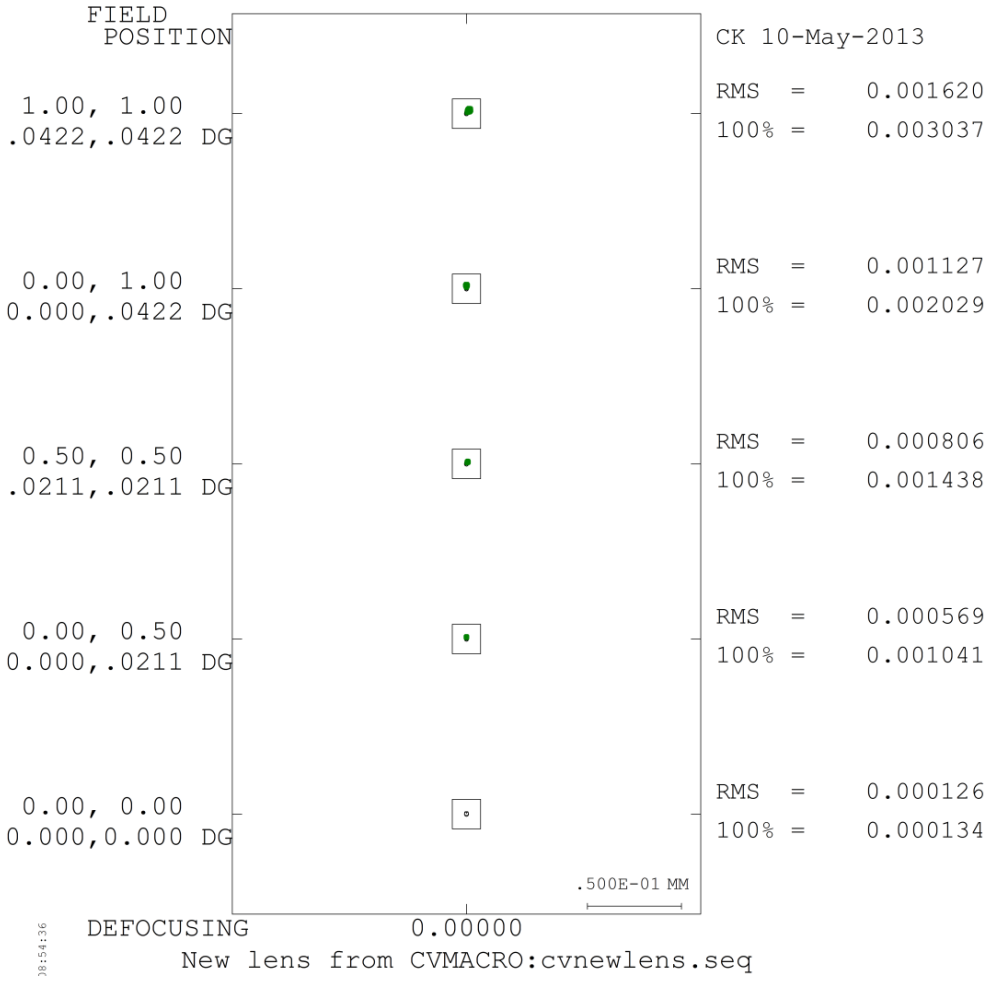

Figure 106 - Spot diagram of the second design

Once again, the maximum RMS spot size equal to $1.620\ \mu m$ is reached for the (1,1) field position. This time the Airy disk diameter is (with the help of (2)):

$$Airy\ disc\ diameter = 2.44\ \lambda\ \frac{f}{D} = 2.44\ 172.5\ 10^{-9}\ \frac{413\ 10^{-3}}{4\ 10^{-2}} \approx 4.346\ \mu m$$

The size of the central ring of this diffraction pattern increases since only the focal length has been changed in (2).

Since the spots are smaller than the diffraction limit, they are actually quite useless because when Code V runs the spot diagram analysis, it consists in a $geometrical$ analysis. This means that light is considered as photons, that can undergo reflection and refraction mechanisms. These are the bases of $Ray\text{-}tracing$. On the other hand, MTF is a $diffraction$ analysis which considers light as a wave. The diffraction limit consists in calculating the diameter of the first Airy disk, the diffraction pattern. Since the spot diagram is a geometrical tool, it does not consider any diffraction phenomenon and displays spots that are smaller than the diffraction limit. This is why Code V proposes to display on the spot diagram the diffraction limit with the help of a small circle in order to recall the user that spots can be meaningless sometimes.

Ray aberration curves

Since this telescope belongs to the Cassegrain family, coma is still the primary aberration that is observed from the ray aberration plot (See Figure 107). Further designs show that this phenomenon disappears once the secondary mirror conic constant varies.

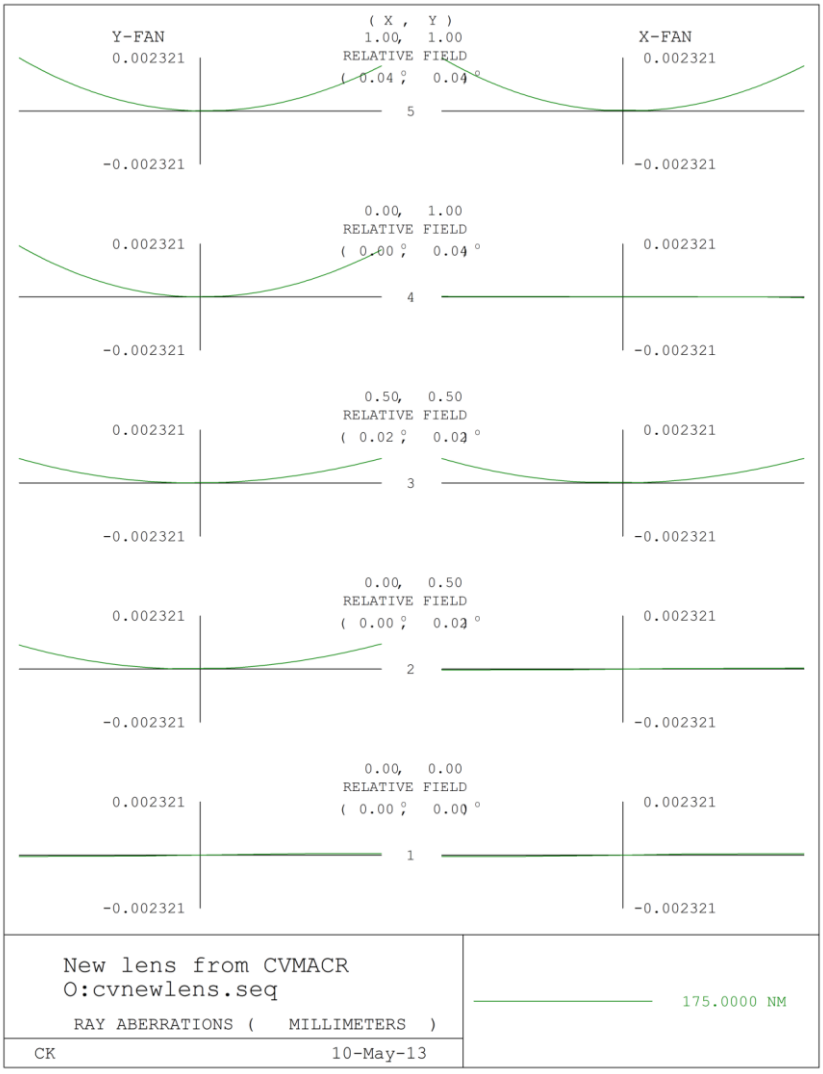

Figure 107 - Ray trace curve of the second design

As I said before, the coma aberration only affects the off-axis rays. Indeed, $Field\ 1$ is not affected, nearly, by any aberration since it is an on-axis field. Moreover, $Field\ 2$ and 3 have both an on-axis X component thus the $X\text{-}fan$ does not show any sign of coma neither.

To confirm these results, I then displayed the aberration analysis that Code V is able to perform. This latter is shown in Table 12. The coma aberration is well the predominant one and this approves the previous statements.

```
THO SO..I

    New lens from CVMACRO:cvnewlens.seq
              Position  1, Wavelength =   175.0 NM
          SA          TCO         TAS         SAS
  1    0.000000    0.000000    0.000000    0.000000
STO   -2.655692    0.044627   -0.000167    0.000000
       2.655692    0.000000    0.000000    0.000000
  3    0.944404   -0.023318   -0.000012   -0.000140
      -0.944471   -0.018283   -0.000118   -0.000039

SUM   -0.000068    0.003025   -0.000296   -0.000179
```

Table 12 - Aberration analysis of the second design

Modulation Transfer Function

Figure 108 below illustrates the optical MTF of this second design that Code V produces. A Matlab analysis of the entire instrument MTF is then performed to check if the MTF is still greater than 10% at the Nyquist frequency. This latter is presented for the (1,1) field position in Figure 109.

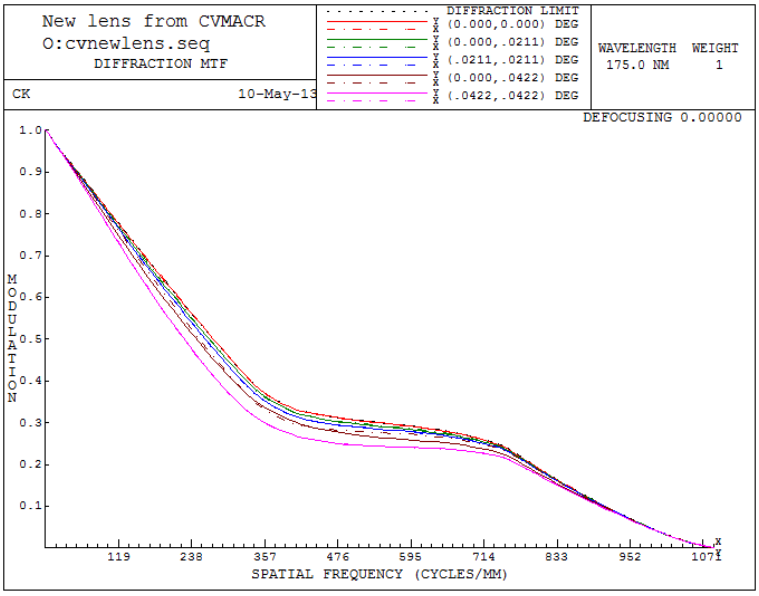

Figure 108 - Optical *MTF* of the second design

We can see that the requirement is still easily verified and that the optimized optical system satisfies the MTF requirement.

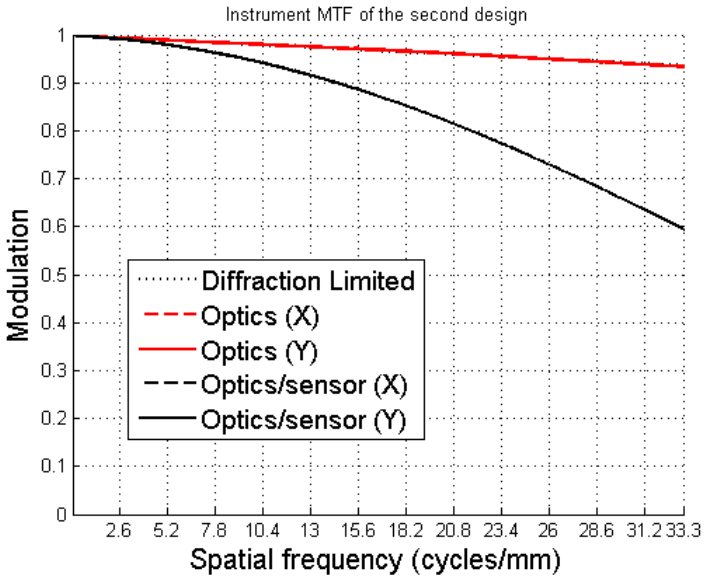

Figure 109 - Instrument *MTF* of the second design

This new design is then quite hopeful since we reached an optical system with a focal length which is long enough to observe during the whole considered mission life and which fulfils the requirements

Encircled energy

The radial energy analysis of this second design is shown in Figure 110. The diameter that encircles 90% of the energy is still really small ($3\ \mu m$) and the concentration power of the telescope is this time again really high. These results strengthen the previous analyses that mention that the system exhibits significant optical performance.

Therefore, all requirements are successfully passed and this optical system is kept for future improvements.

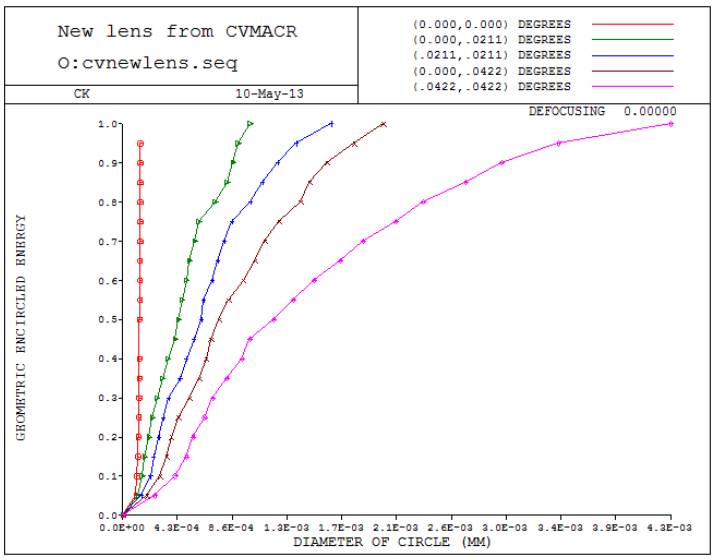

Figure 110 - Radial energy analysis of the second design

5.2.2.4. Squared primary mirror

I replace now the circular primary mirror by a squared one. This in fact increases the aperture of the telescope and the captured incident photons number. The only thing to do is thus to replace in the surface properties the primary mirror shape, re-optimize the system and run all the analysis tools.

The new dimensions of this telescope are presented in Table 13. These are a little bit different from those of the previous design.

Surface #	Surface Name	Surface Type	Y Radius	Thickness	Glass	Refract Mode	Y Semi-Aperture	X Semi-Aperture
Object		Sphere	Infinity	Infinity		Refract		
1	Obscuration	Sphere	Infinity	85.0000		Refract	40.0000	40.0000
Stop	Primary_mirror	Conic	-215.1051 V	-75.0000 V		Reflect	40.0000	40.0000
3	Secondary_mirror	Conic	-88.0296 V	125.0000 V		Reflect	12.2739	12.2739
Image		Sphere	Infinity	0.0000		Refract	0.4324	0.4324
End Of Data								

Table 13 - Dimensions of the second design with a squared primary mirror in *mm*

The advantage of the basic second design remains, namely a small secondary diameter.

The $2D$ and $3D$ views of this new telescope are represented in Figure 111:

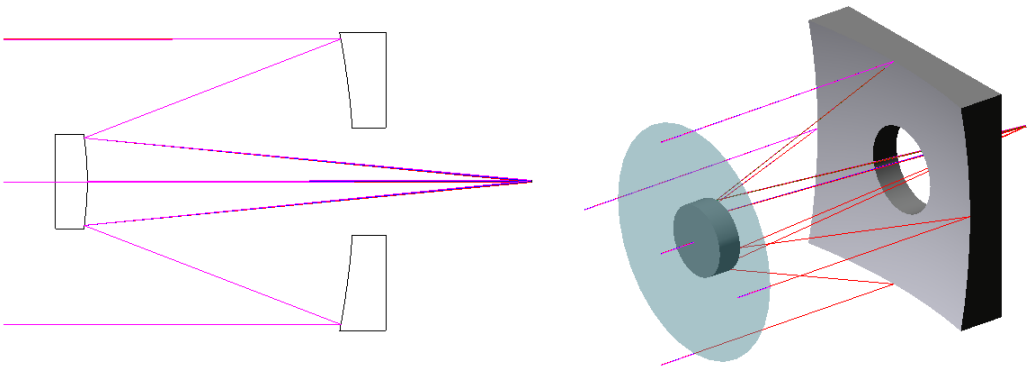

Figure 111 - *2D* and *3D* views of the second design with a squared primary mirror

As explained before, some fields are hidden while some others are confused.

Image quality analysis

In the last section, which is dedicated to the first design, I checked if the optical performances of the telescope were maintained by changing the shape of the primary mirror. It was the case and this is actually still true for this design.

Indeed, the new optimization that is run after having changed the primary mirror shape slightly alters the telescope dimensions and no remarkable change is noticed in its optical performance. Therefore, the images related to the analysis tools are not provided here since they do not bring any further relevant information.

5.2.2.5. Conclusion

The second design was developed to check if it was possible to increase the focal length in order to observe the Io's torus as long as possible while satisfying the requirement on the resolution. I therefore re-optimized the first design with the updated EFL value.

The new Cassegrain telescope respected all the optical requirements. Indeed, the spot size of this optical system is still really small and the MTF acceptable. Then, the energy concentration of the system was also checked.

In addition, the secondary mirror's diameter has sorely decreased. This represents a great improvement in the signal-to-noise ratio since the signal that enters the Cassegrain telescope increases as the obscuration decreases.

The dimensions of this second design fit much better than before the available space since all the constraints are tight.

The imaging performances of the telescope were conserved through the shape change of the primary mirror. This modification is really interesting since it improves the signal-to-noise ratio.

Finally, this focal length achievement paves the way to other designs that incorporate more realistic input parameters.

5.2.3. Third design - Larger FoV

Once a long focal Cassegrain telescope was designed, I decided to enlarge the considered FoV. Actually, the idea is to "degrade" the telescope performance by letting increase the spot size while respecting the required resolution. The telescope is thus designed and optimized by considering a larger FoV. Even if the spot will be greater than before, it will still be acceptable and the telescope will exhibit a larger FoV imaging ability (Habraken, Salvador, & Kintziger, (Personal communications), 2013, March 19).

Designing a telescope whose FoV is limited to that of the observed object is impossible. Indeed, the pointing accuracy of the telescope is limited by the ADCS and this one is maybe not accurate enough to directly point the target and take images. This subsystem only brings the telescope line of sight at a certain distance from the target. This latter is actually equal to the ADCS pointing accuracy and the telescope, in order to locate the target and track it, has to be able to image a larger FoV. The smallest SFoV that the optical system has to be able to image is equal to the pointing accuracy of the ADCS as I show it in the following subsection.

5.2.3.1. Field of view

As explained before in the case of ExoplanetSat, the pointing accuracy of the MAI-200 approaches $60\ arcsec$[33] (Smith, et al., 2012) so the minimum half FoV that the optical system should be able to image with high precision is at least $60\ arcsec$. Indeed, the coarse pointing subsystem of ExoplanetSat has first to target the star which is then located in a circle of $60\ arcsec$ and maybe not centred on it as shown in Figure 112. Thus the image quality has to be high enough within this entire circle in order to be able to locate the star, enable the fine pointing and centre it on the detector (piezo stage). The same situation was presented before when talking about the ALL-STAR's pointing accuracy and needed FoV.

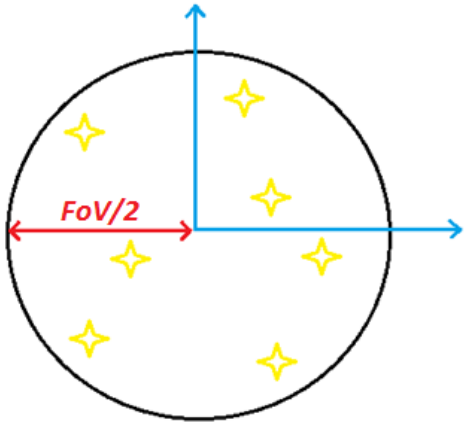

Figure 112 - Coarse pointing accuracy

The required FoV that has to be imaged for the present mission was specified through the requirement *"The entire torus has to be seen"*. The enlargement of the FoV takes into account the attitude control pointing accuracy. I presented before three ADCS who could be used into this Cubesat: the MAI-200 (ExoplanetSat), the $iADCS$-100 and the $XACT$.

As MIT reached a $60\ arcsec$ pointing accuracy with the MAI-200 and that the pointing accuracy of the $iADCS\ 100$ is commercially announced at $\ll 1°$ (the same as the MAI-200) (BerlinSpacetechnologies), I decided to fix the image FoV at $0.25°$ (Habraken, Salvador, & Kintziger, 2013, February 27). Finally, the pointing accuracy of the $XACT$ and SDS-1 are said to be approximately $\pm 0.02°$ in all 3-axis so this considered FoV is much larger than the pointing accuracy in this case (BlueCanyonTechnologies).

Moreover, I contacted Berlin Space Technologies to get more information about the pointing accuracy of the $iADCS$-100. I was answered that it all depends on the Cubesat alignment. What we can reasonably expect from the ADCS is a pointing accuracy of the order of a few $arcmins$ to $0.1°$, errors due to the Cubesat misalignment then have to be added to this result. A solution to this problem might be to track a bright star and measure a

[33] With their own sensors since the commercial information of this $ADCS$ state a pointing accuracy of approximately $1°$ with supplied sensors (CubeSatKit).

reference with the star tracker: the alignment errors would then be determined. However, Cubesats are usually subject to large temperature variations and these measurements should often be redone at different temperatures in order to get updated values (Segert & Kintziger, 2013, March 23).

As we expose above, we can calculate the entire or diagonal FoV with the help of (6) (if we consider a squared detector):

$$FoV_{diag} = \frac{FoV}{\cos 45°} = \frac{0.5°}{\frac{\sqrt{2}}{2}} = 0.71°$$

In the same way, we can calculate the number of pixels that are needed on the detector's side with such a telescope ($0.5° = 30\ arcmin$):

$$NoP_{EFL\ max} = \frac{FoV}{\theta_{max\ EFl}} = \frac{30}{0.12} = 250$$

The new field positions are thus now:

Field position	X coordinate (°)	Y coordinate (°)
Field 1 (0,0)	0	0
Field 2 (0,0.5)	0	0.125
Field 3 (0.5,0.5)	0.125	0.125
Field 4 (0,1)	0	0.25
Field 5 (1,1)	0.25	0.25

Table 14 - Field positions of the third design

The only wavelength that is taken into account is the baseline one of $172.5\ nm$ and all the optimization constraints remain the same.

Results

The spot diagram of the new optical system is shown in Figure 113.

As we can see, the coma pattern has really been enlarged. This can be understood by reminding that coma is proportional to the field and that it has been multiplied by more than 6. This induced a spot that completely goes out of the pixel sketch. This cannot be accepted considering the corresponding requirement. No more analysis tool is used since a mission requirement has already been violated.

I thus reached a point where I had to find a solution in order to get an optical system that fulfilled the requirement on the resolution with the new field positions. I then tried to reduce a bit the FoV but I found an upper limit around $0.1°$. Indeed, above this value, the spot starts to go out of the detector's pixel. I decided that it was not enough to really get a

telescope that could identify the target with the given ADCS. According to Tom Segert, the pointing accuracy can reach a value of 0.1° if the satellite misalignment is high.

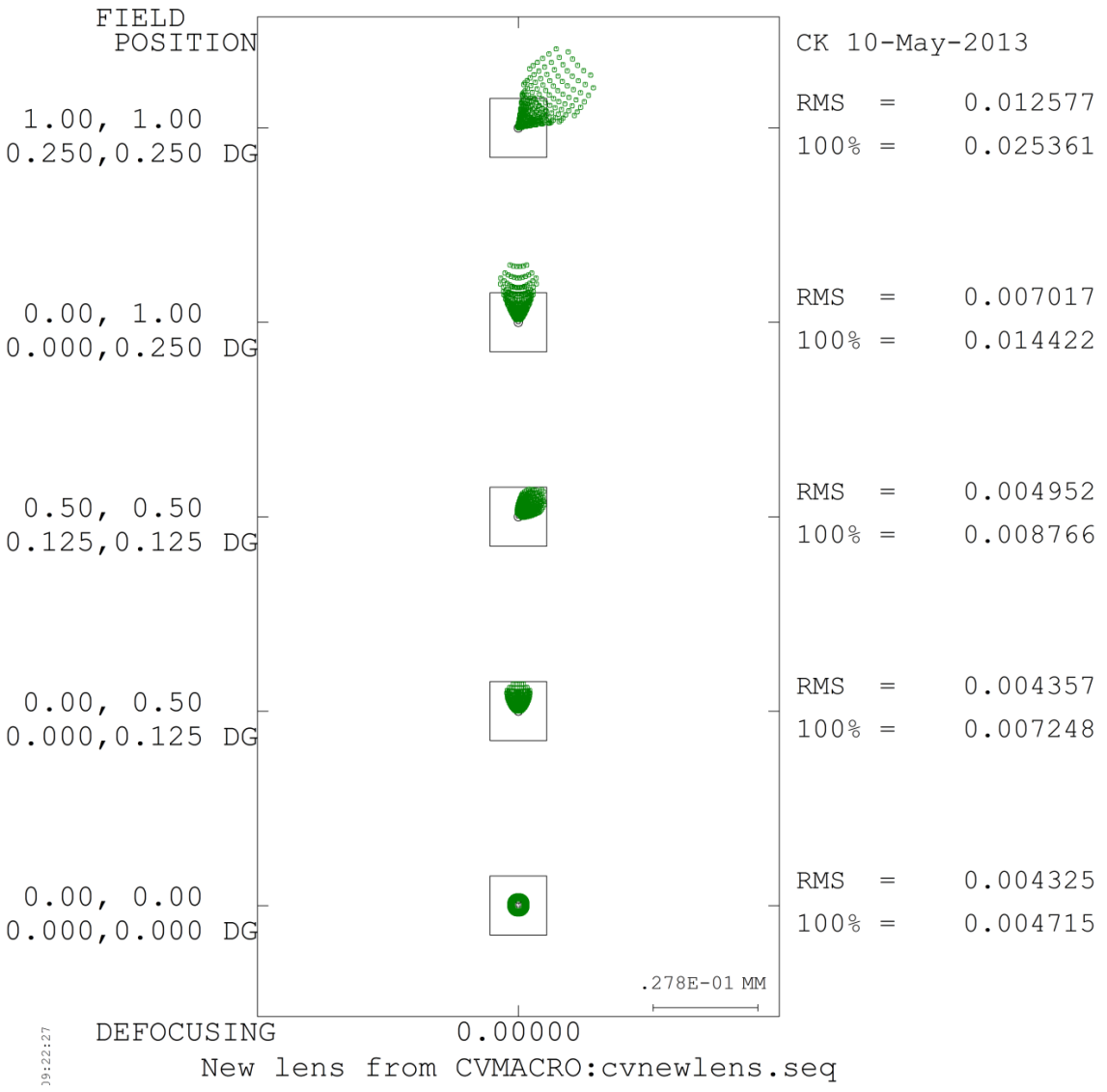

Figure 113 - Spot diagram of the third design

The second thing that I did was to let vary the primary conic constant in order to design a Ritchey-Chrétien telescope instead of a Cassegrain type since this alternative does not violate the requirements. This new free parameter led me to the fourth design.

5.2.4. Fourth design - The Ritchey-Chrétien solution

The objective here is to let the primary mirror conic constant vary during the optimization process in order to obtain a Ritchey-Chrétien telescope and a smaller spot size. This new design process takes into account more constraints, namely, those on the radius of curvature and conic constants of the mirrors. This intends to generate a system that is manufacturable and really usable in practice.

The same large FoV is imposed and the field positions remain the same. Finally the baseline wavelength of $172.5\ nm$ is considered.

5.2.4.1. Optimization process

Constraints

I have to introduce in the program some constraints on the radii of curvature of the mirrors and their conic constants. These are lower limits of respectively $100\ mm$ and -5[34]. The whole set of constraints that I entered into Code V is presented in Table 15.

Variable	Value
Focal length	$413\ mm$
Primary-secondary distance	$< 8\ cm$
Backfocus	$< 128\ mm$
Primary mirror's conic constant	< -1
Secondary mirror's conic constant	< -1
Primary mirror's conic constant	> -5
Secondary mirror's conic constant	> -5
Primary mirror's radius of curvature	$> 100\ mm$
Secondary mirror's radius of curvature	$> 100\ mm$

Table 15 - Optimization constraints of the fourth design

Results

The dimensions of this new telescope are presented in Table 16.

Surface #	Surface Name	Surface Type	Y Radius	Thickness	Glass	Refract Mode	Y Semi-Aperture
Object		Sphere	Infinity	Infinity		Refract	
1	Obscuration	Sphere	Infinity	90.0000		Refract	40.0000
Stop	Primary_mirror	Conic	-231.9222 V	-80.0000 V		Reflect	40.0000
3	Secondary_mirror	Conic	-100.0000 V	128.0000 V		Reflect	12.9010
Image		Sphere	Infinity	0.0000		Refract	2.5536
End Of Data							

Table 16 - Dimensions of the fourth design in *mm*

[34] A few explanations about these values are provided in Appendix B at the end of this report.

This telescope still proposes a smaller secondary mirror than the first design does. Modifying some of the previous constrains still allows a better configuration, from that point of view, than the first design in terms of SNR.

Moreover, the conic constants of the primary and secondary mirror are respectively equal to -1.0688 and -3.7945. These values verify the constraints that I present in Appendix B and constitute a great improvement compared with the previous attempts.

The next figure shows $2D$ and $3D$ views of this new Ritchey-Chrétien telescope.

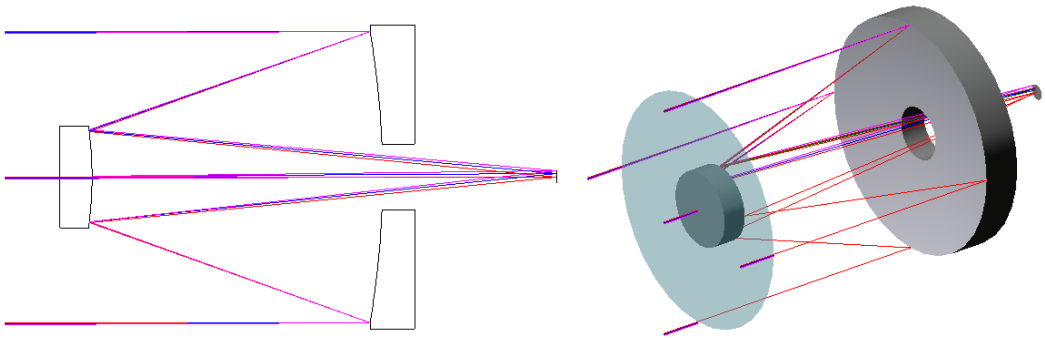

Figure 114 - *2D* and *3D* views of the fourth design

5.2.4.2. Image quality analysis

After the optimization process, I have to check if this new free parameter, the secondary mirror's conic constant, permits to reach a system that fulfils the requirements. As before, I start with the spot diagram and then, if this one is passed, I continue with the others. With these new constraints on backfocus and mirror interdistance[35], I reached an optical system the spot diagram of which seemed to be acceptable. Hereafter are presented the optical analyses for this new telescope.

Spot diagram

The spot diagram is shown in Figure 115. We can immediately see that the spot is well confined inside a single pixel and that the Ritchey-Chrétien solution seems to be viable. As before, the RMS and 100% spot sizes are written on the right of the figure.

The maximum RMS spot size is reached at the corner (1,1) and is equal to $7.57\ \mu m$. This is a great improvement in comparison with the previous Cassegrain solution which exhibits, for the same field position, a spot of $12.577\ \mu m$ which was located completely out of the pixel. These new spots are completely located inside a single pixel, which fulfils the requirement. Therefore, giving more available space to Code V permits to reach an optical system respecting the new requirements and of which spot diagram is even better than before.

[35] Appendix B explains why changes in these constraints are necessary.

Since the spot size requirement is passed, I perform further analyses to check if the Ritchey-Chrétien telescope is a good solution to enlarge the FoV of the system.

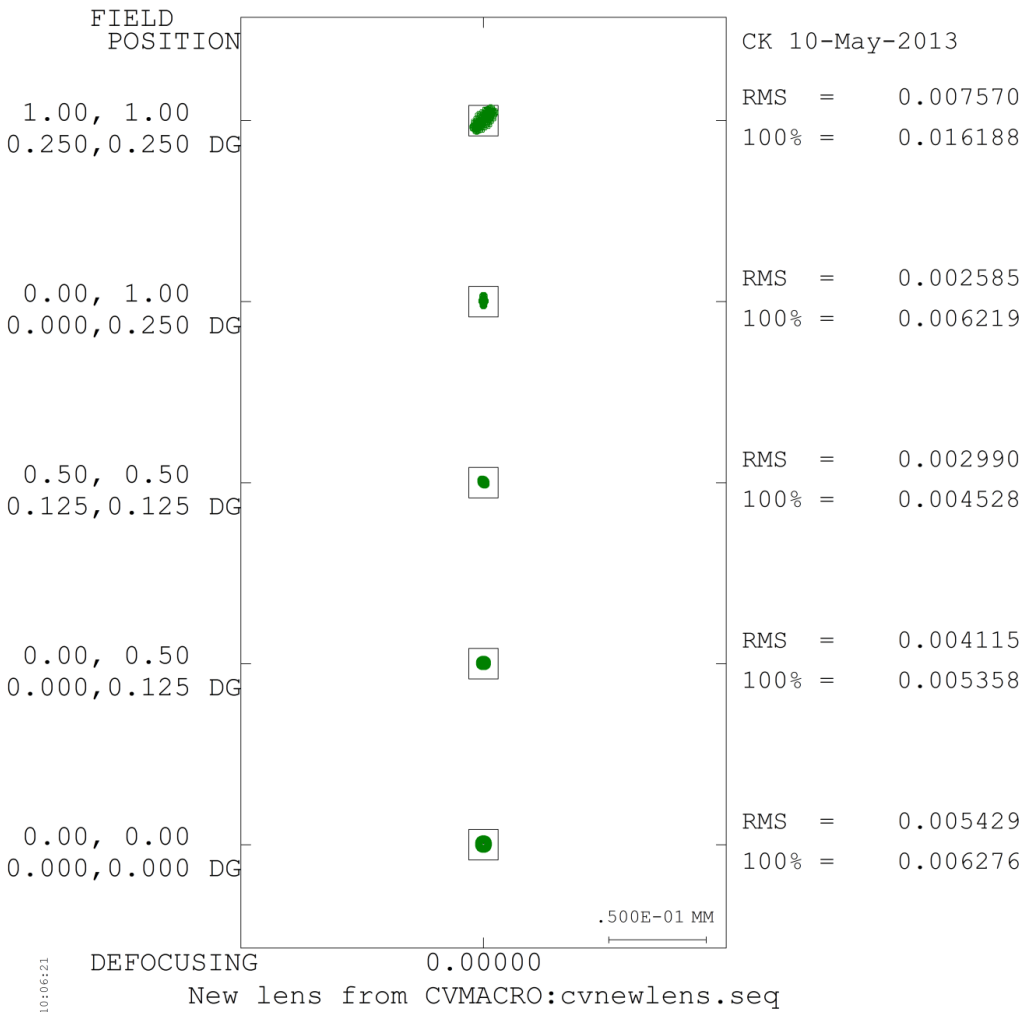

Figure 115 - Spot diagram of the fourth design

Ray aberration curves

This section exposes the aberration curves of the Ritchey-Chrétien telescope that Code V produces with the new constraints. The aberration curves become a little bit different (See Figure 116). Actually, we cannot identify a prevailing coma aberration anymore. Different aberrations generally exist in Ritchey-Chrétien systems but the limiting aberrations usually are astigmatism and field curvature, as it is free of coma, (Fischer, Tadic-Galeb, & Yoder, 2008).

Other aberrations than coma clearly appear since on-axis field positions also exhibit now non-horizontal aberration curves. I checked these assumptions with the help of the aberration analysis in Table 17. PTZ stands this time for Petzval field curvature aberration (Synopsys, Code V Prompting Guide, 2002).

THO SO..I

New lens from CVMACRO:cvnewlens.seq
Position 1, Wavelength = 175.0 NM

	SA	TCO	TAS	SAS	PTZ
1	0.000000	0.000000	0.000000	0.000000	0.000000
STO	-2.118863	0.227427	-0.005425	0.000000	0.008624
	2.264748	0.000000	0.000000	0.000000	
3	0.775237	-0.116942	-0.000410	-0.004330	-0.020000
	-0.927626	-0.110749	-0.004407	-0.001469	
SUM	-0.006504	-0.000264	-0.010242	-0.005800	-0.011376

Table 17 - Aberration analysis of the fourth design

The predominant aberrations are the spherical one, astigmatism and field curvature. Indeed, the aberration curves do not show anymore coma aberration but exhibit the typical S-shape of the spherical aberration. The astigmatic straight line is superposed to this S curve.

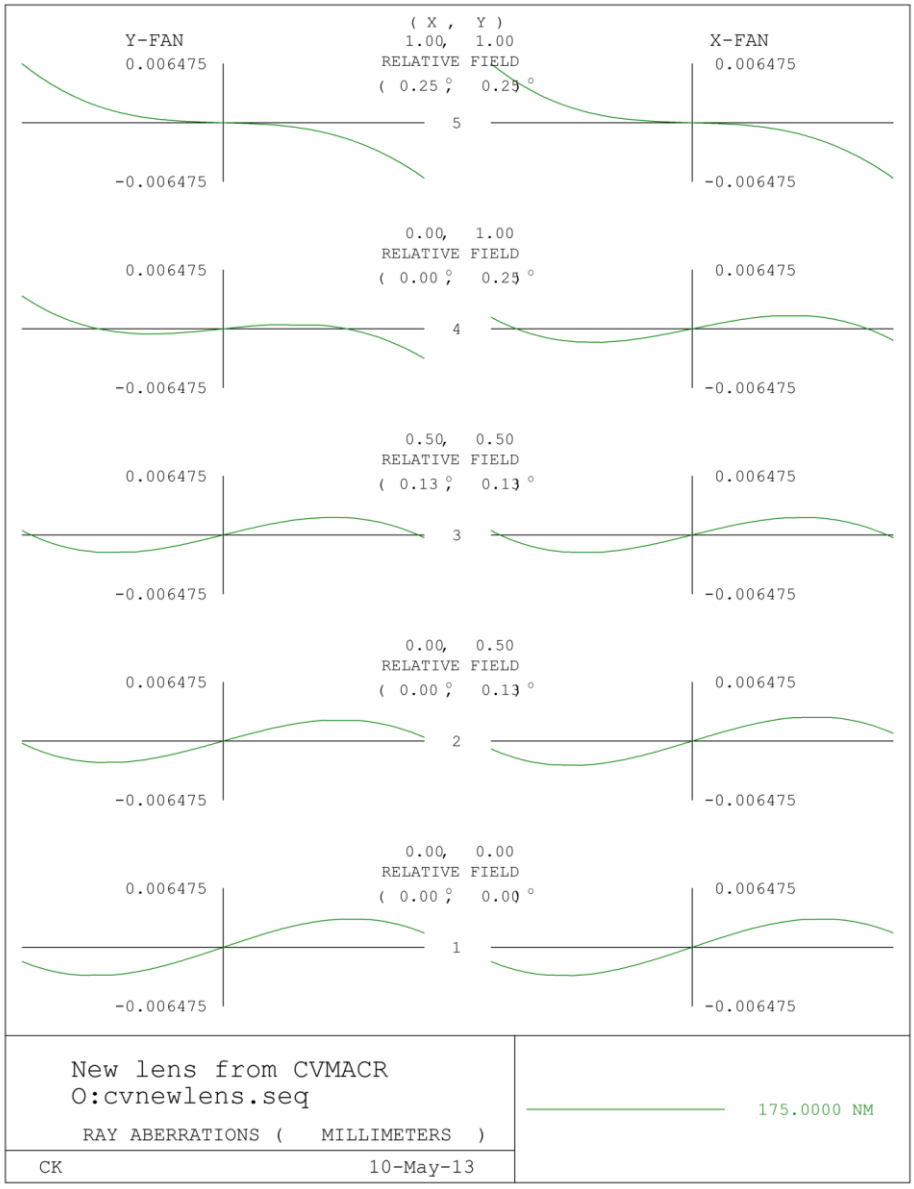

Figure 116 - Ray trace curve of the fourth design

Modulation Transfer Function

The optical MTF plot of this Ritchey-Chrétien optical system is presented in Figure 117.

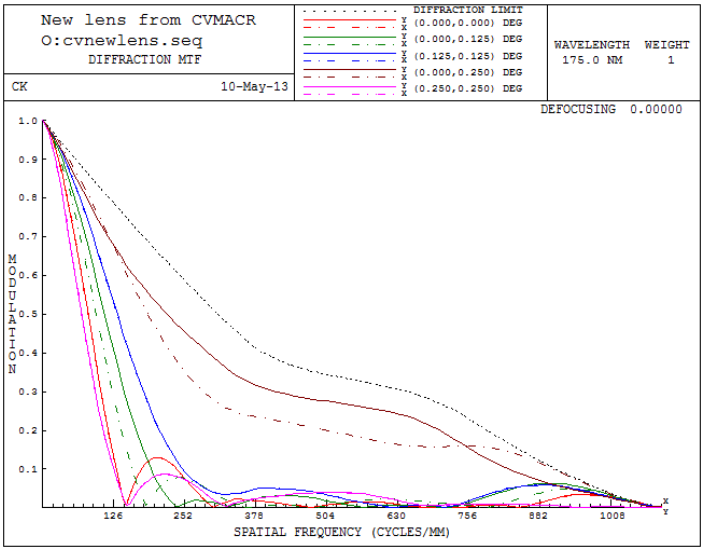

Figure 117 - Optical *MTF* of the fourth design

A great MTF degradation exists in the system compared with the previous designs. In fact, it becomes more and more deformed. Thereafter is presented the MTF curves that I obtain by taking into account the detector's MTF:

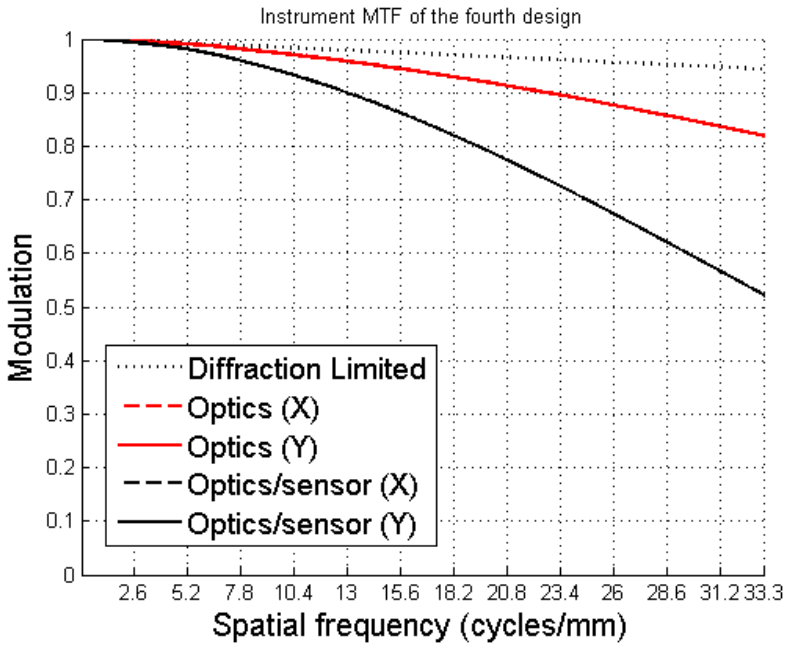

Figure 118 - Instrument *MTF* of the fourth design

What we can conclude is that this telescope does not violate the MTF requirement and can be accepted as an optical system which is able to enlarge the FoV. Indeed, the MTF value at the Nyquist frequency approaches 52%.

Encircled energy

The final evaluation that I perform on this system is the radial energy analysis. The results are presented in Figure 119.

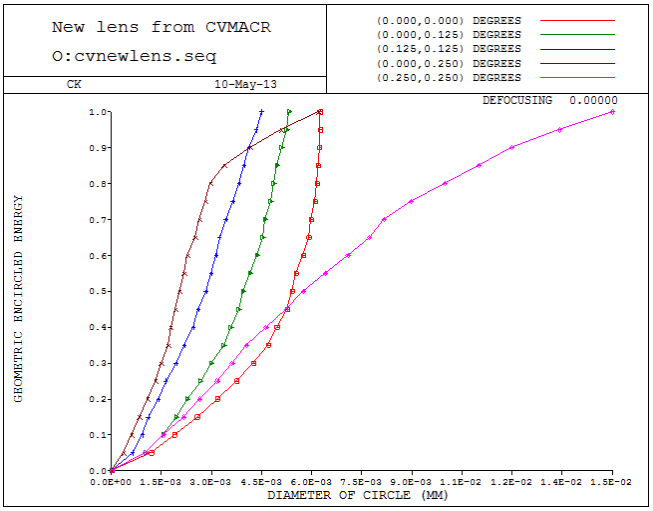

Figure 119 - Radial energy analysis of the fourth design

As for the previous design, the same conclusion can be drawn: the energy concentration falls and the entire spot is more diffused within the pixel. Indeed, the field curves are much more flattened than before. That is the result of degrading the telescope quality in order to be able to image a greater FoV as explained before. However, 80% of the energy is located inside a circle the diameter of which is $11\ \mu m$, which is less than the detector's pixel size.

Even though the energy concentration on the pixel is more distributed than that of the two first designs, this Ritchey-Chrétien configuration displays really good performance while respecting the new constraints on radii of curvature and conic constants. Indeed, all the requirements on spot diagrams, MTF and radial energy are verified.

We can finally mention that the largest field position has the most flattened curve since its induced spot size is the largest.

5.2.4.3. Squared primary mirror

The new dimensions of the squared primary mirror Ritchey-Chrétien telescope are the following:

Surface #	Surface Name	Surface Type	Y Radius	Thickness	Glass	Refract Mode	Y Semi-Aperture
Object		Sphere	Infinity	Infinity		Refract	
1	Obscuration	Sphere	Infinity	90.0000		Refract	40.0000
Stop	Primary_mirror	Conic	-231.9222 V	-80.0000 V		Reflect	40.0000
3	Secondary_mirror	Conic	-100.0000 V	128.0000 V		Reflect	12.9010
Image		Sphere	Infinity	0.0000		Refract	2.5536
End Of Data							

Table 18 - Dimensions of the fourth design with a squared primary mirror in *mm*

We can conclude that this change of primary mirror shape does not introduce large variations in the telescope's dimensions. A small secondary diameter is still in use, which is appropriate to diminish the obscuration on the primary mirror. The $2D$ and $3D$ representations of this design are shown in Figure 120.

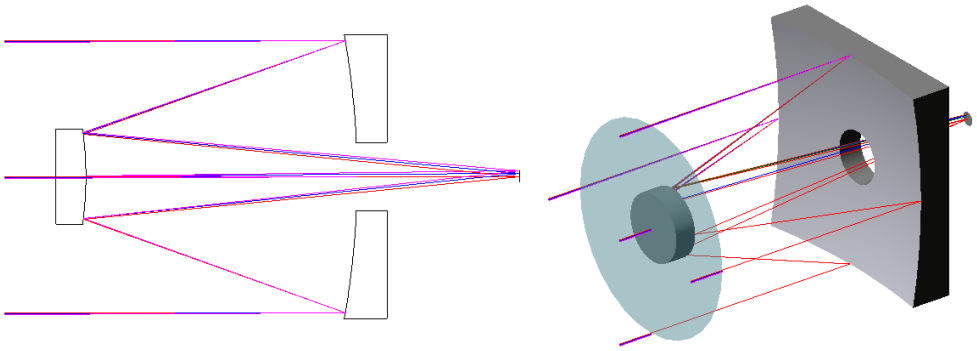

Figure 120 - *2D* and *3D* views of the fourth design with a squared primary

Image quality analysis

Since the squared primary mirror option is nearly the same as the circular one, the image quality of this configuration is also equally the same as before. Indeed, changing the shape of the primary mirror slightly alters its dimensions after being re-optimized. For the sake of clarity, I do not show them since they are quite redundant. Even if, in this case, the Ritchey-Chrétien alternative is used, this ascertainment proved to be valid.

5.2.4.4. Conclusion

This new alternative was aimed to try a new alternative to enlarge the FoV of the system. In addition, I investigated if relaxing a bit some of the constrains could allow the use of mirrors whose radii of curvature and conic constants respected the new requirements exposed in Appendix B. In fact, these are some of the parameters that fix the potential manufacturability of the mirrors. Eventually, the low-cost aspect of the Cubesat mission also bans the use of exotic, and thus expensive, surfaces. A new optimization was thus performed with an additional parameter, which was the primary conic constant, together with the corresponding constraints. These latter were an upper and a lower limit of respectively -1 and -5.

The new constrains finally permit to reach such a system which, in addition, fulfils all the optical quality requirements. The spot size actually increases but does not overpass the pixel size. On the other hand, the MTF quality decreases but still respects the required level at the Nyquist frequency.

This new option still manifests the advantage of a small secondary mirror and the system global dimensions take advantage of the available space since the constraints are tight. Once I reached this design, I decided then to optimize it by considering a larger spectrum. This supplementary parameter led me to the fifth design.

5.2.5. Fifth design - Larger Spectrum

This new optimization process has the goal to take into account the fact that the incoming spectrum is not only a single ray but a bit more complex. In fact, as presented in Figure 5, the spectral emissions of the Io's torus are not simple rays. The spectrum near the baseline wavelength of $172.5\,nm$ is not a ray but actually a doublet (emission doublet of $SIII$) and has to be considered in Code V. Finally, the same FoV is considered.

5.2.5.1. Spectrum

A more detailed evaluation of the incoming light spectrum is established in order to take into account the fact that it is not simply a single emission ray.

As presented in Figure 121 (right), the considered spectrum consists in an emission doublet approximately centred around the baseline wavelength of $172.5\,nm$. As I mentioned before, a potential bandpass filter centred on $172.5\,nm$ was proposed in order to select the desired part of the spectrum.

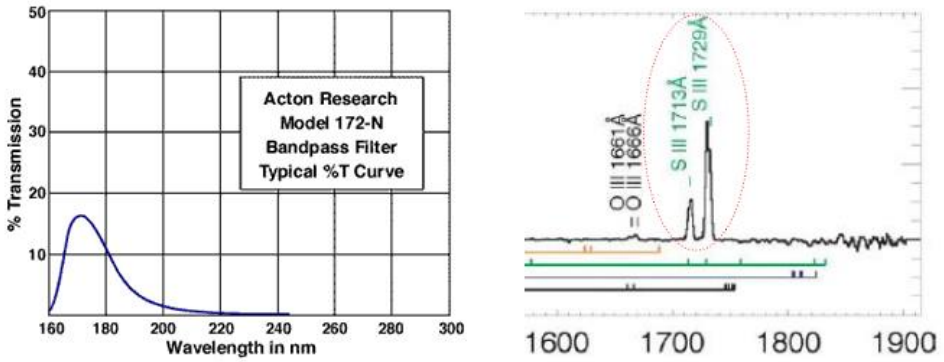

Figure 121 - *Left:* Princeton filter (Princeton Instruments). *Right:* considered spectrum (Adapted from (Salvador, 2012))

With these data, I use the Matlab software to get the spectrum that enters the telescope aperture through the filter. The multiplication of these two curves thus gives the total spectrum to be entered into Code V (Figure 122).

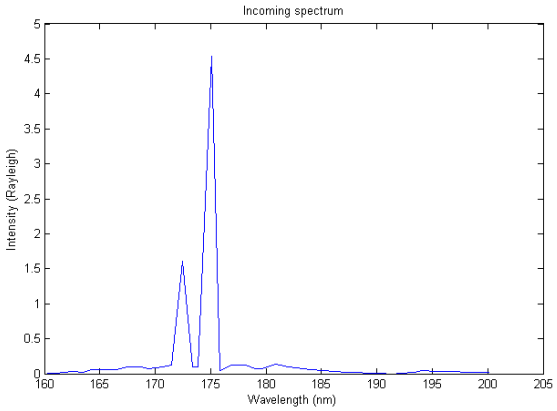

Figure 122 - Incoming spectrum

Actually, in case of an exact calculation, I should also consider the detector response to take into account its sensitivity curve. Since no detector has been imposed yet, I cannot perform this task.

Once I have this entrance spectrum, I can use the $Spectral\ Analysis$ (SPE) option of Code V under $Analysis \rightarrow System \rightarrow Spectral\ Analysis$ in order to set the right weight to each wavelength. This option analyses the input spectral curve (the one obtained with Matlab) and generates in output the right weight for each wavelength. As it is shown in Figure 123, I have to enter the wavelengths and their respective intensity (with the help of the Matlab curve).

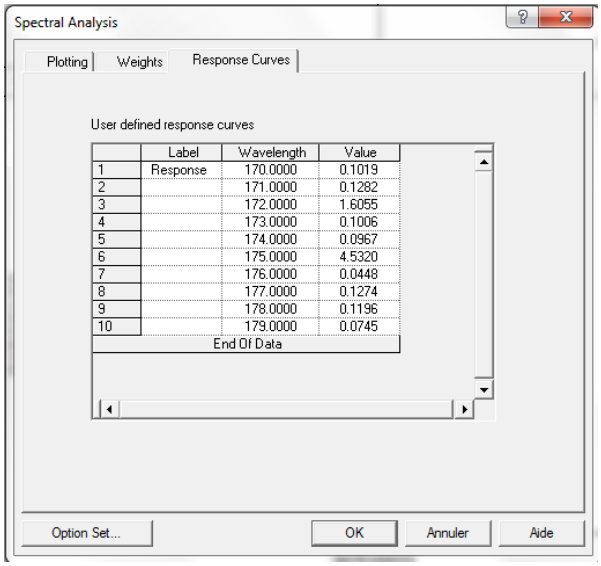

Figure 123 - Spectral analysis Code V option

Once this task is done, Code V shows the spectral response in Figure 124, and replaces the previously entered weights by the ones it obtains.

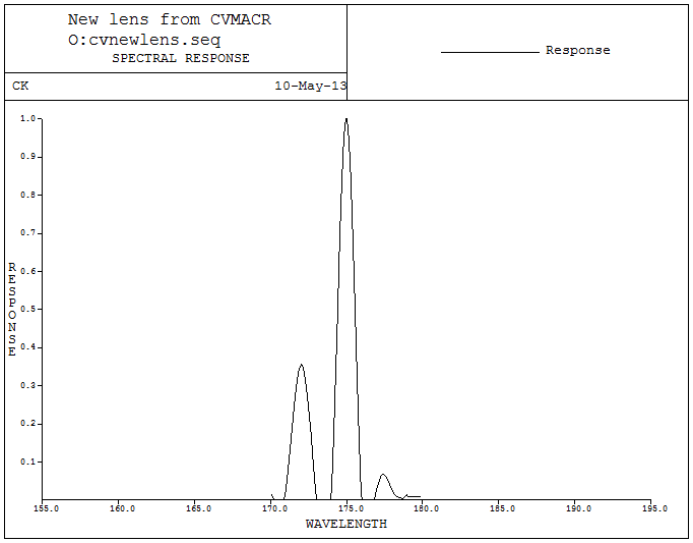

Figure 124 - Code V calculated spectral response

5.2.5.2. Optimization process

This new optimization process has thus the goal of re-optimizing the previous design while taking into account more precisely the incoming light spectrum. The same constrains are still used here.

Results

The new dimensions of the system are presented in the table below:

Surface #	Surface Name	Surface Type	Y Radius	Thickness	Glass	Refract Mode	Y Semi-Aperture
Object		Sphere	Infinity	Infinity		Refract	
1	Obscuration	Sphere	Infinity	90.0000		Refract	40.0000
Stop	Primary_mirror	Conic	-231.9222 V	-80.0000 V		Reflect	40.0000
3	Secondary_mirror	Conic	-100.0000 V	128.0000 V		Reflect	12.9010
Image		Sphere	Infinity	0.0000		Refract	2.5536
End Of Data							

Table 19 - Dimensions of the fifth design in *mm*

The system is not really different. This can be understood by thinking to the reflective nature of the optical system. Since I only use mirrors (lenses would be ineffective in the UV spectrum), the reflective law is the same for each wavelength and the system is supposed to react in the same way for each[36]. If I had been in charge of designing a camera with lenses which is supposed to image in the visible spectrum, this spectrum change would have led to significant system modifications since the refractive $Snell\text{-}Descartes$ law depends on the selected wavelength.

Moreover, the selected filter has its most significant response centred on the baseline wavelength that I previously introduced into Code V as well as the emission doublet so the largest weights, as presented in Figure 125, are still located around the baseline wavelength of $172.5\ \mathrm{nm}$.

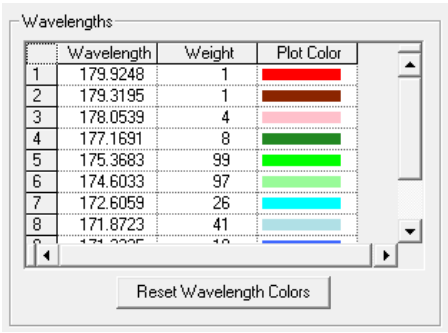

Figure 125 - Wavelength weights

Therefore, all the dimensions' characteristics of the previous design, like a small secondary mirror, are maintained.

[36] As long as no particular coating is considered, which is the case here. Further analyses should take into account the coatings introduced earlier.

Hereafter are shown some $2D$ and $3D$ views of this new telescope.

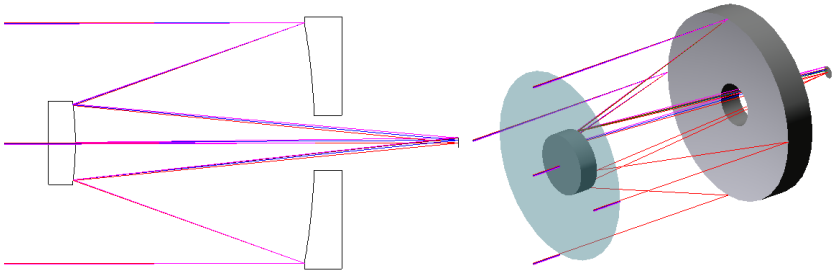

Figure 126 - *2D* and *3D* views of the fifth design

5.2.5.3. Image quality analysis

With this new entered spectrum and optimized system, I then have to check if all the optical requirements are fulfilled. The same tools as before are used and they are presented below.

Spot diagram

The spot diagram of this fifth design is presented below.

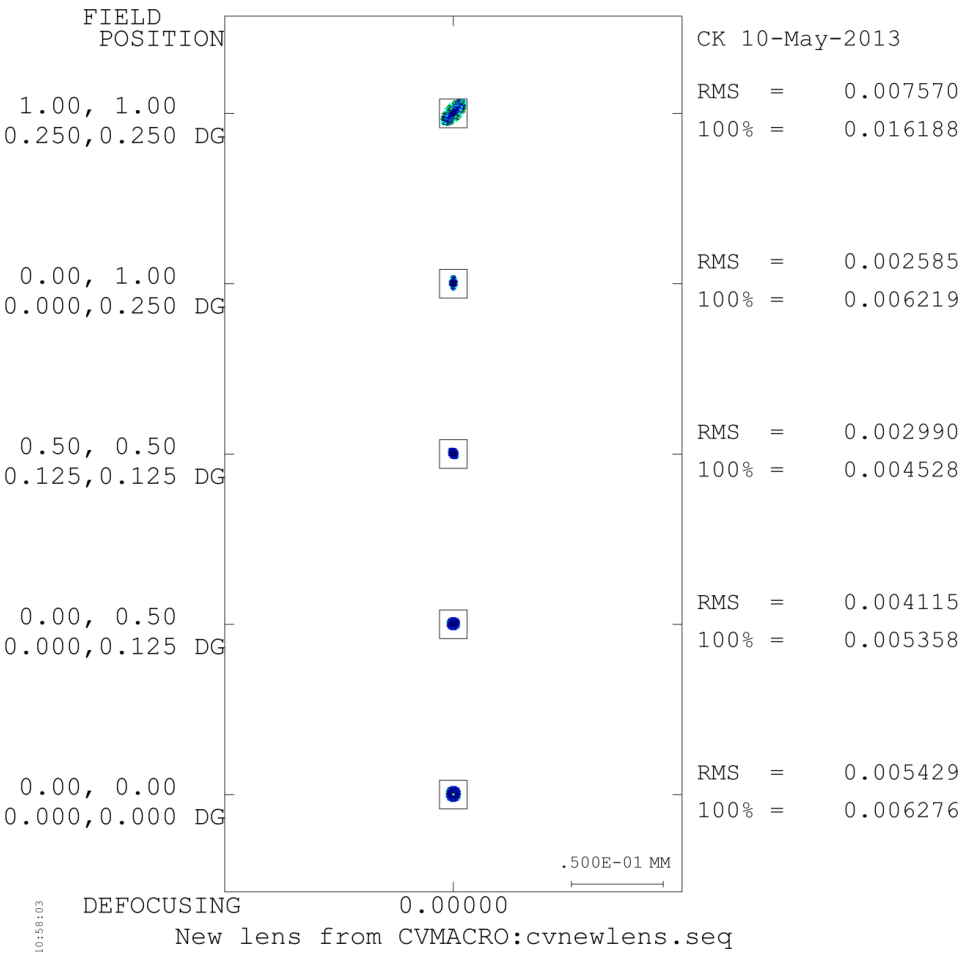

Figure 127 - Spot diagram of the fifth design

Several colours now appear in the spot diagram meaning that different wavelengths are considered and plotted by the software. The different coloured patterns appear quite close to each other and centred inside the previous design spot. Therefore, as we can see on the right of the figure, the RMS and 100% spot sizes of the spot are not different from those of the previous designs.

We can then conclude that this new optimized system can be accepted with respect to the spot diagram criterion.

Ray aberration curves

Once the spot diagram criterion is passed, its ray aberration curves can be analyzed. The figure that Code V produces is shown in Figure 128.

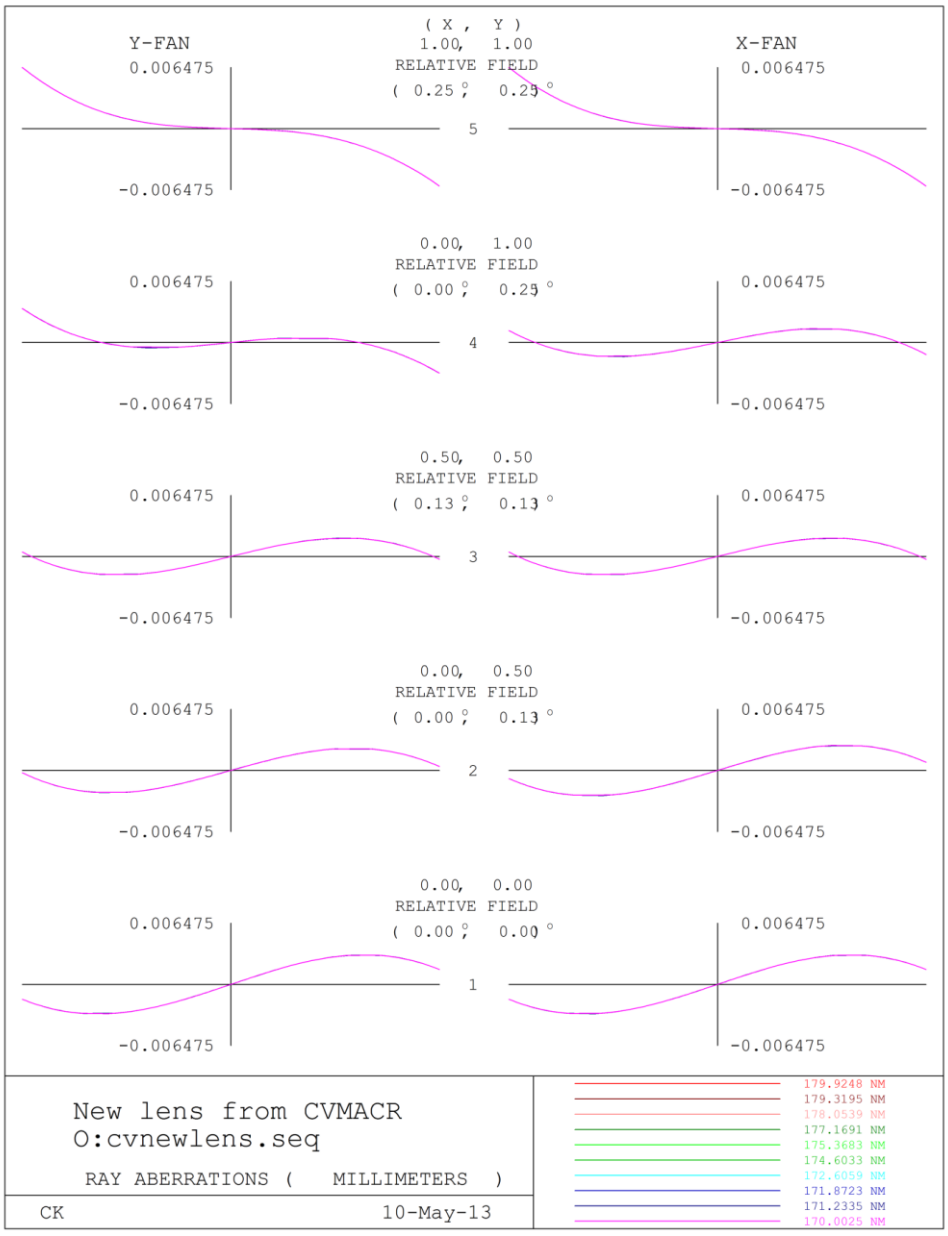

Figure 128 - Ray trace curve of the fifth design

The same curves as before are still observed and the same aberrations, that is, spherical aberration, astigmatism and field curvature, are predominant. Finally all the curves are confused since no chromatic aberration is present in the system.

Modulation Transfer Function

The optical MTF of the system can now be evaluated.

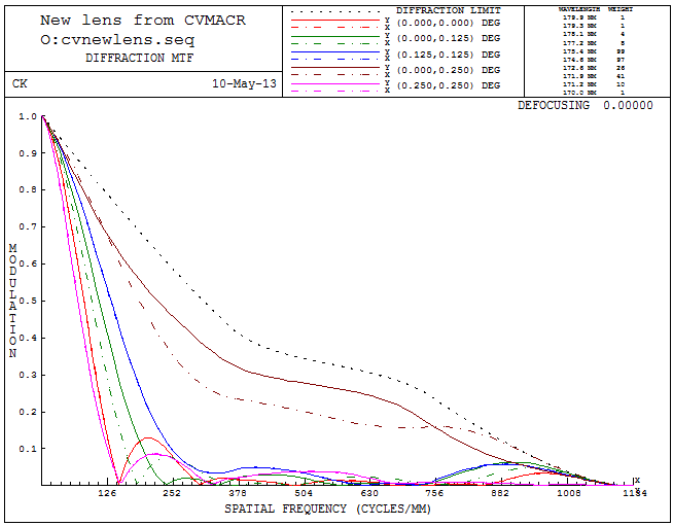

Figure 129 - Optical *MTF* of the fifth design

I then execute the same Matlab analysis as before to check if this system respects the MTF requirement when taking into account the detector's MTF. The results are presented in Figure 130.

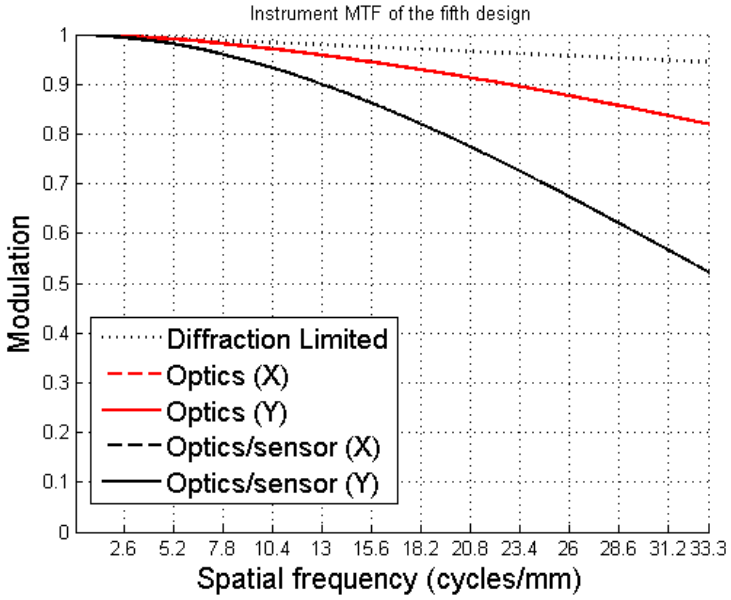

Figure 130 - Instrument *MTF* of the fifth design

We can observe that this system is still acceptable even if the MTF seems to be really degraded. Indeed, the MTF is greater than 10% at the Nyquist frequency. I thus obtain a

system which is still able to image the entire Io's torus while considering a more realistic spectrum.

Encircled energy

The last Code V tool that I use is the radial energy analysis.

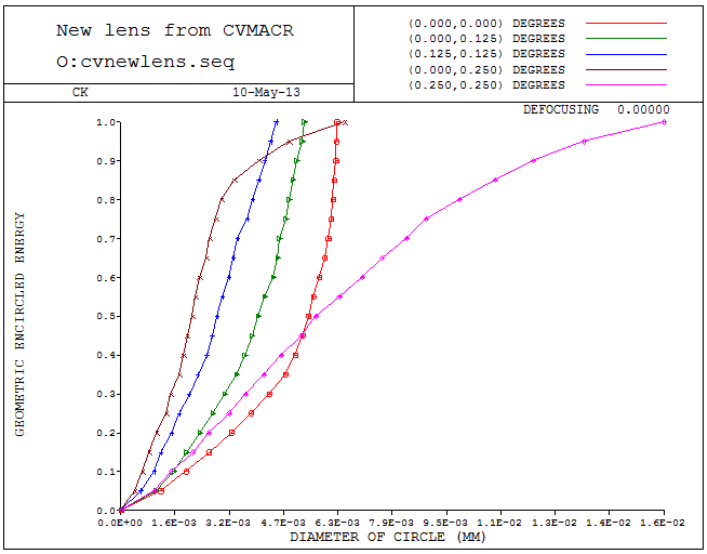

Figure 131 - Radial energy analysis of the fifth design

As the spot size increases, the energy concentration over the spot decreases since a larger circle is needed to contain a given energy quantity. Therefore, the field curves that are represented in the figure are much more flattened than those of the first designs the spots of which are extremely small. 80% of the energy is situated inside a circle of an approximate diameter of $11\ \mu m$.

5.2.5.4. Tolerancing

Since I have an optical system that fulfils all the requirements and overcomes the previous encountered problems, I can finally perform the system tolerancing.

This study imposes little changes on the system's dimensions in order to determine its sensitivity to manufacture, alignment and placement errors for example. Once these tiny variations are made, the software calculates the induced spot size changes and stores the results.

Then, it runs again the sequence of instructions to perform the same process a given number of times in order to calculate a Gaussian distribution for the spot diameter. The results are presented in the form of tables which show the probabilistic values of the spot.

The simplest way to use the tolerancing option of Code V consists in writing a $Macro$ file which is made of sequences of operations that Code V executes[37]. The $Macro$ file that I prepared is presented in Appendix C. It is constituted by two tolerances' categories: the first is the fabrication tolerances while the second concerns the alignment tolerances. These first ones take into account the manufacturing errors that are made by the company that fabricates the mirrors while the second class accounts for mirrors' placement errors done by the assembler.

The compensators are also defined in this $macro$ file. These are the parameters that are modified after assembling to compensate for the manufacture and assembling errors. In this case, as it is often done, I chose the backfocus variable as the only compensator of the system (Fischer, Tadic-Galeb, & Yoder, 2008). This means that, when the telescope will be assembled, the only parameter still variable is the distance between the detector and the secondary mirror. Indeed, this is the easiest way to do as the detector plane can often be adjusted mechanically in order to refocus the system.

An error function must be mentioned to Code V during tolerancing. Actually, it is quite the same functioning as the $Automatic\ Design$ procedure: Code V tries to minimize the error function to determine the value that will have to be applied to the compensators. For this project, I decided to choose the RMS spot diameter. This means that Code V tries to keep the image spot as small as possible when fixing the compensators' values. This is intended to always keep a spot that fulfils the mission requirements (Mazzoli & Kintziger, 2013, March 28).

What I tried to do was to begin with really tight values not to sorely degrade the design and then increase them to identify the most sensitive ones. Afterwards I could release step by step all the tolerances by given quantities: the most sensitive parameters had to be changed by small increments whereas the others could bear greater variations (Fischer, Tadic-Galeb, & Yoder, 2008).

Once the increments were done, I had to enter into the $Command\ Window$ the command "$in\ tol$" in order to run again the tolerancing $Macro$ and Code V performed the analysis once more. The most sensitive parameters revealed to be the primary mirror's conic constant and the X and Y mirrors' displacements. Of course, the $Z\text{-}tilt$, which means rotating the system around the Z-axis, is an insensitive parameter since the system is rotationally symmetric around this axis. Hereafter the results are presented.

[37] Actually, all the design, analyses and other options of Code V can be done and used with the help of such files. This method is extremely fast as the only thing to do, once the user is used to Code V commands and know them by heart, is to write a text file in which the commands are written, then load it into the $Command\ window$ of Code V and press enter. The system and the analyses are then immediately performed. As the user employs the interface mode of Code V, he can checks which commands Code V executes in the $Command\ window$ and learn them in order to later use the software with the help of $Macro$ files and go faster.

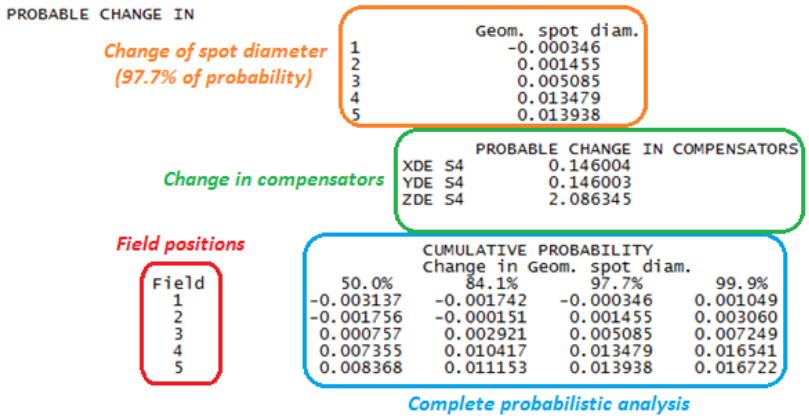

Table 20 - Tolerancing results of the fifth design in *mm*

What Code V shows is actually first the geometrical spot diameter RMS change that can be expected within 97.7% of all cases for all field positions (from 1 to 5). Then, Code V displays the variations in compensators that have to be applied[38]. And finally, the complete probabilistic changes in the RMS geometrical spot diameter can be found in the last text file section. These results are listed from 1 to 5, the five field positions.

The predicted spot size changes by Code V are really important since the largest, in the corner of the detector $(1,1)$, rises to $13.938\ \mu m$. Such variations cannot be accepted since the resolution criterion states that the spot diameter must be included in a single $15\ \mu m$ pixel. Indeed, the largest spot size of this design is $7.57\ \mu m\ RMS$ for the same field position. Thus, the predicted spot size at this field is approximately: $7.57\ \mu m + 13.938\ \mu m = 21.508\ \mu m\ RMS$.

This cannot be accepted and actually this design is not efficient enough. I therefore had to change something in the optimization process to overcome this problem. If we wanted this telescope to be manufactured and to work properly with a high probability, this would be extremely expensive since the tolerances would be really tight. In addition, actual technologies might not achieve the desired level of precision.

5.2.5.5. Squared primary mirror

Since this design is not acceptable, there is no need to investigate a squared primary mirror alternative.

5.2.5.6. Conclusion

What I learned from this design is that even if all the optical requirements are verified , this time the system is too sensitive with respect to manufacture tolerances.

[38] XDE, YDE and ZDE stand for the X, Y and Z coordinates of the detector and S_4 means that it is the 4^{th} surface of the optical system.

Fabricating such a system would induce extremely high costs since the tolerances that have to be respected are too tight.

Since the Cubesat platform's main goal is to propose a low-cost alternative to usual space missions, this problem cannot be neglected. I had to find a design that can be manufactured at reasonable cost, therefore the fabrication tolerances have to be looser.

Therefore I relaxed once more my constraints. The only one on which I could still act was the backfocus. The limit I have to respect is $13\ cm$ so this is the value I then input in Code V. This led me to the sixth design.

5.2.6. Sixth design - Better tolerancing

This new design aims to reach a less sensitive optical system to fabricate it at lower costs and therefore respect the Cubesat philosophy.

The same FoV and field positions are entered in Code V. The enlarged spectrum is also considered through this optimization process.

5.2.6.1. Optimization process

To perform this new optimization process, I thus change the backfocus constrain which is now equal to the maximum value imposed: $130\ mm.$.

Constraints

In Table 21 the set of constrains is presented.

Variable	Value
Focal length	$413\ mm$
Primary-secondary distance	$< 8\ cm$
Backfocus	$< 130\ mm$
Primary conic constant	< -1
Secondary conic constant	< -1
Primary conic constant	> -5
Secondary conic constant	> -5
Primary mirror's radius of curvature	$> 100\ mm$
Secondary mirror's radius of curvature	$> 100\ mm$

Table 21 - Optimization constraints of the sixth design

Results

The dimensions of this sixth design are presented in Table 22

Surface #	Surface Name	Surface Type	Y Radius	Thickness	Glass	Refract Mode	Y Semi-Aperture
Object		Sphere	Infinity	Infinity		Refract	
1	Obscuration	Sphere	Infinity	90.0000		Refract	40.0000
Stop	Primary_mirror	Conic	-233.5238 V	-80.0000 V		Reflect	40.0000
3	Secondary_mirror	Conic	-102.5031 V	130.0000 V		Reflect	13.0921
Image		Sphere	Infinity	0.0000		Refract	2.5533
End Of Data							

Table 22 - Dimensions of the sixth design in *mm*

Code V takes advantage of this new constraint as it pushes the detector further from the secondary mirror. Then, the mirrors are separated as far as possible as the interdistance constraint is tight. Of course, the radii of curvature and conic constant constraints are fulfilled.

Since the secondary mirror's diameter is only $13.09\ mm$, the part of the primary mirror which suffers from obscuration is approximately equal to 10.71%. As these numbers cannot be easily interpreted, if we consider the SNR Matlab code presented before, this obscuration reduction induces a shortening of the observation time of approximately $1\ min$. This is a substantial amelioration since the accesses to the Io's torus, as presented with the help of STK, typically last in the best case $35\ min$ and that every minute is worth to be saved for security.

Figure 132 presents $2D$ and $3D$ models of the new optical system.

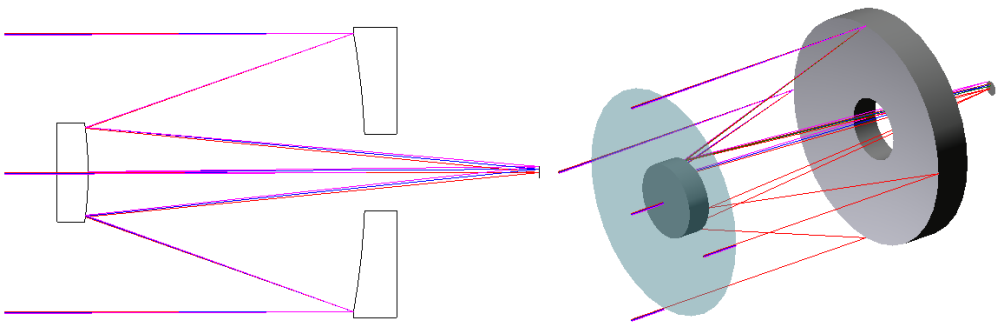

Figure 132 - *2D* and *3D* views of the sixth design

5.2.6.2. Image quality analysis

Spot diagram

The spot diagram of the telescope is presented in Figure 133. We can immediately see that RMS spot sizes are well under the $15\ \mu m$ requirement. Different colours still appear since several wavelengths are taken into account.

The maximum observed spot size appears in the corner of the detector $(1,1)$ and is equal to $7.82\ \mu m$ whereas the smallest one is the $(0.5,0.5)$ field's spot which is equal to

$1.62\ \mu m$. As said before, the different coloured patterns are mixed or very close to each other so the enlarged spectrum does not really affects the spot size.

One could think that I could enlarge the FoV much more than $0.25°$ and re-optimize the system since the spot size is really small. However, I have to keep in mind that errors that widen the spot have still to be taken into account. For example, I already showed the tolerancing problem which yielded to a low-performance fifth design. Then, the environmental changes, like temperature variations, also impact the optical performance of the telescope since optical degradations are due to material thermal expansion.

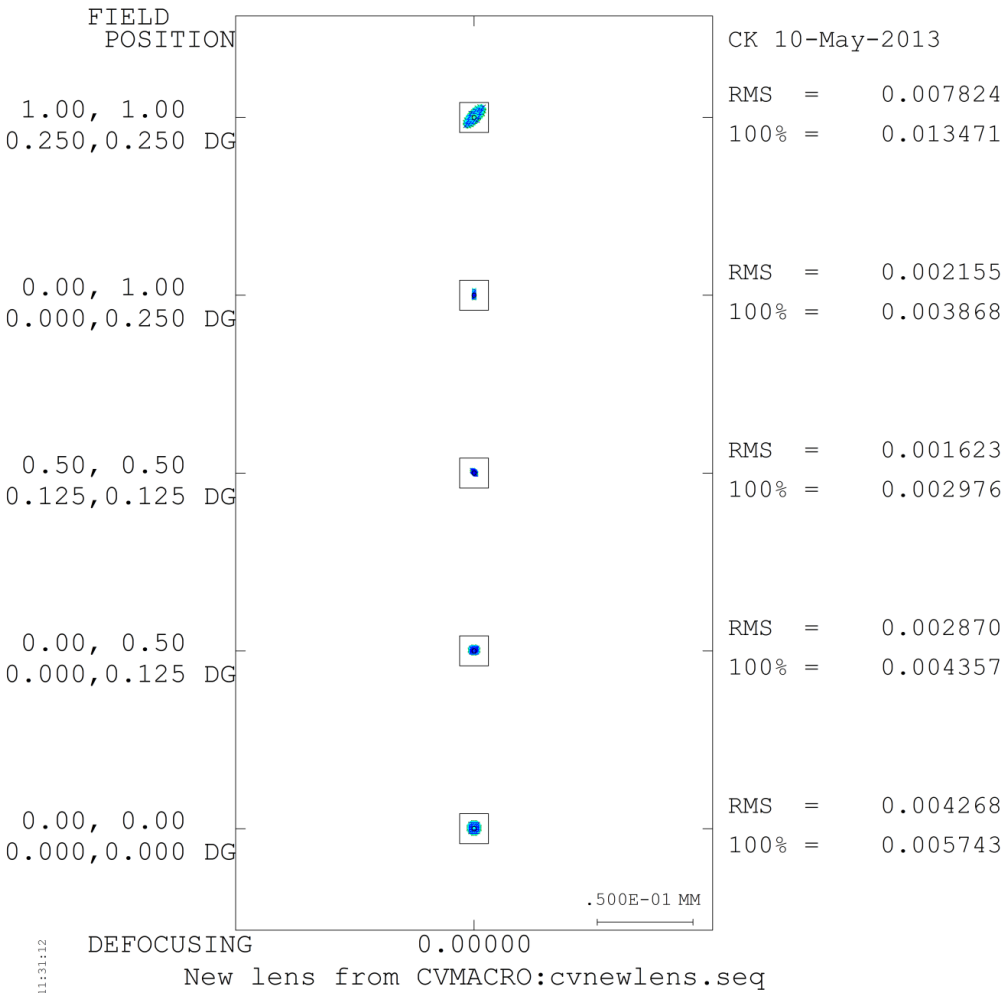

Figure 133 - Spot diagram of the sixth design

Ray aberration curves

The ray aberration curves of this sixth design are shown in Figure 134. In opposition to the fifth design where spherical aberration was observed, this new optical design's aberrations seem to be dominated by astigmatism. Indeed, the represented curves take the form of a straight line.

Finally, all the wavelength curves in Figure 134 are superimposed to each other as for the previous design since no chromatic aberration is caused by reflective surfaces.

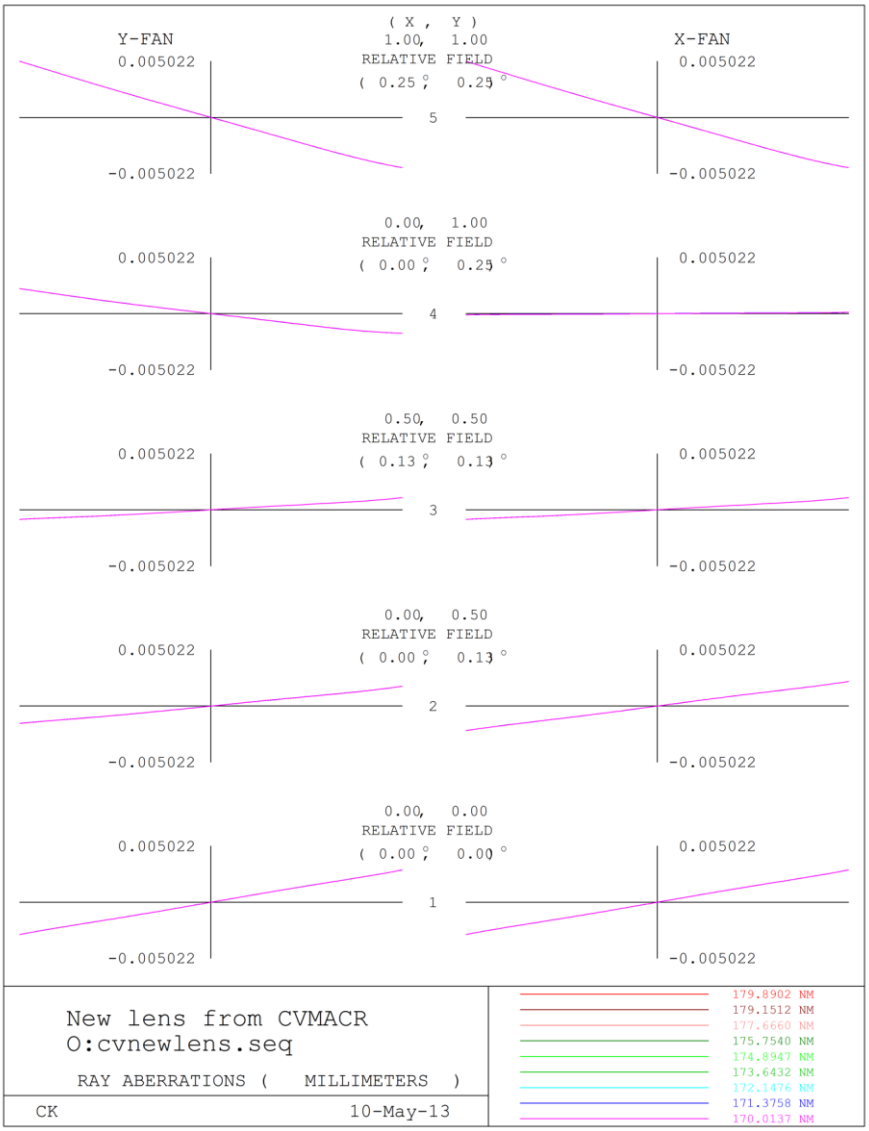

Figure 134 - Ray trace curve of the sixth design

This observation is corroborated by the aberration analysis, that is presented in Table 23. As we can see, the major aberrations that are present in the system are astigmatism and field curvature while other aberrations are really weak.

THO SO..I

New lens from CVMACRO:cvnewlens.seq
Position 1, Wavelength = 174.9 NM

	SA	TCO	TAS	SAS	PTZ
1	0.000000	0.000000	0.000000	0.000000	0.000000
STO	-2.075566	0.224318	-0.005387	0.000000	0.008564
	2.228569	0.000000	0.000000	0.000000	
3	0.771233	-0.115695	-0.000352	-0.004208	-0.019512
	-0.924685	-0.108738	-0.004262	-0.001421	
SUM	-0.000449	-0.000116	-0.010001	-0.005629	-0.010947

Table 23 - Aberration analysis of the sixth design

What we can think is that the constraints that I input in order to obtain the fifth design were fairly too strict that Code V did not manage to annihilate the spherical aberration.

Modulation Transfer Function

Hereafter the Code V optical MTF analysis is presented.

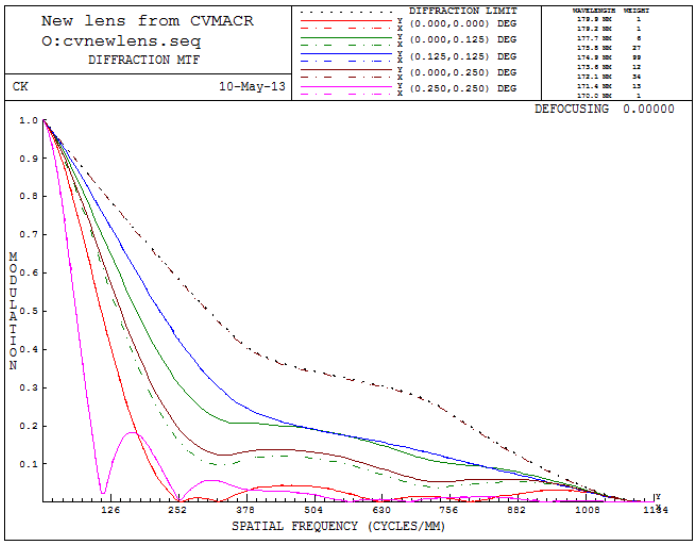

Figure 135 - Optical *MTF* of the sixth design

The obscuration effect can still be observed as it really deforms the original diffraction limit straight line into a curved figure. The line corresponding to the corner field position (1,1) is still the worst. The complete MTF is illustrated in Figure 136.

The MTF value at Nyquist frequency is well above the 10% requirement and this new design respects this second requirement.

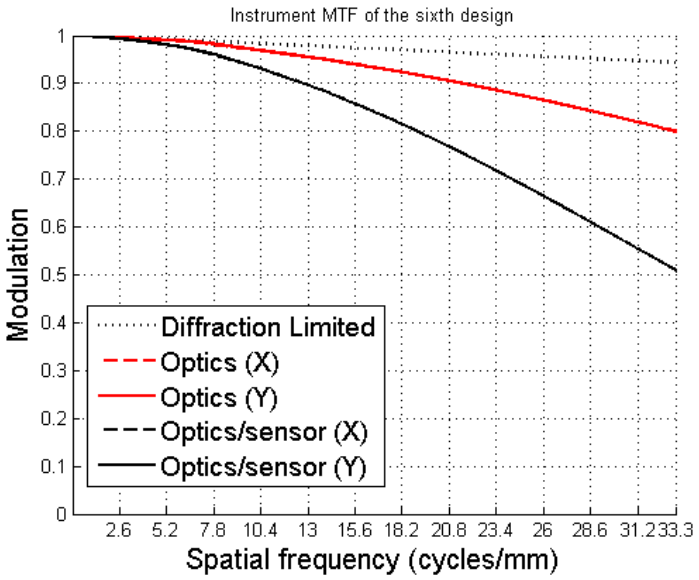

Figure 136 - Instrument *MTF* of the sixth design

Encircled energy

In Figure 137 the corner field position (1,1) has a less tilted curve than the other ones. It means that this is the field position which induces the major spot enlargement.

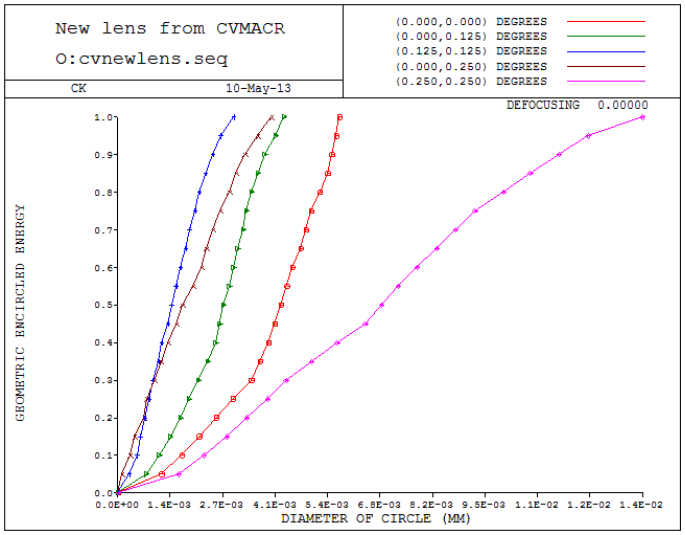

Figure 137 - Radial energy analysis of the sixth design

We can therefore see that 80% of the total spot energy is located into a circle of which diameter approaches $9.5\ \mu m$.

5.2.6.3. Tolerancing

I check here if the new optical system is less sensitive than the previous one. In fact, if tight tolerances must be respected, the system cost increases and can even be infeasible. That was the case of the previous design and it had to be aborted. The new tolerance results are shown in Table 24.

PROBABLE CHANGE IN

	Geom. spot diam.
1	0.006806
2	0.007791
3	0.009741
4	0.008722
5	0.004850

PROBABLE CHANGE IN COMPENSATORS

XDE S4	0.145224
YDE S4	0.145223
ZDE S4	2.084129

CUMULATIVE PROBABILITY
Change in Geom. spot diam.

Field	50.0%	84.1%	97.7%	99.9%
1	0.003251	0.005029	0.006806	0.008584
2	0.004080	0.005935	0.007791	0.009647
3	0.005520	0.007631	0.009741	0.011852
4	0.004905	0.006814	0.008722	0.010630
5	0.001948	0.003399	0.004850	0.006301

Table 24 - Tolerancing results of the sixth design in *mm*

The spot size increase is quite uniformly split between the different field points. Whereas the previous design corner field spot size increase was approximately $13\ \mu m$, it is only now

$4.85\ \mu m$. Since this field is the most problematic it consists in a great improvement. Even if the spot size enlargement at other field positions is greater than before, the initial spot dimensions are so tiny at these positions that this does not really become a problem. In Table 25 the probabilistic size spots are listed for each field positions when taking into account the tolerances.

Field position	Initial RMS spot size (μm)	Spot size change (μm)	Total spot size (μm)
Field 1 (0,0)	4.268	6.806	11.074
Field 2 (0,0.5)	2.870	7.791	10.661
Field 3 (0.5,0.5)	1.623	9.741	11.364
Field 4 (0,1)	2.155	8.722	10.877
Field 5 (1,1)	7.824	4.850	12.674

Table 25 - Probabilistic spot sizes with tolerances in *μm*

These new spot values are still in accordance with the spot size requirements. Therefore, even if quite loose tolerances are applied to the system, the spot sizes are still acceptable. The relaxed constraints thus permit to reach a system that fulfils all the optical performance requirements with acceptable fabrication tolerances.

5.2.6.4. Environmental change analysis

Since I eventually have an optical system that fulfils all the requirements and manufacture conditions, I can now perform an environmental change analysis with Code V. It intends to predict spot size variations due to environmental changes.

In fact, temperature deviations cause thermal expansion of the Cubesat and mirror materials and therefore deform the structure. This can induce optical degradations since the optical surfaces do not exhibit the expected shape and has to be taken into account.

The $Environmental\ Change$ option of Code V consists in reconfiguring the $System\ Data$ parameters by new user-specified values and calculating the deformations of the surfaces to predict spot size changes.

As explained before, this option actually does not make any analysis but only imposes dimension changes and the user has then to run the desired analysis tools (such as the $Spot\ diagram$) on his own to visualize the optical degradations (Synopsys, Code V Reference Manual, 2012).

A sequence is run with a different entered temperature at each time and then the induced spot size change is calculated at each field position. The temperature increment chosen is equal to $20°C$. I also have to mention to the software that mirrors are made of aluminium because it is light and common in UV spatial applications (Fischer, Tadic-Galeb, & Yoder, 2008). The tables below lists the results of these operations.

Field position	Initial spot size (20°)	Spot size variation ($D_{final} - D_{initial}$)		
		40°	**60°**	**80°**
Field 1 (0,0)	4.268	1.979	3.957	5.936
Field 2 (0,0.5)	2.870	1.964	3.936	5.910
Field 3 (0.5,0.5)	1.623	1.859	3.803	5.767
Field 4 (0,1)	2.155	−0.462	0.838	2.626
Field 5 (1,1)	7.824	−1.749	−3.308	−4.408

Table 26 - Environmental spot size variations in *µm* (*increasing temperatures*)

Field position	Initial spot size (20°)	Spot size variation ($D_{final} - D_{initial}$)		
		0°	**−20°**	**−40°**
Field 1 (0,0)	4.268	−1.979	−3.95	−2.599
Field 2 (0,0.5)	2.870	−1.915	−1.687	0.279
Field 3 (0.5,0.5)	1.623	−0.638	1.050	2.975
Field 4 (0,1)	2.155	1.622	3.476	5.449
Field 5 (1,1)	7.824	1.836	3.718	5.627

Table 27 - Environmental spot size variations in *µm* (*decreasing temperatures*)

Some field position spot sizes increase while others decrease for the same temperature change. With the help of these data, I can therefore add these thermal spot size variations to the tolerancing changes to obtain a total spot size. The total spot size variations due to temperature changes and tolerances are shown in Figure 138.

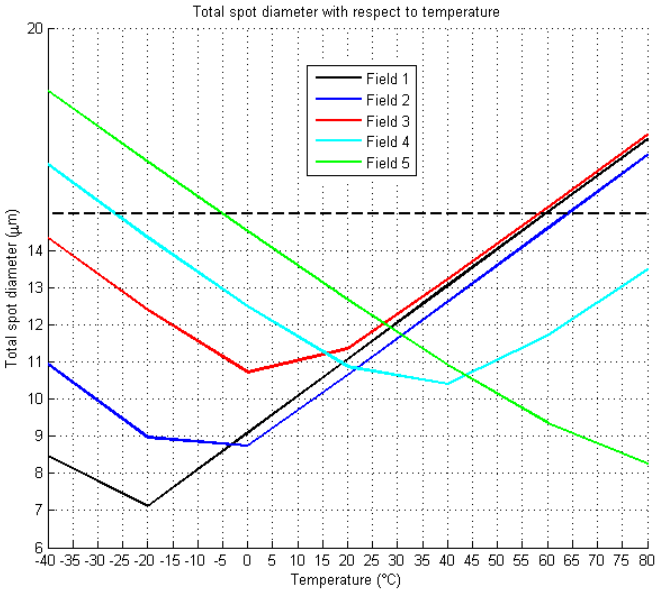

Figure 138 - Total spot diameter with respect to temperature in *µm*

We can approximate the temperature range within which the spot size requirement is fulfilled. Indeed, a dashed line represents the upper limit of the spot diameter. By doing so, the lower and upper values are thus respectively approximately $-5°C$ and $58°C$. The allowed temperature variations are then from $-25°$ to $+38°$.

The temperature range is quite narrow since generally, on Cubesat platforms, passive techniques are used to reduce costs and save place and thus large temperature variations are often undergone by the Cubesat.

A complete thermal analysis shall be done to determine the exact thermal environment of the Cubesat and the temperature range that it will undergo.

5.2.6.5. Jitter induced image degradation

Another disturbance which induces image degradation and can be taken into account is $jitter$. Jitter is the line-of-sight (LOS) movements due to vibrations inside the spacecraft structure. These vibrations induce an image blurring that must be controlled in order to get images satisfying the required optical quality. One way to do it is to implement a $jitter\ MTF$ that is multiplied to the previous instrument (optical system + detector) MTF.

Although different sources of vibrations exist, they can all be taken into account within a single equation (Genberg, Michels, & Doyle) (Tantalo, 1996):

$$MTF_{jitter}(f) = e^{-2\pi^2\sigma^2 f^2}$$

where

- σ^2 is the LOS jitter variance from all sources (often expresses in μrad)
- f the spatial frequency

Jitter noise measures are actually needed. For example the team responsible for the ExoplanetSat project did measures to assess the jitter noise reduction which was actually the preponderant and most problematic source of noise (Pong, Lim, Smith, Miller, Villaseñor, & Seager, 2010). The jitter noise due to the ADCS (MAI-200) was equal to $53\ arcsec \approx 256\ \mu rad$ and was reduced to $1.8\ arcsec \approx 8.72\ \mu rad$ with the piezo electric stage. This is also the jitter performance predicted for the Proba-2 spacecraft's ADCS (Mazy, Lecat, & Defise, 2003). Typical jitter values of space based platforms range from 20 to $60\ \mu rad$ (Tantalo, 1996) but since a Cubesat is considered, the values in this case may be much higher (as seen with the MAI-200 case).

In order to analyze jitter in a proper way, a $Finite\ Element\ Analysis\ (FEA)$ shall be carried out. It takes into account the vibration modes of the spacecraft and determines properly the jitter variance (σ^2) (Genberg, Michels, & Doyle). This can be carried out for Cassegrain telescopes and specific softwares were designed to reach this goal (for example $SigFit$). As the integration time increases, more frequencies contribute to the LOS jitter and the image degrades (Genberg, Michels, & Doyle).

Because no precise value of jitter is available in our case, I decided to plot the total MTF until it reached the minimum required. Then the maximum respective jitter noise value could be found. The results I obtain for this design are presented in Figure 139. The jitter

degradation has to be taken into account since the MTF curves are well lower than before. The maximum jitter noise variance that can be supported by the system is approximately $70\ \mu rad \approx 14.44\ arcsec$. This is not really high and jitter could be a problem since Cubesats' ADCS are not as efficient as those of larger spacecrafts. The $XACT$ from $Blue\ Canyon\ Technologies$ is said to be "low jitter" (BlueCanyonTechnologies) but actually no real value is cited[39]. More investigations shall be done to know exactly if this Cubesat will be subject to jitter or not with the help of a FEA.

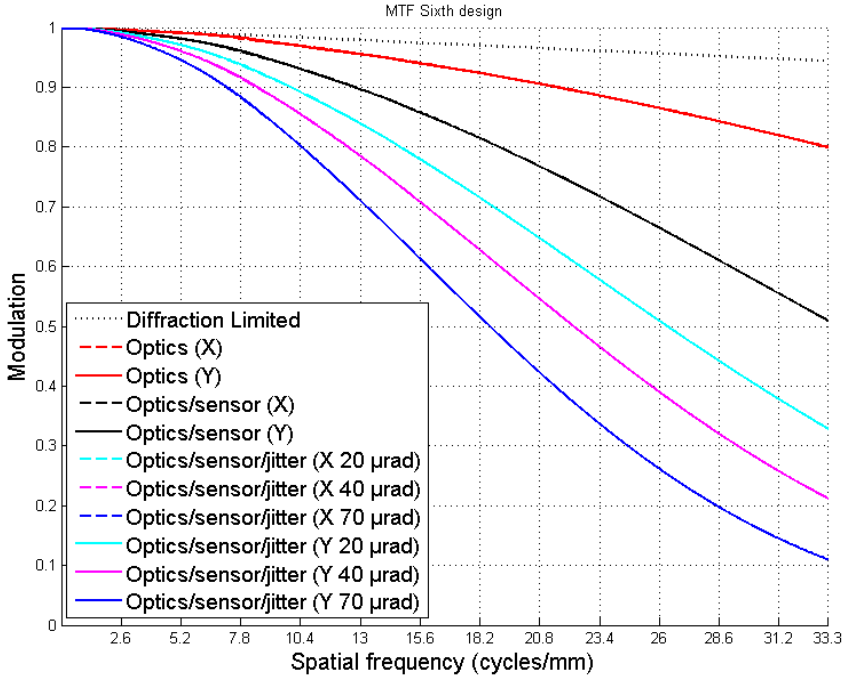

Figure 139 - Instrument *MTF* of the sixth design when taking into account jitter

5.2.6.6. Squared primary mirror

To conclude, I eventually change the shape of the primary mirror to check if all the previous analyses remain valid. I therefore perform exactly the same optimization process after having applied this modification to the initial system. The new characteristics of the telescope are presented below.

System Data... | Surface Properties...

Surface #	Surface Name	Surface Type	Y Radius	Thickness	Glass	Refract Mode	Y Semi-Aperture
Object		Sphere	Infinity	Infinity		Refract	
1	Obscuration	Sphere	Infinity	90.0000		Refract	40.0000
Stop	Primary_mirror	Conic	-233.5238 V	-80.0000 V		Reflect	40.0000
3	Secondary_mirror	Conic	-102.5031 V	130.0000 V		Reflect	13.0921
Image		Sphere	Infinity	0.0000		Refract	2.5533
End Of Data							

Table 28 - Dimensions of the sixth design with a squared primary mirror in *mm*

[39] This is for sure the same problem as knowing the exact pointing accuracy of an ADCS since it depends on the Cubesat's configuration.

By doing so, the initial system characteristics are saved and all the previous statements are still effective. In Figure 140 this last design's $2D$ and $3D$ representations are presented.

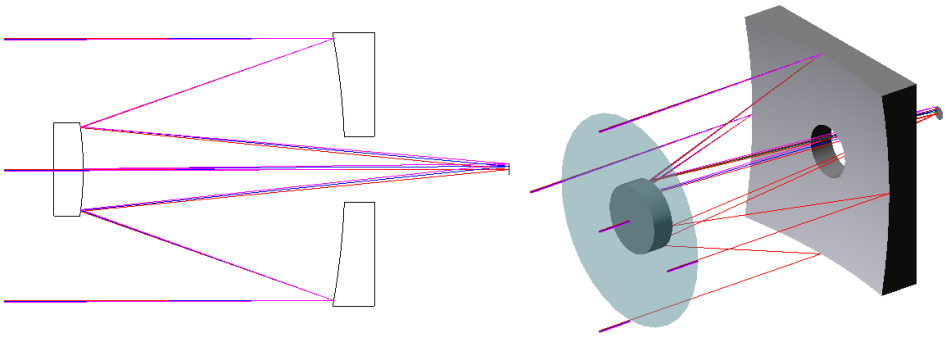

Figure 140 - *2D* and *3D* views of the sixth design with a squared primary

Image quality analysis

They all remain valid so they are not exposed here.

5.2.6.7. Conclusion

This sixth design was aimed to obtain a less sensitive system with respect to tolerances.

New available space allows Code V to reach a design that is more robust with respect to manufacture errors. In fact, even if the spot diameter variations seem to be greater than before, they are actually distributed through the field positions in such a way that they are acceptable. Indeed, smallest field spot sizes are associated to largest spot size changes and the total spot is at each time smaller than the requirement.

A jitter MTF analysis was also performed. The conclusion is that jitter noise can lead to serious image degradation and that it has to be controlled in order to fulfil the optical quality specifications. Yet detailed finite element analyses must be carried out to assess this degradation.

This final design satisfies our requirements and is thus able to image the entire Io's torus during the whole mission duration. A large enough field is available to be sure that the target is always visible despite the attitude pointing errors induced with the supplied ADCS. The entire spectrum of interest is taken into account and tolerancing is passed.

In Figure 141 are presented the radii of curvature, conic constants and diameters of this last design when compared to typical real values. These are real mission payloads' characteristics that drove the elaboration of the constraints on radius of curvature and conic constants for the fifth design.

The mirrors of the sixth design are also represented. The primary mirror belongs to the neighbourhood of the other mirrors but the secondary mirror is quite outside of it. It may be quite expensive and further investigations are needed to answer this question.

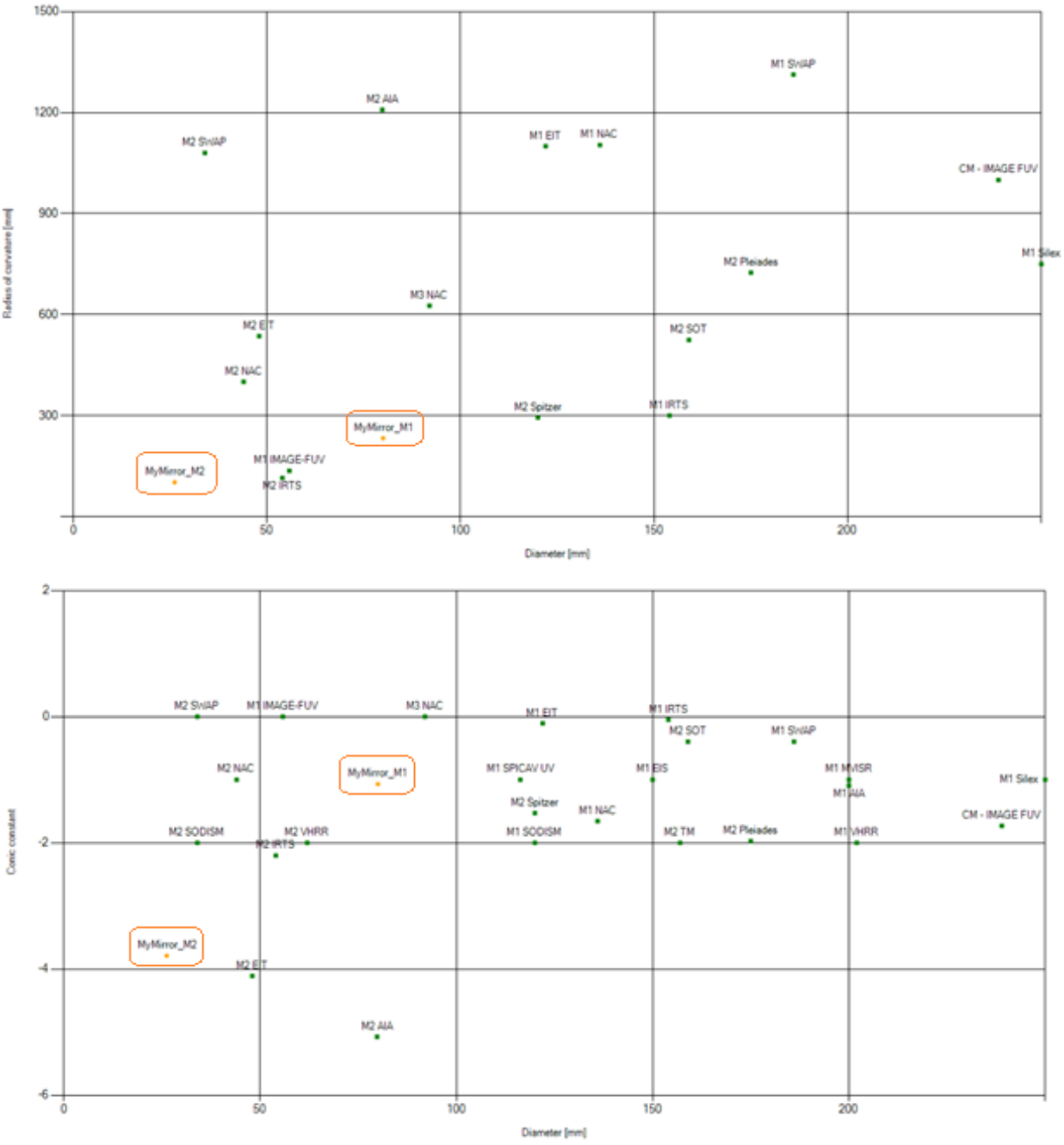

Figure 141 - Radii of curvature *(Top)* and conic constants *(bottom)* of the last design and real missions (© CSL)

5.3. *CAD* models

Once I obtained a satisfying optical design, I decided to incorporate it inside a real Cubesat structure to investigate the mechanical configuration. What I did was to first use a $1.5\,U$ Cubesat skeleton structure in order to have the telescope and the proximity electronics in one box. Then this $1.5\,U$ payload could be "plugged" to another $1.5\,U$ entirely dedicated to the other satellite systems like the ADCS and EPS. The result thus forms a classical $3U$ Cubesat structure while being modular and flexible

I consulted the available CAD models from Pumpkin and selected the last version of the $1.5\,U$ skeleton platform (Pumpkin, 2013). Once I had the model, I exported that of the telescope from Code V[40].

Once I had these two representations of the structure and the optical system, I had to find a way to attach them to each other. The model draws inspiration from the $OUFTI$-1 configuration: endless screws are placed along the structure to support the electronic cards. In addition, the solution I imagined was to elaborate a fixation that links the primary mirror to the endless screws while the secondary mirror would be fixed to the platform upper plate.

Yet the upper plate increases the obscuration on the primary mirror. This leads to an increase of approximately $30\,sec$ of the observation time and degrades the MTF of the optical system. This has to be taken into account since the MTF requirement could be jeopardized by this disposition.

If we consider thermal variations, the two mirrors undergo dilatations from different parts of the Cubesat: the primary mirror follows the endless screws while the secondary mirror accompanies the upper plate movements. This can lead to non predicted behaviours since the thermal analysis that I performed earlier supposed that both mirrors are actually connected by spacers (Synopsys, Code V Reference Manual, 2012). A thorough analysis is needed to investigate this option.

Another possibility is to use the typical truss structure of Cassegrain telescopes which is shown in Figure 142. This way, the two mirrors are connected to each other and the previous analysis is still relevant. For example NASA studied a deployable truss structure for a Cassegrain telescope onboard a $6\,U$ nanosatellite (Agasid, Rademacher, McCullar, & Gilstrap, 2010). In this configuration, the parameters after which we should look are thermal expansion coefficients. Indeed, if differences on these parameters exist through the structure, some components can undergo differential stresses and optical quality could degrade.

[40] What is interesting is that the user can specify if rays have to be included to the optical system. One can also add bunch of rays with different incidence angles or from given origin points. I therefore included the rays that could be visible on previous 2D and 3D views of the telescope inside the sixth design CAD model.

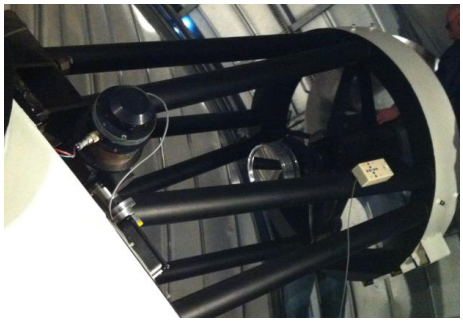

Figure 142 - Cassegrain truss structure (*1m* diameter Cassegrain telescope of the Observatory of Calern)

Even if the second method seems to be more accurate, we decided to implement the first one to benefit from $OUFTI$-1's experience. I therefore employed the same parts as the ones used by $OUFTI$-1: endless screws, midplane standoff, spacers and $M3$ screws. The midplanes are pieces that intend to fix the endless screws to the Cubesat platform with the help of $M3$ screws. As they are four endless screws, four midplanes and four $M3$ screws are needed. These are shown in Figure 143. Each midplane has two holes: one to hold the endless screw and the other one for the $M3$ screw. In addition spacers are aimed to separate the different parts that are fixed on the endless screws.

Figure 143 - Midplane standoff and *M3* screw

I created a cross-shape fastener that can host the primary inside an annular ring, as illustrated in Figure 144. The centre hole inside the piece is of course to let light pass.

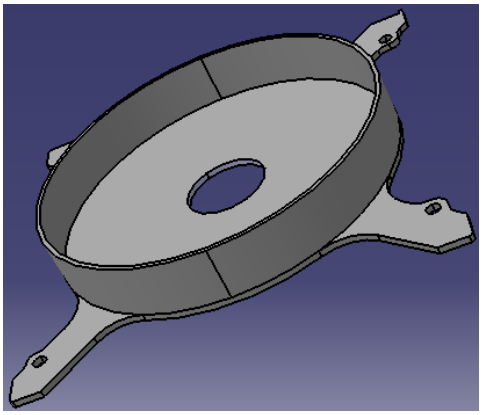

Figure 144 - Primary mirror fixation

Each of the branches of this fixation has a hole in which the endless screws can be inserted. The circular mirror has an advantage over the squared-profile mirror when designing such a

fixation. Indeed, rotational symmetry designs often lead to circular symmetry in their mounts. It usually simplifies their design because a continuous force can be applied around their rims. Even if great forces can be applied with such mountings, the assembler has to keep in mind that this can deform the optical surfaces and degrade their performance (Yoder, 2008). Since the mirrors here are very small and stiff, this should not be a problem. The problem appears when very large mirrors are used and that the mirror's deformations have to be balanced by applying forces on multiple contact points behind the mirror.

Then, the detector and proximity electronics had to be placed. The position of the detector is determined from the optical analyses. Since no more space was available behind the detector (See Figure 145), I had to place a proximity electronic card before the focal plane. In this configuration the card must be drilled in its centre to let the light pass and reach the detector[41]. These two electronic cards have small holes at their corners through which the endless screws pass and they are separated with $25\ mm$ spacers as it was actually done in $OUFTI$-1. Other spacers were placed between the drilled electronic card and the primary mirror. Spacers are expected between the primary mirror and the upper plate, but are not shown in the following figures.

The entirely[42] mounted system is presented in Figure 145. One side plate is hidden for clarity.

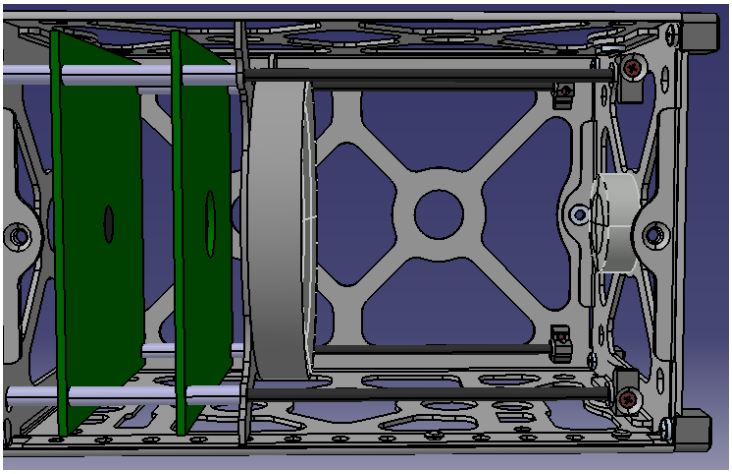

Figure 145 - Payload assembly

Such a disposition may be a problem as far as the thermal design is concerned. Indeed, the electronics might dissipate a lot. Therefore, the primary mirror could undergo thermal variations while the secondary mirror sees deep space. Such gradients can be taken into account in more complex thermal analyses with Code V. Eventually, a complete thermal analysis can be carried out within the ESATAN-TMS software and a thermo-mechanical design in Samcef, for example.

[41] I asked to a few Electrical Engineering students if it was possible and I was answered that it was.
[42] The filter is not included in this model but there is far enough place between the two mirrors. Indeed, custom sizes can be requested if standard ones do not fit the actual configuration (Princeton Instruments).

5.4. Baffle system

This section illustrates a preliminary study of the optical baffle of such a system. Indeed, Cassegrain telescope always suffer from stray light when they are not provided with a baffle system (Fischer, Tadic-Galeb, & Yoder, 2008). In general, reflective systems such as Cassegrain telescopes are equipped with two baffles which consist in two truncated cones situated near the primary and secondary mirrors (Terebizh, 2001). Without such baffles, the image object would be washed-out (Agasid, Rademacher, McCullar, & Gilstrap, 2010).

Different sources of stray light may perturb image acquisitions like a bright source shining in front of the system that reaches the detector as unwanted light. In Cassegrain systems, this can happen by "straight shots" as presented in Figure 146 (Gauvin & Freniere).

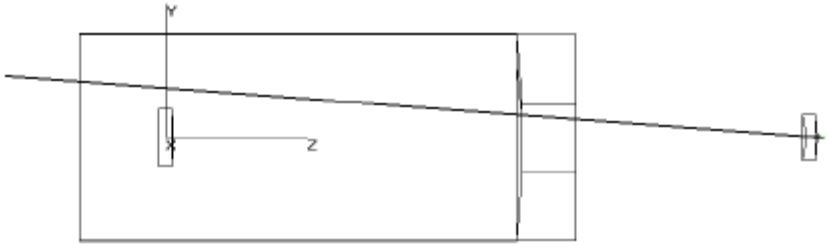

Figure 146 - Straight shot (Gauvin & Freniere)

Straight shots can occur especially when the central obstruction is loo large[43]: light out of the FoV can thus come into the telescope, pass next to the secondary mirror and through the primary hole and then strike the detector. This phenomenon can lead to catastrophic results if sunlight for example is allowed to enter the telescope (Gauvin & Freniere). With regards to the straylight the sixth design, with its smaller secondary mirror, is thus better suited than the first one. In addition, the strategy to observe the Io's torus in eclipse suppresses the stray light from the sun effects. Other sources, however, must be taken into account such as the Earth or the Moon. Detailed analyses are then necessary.

One way to eliminate these straight shots is to elaborate baffles that avoid such mechanisms. These rays that do not follow the typical two-reflections path and bypass the two mirrors have to be filtered in order to get high-quality images. Analytical algorithms were developed in order to design the optimal baffle for any Cassegrain telescope. For example, Terebizh elaborated an analytical algorithm based on ray-tracing formulas in order to get the optimum configuration of baffles. The optimum situation occurs when the obstruction is the smallest while still blocking the straight-shot rays. This situation is unique and depends on the telescope characteristics (Terebizh, 2001). This algorithm actually consists in minimizing an error function while using the ray-tracing analytical formulas and gives the exact solution for an optimal baffle design. A representation of baffles that filter

[43] Indeed, the larger secondary mirror's diameter, the larger needed primary mirror's hole.

straight shot rays is presented in Figure 147 (Agasid, Rademacher, McCullar, & Gilstrap, 2010).

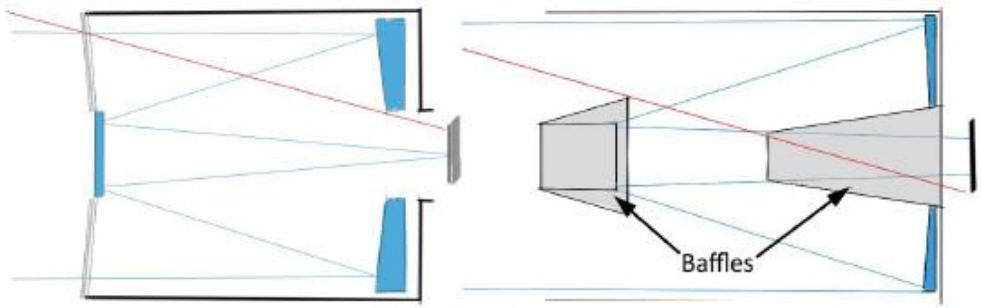

Figure 147 - Example of possible baffles (Agasid, Rademacher, McCullar, & Gilstrap, 2010)

What is done here is a preliminary study to approximate the optimum solution. In fact, by using several ray bundles with the help of optical softwares, we can design the needed baffles for a Cassegrain telescope. A first on-axis ray bundle has to be traced, then a second one back from the detector to the secondary and finally a third one which takes into account the FoV of the system[44]. These three ray bundles are represented in Figure 148. These latter are the most critical since they are the rays which limit the size of the baffles (Gauvin & Freniere).

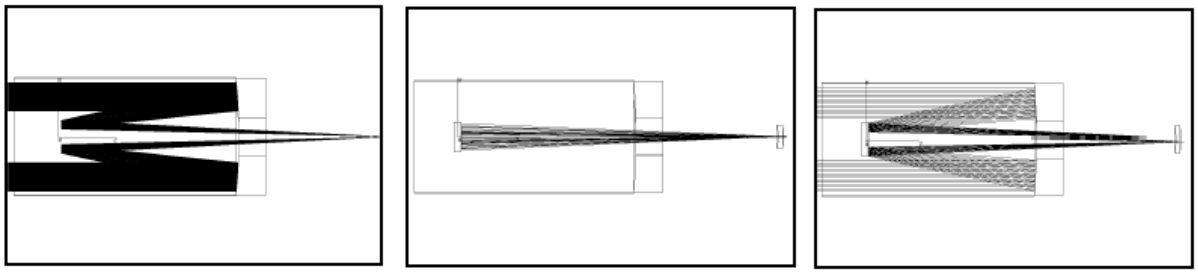

Figure 148 - Ray bundles for baffle design: on-axis *(Left)*, back from the detector *(middle)* and off-axis *(right)* (Adapted from (Gauvin & Freniere))

The off-axis ray bundle is used in order to determine the secondary baffle that slightly vignettes these rays. We have to start from the outside of the secondary mirror and extend the tube till reaching the most inner ray of the off-axis bundle. Then, the method to create the primary baffle is the following: extruding a tube from the primary hole boundaries that follows the inside FOV ray bundle while verifying whether any of these off-axis rays hit the detector or on-axis ray bundles (Gauvin & Freniere).

In Figure 149 is represented an example of each step of the baffles' construction and the resulting device.

[44] These third off-axis rays have thus an incident angle equal to the SFoV of the optical system.

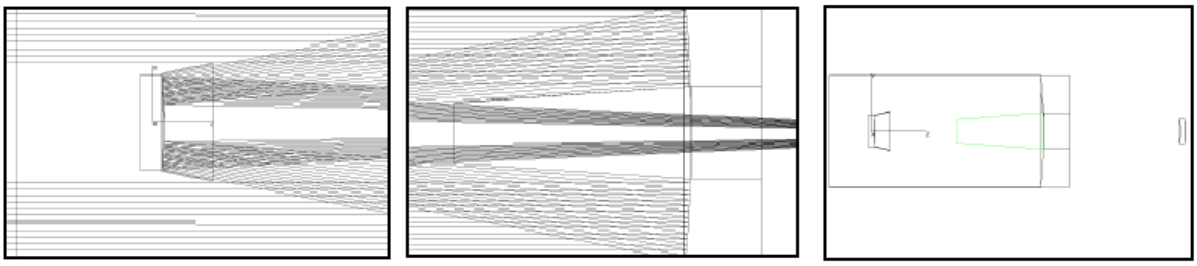

Figure 149 - Baffles' construction (Adapted from (Gauvin & Freniere))

I therefore performed this process with the help of Code V. I used the $View\ Lens$ option in order to trace the needed ray bundles. In Figure 150 the on-axis ray bundle is presented and is composed of 500 rays uniformly distributed over the telescope aperture. The vertical black straight line before the secondary mirror in Catia is actually the virtual obscuration surface which is composed of multiple points. The rays outside the secondary mirror pass through this surface without being perturbed whereas the rays that reach the obscuration zone are blocked.

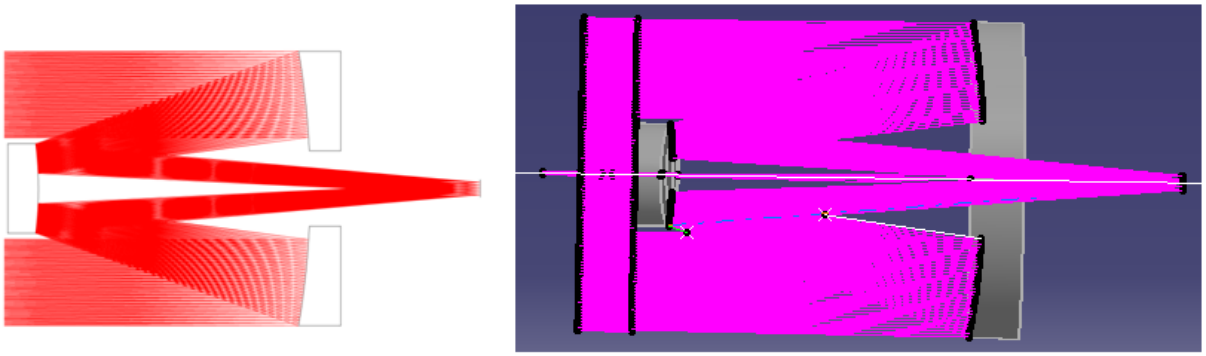

Figure 150 - On-axis ray bundle of the sixth design in Code V and Catia

The way I actually performed the introduced method was to print a large view of each ray bundle in order to apply the appropriate operations by hand. This is of course not the most accurate method but it is the easiest one. Once I had the baffle dimensions, I then did the same operations with Catia in order to check them and realize CAD models of the baffles.

For a more detailed optical design, the Terebizh algorithm or a computer program as ASAP shall be used to get high-quality results. This approach here only consists in a preliminary study and the results quality is therefore not the same as that needed when fabricating the optical system.

In Figure 151 the primary and secondary baffles' CAD models are presented. These are rotationally symmetric bodies that have to be placed on their respective mirror to block the straight shot rays. The secondary mirror baffle also has a first cylinder with the exact size to cover the outer diameter of the secondary mirror. This way, the baffle can be positioned easily around the secondary mirror.

The material of the baffles shall be light for mass-saving purposes and the coating is such that light is absorbed in the considered wavelength range for which the detector is sensitive which shall be the FUV.

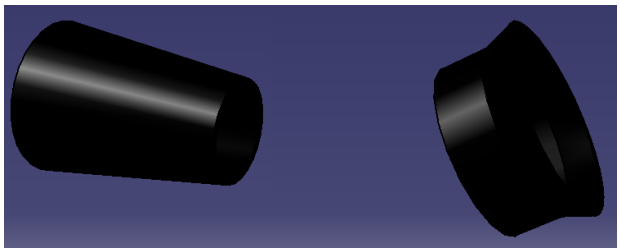

Figure 151 - Primary and secondary baffles *CAD* models

Antireflection coatings are available from CVI Melles Griot for example. A suitable one for the considered wavelength of $172.5\ nm$ is presented in Figure 152 (CVIMellesGriot). This coating has a reflectivity lower than 1% in the FUV spectral range.

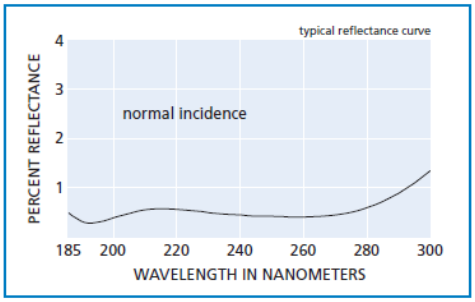

Figure 152 - Antireflection coating in the FUV spectral range (CVIMellesGriot)

Figure 153 presents the whole[45] assembly of the Cubesat and the optical parts.

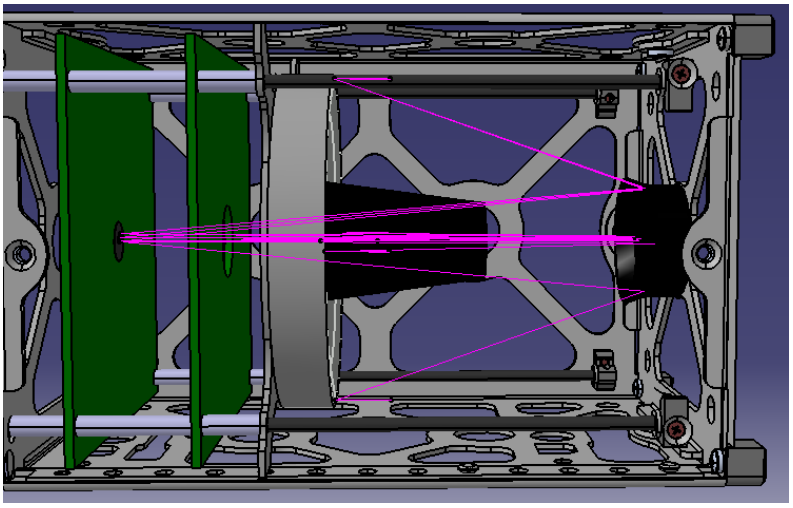

Figure 153 - Baffles positioned into the Cubesat structure

We can see that the marginal rays of the system, those who reach the primary mirror edge, graze both mirrors' baffles and then reach the detector. The total mass of the mirrors is

[45] Without the filter.

approximately equal to $150\ g$ while that of the total assembly approaches $600\ g$. The centre of gravity of the system is near the primary mirror since it is the heaviest part of the internal components.

Generally, these Cassegrain telescope baffles are usually complemented by another one that encompasses the overall optical system. It consists in a set of annular vanes the goal of which is to minimize the effect of light reflections on the outside tube of the telescope (Agasid, Rademacher, McCullar, & Gilstrap, 2010). This system is depicted in Figure 154. The same system was presented with the THEIA optical payload of the ALL-STAR Cubesat.

Figure 154 - Annular baffle system

In order to prevent the last designed telescope to suffer from such reflections, we could incorporate the entire optical system inside a black box attached to the endless screws. Vanes can be added inside the box, as presented in Figure 154, to decrease stray light effects. Indeed, in the configuration presented in Figure 153, light reflections appear due to the reflective character of the Cubesat inside walls. Another solution is to paint the inside of the Cubesat with an adequate coating in order to attenuate these reflections. The same coating as that of the baffles may be used for example.

In this work real problematic sources may enter the FoV when targeting the Io's torus during the considered period of time. This also depends on the Cubesat's orbit, but this parameter remains uncertain.

An ASAP analysis is then necessary to analyze the effects of stray light in the system. This software is a non sequential program, as opposed to Code V, that can perform stray light analyses. Since it is non sequential optical software, surfaces can be defined in any order, this do not change anything to the problem. The virtual surface that I presented before in order to simulate the secondary mirror obscuration is not needed in this case. Random directions rays throughout the system can be generated and all kind of reflections can be simulated. Indeed, the rays go from one surface and come back to it after multiple reflections since the software is non sequential and these mechanisms are well suited for stray light evaluation inside an optical system.

5.5. Calibration

The calibration of the telescope has to be performed first on the ground and if possible on orbit to take into account real space conditions. This latter could be achieved with the help of another telescope that takes a picture of the Io's torus at the same time (Salvador, 2012).

UIT was calibrated for example on the ground with the help of another Cassegrain telescope. A hydrogen lamp was placed at this second telescope's focal point to illuminate UIT by a simulated star (Stecher, et al., 1992).

The calibration of HUT was achieved in orbit by using a quartz mercury discharge tube to detect and track the sensitivity degradation of the optical system. However, this could not perform wavelength and photometric calibrations (Durrance, Kriss, Blair, Kruk, & Espey, 1994).

The instrument is for the moment calibrated at $20°C$, the default optimization temperature of Code V. This is also approximately the temperature in a clean room where the instrument will be assembled and tested optically. Further analyses are required to know more specifically the defocus and changes induced at a different temperature.

5.6. Mass and power budgets

The mass budget when using the $iADCS\text{-}100$ is exposed hereafter[46]. Deployable solar panels are also taken into account. The power and mass of the $iADCS\text{-}100$ are commercially available values.

Item	Mass (g)
Mirrors	150
Detector	300
Proximity electronics	500
On-board computer	500
iADCS-100	250
Structure	800
Deployable solar arrays	2000
Total	4500
Total (20% margin)	5400

Table 29 - Mass budget of the satellite

[46] The other values are taken from: (Salvador, UV imager onboard a 3U Cubesat platform: Preliminary feasibility study, 2012)

The power budget is illustrated in Table 30.

Item	Power (W)
Detector	5
Proximity electronics	5
On-board computer	10
iADCS-100	2
Total	22
Total (20% margin)	26.4

Table 30 - Power budget of the satellite

Conclusion

This feasibility study investigated the implementation of an ultraviolet imager onboard a Cubesat platform. After a brief presentation of the scientific objectives of the mission, the requirements and suitable detectors were introduced. Similar Cubesat projects were also studied to benefit from their experience when elaborating the Cubesat's subsystems.

A mission analysis was then carried out to identify the available observation periods by considering different orbits. These accesses were highlighted with the help of the STK software. A suitable constellation was also envisaged to observe the Io's torus during the whole Juno's lifetime.

A brief optics theory summary was subsequently proposed in order to understand the concepts of the following optical design chapter. Preliminary calculations of the field of view and the focal length were first needed. Commercial filters and coatings were then presented. Moreover, a photometric budget was accomplished to verify that the eclipse duration was long enough to reach the desired signal-to-noise ratio. The optical design process then started.

A final design was achieved through several modifications and adaptations of the first preliminary studies. Indeed, this first design was aimed to check the viability of implementing our Cassegrain telescope in a $1.5U$ Cubesat. I therefore verified that this could be done with a first short focal length system.

Then, I tried to increase the focal length in order to make it useful as long as possible during the mission period of time. What I obtained was a more specific telescope the secondary mirror of which was much smaller. It actually also improved the SNR.

After the focal length of the system was increased, I tried to enlarge the considered FoV in order to take into account the pointing errors of the spacecraft. I then had to tackle with a few problems: the Cassegrain solution did not permit to image a large enough FoV. I thus tried another solution: the Ritchey-Chrétien telescope.

At this point, the optical system was able to image the Io's torus during the whole mission and with a wide enough FoV. However, as explained in Appendix B, omitted constraints led me to an exotic design that could not actually be fabricated and I had to find a solution to get another working optical system. Thus I finally came back to a previous design and imposed additional constraints. The fourth design resulted from these operations.

In the fifth design, the enlarged spectrum was also taken into account. This new optimization process did not really modify the system but was in fact useful to check if the optical performance were still verified.

A new problem then appeared: the system was too sensitive with respect to manufacture tolerances. In fact, small fabrication errors could lead to large optical degradations. The predicted optical performance of the system could then be largely overestimated. The sixth design was thus the solution since relaxed constraints permitted to reach a more stable equilibrium point.

I discovered that neglecting tiny details led to large problems at some times. Tackling with these problems is actually the most rewarding experience that I keep from this work since I had to find solutions and check them afterwards. Even if optimizing a "simple" Cassegrain telescope seems to be an easy task, this work shows that it can sometimes be quite hard if the user omits some critical details that can easily put himself to rout.

Perspectives

The final design verifies all the requirements that were established in order to achieve the scientific goals. Degradations of the MTF due to jitter were also examined. However, the coatings were not considered and the reflectivity of the mirrors was supposed to be equal to 100% at all wavelengths. Further studies, out of the scope of this work, are required to take into account these parameters. A detailed stray light analysis must be performed to assess the baffle's efficiency. Indeed, Code V is not able to perform such analyses since it is a sequential program. The ASAP software may be used for this operation for example. A ghost analysis shall also be executed.

The electronics and the detector also have to be selected. Several kinds of UV sensors are available and studies are needed to identify the most appropriate to the present case. In particular, we should check if the use of a MCP is mandatory since avoiding high voltages simplifies the system's design and increases its reliability.

A specific thermal design must be elaborated to identify the temperatures that the spacecraft will undergo in space. A thermo-mechanical model of the instrument may also identify the vibrations to which the spacecraft is subject. A more accurate jitter analysis could then be accomplished.

Eventually, the manufacturability of the mirrors has to be checked to know if they are not too expensive for a Cubesat mission, specially the secondary mirror.

Bibliography

Agasid, E., Rademacher, A., McCullar, M., & Gilstrap, R. (2010). *Study to Determine the Feasibility of a Earth Observing Telescope Payload for a 6U Nano Satellite.* NASA.

BenMoussa, A., Hochedez, J., Schühle, U., Schmutz, W., Haenen, K., Stockman, Y., et al. (2005). *Diamond Detectors for LYRA, the solar VUV radiometer on board PROBA2.* Elsevier.

BerlinSpacetechnologies. (n.d.). *iADCS-100*. Retrieved 2013, from Berlin Space Technologies: www.berlin-space-tech.com

Bernhardt, M., Borth, A., Brennan, R., Galgana, E., Gangar, P., Kemis, A., et al. (2009). *RTICC- Rapid Terrestrial Imaging Cubesat Constellation - Preliminary Design Report.* University of Washington - Department of Aeronautics and Astronautics.

BlueCanyonTechnologies. (n.d.). *XACT - fleXible ADCS Cubesat Technology.* Retrieved 2013, from Blue Canyon Technologies: http://www.BlueCanyonTech.com

Bonfond, B., & Kintziger, C. (2013, March 26). *(Personal communications).* March 26th 2013.

Bonfond, B., Grodent, D., Gérard, J.-C., Stallard, T., Clarke, J.-T., Yoneda, M., et al. (2011). *Auroral evidence of Io's control over the magnetosphere of Jupiter.*

Bouwmeester, J., Aalbers, G., & Ubbels, W. *Preliminary Misson Results And Project Evaluation of the Delfi-C³ Nano-Satellite.* Delft University of Technology.

Brown, J. (2010). *ALL-STAR Microgravity Structural Deployment and Attitude Control Test.* Boulder: University of Colorado.

Conneely, T., & Lapington, J. (2011). *Picosecond imaging using a capacitive charge division readout.* University of Leicester.

Cubesat. (2013). *Cubesat*. Retrieved 2013, from http://www.cubesat.org/index.php

CubeSatKit. (n.d.). *MAI-200 ADACS flyer.* Retrieved 2013, from CubeSat Kit: http://www.cubesatkit.com/

Cutler, J. W., Ridley, A., & Nicholas, A. (2011). *Cubesat Investigating Atmospheric Density Response to Extreme Driving (CADRE).*

CVIMellesGriot. *All Things Photonic - The CVI Melles Griot Technical Guide.* CVI Melles Griot.

Daw, A. (2012). *Internal Research and Development (IRAD) - Step-2 Proposal.* NASA.

DelfiSpace. (n.d.). *Delfi-C³*. Retrieved 2013, from Delfi Space: http://www.delfispace.nl/index.php/delfi-c3/delfi-c3-mission

Dell'Elce, L., & Kintziger, C. (2013). *(Personal Communications).*

DelMarPhotonics. (2013). *Del Mar Phtonics*. Retrieved 2013, from Del Mar Photonics: http://www.dmphotonics.com/MCP_MCPImageIntensifiers/microchannel_plates.htm

Dixon, W. V., Blair, W. P., Kruk, J. W., & Romelfanger, M. L. (2013). *The Hopkins Ultraviolet Telescope: The Final Archive.* Publications of the Astronomical Society of the Pacific.

Durrance, S. T., Kriss, G. A., Blair, W. P., Kruk, J. W., & Espey, B. R. (1994). *The Hopkins Ultraviolet Telescope Handbook.* Baltimore, Maryland: Center for Astrophysical Sciences - The Johns Hopkins University.

eoPortal. (2013). *Satellite Missions*. Retrieved 2013, from eoPortal: https://directory.eoportal.org/web/eoportal/satellite-missions/a/all-star

Feautrier, P. (2011). *Détection UV-VISIBLE-IR.* IPAG.

Fischer, R. E., Tadic-Galeb, B., & Yoder, P. R. (2008). *Optical System Design.* Mc Graw Hill.

Gauvin, M. A., & Freniere, E. R. *Reducing stray light in Opto-Mechanical Systems.* Lambda Research Corporation.

Genberg, V. L., Michels, G. J., & Doyle, K. B. *Integrated modeling of jitter MTF due to random loads.* MIT.

Goldstein, A. M., & Kady, C. T. (2012). *Active Pointing, on a Budget - The Sun Devil Satellite 1 (SDS-1) and The Flare Inition Doppler Imager (FIDI).* Sun Devil Satellite Laboratory.

Goodman, J. W. (1996). *Introduction to Fourier Optics.* McGraw-Hill.

Habraken, S., Salvador, L., & Kintziger, C. (2013, February 27). *(Personal communications).* February 27th 2013.

Habraken, S., Salvador, L., & Kintziger, C. (2013, March 19). *(Personal communications).* March 19th 2013.

Halain, J., & Auchère, F. (2010). *EUI EUV filters specifications.* Liège: CSL Internal Report.

Joseph, C. L. (1995). *UV Image Sensors and Associated Technologies.* Springer - Experimental Astrophysics.

Kalman, A., Reif, A., Berkenstock, D., Mann, J., & Cutler, J. (2008). *MISC - A Novel Approach to Low-Cost Imaging Satellites.* 22nd Annual AIAA/USU Conference on Small Satellites.

Kerschen, G., & Kintziger, C. (2013, March 13). *(Personal Communications).* March 13th 2013.

Lapington, J. (2007). *Detector Technologies for WSO.* Leicester: WSO Detector Workshop.

Lecat, J., Thome, M., & Defise, J. (2005). *PROBA II SWAP - Design Report.* CSL Internal Report.

Lee, S. *CubeSat Design Specification Rev.12.* San Luis Obispo: Cal Poly.

MathWorks. (n.d.). Retrieved 2013, from MathWorks: http://www.mathworks.nl/products/global-optimization/examples.html?file=/products/demos/shipping/globaloptim/opticalInterferenceDemo.html

MaylandAerospace. (2009). *IMI-100 Miniature 3-axis ADACS Product Specification.* Retrieved 2013, from miniADACS: http://www.miniADACS.com

Mazy, E., Lecat, J., & Defise, J. (2003). *SWAP Optical Design and Performances.* Angleur: CSL.

Mazzoli, A., & Kintziger, C. (2013, March 28). *(Personal communications).* March 28th 2013.

PhysOrg. (2012). *Students building satellite to help NASA learn more about solar flares.*

Pong, C. M., Lim, S., Smith, M. W., Miller, D. W., Villaseñor, J. S., & Seager, S. (2010). *Achieving high-precison pointing on ExoplanetSat: Initial feasibility analysis.* MIT Open Access Articles.

Princeton Instruments. (n.d.). Retrieved 2013, from Princeton Instruments: http://www.princetoninstruments.com/products/optical_filters/curve_library.aspx#1

Pumpkin, I. (2013). *3D CAD Design.* Retrieved 2013, from Cubesat Kit: http://www.cubesatkit.com/content/design.html

Rowland, D. (2009). *The Firefly Mission - Understanding Earth's most powerful natural particle accelerator.* CubeSat Developer's Workshop.

Salvador, L. (2012). Spacecraft payload design. From http://www.amazon.com/Spacecraft-Thermal-Control-Handbook-Volume/dp/188498911X.

Salvador, L. (2012). *UV imager onboard a 3U Cubesat platform: Preliminary feasibility study.* CSL Internal report.

Salvador, L., & Kintziger, C. (2013). *(Personal Communications).*

Segert, T., & Kintziger, C. (2013, March 23). *(Personal communications).* March 4th 2013.

Selva, D., & Krejci, D. (2011). *A survey and assessment of the capabilities of Cubesats for Earth observation.* Elsevier.

Siegmund, O., Vallerga, J., McPlate, J., & Tremsin, A. (2004). *Next generation microchannel plate detector technologies for UV Astronomy.* SPIE Digital Library.

Smith, M. W., Seager, S., Pong, C. M., Villaseñor, J. S., Ricker, G. R., Miller, D. W., et al. (2012). ExoplanetSat: Detecting transiting exoplanets using a low-cost CubeSat platform. In E. Jacobus, & M. Oschmann, *Space Telescopes and Instrumentation 2010: Optical, Infrared, and Millimeter Wave.* Cambridge.

Smith, W. J. (2008). *Modern Optical Engineering - The Design of Optical Systems.* Mc Graw Hill.

Stecher, T. P., Baker, G. R., Bartoe, D. D., Bauer, F. H., Blum, A., Bohlin, R. C., et al. (1992). *The Ultraviolet Imaging Telescope: Design and Performance.* The Astrophysical Journal.

Steffl, A. J., Stewart, A. I., & Bagenal, F. (2004). *Cassini UVIS observations of the Io plasma torus.* Science Direct.

Synopsys. (2002). *Code V Prompting Guide.* Optical Research Associates.

Synopsys. (2012). *Code V Reference Manual.* Optical Research Associates.

Tantalo, F. J. (1996). *Modeling the MTF and Noise Characteristics of an Image Chain fr a Synthetic Image Generation System.* Rochester Institute of Technology.

Terebizh, V. (2001). *Optimal Baffle Design in a Cassegrain Telescope.* Kluwer Academic Publishers.

Thomas, N., Bagenal, F., Hill, T., & Wilson, J. (2004). The Io Neutral an Plasma Torus. In F. Bagenal, T. E. Dowling, & W. B. McKinnon, *Jupiter. The planet, satellites and magnetosphere* (pp. 561-591). Cambridge: Cambridge University Press.

Thomsen, M. (2005). *Michael's List of Cubesat Satellite Missions*. Retrieved 2013, from http://mtech.dk/thomsen/space/cubesat.php

Uslenghi, M. (2007). *Detectors for the FCU - WSO/UV.* Leicester: WSO Detector Workshop.

Verhoeven, C., & Ubbels, W. *DELFI-C³, past, present and future.* Delft University of Technology.

Waltham, N., Prydderch, M., Mapson-Menard, H., Pool, P., & Harris, A. (2006). *Development of a thinned back-illuminated CMOS Active Pixel Sensor for Extreme Ultra-Violet Spectroscopy and Imaging in Space Science.* 7th International Conference on Position Sensitive Detectors.

Weggelaar, W. (2008). *Delfi-C³ - Realizing the First Dutch Student Nanosatellite & OSCAR.* Delft University of Technology.

Wilson, R. (2007). *Reflecting Telescope Optics - Basic Design Theory and its Historical Development.* Springer.

Woellert, K., Ehrenfreund, P., Ricco, A. J., & Hertzfeld, H. (2010). *Cubesats: Cost-effective science and technology platforms for emerging and developing nations.* Elsevier.

Yoder, P. R. (2008). *Mounting Optics in Optical Instruments.* SPIE Press.

Appendix A
Obscuration effect on the MTF

A virtual surface must be inserted before the primary mirror in order to take into account the obscuration of the secondary mirror. Figure 155 illustrates the resulting error on the MTF curves if this surface is neglected.

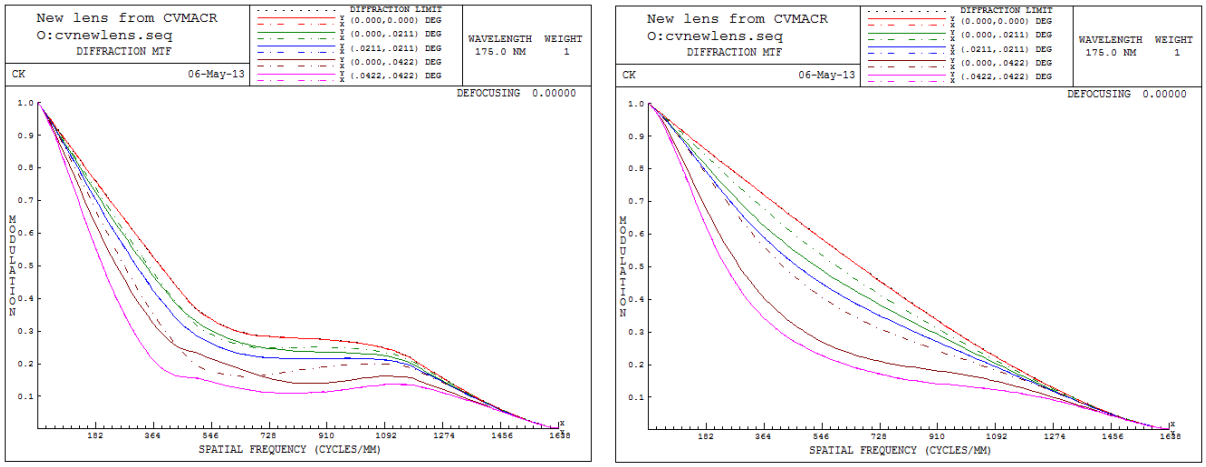

Figure 155 - *MTF* with obscuration vs. *MTF* without obscuration

The diffraction limited curve is intensely deformed and is not a simple decreasing line. In fact, the response of the system drops at low frequencies but raises slightly at high frequencies, although the cutoff frequency remains unchanged as illustrated theoretically in Figure 156. This is the consequence of shifting light from the central Airy disk to outer rings in the diffraction pattern (Smith W. J., 2008).

In Figure 156, the MTF curves are represented for different theoretical situations of obscuration. For situation A, no obscuration is inserted while it increases from a factor 0.25 in B to 0.75 in D.

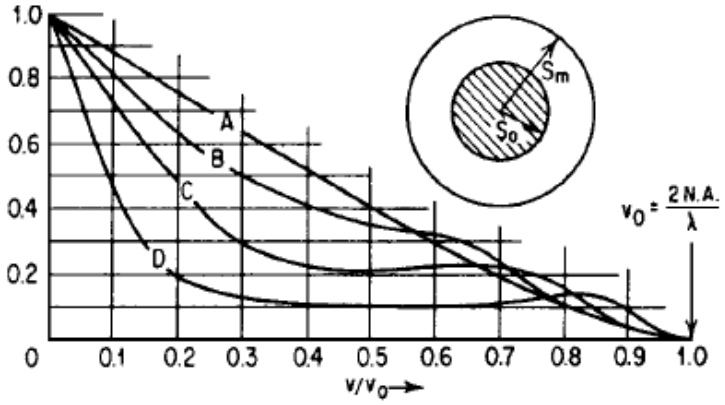

Figure 156 - The effect of central obscuration on the *MTF* of an aberration-free system (Smith W. J., 2008)

The same behaviour is represented in Figure 157 (Wilson, 2007)

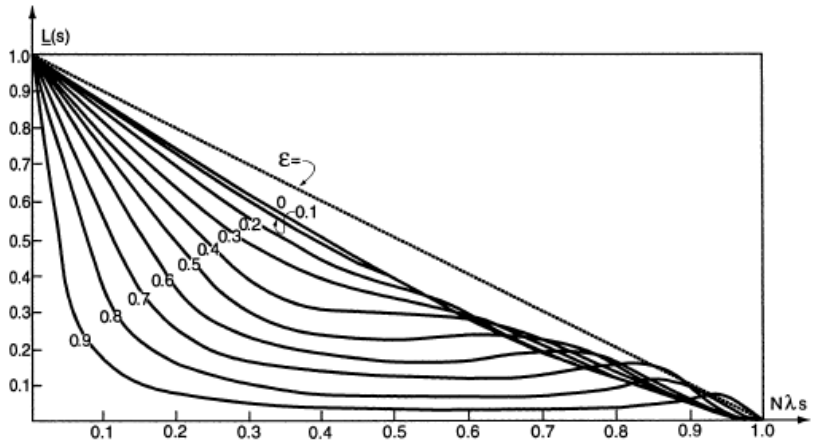

Figure 157 - *MTF* for a circular pupil free of aberration with central obstruction ε (Wilson, 2007)

In both Figure 156 and Figure 157, we recover the deformation behaviour of the MTF curves when an obscuration is inserted into the optical system. What we observed earlier practically is thus theoretically justified now.

This mechanism can be used as a benefit in specific applications. For example, a central obstruction could improve the resolution of double stars. An interesting limit case would be an infinitely narrow annular aperture ($\varepsilon \to 1$) giving a sharp peak near the limit of resolution. This would be actually the analogous situation of Young's double slit aperture in a $2D$ space with a peak occurring at the spatial frequency of the fringes (Wilson, 2007).

Appendix B
Mirror Manufacturability

Once I performed the optimization in order to get a Ritchey-Chrétien telescope, I did not enter any constraint that imposed a lower value for both mirrors' conic constants. I only input an upper limit.

Yet Code V found a conic constant of -16 for the secondary mirror. Fabricating a mirror with such a conic constant would either be extremely expensive or impossible (Mazzoli & Kintziger, 2013, March 28).

The fourth design that I first realized was thus theoretically acceptable but in practice infeasible. From a database of CSL, typical values for existing mirrors could be found. These are shown in Figure 158 and Figure 159.

The data are parameters of mirrors that were fabricated for real missions. In order for the mirrors to be practically manufacturable, additional constraints must be imposed. From the figure, we decided to select the following values.

Parameter	Value
Radius of curvature	$min\ 100\ mm$
Conic constant	$min\ -5$

Table 31 - New requirements on radius of curvature and conic constant

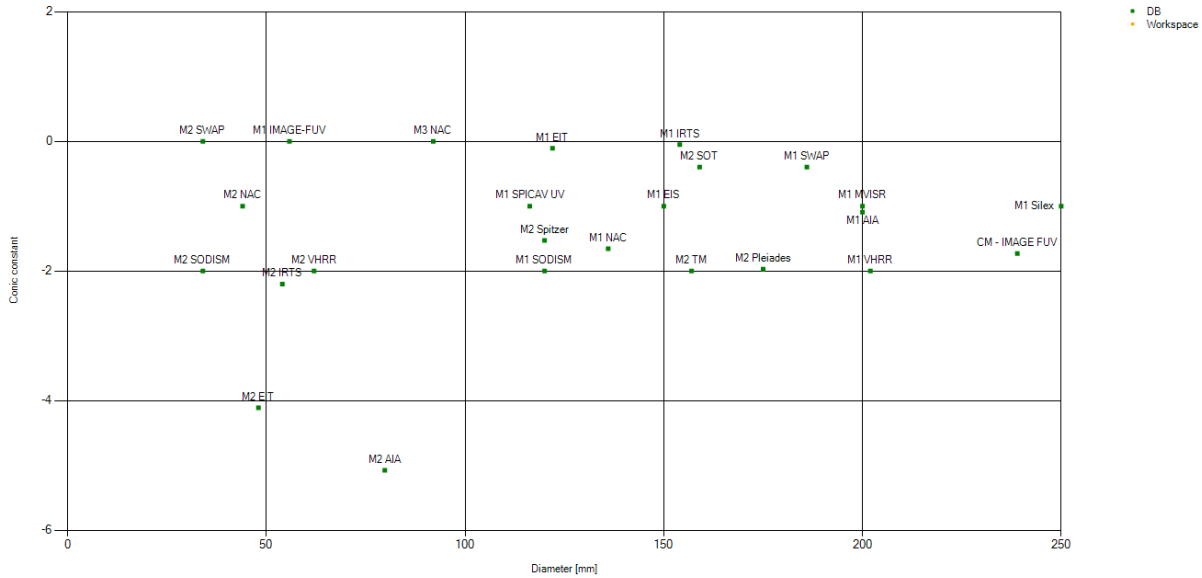

Figure 158 - Typical conic constant values (© CSL)

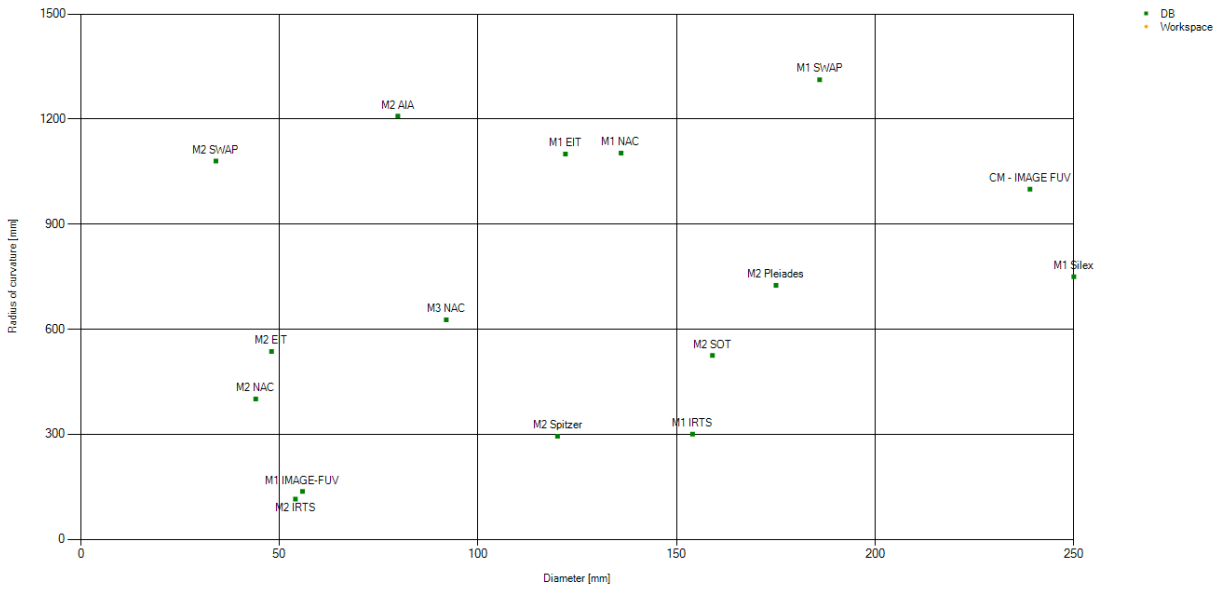

Figure 159 - Typical radius of curvature (© CSL)

Since the design was actually infeasible, I had to re-optimize it while taking into account these new requirements. Therefore, I entered these new constraints in Code V and tried to obtain a more feasible telescope.

The results were catastrophic. The spots of the generated systems were incredibly large and their optical performances a disaster. Since the system was highly optimized with respect to previous constraints, Code V did not manage to reach another optimized system for the new requirements.

This situation can be explained as follows (See Figure 160)(MathWorks). We can imagine this representation as "valleys" and "hills" that respectively replace the minimum and maximum solutions of the problem. If the solution 1 was the optimized problem of the fourth design and the solution 2 the one of the new constrained problem, since a great distance separates them, the algorithm is not able to go out from the first "valley", get through the intermediary "hills" and reach the right next "valley".

This is maybe the phenomenon that happened and hindered me to find a right solution of the problem (Mazzoli & Kintziger, 2013, March 28).

The advice that Alexandra Mazzoli gave me were to re-optimize a previous simpler design for which I had not yet too many constraints. I restarted the same operation on the second design, which exhibits a long focal length but a small FoV imaging ability. This is indeed the first design preceding the Ritchey-Chrétien solution (since the third design was not acceptable).

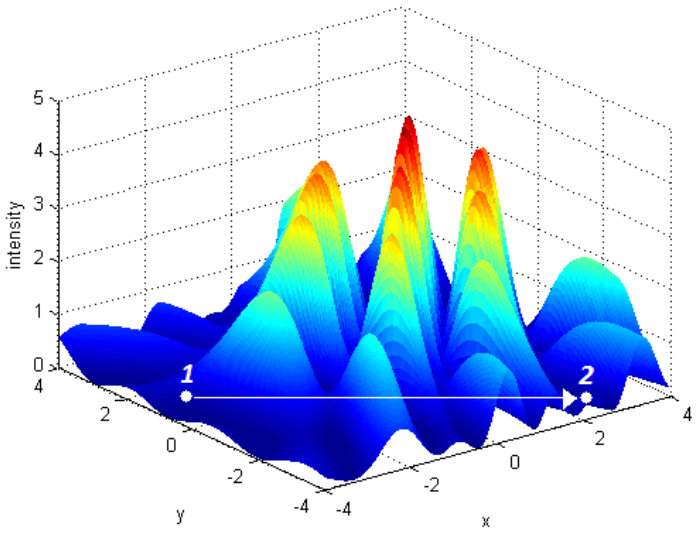

Figure 160 - Optimization problem example (MathWorks)

The telescope I obtained through this new optimization process was not acceptable. Actually, the spot diagram directly showed that the spot size was too large to be included into a single pixel.

What I decided to do was to relax a little bit the constraints on the backfocus and the mirrors' interdistance. Since my ultimate requirements were respectively $13\ cm$ and $8\ cm$ for each parameter, I had some margin left. The way I performed this task was to increase both parameters by $1\ mm$ at each step if the optimized system was not accepted. I finally reached an acceptable telescope for which backfocus and mirrors' interdistance were respectively equal to $128\ mm$ and $8\ cm$, i.e. the constraints implemented for the fourth design.

Appendix C
Tolerance study macro file

Some comments are introduced inside the macro in order to explain some of the commands. They all look like a first acronym which stands for the tolerance name, then the surface on which it is applied and finally its value (Synopsys, Code V Prompting Guide, 2002).

```
! Define tolerance
!*****************
 DEL TOL Sa                        ! Delete tolerance on all surfaces
 DEL CMP Sa                        ! Delete compensators on all surfaces
 FRZ Sa                            ! Froze all surfaces
 FRW 546                           ! Wavelength for fringe measurement

! Primary fabrication
!********************
 ^sur == (SLB S'Primary_mirror')
 DLF S^sur 5                        ! tol testplate
 DLR S^sur 0.001*(RDY S^sur)        ! tol radius
 DAK S^sur 0.005                    ! tol conic constant


! Primary alignment
!******************
!DIS S^sur..^sur 0.01              ! DSX + DSY = tol displacement of group
in X and Y
!DSZ S^sur..^sur 0.01              ! tol displacement of group in Z
!BTI S^sur..^sur 0.0001            ! BTX + BTY = tol tilt of group in XZ and
YZ
!BRL S^sur..^sur 0.005             ! tol rotate group about Z

 DEC S^sur 0.035                   ! DLX + DLY = tol displacement of surface
in X and Y
 DLZ S^sur 0.035                   ! tol displacement of surface in Z
 TIL S^sur 0.0001  !radians        ! DLA + DLB = tol tilt of surface about X
and Y
 DLG S^sur 0.001                   ! tol tilt of surface about Z

!TIR S^sur 0.005       !mm         ! TRX + TRY = alternate to TIL at CA (au
centre)

! Secondary fabrication
!**********************
 ^sur == (SLB S'Secondary_mirror')
 DLF S^sur 5                        ! tol testplate
 DLR S^sur 0.001*(RDY S^sur)        ! tol radius
 DAK S^sur 0.01                     ! tol conic constant


! Secondary alignment
!********************
!DIS S^sur..^sur 0.01              ! DSX + DSY = tol displacement of group
in X and Y
```

```
!DSZ S^sur..^sur 0.010            ! tol displacement of group in Z
!BTI S^sur..^sur 0.001            ! BTX + BTY = tol tilt of group in XZ and
YZ
!BRL S^sur..^sur 0.001            ! tol rotate group about Z

 DEC S^sur 0.035                  ! DLX + DLY = tol displacement of surface

in X and Y
 DLZ S^sur 0.035                  ! tol displacement of surface in Z
 TIL S^sur 0.0001                 ! DLA + DLB = tol tilt of surface about X
and Y
 DLG S^sur 0.001                  ! tol tilt of surface about Z

!TIR S^sur 0.005                  ! TRX + TRY = alternate to TIL at CA


! Define compensators
!********************

! Detector position

 XDC Si 0                          !control of x displacement of new axis
 YDC Si 0                          !control of y displacement of new axis
 ZDC Si 0                          !control of z displacement of new axis



! Save lens
!**********
 SAVE
C:\Users\hp\Documents\ULg\2Master\TFE\DesignCassegrain\CODEV\Optimisespectr
eelargi\temp1

 PTH SEQ
C:\Users\hp\Documents\ULg\2Master\TFE\DesignCassegrain\CODEV\Optimisespectr
eelargi

! Using tolfdif macro
!********************

 in tolfdif temp1 tol_crit_spotrms tol_auto YYNN
```